

DEVELOPMENT OF A NEW SEISMIC ISOLATOR NAMED “BALL RUBBER
BEARING”

A THESIS SUBMITTED TO
THE GRADUATE SCHOOL OF NATURAL AND APPLIED SCIENCES
OF
MIDDLE EAST TECHNICAL UNIVERSITY

BY

CENAN ÖZKAYA

IN PARTIAL FULFILLMENT OF THE REQUIREMENTS
FOR
THE DEGREE OF DOCTOR OF PHILOSOPHY
IN
CIVIL ENGINEERING

DECEMBER 2010

Approval of the thesis:

DEVELOPMENT OF A NEW SEISMIC ISOLATOR NAMED “BALL RUBBER BEARING”

submitted by **CENAN ÖZKAYA** in partial fulfillment of the requirements for the degree of **Doctor of Philosophy in Civil Engineering Department, Middle East Technical University** by,

Prof. Dr. Canan Özgen
Dean, Graduate School of **Natural and Applied Sciences**

Prof. Dr. Güney Özcebe
Head of Department, **Civil Engineering**

Assist. Prof. Dr. Alp Caner
Supervisor, **Civil Engineering Dept., METU**

Prof. Dr. Uğurhan Akyüz
Co-Supervisor, **Civil Engineering Dept., METU**

Examining Committee Members:

Prof. Dr. Polat Gülkan
Civil Engineering Dept., METU

Assist. Prof. Dr. Alp Caner
Civil Engineering Dept., METU

Prof. Dr. Murat Dicleli
Engineering Sciences Dept., METU

Prof. Dr. Kemal Önder Çetin
Civil Engineering Dept., METU

Prof. Dr. Mehmet Nuray Aydınoğlu
KOERI Earthquake Engineering Dept., Boğaziçi University

Date:

08 DECEMBER 2010

I hereby declare that all information in this document has been obtained and presented in accordance with academic rules and ethical conduct. I also declare that, as required by these rules and conduct, I have fully cited and referenced all material and results that are not original to this work.

Name, Last Name : Cenan Özkaya

Signature :

ABSTRACT

DEVELOPMENT OF A NEW SEISMIC ISOLATOR NAMED “BALL RUBBER BEARING”

Özkaya, Cenan

Ph.D., Department of Civil Engineering

Supervisor: Assist. Prof. Dr. Alp Caner

Co-Supervisor: Prof. Dr. Uğurhan Akyüz

December 2010, 205 pages

The experimental research presented in this dissertation aims to develop a new rubber-based seismic isolator type on the basis of the idea that the damping of a conventional annular elastomeric bearing (EB) can be increased by filling its central core with small diameter steel balls, which dissipate energy via friction inside the confined hole of the bearing during their movements under horizontal loads. The proposed bearing type is called “Ball Rubber Bearing (BRB)”. A large set of BRBs with different geometrical and material properties are manufactured and tested under reversed cyclic horizontal loading at different vertical compressive load levels. Effect of supplementary confinement in the central hole of the bearing to performance of BRB is studied by performing some additional tests. Test results are used to develop design equations for BRB.

A detailed non-linear finite element model is developed to verify the test results. The proposed analytical model is determined to simulate the structural hysteretic behaviour of the bearings. In design of BRBs, the proposed design guideline can be used in conjunction with the proposed non-linear finite element analysis.

Extensive test results indicate that steel balls do not only increase the energy dissipation capacity of the elastomeric bearing (EB) but also increase its horizontal and vertical stiffness. It is also observed that the energy dissipation capacity of a BRB does not degrade as the number of loading cycles increases, which indicates remarkably reliable seismic performance.

Keywords: Seismic Isolator, Rubber, Steel Ball, Energy Dissipation, Friction

ÖZ

BİLYELİ KAUÇUK MESNET OLARAK ADLANDIRILAN YENİ BİR SİSMİK İZOLATÖRÜN GELİŞTİRİLMESİ

Özkaya, Cenan

Doktora, İnşaat Mühendisliği Bölümü

Tez Yöneticisi: Yrd. Doç. Dr. Alp Caner

Ortak Tez Yöneticisi: Prof. Dr. Uğurhan Akyüz

Aralık 2010, 205 sayfa

Bu tezde sunulan deneysel çalışma yaygın olarak kullanılan elastomer mesnedin ortasında açılan deliğe küçük çaplı çelik bilyeler doldurulması ve bu bilyelerin yatay yüklerden kaynaklanan ötelenmeler altında sürtünme vasıtası ile deliğin içerisinde enerji sönümlenmesi neticesinde elastomer mesnedin enerji sönümlenme kapasitesini arttırarak yeni bir kauçuk esaslı sismik izolatör tipi geliştirmeyi amaçlamaktadır. Önerilen mesnet tipi “Bilyeli Kauçuk Mesnet (BKM)” olarak adlandırılmaktadır. Değişik geometrik ve malzeme özelliklerine sahip çok sayıda BKM üretilmiş ve değişik düşey yükler altında tersinir çevrimsel yatay yükleme testleri gerçekleştirilmiştir. Mesnedin ortasındaki delikteki ilave sargı etkisinin BKM’in performansına olan etkisini araştırmak için bazı ilave testler yapılmıştır. Test sonuçları, BKM’in tasarım denklemlerini geliştirmek için kullanılmıştır.

Test sonuçlarını doğrulamak için detaylı bir lineer olmayan sonlu elemanlar modeli oluşturulmuştur. Önerilen analitik modelin mesnetlerin histeretik davranışını yansıttığı

görülmüştür. BKM'lerin tasarımında, önerilen lineer olmayan sonlu elemanlar modeli ve tasarım denklemleri beraber kullanılabilir.

Çok sayıda test sonucu, çelik bilyelerin enerji sönümlemekle beraber aynı zamanda elastomer mesnetin yatay ve düşey rijitliğini de arttırdığını ortaya koymuştur. Bilyeli Kauçuk Mesnetlerin (BKM) enerji sönümleme kapasitelerinin artan yük döngüleri altında azalmadığı gözlemlenmektedir ki bu da BKM'in oldukça güvenilir sismik performansını ortaya koymaktadır.

Anahtar Kelimeler: Sismik İzolatör, Kauçuk, Çelik Bilye, Enerji Sönümleme, Sürtünme

ACKNOWLEDGEMENTS

This study was conducted under the supervision of Assist. Prof. Dr. Alp Caner. I wish to express my deepest appreciation to him for his suggestions in the creation of the scope of this study. Moreover, I am indebted to him for his criticism and encouragement throughout the study and my life.

I owe special thanks to my co-supervisor Prof. Dr. Uğurhan Akyüz for his continuous support during this study.

I would like to give my sincere thanks to Prof. Dr. Murat Dicleli, Prof. Dr. Kemal Önder Çetin, Prof. Dr. Polat Gülkan and Prof. Dr. Mehmet Nuray Aydınoglu for their precious contributions.

I owe special thanks to staff of Structural Mechanics Laboratory of Civil Engineering Department, METU.

I would like to give my thanks to Özdekan Rubber Industry for supplying elastomeric bearings with supplementary materials and for repairing the test equipment.

This study would be impossible without the financial support of TÜBİTAK. I present my special thanks to TÜBİTAK for financially supporting two research projects called 107M537 and 109M323.

Last, but not least thanks to my family for being with me all the way.

TABLE OF CONTENTS

ABSTRACT.....	iv
ÖZ.....	vi
ACKNOWLEDGEMENTS.....	viii
TABLE OF CONTENTS	ix
LIST OF TABLES	xii
LIST OF FIGURES	xiv
LIST OF SYMBOLS.....	xxi
ABBREVIATIONS.....	xxvi
CHAPTER	
1. INTRODUCTION.....	1
1.1. General.....	1
1.2. Objective and Scope	4
1.3. Summary of Findings	6
2. LITERATURE SURVEY	8
2.1. General.....	8
2.2. Seismic Isolation Systems.....	8
2.2.1. General Information on Rubber Isolators.....	8
2.2.2. General Information on Sliding Isolators.....	11
2.2.3. Other Systems	14
2.3. Studies on Rubber Isolators.....	14
2.3.1. Elastomeric Bearings (EBs).....	14
2.3.2. High Damping Rubber Bearings (HDRBs).....	18
2.3.3. Lead Rubber Bearings (LRBs).....	20
2.4. Studies on Sliding Isolators	23
2.4.1. Friction Pendulum System (FPS).....	23
2.4.2. Other Systems	23

2.5. Testing of Seismic Isolation Systems	24
2.6. Response of Seismically Isolated Structures	26
3. TEST SET UP & TESTING PROGRAM.....	29
3.1. General.....	29
3.2. Test Equipment	29
3.3. Data Acquisition System.....	32
3.4. Test Program	33
3.5. Mechanical Properties of BRBs	36
3.6. Materials Utilized in Test Bearings	37
3.7. Design of Test Bearings.....	39
4. DEVELOPMENT OF BALL RUBBER BEARING (BRB)	48
4.1. Initial Tests	48
4.2. Ball Rubber Bearings (BRBs)	48
4.3. Ball Rubber Bearing (BRB) Tests and Results	53
4.3.1. Effect of Presence of Steel Balls	53
4.3.2. Effect of Steel Ball Diameter.....	56
4.3.3. Effect of Diameter of Central Hole in the Bearing...	59
4.3.4. Effect of Magnitude of Horizontal Displacement	60
4.3.5. Non-linear Finite Element Analysis-Cyclic Loads...	62
4.3.6. Effect of Level of Vertical Compression Force	66
4.4. Vertical Compression Tests	74
4.5. Variation of Energy Dissipation Capacities (EDC) of Ball Rubber Bearings with Number of Cycles	83
4.6. Service Load Tests	85
4.7. Effect of Supplementary Confinement.....	87
4.7.1. Tests with Steel Washer Plates.....	87
4.7.2. Tests with FRP Wraps	91
5. DESIGN GUIDELINE	94
5.1. General.....	94
5.2. Yield Displacement (d_y)	94
5.3. Characteristic Strength (Q_d)	97
5.4. Secondary Stiffness (K_2)	100
5.4.1. $D/d=3.75$ (80 mm Hole Diameter)	102
5.4.2. $D/d=3.0$ (100 mm Hole Diameter)	103

5.4.3. D/d=2.5 (120 mm Hole Diameter)	104
5.4.4. D/d=2.0 (150 mm Hole Diameter)	104
5.5. Conformance of Proposed Design Equations and Test Data	105
5.6. Design Example	108
5.6.1. Practical Design Approach	108
5.6.2. Design Evaluation with Non-linear Time History Analysis.....	114
6. SUMMARY AND CONCLUSION	121
6.1. Summary	121
6.2. Conclusion	122
6.3. Recommendations for Future Researches.....	124
REFERENCES	125
APPENDICES	134
A: Test Results	134
B: Experimental Hysteresis Loops.....	152
C: Load-Displacement Graphs of Vertical Compression Tests	197
D: CD (Test Data).....	On the Back Side of the Thesis
VITA	204

LIST OF TABLES

TABLES

Table 3.1.	Input Data of the Design Values	40
Table 3.2.	Conformance of Test EBs to AASHTO Requirements.....	45
Table 4.1.	Effect of Presence of Steel Balls ($D/d=3.0$, $P_{ver}=120$ kN- $\sigma_{avg}=1.7$ MPa)	54
Table 4.2.	Effect of Steel Ball Diameter on Main Response Parameters of BRBs ($D/d=3.0$ and $P_{ver}=120$ kN- $\sigma_{avg}=1.7$ MPa)	57
Table 4.3.	Effect of Steel Ball Diameter on Main Response Parameters of BRBs ($D/d=2.0$ and $P_{ver}=120$ kN- $\sigma_{avg}=1.7$ MPa)	58
Table 4.4.	Effect of Hole Diameter on Main Response Parameters of BRBs ($d_{sb}=1.65$ mm and $P_{ver}=200$ kN- $\sigma_{avg}=2.8$ MPa).....	59
Table 4.5.	Material Properties Used in the F.E. Analyses.....	64
Table 4.6.	Effect of Vertical Compression Level on Main Response Parameters of BRBs ($D/d=2.5$, $d_{sb}=1.65$ mm).....	67
Table 4.7.	Characteristic Strength vs. Vertical Load for EBs with $D/d=3.75$	70
Table 4.8.	Vertical Compression Tests and Test Results (For One Bearing).....	75
Table 4.9.	Calculation of Vertical Load Resisted by Steel Balls	76
Table 4.10.	Conformance of Test BRBs to AASHTO Requirements.....	80
Table 4.11.	Variation of EDC for Different Diameter Ratios (a) $D/d=3.75$ (b) $D/d=2.5$ (c) $D/d=2.0$	85
Table 4.12.	Comparison between Characteristic Strengths Observed in Seismic & Service Load Tests	86
Table 4.13.	Characteristic Strengths of FRP Confined BRBs & BRBs	93
Table 5.1.	Contribution of Steel Balls to Secondary Stiffness under High Vertical Compressive Loads ($D/d=2.0$)	105

Table 5.2.	Basic Features of Ground Motions Utilized In NLTH Analyses [85, 86]	116
Table 5.3.	NLTH Analyses Results.....	119
Table A.1.	Test Results-1.....	134
Table A.2.	Test Results-2.....	142
Table A.3.	Test Results-3.....	149

LIST OF FIGURES

FIGURES

Figure 1.1.	Effect of Period on (a) Acceleration and (b) Displacement [6]	3
Figure 1.2.	Effect of Damping on (a) Acceleration and (b) Displacement [6]	4
Figure 1.3.	Plan View of a Ball Rubber Bearing (BRB)	6
Figure 2.1.	Sectional View of a Rubber Bearing [10]	9
Figure 2.2.	Placement of the Lead Core	9
Figure 2.3.	Typical Hysteresis Loop of a LRB	21
Figure 2.4.	Prototype-Test of a Big LRB [51]	25
Figure 3.1.	View of the Test Equipment Used in Reversed Cyclic Tests	30
Figure 3.2.	Schematic Layout of the Test Equipment Used in Reversed Cyclic Tests	30
Figure 3.3.	Connection of Load cell to Push-Pull Plate	31
Figure 3.4.	View of the Test Equipment Utilized in Vertical Compression Tests	32
Figure 3.5.	View of the Data Acquisition System	32
Figure 3.6.	View of the Control Panel-1	33
Figure 3.7.	View of the Control Panel-2	34
Figure 3.8.	Displacement Patterns with (a) Constant Amplitude and (b) Incremental Amplitude	35
Figure 3.9.	View of Test Set-Up During a Test	36
Figure 3.10.	Bilinear Horizontal Force-Displacement Relation	36
Figure 3.11.	Rubber Layers and Steel Shims	38
Figure 3.12.	Dimensions of the Test Bearings for $D/d=3.0$	40
Figure 3.13.	Compressive Stress Check for Test EBs	46
Figure 3.14.	Compressive Strain Check for Test EBs	47

Figure 4.1.	Steel Balls With 1.65 mm Diameter.....	49
Figure 4.2.	Steel Balls with Average 3 mm Diameter (min. 2-max. 4 mm).....	49
Figure 4.3.	Steel Balls with Average 5 mm Diameter (min. 4-max. 6 mm).....	50
Figure 4.4.	Hysteresis Loops Observed in Tests-1 st Case.....	51
Figure 4.5.	Hysteresis Loops Observed in Tests-2 nd Case.....	51
Figure 4.6.	Critical Void Ratio (CVR) for Steel Balls [71].....	52
Figure 4.7.	Hysteresis Loops of Bearings with and without Fill Material.....	53
Figure 4.8.	Hysteresis Loops of Constant and Incremental Amplitude Tests	55
Figure 4.9.	Variation of Vertical Load during Test-105.....	56
Figure 4.10.	Effect of Steel Ball Diameter-(D/d=3.0 and $P_{ver}=120$ kN- $\sigma_{avg}=1.7$ MPa)	57
Figure 4.11.	Effect of Steel Ball Diameter-(D/d=2.0 and $P_{ver}=120$ kN- $\sigma_{avg}=1.7$ MPa)	57
Figure 4.12.	Contact Radius of Rigid Spheres [69].....	58
Figure 4.13.	Effect of Hole Diameter ($d_{sb}=1.65$ mm, $P_{ver}=200$ kN- $\sigma_{avg}=2.8$ MPa)	60
Figure 4.14.	Effect of Magnitude of Horizontal Displacement-(D/d=2.0 and $P_{ver}=120$ kN- $\sigma_{avg}=1.7$ MPa).....	61
Figure 4.15.	Effect of Magnitude of Horizontal Displacement-(D/d=3.75 and $P_{ver}=120$ kN- $\sigma_{avg}=1.7$ MPa).....	61
Figure 4.16.	β_{eq} vs. γ_{max} of Test Data	62
Figure 4.17.	General View of the Finite Element Model (D/d=3.0)	63
Figure 4.18.	View of 8-node Solid Elements	64
Figure 4.19.	Bi-linear Material Definition for Steel Balls.....	65
Figure 4.20.	Horizontally Deformed BRB in F.E. Analysis	66
Figure 4.21.	Comparison between Test and F.E. Analysis Results	66
Figure 4.22.	Effect of Vertical Compression Level (D/d=2.5).....	67
Figure 4.23.	β_{eq} vs. σ_{avg} of Test Data.....	68
Figure 4.24.	β_{eq} vs. Q_d/P_{ver} of Test Data	68
Figure 4.25.	($Q_{d,EB}/Q_{d,BRB}$) of Test Data	69
Figure 4.26.	Friction Coefficients for Steel Balls with $d_{sb}=1.65$ mm (For One Bearing).....	70
Figure 4.27.	Void Ratio at Zero Vertical Strain and at 20% Vertical Strain [69]	71

Figure 4.28.	Horizontal Strain Distribution in a BRB under Vertical Compression ($D/d=3.0$ and $P_{ver}=300$ kN- $\sigma_{avg}=4.2$ MPa)	72
Figure 4.29.	Free Body Diagram of Interacting Steel Balls	73
Figure 4.30.	Vertical Load-Strain Graphs of Test-A7 & Test-A8.....	75
Figure 4.31.	Contribution of Central Core to Vertical Load Resistance ($D/d=3.0$,.... $P_{ver}=300$ kN) (a) BRB (b) annular EB.....	77
Figure 4.32.	Schematic View of a Horizontally Deformed BRB	78
Figure 4.33.	Bulged Bearings under $P_{ver}=500$ kN	78
Figure 4.34.	Compressive Strains in (a) BRB (b) annular EB with $D/d=3.0$ under ... $P_{ver}=300$ kN	80
Figure 4.35.	Compressive Stress Check for Test BRBs	82
Figure 4.36.	Compressive Strain Check for Test BRBs	82
Figure 4.37.	Variation of EDC for $D/d=3.75$	83
Figure 4.38.	Variation of EDC for $D/d=2.5$	84
Figure 4.39.	Variation of EDC for $D/d=2.0$	84
Figure 4.40.	Service Load Tests of BRBs ($D/d=3.0$)	86
Figure 4.41.	Plan View of Steel Washer Plates	88
Figure 4.42.	Effect of Vertical Load Level on Bearings with Washer Plates ($D/d=3.0$).....	88
Figure 4.43.	Steel Washer Plates with Steel Balls (Washer Hole Diameter: 17.5 mm)	89
Figure 4.44.	Effect of Vertical Load on Steel Washer Plates (Hole Diameter: 17.5 mm) & 1.65 mm Steel Balls.....	89
Figure 4.45.	Steel Washer Plates With Steel Balls (Washer Hole Diameter: 80 mm)	90
Figure 4.46.	Effect of Vertical Load on Steel Washer Plates (Hole Diameter: 80 mm) & 1.65 mm Steel Balls	90
Figure 4.47.	FRP Wraps (Before Testing).....	91
Figure 4.48.	FRP Wraps (After Testing)	92
Figure 4.49.	Effect of Vertical Load on FRP Confined BRB ($D/d=3.0$).....	92
Figure 5.1.	Log-Normal Distribution of Test Data for Yield Displacement	95
Figure 5.2.	Test Data for Yield Displacement With 90% Confidence Interval.....	96
Figure 5.3.	Log-Normal Distribution of Test Data for Characteristic Strength	97
Figure 5.4.	Test Data for Characteristic Strength With 90% Confidence Interval (1 Bearing)	98

Figure 5.5.	Q_d vs. γ_{max} of Test Data	99
Figure 5.6.	Contribution of Steel Balls to K_2	100
Figure 5.7.	Variation of Angle of Friction with Shear Strain for Well-Graded and Poorly-Graded Granular Materials [82]	101
Figure 5.8.	Contribution of Steel Balls to K_2 (D/d=3.75)	102
Figure 5.9.	Contribution of Steel Balls to K_2 (D/d=3.0)	103
Figure 5.10.	Contribution of Steel Balls to K_2 (D/d=2.5)	104
Figure 5.11.	Contribution of Steel Balls to K_2 (D/d=2.0)	105
Figure 5.12.	Design Equations and Test-8	106
Figure 5.13.	Design Equations and Test-55	106
Figure 5.14.	Design Equations and Test-130	107
Figure 5.15.	Design Equations and Test-209	107
Figure 5.16.	Design Equations and Test-121	108
Figure 5.17.	Flowchart for Design of BRBs.....	109
Figure 5.18.	Design Spectrum for PGA=0.4g and $S_c=1.5$ [6]	109
Figure 5.19.	Average Spectrum of Design Spectrum Compatible Ground Motions	117
Figure 5.20.	SRSS Spectra of Selected Earthquake Records-Un-Scaled	117
Figure 5.21.	SRSS Spectra of Selected Earthquake Records-Scaled	118
Figure 5.22.	View of the SDOF Model [87].....	118
Figure 5.23.	Hysteresis Loops Observed in NLTH Analyses Using Izmit-Transverse Record	120
Figure B.1.	Hysteresis Loop of Test-8	152
Figure B.2.	Hysteresis Loop of Test-9	153
Figure B.3.	Hysteresis Loop of Test-14	153
Figure B.4.	Hysteresis Loop of Test-16	154
Figure B.5.	Hysteresis Loop of Test-17	154
Figure B.6.	Hysteresis Loop of Test-18	155
Figure B.7.	Hysteresis Loop of Test-19	155
Figure B.8.	Hysteresis Loop of Test-34	156
Figure B.9.	Hysteresis Loop of Test-35	156
Figure B.10.	Hysteresis Loop of Test-36	157
Figure B.11.	Hysteresis Loop of Test-37	157
Figure B.13.	Hysteresis Loop of Test-38	158

Figure B.13.	Hysteresis Loop of Test-51	158
Figure B.14.	Hysteresis Loop of Test-52	159
Figure B.15.	Hysteresis Loop of Test-53	159
Figure B.16.	Hysteresis Loop of Test-54	160
Figure B.17.	Hysteresis Loop of Test-55	160
Figure B.18.	Hysteresis Loop of Test-56	161
Figure B.19.	Hysteresis Loop of Test-57	161
Figure B.20.	Hysteresis Loop of Test-61	162
Figure B.21.	Hysteresis Loop of Test-62	162
Figure B.22.	Hysteresis Loop of Test-82	163
Figure B.23.	Hysteresis Loop of Test-83	163
Figure B.24.	Hysteresis Loop of Test-84	164
Figure B.25.	Hysteresis Loop of Test-85	164
Figure B.26.	Hysteresis Loop of Test-86	165
Figure B.27.	Hysteresis Loop of Test-93	165
Figure B.28.	Hysteresis Loop of Test-94	166
Figure B.29.	Hysteresis Loop of Test-95	166
Figure B.30.	Hysteresis Loop of Test-96	167
Figure B.31.	Hysteresis Loop of Test-97	167
Figure B.32.	Hysteresis Loop of Test-98	168
Figure B.33.	Hysteresis Loop of Test-99	168
Figure B.34.	Hysteresis Loop of Test-100	169
Figure B.35.	Hysteresis Loop of Test-101	169
Figure B.36.	Hysteresis Loop of Test-102	170
Figure B.37.	Hysteresis Loop of Test-103	170
Figure B.38.	Hysteresis Loop of Test-104	171
Figure B.39.	Hysteresis Loop of Test-105	171
Figure B.40.	Hysteresis Loop of Test-106	172
Figure B.41.	Hysteresis Loop of Test-107	172
Figure B.42.	Hysteresis Loop of Test-112	173
Figure B.43.	Hysteresis Loop of Test-113	173
Figure B.44.	Hysteresis Loop of Test-114	174
Figure B.45.	Hysteresis Loop of Test-120	174
Figure B.46.	Hysteresis Loop of Test-121	175

Figure B.47.	Hysteresis Loop of Test-122	175
Figure B.48.	Hysteresis Loop of Test-123	176
Figure B.49.	Hysteresis Loop of Test-124	176
Figure B.50.	Hysteresis Loop of Test-125	177
Figure B.51.	Hysteresis Loop of Test-126	177
Figure B.52.	Hysteresis Loop of Test-127	178
Figure B.53.	Hysteresis Loop of Test-128	178
Figure B.54.	Hysteresis Loop of Test-129	179
Figure B.55.	Hysteresis Loop of Test-130	179
Figure B.56.	Hysteresis Loop of Test-131	180
Figure B.57.	Hysteresis Loop of Test-132	180
Figure B.58.	Hysteresis Loop of Test-133	181
Figure B.59.	Hysteresis Loop of Test-134	181
Figure B.60.	Hysteresis Loop of Test-135	182
Figure B.61.	Hysteresis Loop of Test-139	182
Figure B.62.	Hysteresis Loop of Test-140	183
Figure B.63.	Hysteresis Loop of Test-141	183
Figure B.64.	Hysteresis Loop of Test-142	184
Figure B.65.	Hysteresis Loop of Test-143	184
Figure B.66.	Hysteresis Loop of Test-144	185
Figure B.67.	Hysteresis Loop of Test-145	185
Figure B.68.	Hysteresis Loop of Test-146	186
Figure B.69.	Hysteresis Loop of Test-147	186
Figure B.70.	Hysteresis Loop of Test-154	187
Figure B.71.	Hysteresis Loop of Test-155	187
Figure B.72.	Hysteresis Loop of Test-156	188
Figure B.73.	Hysteresis Loop of Test-157	188
Figure B.74.	Hysteresis Loop of Test-158	189
Figure B.75.	Hysteresis Loop of Test-159	189
Figure B.76.	Hysteresis Loop of Test-160	190
Figure B.77.	Hysteresis Loop of Test-161	190
Figure B.78.	Hysteresis Loop of Test-175	191
Figure B.79.	Hysteresis Loop of Test-176	191
Figure B.80.	Hysteresis Loop of Test-177	192

Figure B.81.	Hysteresis Loop of Test-178	192
Figure B.82.	Hysteresis Loop of Test-204	193
Figure B.83.	Hysteresis Loop of Test-205	193
Figure B.84.	Hysteresis Loop of Test-206	194
Figure B.85.	Hysteresis Loop of Test-207	194
Figure B.86.	Hysteresis Loop of Test-208	195
Figure B.87.	Hysteresis Loop of Test-209	195
Figure B.88.	Hysteresis Loop of Test-210	196
Figure C.1.	Hysteresis Loop of Test-A1	197
Figure C.2.	Hysteresis Loop of Test-A2	198
Figure C.3.	Hysteresis Loop of Test-A3	198
Figure C.4.	Hysteresis Loop of Test-A4	199
Figure C.5.	Hysteresis Loop of Test-A5	199
Figure C.6.	Hysteresis Loop of Test-A6	200
Figure C.7.	Hysteresis Loop of Test-A7	200
Figure C.8.	Hysteresis Loop of Test-A8	201
Figure C.9.	Hysteresis Loop of Test-A9	201
Figure C.10.	Hysteresis Loop of Test-A10	202
Figure C.11.	Hysteresis Loop of Test-A11	202
Figure C.12.	Hysteresis Loop of Test-A12	203

LIST OF SYMBOLS

A	Plan area of an EB
A_{core}	Area of the central core
A_r	Area of the overlap between top and bottom bonded areas of the horizontally deformed bearing
A_{rubber}	Plan area of an EB excluding the central hole
B	Reduction in response due to energy dissipation
B_s	Strain-displacement matrix
C	Elasticity matrix
c	Cohesion
c_b	Viscous damping coefficient of the bearing
c_c	Thickness of the rubber cover at the sides
D	Outer diameter of the annular bearing
d	Internal hole diameter
D_b	Bonded diameter
d_b	Bearing displacement
d_g	Ground displacement
d_{max}	Maximum displacement
d_s	Service load displacement in the horizontal direction
d_{sb}	Steel ball diameter
d_{ver}	Vertical displacement
d_y	Yield displacement
$d_{\gamma=50\%}$	Horizontal displacement corresponding to 50% shear strain
E	Elasticity Modulus
e	Void ratio
E_c	Instantaneous compression modulus of the rubber-steel composite under the specified level of vertical load
E_D	Energy dissipated by viscous damping

$E_{eq, sb}$	Equivalent elastic modulus of steel balls
E_I	Energy input into the structure
E_K	Kinetic energy of the mass associated with its motion relative to the ground
E_s	Sum of the energy dissipated by yielding and the recoverable strain energy of the system
E_Y	Energy dissipated by yielding
F_b	Bearing force
f_L	A correction factor accounting for the contribution of lead-core to secondary stiffness
F_{max}	Maximum horizontal force
F_n	Normal force at the contact
F_s	Shear force at the contact
f_s	Resisting force for the inelastic system
$f_x(x)$	Probability density function
F_y	Yield strength
$F_{y, steel}$ shims	Yield strength of steel shims
$F_{\gamma=50\%}$	Horizontal force corresponding to 50% shear strain
G	Shear modulus of rubber
g	Gravitational acceleration
h	Height of the bearing excluding external steel anchors
h_s	Thickness of steel shims
K	Bulk Modulus
k	Elastomer material constant
K_{eff}	Effective stiffness
$K_{eff, ver}$	Effective vertical stiffness
K_h	Horizontal stiffness of an EB
K_n	Element stiffness in normal direction
K_s	Element stiffness in shear direction
K_{st}	Stiffness matrix of the element assemblage
K_{ver}	Vertical stiffness
K_1	Primary slope (stiffness) of the bilinear hysteresis curve
K_2	Secondary slope (stiffness) of the bilinear hysteresis curve
$k_{\alpha C/2}$	Values of the standard normal variate with cumulative probability levels $\alpha C/2$ and

	$1 - \alpha C/2$
m	Mass supported by the bearing
m_m	An integer controlling the smoothness of the transition from elastic to plastic response
N	A parameter used in stability calculations
n	Number of internal rubber layers
P	A parameter used in stability calculations
P_{ver}	Vertical compressive load
$P_{ver,BRB}$	Vertical load values measured at a specified vertical displacement in a BRB
$P_{ver,EB}$	Vertical load values measured at a specified vertical displacement in an EB
$P_{ver,3.4}$	Vertical compressive load corresponding to 3.4 MPa average compressive stress
PGA	Peak ground acceleration
Q_d	Characteristic strength
$Q_{d,BRB}$	Characteristic strength of ball rubber bearing
$Q_{d,CBRB}$	Characteristic strength of confined ball rubber bearing
$Q_{d,EB}$	Characteristic strength of elastomeric part
$Q_{d,lower}$	Lower limit of characteristic strength
$Q_{d,serv}$	Characteristic strength under horizontal loads simulating service loading conditions
$Q_{d,upper}$	Upper limit of characteristic strength
R	Radius of sphere
r_c	Contact radius
S	Shape factor
S_a	Spectral acceleration
S_c	Site coefficient
t	Single rubber layer thickness
T_b	Longer corner period
T_{eff}	Effective period
t_{max}	Thickness of the thickest rubber layer in the EB
t_r	Total rubber thickness
V_s	Volume of solids
V_v	Volume of voids
x	Variable
Y_y	A dimensionless parameter

Z_z	Non-dimensional hysteretic displacement components
α	Ratio of secondary to primary stiffness
α_r	An empirical coefficient determined from test data
β	Parameter defining the variation of acceleration over a time step and determining the stability and accuracy characteristics of the Newmark's method
β_{eq}	Equivalent viscous damping ratio
β_f	A dimensionless parameter
ΔF_n	Incremental normal force
ΔF_s	Incremental shear force
Δn	Relative displacement in normal direction at a contact
Δs	Relative displacement in shear direction at a contact
ε_c	Vertical compressive strain
ϕ	Friction angle
ϕ_p	Peak friction angle
γ_{max}	Maximum shear strain
γ_c	Shear strain due to vertical compressive load
γ_r	Shear strain due to rotation
$\gamma_{s,eq}$	Shear strain due to seismic design displacement
$\gamma_{s,s}$	Shear strain due to service load displacement
κ	Parameter defining the variation of acceleration over a time step and determining the stability and accuracy characteristics of the Newmark's method
ζ	Standard deviate of $\ln x$
λ	Mean value of $\ln x$
ψ	Ratio of vertical compressive load resisted by steel balls
σ_{avg}	Average vertical stress
σ_{core}	Vertical stress in the central core
σ_{dev}	Standard deviate of x
σ_s	Service average compressive stress due to total unfactored load
μ	Coefficient of friction
μ_{mean}	Mean value of x

τ_t	A dimensionless parameter
ν	Poisson's ratio
θ	Maximum service rotation due to unfactored total load

ABBREVIATIONS

AASHTO	American association of state highway and transportation officials
ADRI	Added damping rubber isolator
BRB	Ball rubber bearing
DSIR	Department of scientific and industrial research of New Zealand
EB	Elastomeric bearing
EDC	Energy dissipation capacity
F.E.	Finite Element
FPS	Friction pendulum system
HDRB	High damping rubber bearing
HLRB	Hybrid lead rubber bearing
KOERI	Kandilli observatory and earthquake research institute
LRB	Lead rubber bearing
NLTH	Nonlinear time history
PGA	Peak ground acceleration
PRB	Peripherally restraining type isolator
PTFE	Polytetrafluoroethylene
RB	Rubber bearing
R-FBI	Resilient friction base isolation system
SMA	Shape memory alloy

CHAPTER 1

INTRODUCTION

1.1. General

Over the last couple of decades, use of seismic isolation technology has become very popular in new design or seismic retrofit of important structures such as bridges, viaducts, buildings, nuclear power plants, museums and historical structures [1, 2]. In general, application of seismic isolation system to structures results in shift in seismic response of structure in such a way that expected seismic damage is minimized or eliminated. Use of such a system in various structures is very important to maintain the rescue operations in the aftermath of an earthquake. Over the years different types of seismic isolation systems are invented and used for the purposes described above.

A purely sliding system composed of granular material (talc) is the earliest and simplest isolation system to be proposed [3]. In 20th century, concept of seismic isolation has been improved significantly and seismic isolation guidelines have been developed. The first use of a rubber isolation system is in 1969 at an Elementary School, in former Yugoslavia [3]. The bearings in this system were unfortunately formed from plain-unreinforced rubber and significant bulging occurred due to vertical compressive loads.

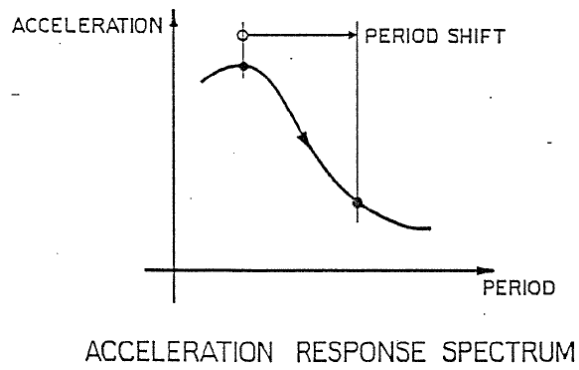
The seismic isolators can be categorized into rubber and sliding types. The most common rubber isolators are; elastomeric bearings, lead rubber bearings and high damping rubber bearings [4]. The most common sliding isolators are; those with a curved

sliding surface such as friction pendulum bearings and those with a flat-sliding surface such as Eradquake bearings [5].

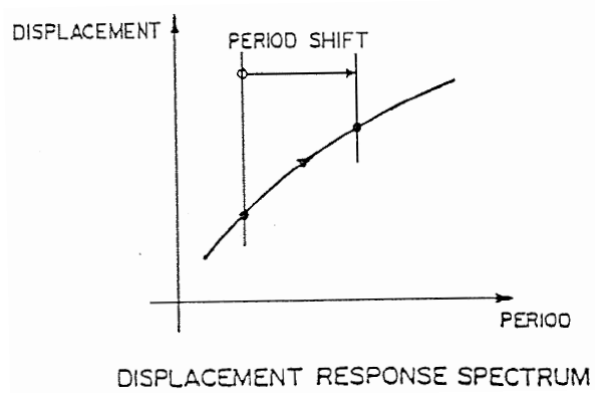
Three basic characteristics of an isolation system are described below [6]:

- The system shall permit horizontal structural movements while developing no instability at vertical load carrying mechanism. Such allowance for horizontal movements will shift natural vibration period to a higher level and can reduce the seismic demands.
- The system shall provide adequate energy dissipation capacity to reduce the force response and structural deformations.
- The system shall provide adequate rigidity under service load levels such as wind and braking forces. Service load levels are typically much lower than seismic loads at high seismic risk regions.

Effect of increasing the natural vibration period of a structure by seismic isolation system is presented in Figure 1.1. With increasing shift in period, seismic forces can decrease in expense of higher structural displacements. The application of seismic isolation system to a rigid structure may adversely affect the structural response at near-fault zones or soft soil sites [7, 8].



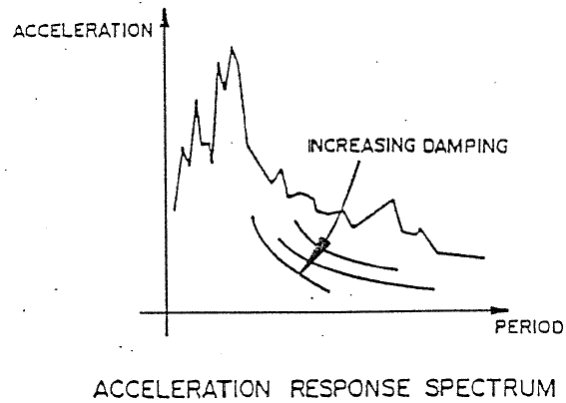
(a)



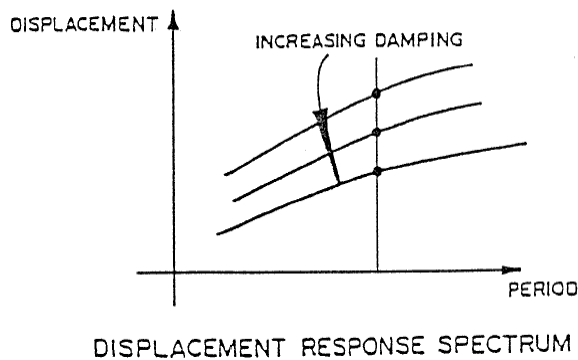
(b)

Figure 1.1. Effect of Period on (a) Acceleration and (b) Displacement [6]

In Figure 1.2, effect of damping on structural displacement and acceleration responses is presented. Energy dissipation mechanisms can reduce acceleration and displacement responses. However, high levels of damping may have some adverse effects on structural responses, which will be discussed in Chapter 2.



(a)



(b)

Figure 1.2. Effect of Damping on (a) Acceleration and (b) Displacement [6]

1.2. Objective and Scope

Two popular seismic isolation systems utilizes different source of energy dissipation mechanism; one being friction and the other one being material characteristic inherent dissipation. At the mean time, seismic isolation systems are still questioned on cost, heat generated during energy dissipation, durability and maintenance related issues. The objective of this dissertation is to develop a new type of rubber based seismic isolation bearing that combines material inherent and friction based energy dissipation mechanisms

in one single bearing while maintaining adequate energy dissipation capacity without significant degradation, as the number of loading cycles increases.

Within this scope, a new bearing system, named as “Ball Rubber Bearing (BRB)” is developed. The bearing is composed of a conventional multi-layered steel-reinforced bearing with its central hole filled with small diameter steel balls used to provide energy dissipation capacity through friction. Briefly, the energy is typically dissipated between contact surfaces upon horizontal movement of the bearing under seismic effects. Since friction is the main source of damping in energy dissipation, the proposed bearing can be accepted as a combination of rubber and sliding bearing where sliding occurs internally within the steel balls. Surrounding rubber material is also designed to provide material characteristic based energy dissipation during cyclic loads.

To accomplish the research objectives, several related tasks are pursued in this investigation:

- Develop a testing program for seismic isolation system.
- Evaluate different types of granular material in terms of cyclic energy dissipation capacity and durability. The granular material is used to fill the inner hole of the bearing closed with a steel cap.
- Describe the mechanical behavior of the new bearing. Develop a non-linear finite element modeling simulating the structural behavior of the bearings.
- Develop design equations for the new bearing using test data and provide illustrative design example.

In the scope of this study, a test program is developed to investigate the prototype bearings, which includes 210 reversed cyclic and 12 vertical only pressure tests. Different types of granular fill materials are tested to observe their energy dissipation capacity. Plan view of the new bearing type is depicted in Figure 1.3.

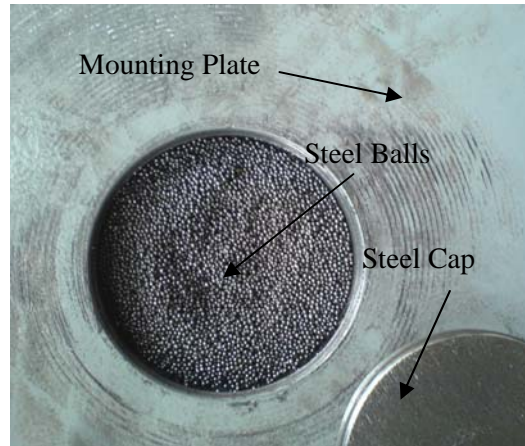


Figure 1.3. Plan View of a Ball Rubber Bearing (BRB)

1.3. Summary of Findings

Based on the results of this research, several findings can be summarized as follows:

- Steel balls with an average diameter of 1.65 mm placed in the central hole of elastomeric bearings provide better performance in terms of damping compared to the other granular materials.
- Its manufacturing process has few steps and its constructability is easy.
- BRB provides equivalent viscous damping ratios around 20% without significant degradation in the energy dissipation capacity, as the number of loading cycles increases.
- Heat generated in the central core due to friction has not a pronounced effect on performance of BRBs since measured temperature is no more than 45-50 °C (i.e. temperature rise about 25-30 °C).
- Steel balls in the central hole of the bearing provide vertical stiffness up to 1.5 times of the elastomeric part. Moreover, the steel balls significantly increase the

horizontal stiffness of the bearing at tests having small shear strain amplitudes, which provides service load rigidity.

- Non-linear finite element simulation and design guideline equations are determined to be adequately represent the structural behavior of the bearing prior to testing.

CHAPTER 2

LITERATURE REVIEW

2.1. General

This chapter summarizes earlier studies and researches on typical seismic isolation systems, testing of seismic isolation systems and seismic response of isolated structures.

2.2. Seismic Isolation Systems

2.2.1. General Information on Rubber Isolators

Elastomeric bearings (EBs) and high damping rubber bearings (HDRBs) are manufactured in multiple layers which are formed by vulcanizing steel shims to thin rubber layers in presence of heat and pressure. These bearings can be stiff in the vertical direction due to restraint provided by steel shims that prevent bulging of rubber layers. On the other hand, rubber layers can provide flexibility to horizontal movement of the bearing. Sectional view of a rubber bearing is presented in Figure 2.1.

Multilayer steel reinforced elastomeric bearings have inherent critical damping ratios around 2%-3% [9]. For this reason, they are usually used with other energy dissipating elements to increase the overall energy dissipation of the system. If high damping is required in an isolation system, LRBs, HDRBs or other high-damping seismic isolation systems can be utilized.

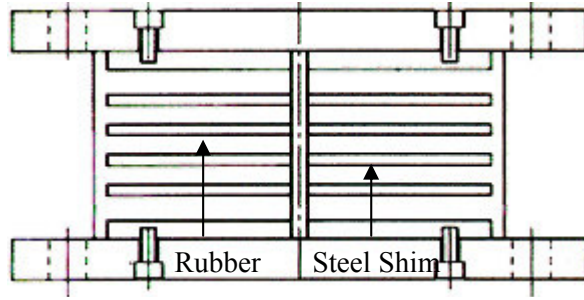


Figure 2.1. Sectional View of a Rubber Bearing [10]

At HDRBs, damping is provided by using a special composition of rubber mix that includes chemical additives [3].

Lead rubber bearings are laminated rubber bearings containing one or more lead plugs that are inserted into holes, as presented in Figure 2.2. The lead core dissipates energy upon shear deformation [3].



Figure 2.2. Placement of the Lead Core (Photo Courtesy of Alga Spa)

Chihiro et al. [11] performed studies on bearings consisting of a laminated rubber cylindrical outer shell with quake absorbing device of granular materials in small diameters packed in it. There is also a brittle shake prevention bar at the periphery of the bearing.

Hardened ceramic balls with small diameters were accommodated in the central hole. Test results revealed that the device has significant energy dissipation capacity. There is limited information about this study.

Hayashi et al. [12] carried out research on silicone rubber bearings. Silicone rubber bearings are reported to be durable and their performance is independent of the temperature changes in the normal range. At small displacements, the authors reported that horizontal stiffness of the silicone rubber bearings is non-linear and damping ratio of silicone rubber bearings is about twice of HDRBs and LRBs. The authors also noted that horizontal stiffness of silicone rubber bearings is about 1/2-1/3 of HDRBs and LRBs at small horizontal displacements.

Dolce et al. [13] proposed a new rubber based seismic isolator with added damping capacity. The proposed seismic isolator is named as “Added Damping Rubber Isolator (ADRI)”. ADRI consists of a low damping elastomeric bearing with viscous material filled in the central hole of the bearing. The authors noted that viscous damping provided by ADRI may be more advantageous than hysteretic damping provided by LRBs etc. at some circumstances like near-fault earthquakes. The authors also noted that ADRI is less sensitive to temperature effects compared to HDRBs and have more stable mechanical properties under repeated cycles. ADRI is reported to lack any scragging or decay phenomena in contrast to LRBs and HDRBs. The experimental results revealed that at 100% shear strain and 0.5 Hz frequency of loading, the effective stiffness of ADRIs are 20%-35% higher than those of elastomeric bearings (EBs) while their energy dissipation capacities are more than twice than those of similar (i.e. with same dimensions and rubber material) EBs. Effective damping ratios up to 19% were observed with ADRI. The authors also noted that further studies are carried out in order to increase the effective damping ratio of ADRI up to 25%-30%.

Matsushita et al. [14] carried out an experimental research on peripherally restraining type seismic isolator (PRB). In PRB, there is a core block made of a synthetic rubber compound having higher energy dissipation capacity (EDC) compared to high damping rubber compound. There is also a peripherally restraining ring made of layers of vulcanized high damping rubber layers and internal reinforcing steel plates. Experimental studies revealed that PRB has a higher EDC and smaller shear strain at failure compared to HDRBs.

Tanaka et al. [15] proposed a new seismic isolator type called “Hybrid Lead Rubber Bearing”. Hybrid lead rubber bearing (HLRB) consists of a LRB on top of a rubber bearing with a stopper. Horizontal stiffness of the rubber bearing is lower than that of the LRB. At low intensity earthquakes, rubber bearing is active and at strong intensity earthquakes, LRB becomes active. There is a stopper to limit the horizontal displacement of the rubber bearing and to transmit the shear forces to LRB at stronger earthquakes. The authors concluded that HLRBs reduce the building response both at weak and strong earthquakes and there was no wind induced problems in the building isolated with HLRBs.

Özden et al. [16] investigated scrap automobile tires as a seismic isolation device. Realizing that since 1950’s, automobile tires have been produced by vulcanizing steel mesh with rubber in different forms, the authors proposed that steel mesh in the tires may have similar effect to internal steel shims in EBs. The authors formed bearings by placing scrap tires on top of each other and tested under horizontal & vertical loads. Experimental results revealed that scrap tires may be used in massive and heavy structures as a seismic isolator due to their inherently high shear modulus. Shear moduli of the scrap tires used in the experimental study were reported to be in between 0.95 MPa-1.85 MPa. As expected, sufficient vertical compressive load is necessary to hold tire layers together.

Kelly [17] developed a rubber seismic isolator in which internal steel plates are replaced with fiber reinforcement. Kelly concluded that fiber-reinforced isolator is efficient as conventional bearings. The main advantage of fiber-reinforced isolator is its low weight and low cost compared to conventional EBs.

2.2.2. General Information on Sliding Isolators

Zhou [18] reported that sand layer, graphite lime mortar layer, slide friction layer, roller and rubber bearings are isolation materials & devices commonly used in China for seismic isolation of buildings. The author noted that four buildings in North China were seismically isolated using sand layers in between 1980-1984. Main advantage of sand layer is its low cost. High residual displacements and sensitivity to foundation settlements are main disadvantages of sand layer as a seismic isolator. Graphite lime mortar layer was used as a seismic isolation layer at twelve buildings in North China during 1986-1987. Its advantages and disadvantages as a seismic isolation system are the same as those of a sand

layer. Zhou reported fourteen buildings in West China that were seismically isolated using sliding friction layer during the period of 1988-1998. The author reported two types of sliding friction layers. One consists of two steel plates with Teflon on interface of both plates. The other consists of two steel plates at bottom and top and one intermediate thicker steel plate. Advantages and disadvantages of slide friction layers are the same as the above mentioned isolation layers. Rollers used in seismic isolation of two buildings in Central China during the period of 1968-1978 are reported to require frequent maintenance.

Xiao et al. [19] studied on low-technology techniques for seismic isolation. The authors tested five materials as seismic isolation layers beneath low rise structures. The materials are sand, lighting ridge pebble, polypropylene, PVC sheet and polythene membrane. They concluded that pebble is a good isolation material. The authors also noted that sliding motion occurs more easily on layers having larger grain size.

Jangid et al. [20] investigated effectiveness of elliptical rods for base isolation. The authors noted that although rolling rods are advantageous since they have low friction coefficients thereby limiting the transmitted acceleration to the superstructure, they may result in high peak displacements and residual displacements due to lacking of re-centering force. Therefore, elliptical rods instead of circular rods were proposed to overcome these problems. According to the authors, elliptical rods provide an ideal isolation system since they have low friction coefficient and have re-centering capability due to eccentricity of the elliptical rods. Increases in the eccentricities of the elliptical rods decrease both peak and residual displacements.

Concept of sliding isolation was combined with pendulum type response resulting in well known seismic isolator called Friction Pendulum System (FPS) [21]. In FPS, isolation is achieved by means of an articulated slider on spherical, concave chrome surface. The slider is faced with bearing material having a maximum friction coefficient of 0.1 at high sliding velocities and a minimum friction coefficient on the order of 0.05 or less at very low sliding velocities, when slider is in contact with the polished chrome surface. Kunde et al. [21] reported that dependency of coefficient of friction to velocity is a characteristic of Teflon-type materials.

Roussis et al. [22] developed a new uplift restraining friction pendulum system consisting of two orthogonal opposing concave beams interconnected through a sliding mechanism permitting tensile forces in the bearing. The authors reported that the proposed system decouples the bi-directional motion along two orthogonal directions. Moreover, the proposed system is capable of providing independent stiffness and energy dissipation along two principal horizontal directions.

Fenz et al. [23] introduced so called triple friction pendulum system consisting of three different multi-spherical sliding bearings. The authors reported that when properly designed, triple friction pendulum bearings provide adaptive stiffness and damping values changing with displacement resulting from the combination of surfaces on which sliding occurs. In order to fulfill the structural design criteria, friction coefficients and radii of curvatures of the surfaces can be adjusted.

Resilient-friction base isolation (R-FBI) system was proposed by Mostaghel et al. [21]. This device consists of concentric layers of Teflon-coated plates that are in friction contact with each other and contains a central core of rubber. This system combines the advantages of the friction with the resiliency of the rubber. The role of the rubber core is to distribute the sliding displacement and velocity along the height of the device. This system provides damping by friction and restoring force.

Another type of seismic isolator called “Eradiquake” consists of a pair of flat sliding plates, a disc bearing to accommodate rotation and a set of urethane springs called mass energy regulators to provide restoring force [5]. The resistance of the bearing to horizontal forces is provided by the frictional resistance between the flat PTFE and stainless steel and by the compression of the mass energy regulators against the upper bearing plate.

General characteristics and test results of a new developed sliding bearing with an elastic restoring force called “The RoGlider” was presented by Robinson et al. [24]. The authors noted that the RoGlider is capable of supporting both heavy and light vertical loads with an efficient coefficient of friction 0.11 and with an elastic restoring force. The RoGlider consists of two stainless steel plates with a PTFE ended puck sitting between the plates. Two rubber membranes are attached to the puck with each being jointed to the top or bottom plates. One of these diagonal rubber membranes undergoes tension and the other

diagonal rubber membrane undergoes compression under horizontal displacement. The rubber membrane in tension provides the restoring force and the other membrane in compression provides little or no restoring force. The authors concluded that the results of preliminary prototype tests were promising.

2.2.3. Other Systems

Wilde et al. [25] proposed a base isolation system for bridges consisting of laminated rubber bearings and a device made of shape memory alloys (SMA). Different responses of SMA at different displacement levels were used to control the displacements of the rubber bearings. The authors also proposed using flexural SMA bars as a damper since SMA adds damping to the system. The authors also noted that the desired response can also be achieved with semi-active or active devices. However, such systems are quite complex since they require special hardware, sensors and maintenance.

Ramallo et al. [26] investigated smart base isolation systems. The authors concluded that smart dampers such as magnetorheological fluid dampers are promising devices in future seismic isolation projects.

2.3. Studies on Rubber Isolators

2.3.1. Elastomeric Bearings (EBs)

Horizontal stiffness of an EB can be expressed by Equation 2.1 [3]:

$$K_h = \frac{GA}{t_r} \quad (2.1)$$

where

- A : plan area of an EB (in m²)
- G : shear modulus of rubber (in kPa)
- K_h : horizontal stiffness of an EB (in kN/m)
- t_r : total rubber thickness (in m)

Vertical stiffness of an EB can be simply expressed by the following equation:

$$K_{ver} = \frac{E_c A_r}{t_r} \quad (2.2)$$

where

A_r : area of the overlap between top and bottom bonded areas of the horizontally deformed bearing [5] (in m²)

E_c : instantaneous compression modulus of the rubber-steel composite under the specified level of vertical load [3] (in kPa)

K_{ver} : vertical stiffness of an EB (in kN/m)

The compression modulus and therefore vertical stiffness of an EB depends on shape factor S which is defined as the ratio of loaded area to bulge free area. Shape factor (S) of an annular bearing can be determined from the following equation [27]:

$$S = \frac{D^2 - d^2}{4t \times (D + d)} = \frac{D - d}{4t} \quad (2.3)$$

where

D : outer diameter of the annular bearing (in m)

d : internal hole diameter (in m)

t : single rubber layer thickness (in m)

Compression modulus of a circular pad can be expressed as:

$$E_c = 6GS^2 \quad (2.4)$$

If the shape factor of the bearing is larger than 10, then compressibility of the bearing should be taken into account by using bulk modulus (K) [3].

Maximum percent shear strain for an EB can be defined as:

$$\gamma_{\max} \% = \frac{d_{\max}}{t_r} \times 100 \quad (2.5)$$

where

d_{\max} : maximum displacement (in m)

t_r : total rubber thickness (in m)

γ_{\max} : maximum shear strain

Robinson [28] reported that prior to the introduction of vulcanized rubber bearings in 1970s, delamination problems were observed leading to the failure of the glued joints between rubber and steel plates. However, in tests, it was found out that vertical loads were usually sufficient to keep the delaminated bearings together.

Adnan et al. [29] concluded that hollow rubber bearings are efficient as seismic isolators. The authors reported that hollow rubber bearings have higher vertical stiffness/horizontal stiffness ratios compared to conventional EBs.

EBs used in practice have high shape factors and therefore they are stiff in the vertical direction in contrast to the horizontal directions. As in stiff systems, vertical component of the earthquake excitation are transmitted to the structure almost unaltered. Some systems for 3D isolation of structures that are also flexible in the vertical direction have been proposed [30]. Rubber pads used in a school building at Skopje, in former Yugoslavia are of this kind. This system has vertical stiffness close to horizontal stiffness. As three dimensional seismic isolators, Tajirian et al. [30] tested EBs having low shape factors resulting in low vertical stiffness. It was confirmed that it would be feasible to use such bearings to isolate stiff buildings with low center of gravity in both horizontal and vertical directions. Tested bearings had different connection details. The authors concluded that the bearings having bolted connections are preferable to the bearings having doweled connections since bearings having bolted connections can accommodate larger horizontal displacements and remain stable even at very low vertical load levels. The authors also noted that when bolted bearings are used, ultimate failure should always occur due to rupture of the elastomer. Bond failure has to be prevented.

Pınarbaşı et al. [31] reported that shear stiffness of EBs increase at low temperatures and the amount of increase depends on the material properties. The authors noted that stresses under constant deformation decreases noticeably under vertical compression and/or shear with time. Vertical compression tests were performed on EBs, up to failure. After yielding of internal steel shims, the authors observed quite high deformations and load capacities before failure. At about three times the yield force, the internal steel shims ruptured. Elastic behavior of EBs was verified since the heights of the EBs were very close to their original heights after removal of the load. The authors also notified importance of “Mullin’s” effect on horizontal behavior of EBs. Due to “Mullin’s” effect, horizontal force and stiffness are higher in the first cycle compared to subsequent cycles. After the first cycle, permanent damage occurs in the molecular structure of the rubber. The authors concluded that preloading relieves “Mullin’s” effect to some extent.

According to Yakut et al. [32], increase of shear stiffness of rubber bearings at low temperatures consists of two components. They noted that increase of shear stiffness due to temperature change is called instantaneous thermal stiffening and thermal stiffening is measured after the bearing temperature reaches ambient temperature. On the other hand, increase of stiffness with time is called crystallization. Yakut et al. reported that there is no record of poor performance of bridge EBs due to low temperature. The authors concluded that AASHTO test procedures for determination of low-temperature properties of EBs are overly conservative.

Kelly [33] concluded that the theoretical analysis used in the prediction of the compression buckling behavior can also be used in prediction of tension buckling behavior and tension buckling load is of the same order as the compressive buckling load. Similarly, the shape of an EB buckled in tension is the same as that of an EB buckled in compression. Kelly noted that tension buckling will not be observed often since tension buckling load is much larger than the tensile load inducing cavitation in the elastomer. Kelly reported that elastomer can sustain tension without cavitation to some extent since rotation of central portion of the elastomeric bearing converts tension to rotated shear. Therefore if shear deformation of the bearing occurs when there is tensile load on the bearing, damages due to cavitation are prevented and the bearing can accommodate large horizontal displacements.

Tsai et al. [34] studied the effect of thinner internal steel reinforcing shims on the buckling load of multilayer EBs. The authors concluded that using thinner internal reinforcing steel shims reduces the weight of the isolators. This modification would change the buckling load. Tsai et al. stated that buckling load decreases with reducing the reinforcement thickness. As the ratio of elastomeric bearing width/steel shim thickness exceed 150, further reduction of the buckling load becomes negligible.

Warn et al. [35] carried out an experimental study on investigation of effect of horizontal displacement on vertical stiffness of EBs and LRBs. The authors concluded that vertical stiffness of all bearings decrease with increasing horizontal displacement. They reported that overlap theory is very conservative in prediction of vertical stiffness of the bearings. They also noted that at a horizontal displacement level equal to the bonded diameter of the bearing, the vertical stiffness of the bearing is about 20% of the initial vertical stiffness.

Braga et al. [36] noted that rubber with low shear modulus may experience vulcanization problems and compounds may experience ageing instability.

2.3.2. High Damping Rubber Bearings (HDRBs)

It is known that HDRBs provide less damping than LRBs. HDRBs have equivalent viscous damping ratios in the order of 10-16% [10]. HDRBs can have higher cost/energy dissipation ratio compared to other isolation systems.

Yoshida et al. [37] reported that high damping rubber possesses both plasticity and viscosity and that the basic properties of high damping rubber such as the direction of stress evolution is similar to those of natural rubber. In HDRBs, rubber is vulcanized together with carbon black, plasticizer, oil etc. and therefore possesses specific characteristics.

High damping rubber is more susceptible to property changes due to heat generated in the cyclic loading and aging effects are more pronounced on stiffness and energy dissipation characteristics compared to low damping rubber [1]. These effects result in difficulties in the prediction of short term and long term properties of the bearings. Moreover, other

difficulties arise in prediction of upper bound and lower bound properties of the bearings used in analyses.

Aiken et al. [38] carried out monotonic shear failure tests and monotonic tension failure tests on HDRBs. In shear failure tests, bearings failed by tensile rupture of the rubber. Bond failure was not observed. In monotonic tension failure tests, very large tensile capacities were observed for bolted HDRBs.

Kelly [39] noted that the horizontal stiffness increases by a factor of six after a shear strain of 250% in tested Bridgestone high damping rubber bearings. Due to stiffening, very high seismic inertial forces may be transmitted to the substructure and such forces may damage the substructure. Kelly also noted that damping in the HDRBs increased with pressure and failure mechanism slightly changed with pressure. In the tests, failure shear strain varied between 475% under a vertical pressure of 10.34 MPa and 560% under zero vertical pressure.

Lee et al. [40] carried out an experimental research on HDRBs of Kalimer to determine their shear modulus and damping. The authors concluded that shear modulus and damping capacity decrease as the number of loading cycles increase and increase as the load rate increases. Lee et al. also concluded from recovery tests that stabilized rubber mechanical properties are recovered after about 3 hours and the rubber behavior approaches its initial properties after 1.5 year of relaxation. The authors noted that the shear modulus and the equivalent damping ratio are more dependent on the maximum shear strain compared to the loading history.

Burtscher et al. [41] investigated a special rubber bearing design in which the internal reinforcing steel shims are inclined by an angle. Due to this inclination, horizontal stiffness is higher in the direction of inclination. In the other direction, horizontal stiffness of the bearing is the same as that of an EB. Bearings having inclined steel shims do not respond in simple shear as the bearings having flat steel shims, making analysis and design process more complicated.

2.3.3. Lead Rubber Bearings (LRBs)

Kunde et al. [21] noted that lead used in LRBs has good fatigue properties during cyclic loading at plastic strains and it is also available at a high purity of 99.9% resulting in predictable mechanical properties. Moreover, mechanical properties of lead are very stable with time. Lead also has a relatively high creep coefficient meaning that under slowly applied deformations such as daily temperature changes, resistance of the lead is small resulting in low yield strength under slow loading rates [5]. Therefore, at loading rates representing daily temperature changes and wind loading, effective horizontal stiffness of a LRB is significantly lower compared to its stiffness under seismic loading. LRBs have equivalent viscous damping ratios up to 28% or more [42].

Robinson [28] reported that in all lead-based devices, the process of recovery of mechanical properties is rapid due to the interrelated processes of recovery, recrystallisation and grain growth and these processes are efficient at ambient temperatures due to low melting point of the lead.

Lead core in LRBs provides excellent energy dissipation capacity when it is fully confined. To provide such a confinement, lead plug is cut longer than the height of the rubber bearing (less than 5% longer) so the lead core is compressed and expands horizontally when the upper steel plate is bolted [43].

Typical hysteresis loop of a lead rubber bearing (LRB) is presented in Figure 2.3.

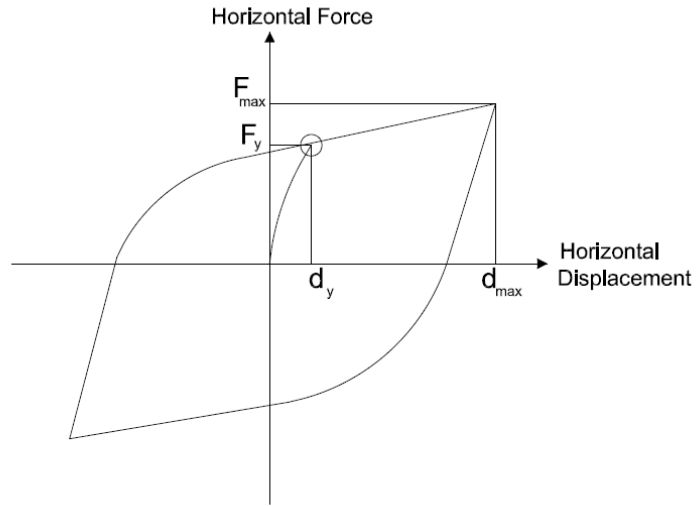


Figure 2.3. Typical Hysteresis Loop of a LRB

Restoring force of a LRB can be expressed by Equation 2.6 [44]:

$$F_{bi} = c_{bi} \dot{d}_{bi} + \alpha_i K_{1i} d_{bi} + (1 - \alpha) F_{yi} Z_{zi} \quad (i=1,2) \quad (2.6)$$

where

c_b : viscous damping coefficient of the bearing

d_b : bearing displacement

d_{max} : maximum displacement (in m)

d_y : yield displacement (in m)

F_b : bearing force (in kN)

F_{max} : maximum horizontal force (in kN)

F_y : yield strength (in kN)

K_1 : primary slope (stiffness) of the bi-linear hysteresis curve (in kN/m)

Z_z : non-dimensional hysteretic displacement components satisfying Equation 2.7

α : ratio of secondary (K_2) to primary stiffness (K_1)

Non-dimensional hysteretic displacement components (Z_z) should satisfy the following non-linear first order differential equation:

$$d_{yi} \frac{dZ_{zi}}{dt} = Y_y \dot{d}_{bi} + \beta_f \left| \dot{d}_{bi} \right| \left| Z_{zi} \right| \left| Z_{zi} \right|^{m_m - 1} - \tau_t \times \dot{d}_{bi} \left| Z_{zi} \right|^{m_m} \quad (2.7)$$

where

Y_y , β_f and τ_t are dimensionless parameters and m_m is an integer constant controlling the smoothness of the transition from elastic to plastic response.

In LRBs, the characteristic strength of the bearing is almost equal to the yield strength of the lead core. The secondary stiffness of a LRB is related to the horizontal stiffness of an EB with the following equation:

$$K_2 = f_L \times K_h \quad (2.8)$$

where

f_L : correction factor accounting for the contribution of lead-core to secondary stiffness

K_2 : secondary slope (stiffness) of the bi-linear hysteresis curve

Contribution of lead to the secondary stiffness of LRBs is in between 0%-20% of the contribution of the rubber part and amount of this contribution depends on the size of the lead plug, degree of confinement and cannot be determined from testing of a representative bearing [43].

In some LRB tests, after repeated cycles, fracture of lead core occurred resulting in reduced effective yield strength and energy dissipation capacity. Test results [43] indicate that the velocity of the motion has a significant effect on mechanical properties of LRBs and that the decrease in effective yield strength and energy dissipation capacity due to heating of the lead core is much higher in large LRBs compared to smaller LRBs. In fact,

after few cycles, the effective yield strength and energy dissipation capacity of an LRB stabilize to an important extent. At high testing velocities, the first-cycle values of these quantities are substantially higher and the drop from these high values in the following cycles is also high compared to the drop observed at lower testing velocities. Heat generated in the lead core is dissipated by conductive steel plates [43].

Doudoumis et al. [45] performed an analytical study on LRBs using finite element micromodels. The authors noted that primary stiffness (K_1) of LRBs is dependent on fabrication details of the bearing and confinement of the lead core. They also noted that the maximum horizontal force is significantly affected by the confinement of the lead core. EDC of the bearing is also affected by the confinement of the lead core, but less affected than maximum horizontal force. The authors also concluded that existence of lead core causes significant disturbance of the smooth distribution of the stresses and strains in the interior of the LRBs.

2.4. Studies on Sliding Isolators

2.4.1. Friction Pendulum System (FPS)

Tsai [46] concluded that local bending moments resulting from the movement of the FPS should be taken into account in the design stage of FPS. The author also noted that breakaway friction force is higher than dynamic friction force and magnitude of resultant of dynamic friction force is both dependent on instantaneous velocity and normal pressure on the FPS.

2.4.2. Other Systems

A new sliding material which has very high wear resistance was developed. The new material called “Xlide” also has low temperature sensitivity [47].

Constantinou et al. [48] reported that response of sliding isolation systems is insensitive to the frequency content of the input motion and sliding isolation systems reduce and spread the earthquake energy over a wide range of frequencies. The authors conducted shake table tests on a system consisting of Teflon disc bridge bearings and displacement control

devices. The displacement control devices provide rigidity under service loading, re-centering capability and supplementary energy damping to the system. Results of the experiments were quite satisfactory since peak acceleration of the deck was smaller than that of the shake table and maximum bearing displacement was smaller than the peak table displacement.

2.5. Testing of Seismic Isolation Systems

Conformance of damping and deformation characteristics of a seismic isolation bearing to design parameters should be verified by prototype tests [6, 49, 50]. Bearings should be rejected if they do not satisfy the minimum requirements.

Full-scale specimens are used in prototype tests if the capacity of the testing equipment is sufficient. Reduced scale specimens are allowed only when the capacities of full-scale specimens exceed the capacity of the testing equipment [6, 49, 50].

In prototype tests, bearings are subjected to loading cycles representing the effects of daily temperature changes, wind and braking and seismic loading. Survivability and service load performance of the bearings after a major seismic event are also checked.

AASHTO Guide Spec. [6] requires that three fully reversed cycles be performed at 1.0, 0.25, 0.5, 0.75, 1.0 and 1.25 times of the seismic design displacement in order to verify the dynamic response of the isolation system during an earthquake and the test velocity should be representative of anticipated seismic event if the performance of the isolation system is affected by velocity. Similar test procedures for isolation bearings are also available at other codes [49, 50]. In general, velocities up to 1 m/sec can cover most of the seismic isolation applications. However, seismic isolation bearings utilized in structures that are located in vicinity of a major fault may be subjected to velocities up to 2.2 m/sec [51]. There are few test equipments in the world that can attain velocities higher than 1.5 m/sec. On the other hand, even if the capacities of the equipments may seem sufficient, there may be some unexpected peculiarities in tests having very high demands [51].

Tests representing effects of daily temperature changes are performed at very slow velocities [6], while the tests representing the effects of wind and braking loading are

performed at moderate velocities. These tests present the resistance of the isolation system under service load conditions.

Aiken [52] studied on considerations and limitations for testing of seismic isolators and dampers. The author noted that testing is necessary to confirm conformance of the physical properties of the devices to those used in the design and demonstrate acceptable behavior of these devices under maximum earthquake loading and to provide some means of a quality control over the bearings. The author also noted that quasi-static testing is the most economical testing method for large devices if the performance of the device is not significantly affected by the loading rate or thermodynamic effects. The author reported that cost of the advanced testing system called SMRD at University of California at San Diego is about \$14.8 million, which of course require very high initial investment. However, such a device is essential for dynamic prototype testing of very large seismic isolation devices such as those in Benecia-Martinez bridge in California.

In general, bearings with larger dimensions may only be tested at test equipments allowing only one bearing, as presented in Figure 2.4.



Figure 2.4. Prototype Test of a Big LRB [51]

Marioni [10] reported that test requirements on HDRBs should be very severe since the mechanical properties of these bearings are much higher than those of EBs. Therefore, an accurate quality system as well as frequent testing is necessary for guaranteed quality and reliability.

2.6. Response of Seismically Isolated Structures

In the design specifications of Highway Bridges in Japan [53], it is stated that ratio of the natural period of the isolated bridge should be 2 or more times the same bridge having hinged bearings. This design procedure is called “Menshin Design”. Menshin means seismic isolation in Japanese.

Tongaokar et al. [54] investigated seismic response of bridges with isolation systems. The authors concluded that sliding isolation systems are more effective for stiff bridges compared to flexible ones.

Designing a structure with seismic isolation system in the vicinity of near-fault requires special attention. Near-fault earthquake records can contain significant wave pulses. At strike-slip type of faults, these pulses control the characteristics of horizontal motion. The period of the main pulse can be between 0.5 sec-5 sec [55].

Ground motions at soft soils are characterized by their high dominant vibration periods [56]. Since horizontal soil stiffness decreases further during earthquakes, vibration periods of the soft soils increase. Destructive effects of soft soils were widely observed at lakebed sites in the Mexico City during 1985 Mexico City earthquake [57]. At structures in the vicinity of near-fault locations and/or located above soft soils, designing an isolation system having a low fundamental frequency can increase the risk of undesired amplification in structural response. Therefore, designing a long period structure with isolation system at above mentioned cases can endanger the structural safety [7, 8].

Jangid et al. [57] studied base isolation of structures that are located at near-fault. The authors concluded that Electricite de France system consisting of flat sliding plates at top of elastomeric bearings may be the optimum choice for structures at near-fault locations.

Kelly [58] concluded that providing additional damping by means of dampers reduces isolator displacements and base shears but increases floor accelerations and inter-story drifts due to increase in the response of higher modes. Since seismic isolators are designed for maximum credible earthquake which is a very rare event, the isolation system may not be effective at smaller magnitude earthquakes. Kelly proposed a solution in which the seismic isolators are very stiff at low shaking levels then softens at design basis earthquake, and stiffens at higher input levels. For elastomeric isolators, depending on the compound, it requires using the increased stiffness and increased damping that is associated with the strain-induced crystallization that occurs in the elastomer at around 150%-200% shear strain.

In case of sliding bearings, Kelly [59] reported that high frequency vibrations occur due to slipping or sticking. Kelly noted that vibrations at these frequencies may not even be present in the ground motion and the system responds by transforming low frequency energy in the ground motion into high-frequency energy in the structure. Nevertheless, these effects are mainly observed in building structures.

Sharma et al. [60] concluded that high initial stiffness of the isolation system results in higher floor accelerations and inter-story drifts in buildings and higher vibration modes are excited. Isolator displacements and base shear forces decrease substantially with increasing initial stiffness of base isolators.

Dicleli [7] studied the effect of supplementary elastic stiffness to reduce the isolator displacements while keeping the substructure forces in the acceptable level. Dicleli concluded that supplementary elastic stiffness provided for instance by low damping EBs is beneficial in reducing isolator displacements while keeping the substructure forces at acceptable levels at moderate to large magnitude earthquakes and near-fault locations. The author also concluded that supplementary elastic stiffness with seismic isolation bearings having high characteristic strengths is beneficial in terms of lower substructure forces. On the other hand, heat generated due to higher characteristic strengths should be taken into account.

LRBs are used at many bridges and buildings. A recent application of LRBs in Turkey is at Sakarya-2 Viaduct near Bilecik. Sakarya-2 viaduct is about 300 meters away from the

southern branch of the North Anatolian fault and is located over potentially liquefiable loose soil. LRBs and EBs with 1100 mm and 1400 mm diameters were utilized. LRBs were utilized for energy dissipation and EBs were utilized for providing supplementary elastic stiffness. The design horizontal displacement of the isolation system is 850 mm [61, 62].

Park et al. [63] proposed two equations for optimal yield ratio of seismic isolators. In the proposed equations, maximum horizontal ground acceleration is the only parameter. For minimum base shear forces, Skinner [63] concluded that optimal yield ratio of seismic isolators is proportional to the earthquake amplitude. As expected, as maximum ground acceleration increases, optimal yield ratio of seismic isolators also increases.

CHAPTER 3

TEST SETUP AND TEST PROGRAM

3.1. General

This chapter presents information on test equipment, data acquisition system, test program, materials utilized in test bearings, mechanical properties of BRBs and design of test bearings.

3.2. Test Equipment

Two test equipments have been utilized in investigation of the bearing systems. The first test equipment that is capable of applying reversed cyclic horizontal loading (reversed cyclic shear loading) to a pair of bearings under a specified vertical compressive load is manufactured in a previous research project, BAP-2002-03-03-04 [64, 65]. Test equipment is located in the Structural Mechanics Laboratory of Civil Engineering Department, METU, as presented in Figure 3.1. Schematic layout of the test equipment is presented in Figure 3.2.

Test equipment is portable and do not need to have a fixed connection to foundation. The portable hydraulic jack uses industry voltage in operation.

A horizontal load of 200 kN is taken as the practical test limit of connection of load cell (F) to push-pull plate (A). In one particular case, push-pull plate connection broke by bending the edge bar shown in Figure 3.3. In later tests, broken bar is replaced by a thicker one. Load cell is connected to push-pull plate by a hinge to allow some rotations during the tests.

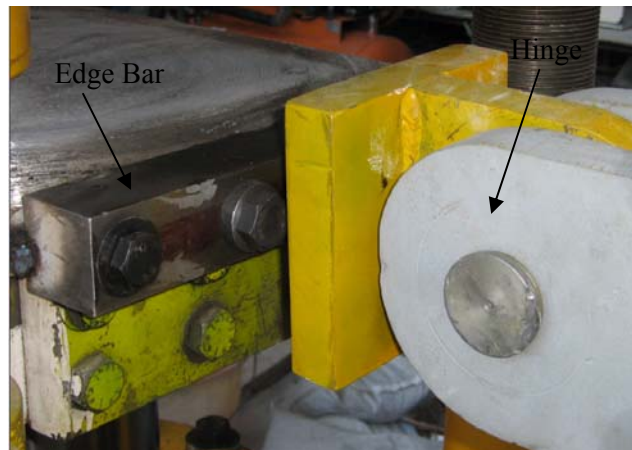


Figure 3.3. Connection of Load Cell to Push-Pull Plate

Load measurement capacity of the load cell (F) connected to the horizontal reversible jack (D) and push-pull plate (A) is 300 kN. LVDT (G) used to measure the push and pull of internal plate has a total stroke capacity of 300 mm.

In the vertical direction, in the first initial 87 tests, a calibrated barometer was utilized for obtaining the level of applied vertical load. At subsequent tests, the barometer is replaced with a load cell (E).

Besides seismic tests, vertical only pressure tests are performed to determine the contribution of steel balls to the vertical stiffness of the bearings. In these tests, another test equipment is utilized. A view of the test equipment that is utilized in vertical compression tests is presented in Figure 3.4. In vertical compression tests, approximately 170 kN is set as upper limit for vertical compressive load due to limitations of available load cells.



Figure 3.4. View of the Test Equipment Utilized in Vertical Compression Tests

3.3. Data Acquisition System

A view of the data acquisition system is presented in Figure 3.5. Data acquisition system called System 6000-Model 6100 Scanner that is manufactured by Vishay Micro-Measurements [66] is utilized in tests. Sample rate of the utilized system is up to 10000 samples per second per channel. System 6000 is operational in between $-10\text{ }^{\circ}\text{C}$ and $+50\text{ }^{\circ}\text{C}$. Model 6100 scanner accepts up to 20 plug-in input cards.



Figure 3.5. View of the Data Acquisition System

3.4. Test Program

Test set-up utilized in this research allows velocities up to 800 mm/s, as input. Back calculated test velocities are in the range of 20-70 mm/s even if test velocities are set as 500 mm/s or 800 mm/s in seismic tests. In service load tests, the lowest attainable velocity of the test-setup, i.e. 2 mm/s is used.

In tests, testing velocity, number of cycles and maximum horizontal displacement demand are input into the computer program of test machine. The bearings are compressed to a certain level of vertical load. Once these parameters are set and test is initiated, cycles succeed each other automatically. Test can be stopped manually when an unexpected condition occurs. The test data can be monitored during the test through a computerized data acquisition system.

Vertical loads and horizontal loads can be applied manually by using a joystick. However, in this case, level of applied load can not be controlled directly. In tests, the joystick is generally used only for the application of vertical loads except at some few tests it is also utilized for manual application of horizontal loads. Views of the control panel and joystick are presented in Figure 3.6 and Figure 3.7, respectively.



Figure 3.6. View of the Control Panel-1

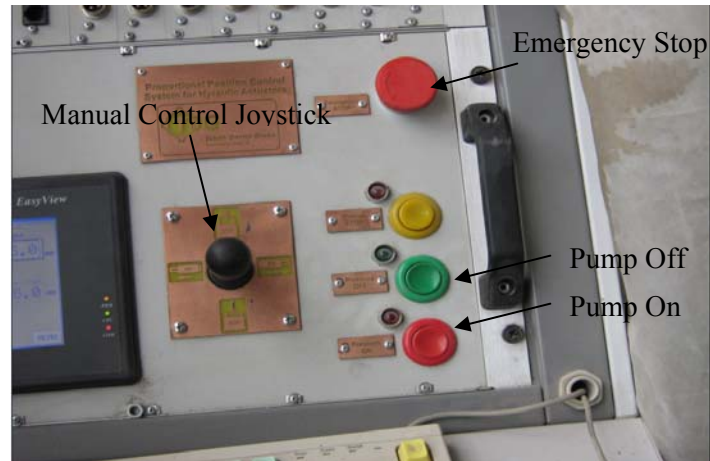
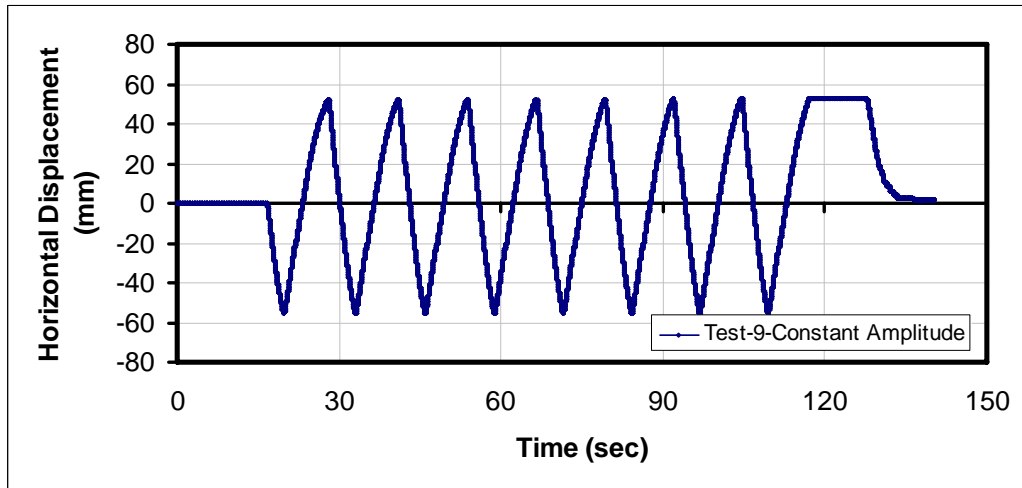


Figure 3.7. View of the Control Panel-2

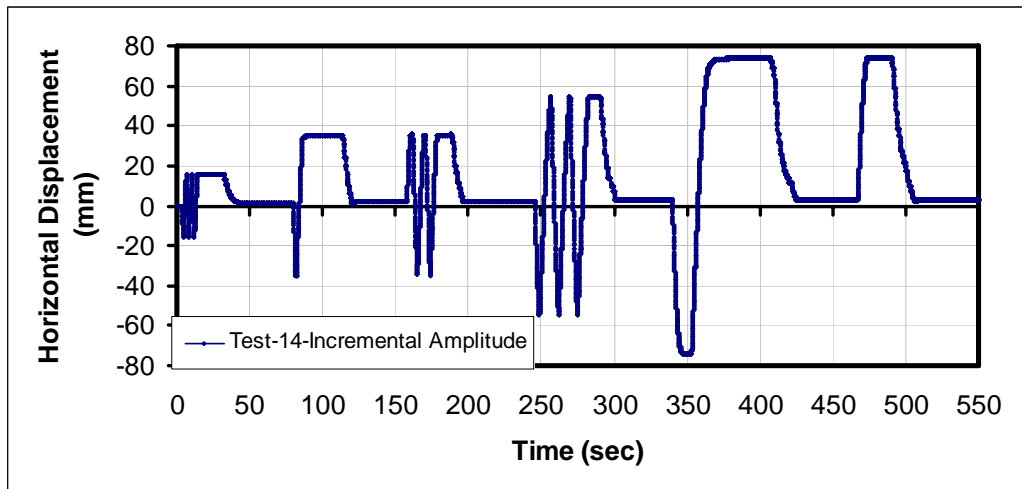
In reversed horizontal loading tests, generally, cycles with constant displacement amplitude are utilized. In addition to successive tests with different displacement amplitudes, some incremental amplitude tests are performed using manual control to check the performance of isolation system at different displacement amplitudes. In Figure 3.8, graphical representations of both constant amplitude and incremental amplitude patterns are presented.

In general, eight cycles are applied to the test bearings in order to observe possible degradations in response. Stability and survivability of the bearings are verified by using the same set of bearings in multiple tests.

During the application of the reversible horizontal displacement, the test set up is observed to allow rotation of the bearings. It is well known that the bearings of a bridge excited by an earthquake can be subjected to rotation in combination with reversible horizontal loads. The magnitude of rotation measured during the tests is around 0.005 ± 0.002 radians which is representative of real case structural responses. Nevertheless, in some tests, restrainers are placed to prevent rotation and not much difference in energy dissipation characteristics of the same bearings are observed at tests with restrained rotations compared to tests with unrestrained rotations.



(a)



(b)

Figure 3.8. Displacement Patterns with (a) Constant Amplitude and (b) Incremental Amplitude

Test results and force-deflection graphs of cyclic horizontal tests are those of two bearings since two bearings are tested simultaneously, as presented in Figure 3.9. Testing two bearings simultaneously is in conformance with specifications [50].



Figure 3.9. View of Test Set Up During a Test

3.5. Mechanical Properties of BRBs

Horizontal force-displacement curves of BRBs can be idealized in a bilinear form as shown in Figure 3.10.

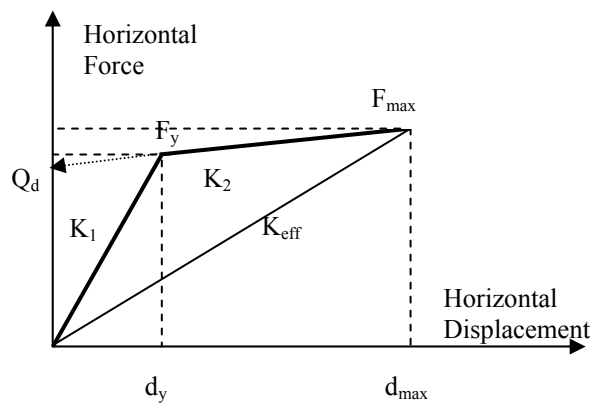


Figure 3.10. Bilinear Horizontal Force-Displacement Relation

where

d_y : yield displacement (in m)

d_{max} : maximum displacement (in m)

- F_{\max} : maximum horizontal force (in kN)
 F_y : yield strength (in kN)
 K_{eff} : effective stiffness (in kN/m)
 K_1 : primary slope (stiffness) of the bilinear hysteresis curve (in kN/m)
 K_2 : secondary slope (stiffness) of the bilinear hysteresis curve (in kN/m)
 Q_d : characteristic strength (in kN)

Using the idealized bilinear relation presented in Figure 3.10, the equivalent viscous damping ratio (β_{eq}) and energy-dissipation capacity (EDC) of a test bearing can be computed from the following expressions:

$$\beta_{\text{eq}} = \frac{4 \times Q_d \times (d_{\max} - d_y)}{2 \times \pi \times K_{\text{eff}} \times d_{\max}^2} \quad (3.1)$$

$$EDC = 4 \times Q_d \times (d_{\max} - d_y) \quad (3.2)$$

Symbols and definitions used in this section and in sections 2.3.1 and 2.3.3 are used in the dissertation.

3.6. Materials Utilized In Test Bearings

Elastomeric bearings used in this study are manufactured by vulcanization of thin steel shims and rubber layers under temperature and pressure. A view of the rubber layers and steel shims before vulcanization is presented in Figure 3.11.

Rubber used in EBs can be either natural rubber or neoprene (polychloroprene) or a mixture of both. Neoprene is known to have more resistance to weathering, heat and flame compared to natural rubber [67]. It has also lower water vapour and air permeability compared to natural rubber. A mixture of neoprene and natural rubber is utilized in rubber formulation of the test bearings since this formulation is frequently used by the bearing manufacturer.



Figure 3.11. Rubber Layers and Steel Shims

Shear modulus of rubber is usually expressed by using Shore Hardness. Rubber compounds used in typical isolation bearings have hardness in the range of 37-60 [9]. Shear modulus of the rubber in EBs can vary between 0.4 MPa and 1.0 MPa based on the selection of Shore Hardness. Shear modulus (G) of test bearings which have outer diameter of (D) 300 mm, inner diameter (d) of 150 mm and total rubber thickness (t_r) of 75 mm can be calculated from Test-4 as follows [68]:

Horizontal displacement corresponding to 50% shear strain can be calculated as:

$$d_{\gamma=50\%} = 0.5 \times t_r = 0.5 \times 75\text{mm} = 37.5\text{mm}$$

At this displacement horizontal force in test is as follows:

$$F_{\gamma=50\%} = 51\text{kN}$$

Plan area of an EB excluding the central hole:

$$A_{rubber} = 0.25 \times \pi \times (0.15^2 - 0.075^2) = 0.053\text{m}^2$$

Shear modulus can be calculated as [68]:

$$G = \frac{F_{\gamma=50\%}}{A_{rubber} \times 2 \times 0.5} \quad (3.3)$$

The factor 2 in denominator of Equation 3.3 accounts for two simultaneously tested bearings (double shear) while the factor 0.5 accounts for 50% shear strain.

$$G = \frac{51kN}{0.053m^2 \times 2 \times 0.5}$$

$$G=962 \text{ kPA} \approx 0.95 \text{ MPa}$$

where

$d_{\gamma=50\%}$: horizontal displacement corresponding to 50% shear strain

A_{rubber} : plan area of an EB excluding the central hole

$F_{\gamma=50\%}$: horizontal force corresponding to 50% shear strain

Calculated shear modulus is only utilized for checking conformance of test bearings to AASHTO [6, 27] requirements presented in Table 3.2, Table 4.9, Figures 3.13, 3.14 and Figures 4.33, 4.34. In Chapter 4 and Chapter 5, test results of EBs and BRBs are utilized in computations.

3.7. Design of Test Bearings

Geometric details of test bearings are presented in Figure 3.12 for a test bearing with an internal hole diameter of 100mm. Different internal hole diameters have been investigated to study the effects of variations in total volume of granular material and shape factor on bearing response. The internal hole cap is designed to be thicker than the anchor plate of elastomeric part to pre-compress the granular material when the cap is closed.

Shape factor, a ratio of loaded area to bulge-free area, of the tested bearings are kept intentionally low in the design stage to increase the ratio of the vertical compressive load shared by the central core and hence, to benefit from the increase in friction during internal sliding of the steel balls.

Bearings are designed with 1/3 scaled loads of a standard highway bridge with simply supported precast prestressed I-girders having a length of 28.5 meters. Design of the bearings with 100 mm internal hole and 120 kN vertical load is presented below. Design of the bearing is performed based on the requirements of AASHTO specifications [6, 27]. In design stage, two AASHTO specifications are used instead of one due to very low shape factors of test bearings. Input data of the design values is presented in Table 3.1.

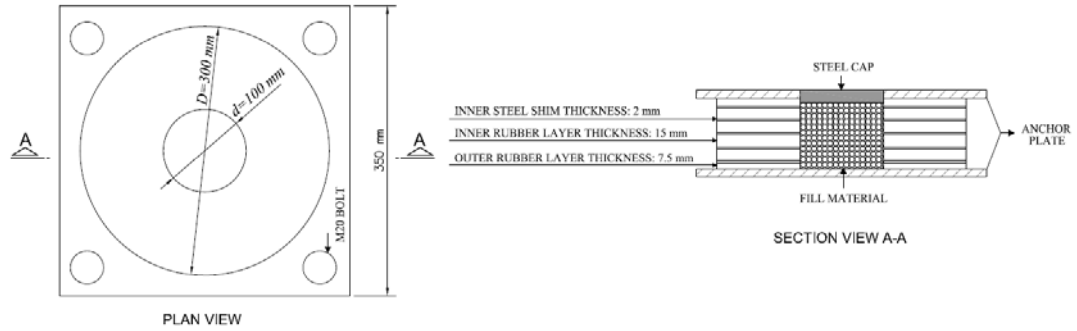


Figure 3.12. Dimensions of the Test Bearings for $D/d=3.0$ (in mm)

Table 3.1. Input Data of the Design Values

Parameter	Value	Unit
c_c	0.005	m
D	0.3	m
d	0.1	m
D_b	0.290	m
d_s	0.015	m
d_{max}	0.12	m
$F_{y,steel\ shims}$	240	MPa
G	0.95	MPa
h_s	0.002	m
P_{ver}	120	kN
t	0.015	m
t_{max}	0.015	m
t_r	0.075	m
θ	0.0075	rads.

where

c_c : thickness of the rubber cover at the sides (in m)

D_b : bonded diameter (in m)

d_s : service load displacement in the horizontal direction (in m)

$F_{y,steel}$: yield strength of steel shims (in kN)

P_{ver}^{shims} : vertical compressive load (in kN)

θ : maximum service rotation due to unfactored total load (in rad.) (misalignment ignored)

Checks according to AAHSTO LRFD 2007 Section 14 [27]:

The unfilled shape factor of the test bearings shown in Figure 3.12:

$$S = \frac{D^2 - d^2}{4t \times (D + d)} = 3.33$$

The area of unfilled bearing is computed as:

$$A_{Rubber} = 0.25 \times \pi \times (D^2 - d^2) = 0.062832m^2$$

The area of filled bearing is computed as:

$$A = 0.25 \times \pi \times D^2 = 0.070686m^2$$

- In order to limit the shear stresses and strains due to vertical compressive load, compressive stress in rubber should be checked:

$$\sigma_s = \frac{120000N}{62832mm^2} = 1.91MPa$$

$$\sigma_s \leq 1.66GS \leq 11MPa \rightarrow 1.91MPa < 5.26MPa \text{ OK} \quad (3.4)$$

- Check vertical strain under compressive stress:

$$\varepsilon_c = \frac{\sigma_s}{6GS^2} = 0.03 < 0.07 \text{ OK} \quad (3.5)$$

- Check effects of rotation and compression in order to ensure no point in the bearing undergoes net uplift:

$$\sigma_s > 0.75GS \left(\frac{\theta}{n} \right) \left(\frac{D}{t} \right)^2 \rightarrow 1.91MPa > 1.78MPa \text{ OK} \quad (3.6)$$

where

ε_c : vertical compressive strain

σ_s : service average compressive stress due to unfactored total load on elastomer part
(in MPa)

n : number of internal rubber layers

- Check effects of rotation, compression and shear:

$$\sigma_s < 2.5GS \left[1 - 0.15 \left(\frac{\theta}{n} \right) \left(\frac{D}{t} \right)^2 \right] \rightarrow 1.91 \text{MPa} < 7.02 \text{MPa OK} \quad (3.7)$$

- Check stability of the bearing:

Check if $2P < N$:

$$P = \frac{\frac{1.92t_r}{L}}{\sqrt{1 + \frac{2L}{W}}} \quad (3.8)$$

$$N = \frac{2.67}{(S + 2.0) \times \left(1 + \frac{L}{4.0W} \right)} \quad (3.9)$$

for circular bearings $W=L=0.8D$:

$$P = \frac{1.92t_r}{(0.80D \times \sqrt{3})} = 0.35 \rightarrow 2P = 0.70 \quad (3.10)$$

$$N = \frac{2.67}{(S + 2.0) \times 1.25} = 0.40 \quad (3.11)$$

where P and N are parameters used in stability calculations.

Since $2P > N$ further investigation of stability is required.

In this case:

$$\sigma_s \leq \frac{GS}{(2P - N)} \rightarrow 1.91MPa < 10.55MPa \quad \text{OK} \quad (3.12)$$

- Check thickness of steel shims since shims should be able to sustain the tensile stresses induced by compression of the bearing:

$$h_s > 3t_{\max} \left(\frac{\sigma_s}{F_{y, \text{steelshims}}} \right) \rightarrow 2mm > 0.36mm \quad \text{OK} \quad (3.13)$$

where

h_s : thickness of the steel shims

t_{\max} : thickness of the thickest rubber layer in the EB

Checks according to AASHTO Guide Specification for Seismic Isolation [6]:

- Shear strain due to vertical compression:

$$\gamma_c = \frac{3SP_{\text{ver}}}{1 + 2kS^2} \approx \frac{P_{\text{ver}}}{A_r GS} \quad (3.14)$$

where k is elastomer material constant.

For $d_{\max} = 0.12$ m & $D_b = 0.290$ m area of the overlap between top and bottom bonded areas of the horizontally deformed bearing (A_r) can be calculated as follows [9]:

$$D_b = D - 2 \times c_c \quad (3.15)$$

$$\chi = \sqrt{D_b^2 - d_{\max}^2} = 0.264m \quad (3.16)$$

$$A_r = 0.5 \left(D^2 \sin^{-1} \left(\frac{\chi}{D_b} \right) - d_{\max} \times \chi \right) = 0.035640 \text{m}^2 \quad [9] \quad (3.17)$$

Thus shear strain due to vertical compression:

$$\gamma_c = 1.06$$

- Shear strain due to seismic design displacement:

$$\gamma_{s,eq} = \frac{d_{\max}}{t_r} = \frac{0.120}{0.075} = 1.6 \quad (3.18)$$

- Shear strain due to rotation:

$$\gamma_r = \frac{(D^2 \theta)}{(2t_r)} = 0.3 \quad (3.19)$$

- For $d_s = \pm 15$ mm, shear strain due to service load displacement:

$$\gamma_{s,s} = \frac{d_s}{t_r} = 0.2 \quad (3.20)$$

where

- γ_c : shear strain due to vertical compressive load
- γ_r : shear strain due to rotation
- $\gamma_{s,eq}$: shear strain due to seismic design displacement
- $\gamma_{s,s}$: shear strain due to service load displacement

Limits in AASHTO Guide Spec. Section 14.3 [6]:

$$\gamma_c = 1.06 \leq 2.5 \quad \text{OK}$$

$$\gamma_c + \gamma_{s,s} + \gamma_r = 1.56 \leq 5.0 \text{ OK}$$

$$\gamma_c + \gamma_{s,eq} + 0.5\gamma_r = 2.81 \leq 5.5 \text{ OK}$$

Checks controlling conformance of the test EBs to AASHTO specifications [6, 27] under 120 kN, 200 kN, 300 kN, 400 kN and 500 kN vertical loads are presented in Table 3.2, Figures 3.13 and 3.14. Bearings with D/d ratios of 3.75, 3.0, 2.5 and 2.0 are included in the table. Bearings with D/d=5.0 are excluded from this table since they are not utilized frequently in the tests and they are not tested under high vertical compressive forces.

Table 3.2. Conformance of Test EBs to AASHTO Requirements

D/d	S	P _{ver}	ϵ_c (Eqn. 3.5)	σ_s (comp) (Eqn. 3.4)	σ_s (comp+rot) (Eqn. 3.6)	γ_c (Eqn. 3.14)
3.75	3.67	120 kN	0.024<0.07 OK	1.83<5.78 OK	1.83<1.96 NOT OK	0.97<2.5 OK
3.75	3.67	200 kN	0.04<0.07 OK	3.05<5.78 OK	3.05>1.96 OK	1.61<2.5 OK
3.75	3.67	300 kN	0.06<0.07 OK	4.57<5.78 OK	4.57>1.96 OK	2.42<2.5 OK
3.75	3.67	400 kN	0.079>0.07 NOT OK	6.09>5.78 NOT OK	6.09>1.96 OK	3.22>2.5 NOT OK
3.75	3.67	500 kN	0.099>0.07 NOT OK	7.62>5.78 NOT OK	7.62>1.96 OK	4.03>2.5 NOT OK
3.0	3.33	120 kN	0.03<0.07 OK	1.91<5.26 OK	1.91>1.78 OK	1.06<2.5 OK
3.0	3.33	200 kN	0.05<0.07 OK	3.18<5.26 OK	3.18>1.78 OK	1.77<2.5 OK
3.0	3.33	300 kN	0.075>0.07 NOT OK	4.77<5.26 OK	4.77>1.78 OK	2.66>2.5 NOT OK
3.0	3.33	400 kN	0.101>0.07 NOT OK	6.37>5.26 NOT OK	6.37>1.78 OK	3.54>2.5 NOT OK
3.0	3.33	500 kN	0.126>0.07 NOT OK	7.96>5.26 NOT OK	7.96>1.78 OK	4.43>2.5 NOT OK
2.5	3.00	120 kN	0.039<0.07 OK	2.02<4.73 OK	2.02>1.60 OK	1.18<2.5 OK
2.5	3.00	200 kN	0.066<0.07 OK	3.37<4.73 OK	3.37>1.60 OK	1.97<2.5 OK
2.5	3.00	300 kN	0.098>0.07 NOT OK	5.05>4.73 NOT OK	5.05>1.60 OK	2.95>2.5 NOT OK

Table 3.2 (Continued)

D/d	S	P _{ver}	ϵ_c (Eqn. 3.5)	σ_s (comp) (Eqn. 3.4)	σ_s (comp+rot) (Eqn. 3.6)	γ_c (Eqn. 3.14)
2.5	3.00	400 kN	0.131>0.07 NOT OK	6.74>4.73 NOT OK	6.74>1.60 OK	3.94>2.5 NOT OK
2.5	3.00	500 kN	0.164>0.07 NOT OK	8.42>4.73 NOT OK	8.42>1.60 OK	4.92>2.5 NOT OK
2.0	2.50	120 kN	0.064<0.07 OK	2.26<3.94 OK	2.26>1.34 OK	1.42<2.5 OK
2.0	2.50	200 kN	0.106>0.07 NOT OK	3.77<3.94 OK	3.77>1.34 OK	2.36<2.5 OK
2.0	2.50	300 kN	0.159>0.07 NOT OK	5.66>3.94 NOT OK	5.66>1.34 OK	3.54>2.5 NOT OK
2.0	2.50	400 kN	0.212>0.07 NOT OK	7.55>3.94 NOT OK	7.55>1.34 OK	4.72>2.5 NOT OK
2.0	2.50	500 kN	0.265>0.07 NOT OK	9.43>3.94 NOT OK	9.43>1.34 OK	5.91>2.5 NOT OK

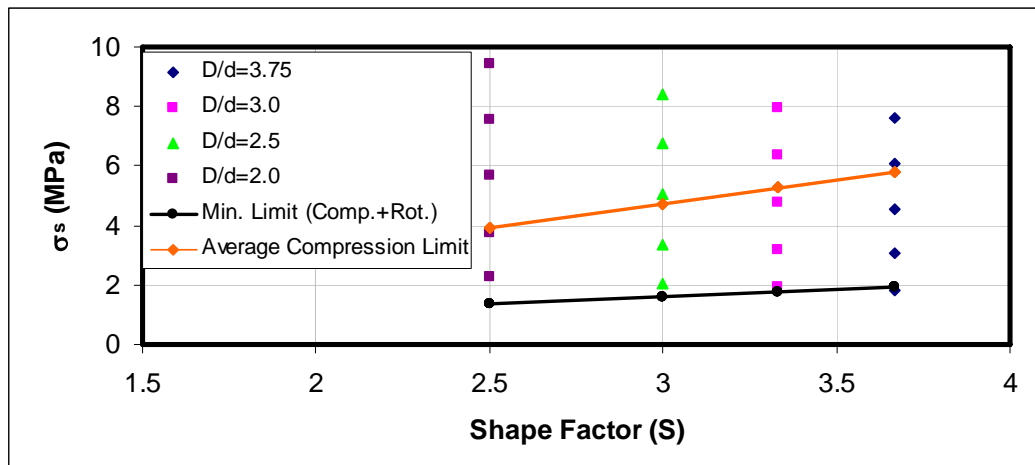


Figure 3.13. Compressive Stress Check for Test EBs

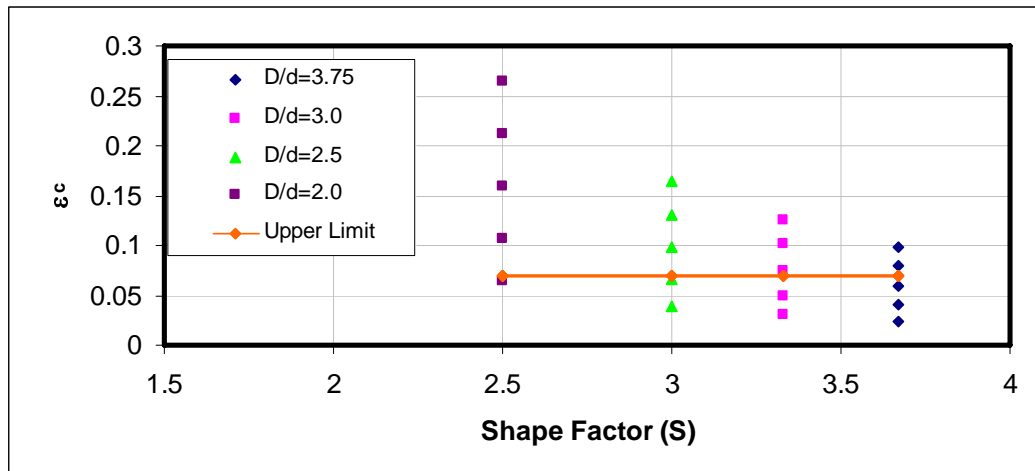


Figure 3.14. Compressive Strain Check for Test EBs

Design checks per requirements of AASHTO specifications [6, 27] indicate that approximately 280 kN of vertical compressive load is the upper limit for the selected EB with no granular fill. Compressive strain, compressive stress and shear strain due to compression or combinations of them are the limiting parameters in design evaluations. Very low shape factors result in significantly high compressive strains under even at moderate levels of vertical compression. The unfilled EB is not recommended to be used at high vertical loads, while the contribution of granular material is expected to reduce the compressive stresses in the elastomeric part that can improve the stability of the bearing. For this reason, the bearings are tested under high vertical loads although the code checks indicate that these bearings do not satisfy code requirements at high vertical compressive loads.

CHAPTER 4

DEVELOPMENT OF BALL RUBBER BEARING (BRB)

4.1. Initial Tests

In initial tests of the experimental program, sand-gravel mix and other granular materials like barite and shredded rubber tires were accommodated in central cores of elastomeric bearings (EBs). Nevertheless, test results indicate that these materials and mixes are unable to provide comparable energy dissipation capacity (EDC) to the existing isolation systems. Energy dissipated by these granular materials is also observed to degrade as the number of loading cycles increases. Sliding and rolling of particles, resistance to volume change, particle interlocking, particle crushing and other sources contribute to frictional resistance [69]. Crushing of granular materials like sand and gravel resulted in such a reduction.

Initial test results contradict the fundamental design requirement of a seismic isolator, as performance of such a device should be stable, predictable and reliable. Thus, a research program was conducted in order to find a reliable material that is capable of dissipating higher energy. Details about initial tests can be found in the research report [64]. Detailed information about all tests is also presented in the appendices and in the CD that is provided with this dissertation.

4.2. Ball Rubber Bearings (BRBs)

Steel balls with small diameters find use in various applications in industry and their costs are low, about 3 USD per kilogram by 2010 prices. Steel balls have preferably lower carbon content and higher manganese content in their composition making them more

resistant to impact [70]. Low carbon ratio also prevents development of surface cracks. Density of a steel ball is in between 7.0 gr/cm^3 - 7.2 gr/cm^3 . Use of steel balls as a fill material as shown in Figure 4.1 have improved durability and reliability of bearings since abrasion of steel is less compared to abrasion of most of the granular materials. During a regular maintenance period, the condition of the bearings can be checked and if needed the bearing can be filled with new steel balls. Similarly, elastomeric bearings (EBs) are very durable and have been shown to be functioning well after over 50 years of service [9].



Figure 4.1. Steel Balls with 1.65 mm Diameter

The test bearings are produced by using steel balls with average diameters (d_{sb}) of 1.65 mm, 3 mm and 5 mm. Views of steel balls having average diameters of 3 mm and 5 mm are presented in Figure 4.2 and Figure 4.3, respectively. Unfilled elastomeric bearings (EBs) are also tested to be used in performance evaluation.



Figure 4.2. Steel Balls with Average 3 mm Diameter (min. 2-max. 4 mm)



Figure 4.3. Steel Balls with Average 5 mm Diameter (min. 4-max. 6 mm)

Five different hole sizes are used in test bearings: 60 mm, 80 mm, 100 mm, 120 mm and 150 mm, corresponding to the diameter (D/d) ratios of 5.0, 3.75, 3.0, 2.5 and 2.0, respectively.

Vertical load can change the response of steel balls to lateral forces and therefore the tests are generally conducted for different vertical compressive load (P_{ver}) levels of 0 kN, 120 kN, 200 kN, 300 kN, 400 kN and 500 kN corresponding to average vertical stresses (σ_{avg}) of 0 MPa, 1.7MPa, 2.8MPa, 4.2MPa, 5.6MPa, 7.1 MPa, respectively. Here average vertical stress is calculated by:

$$\sigma_{avg} = \frac{P_{ver}}{A} \quad (4.1)$$

where

A : plan area of an EB (in m^2)

P_{ver} : vertical compressive load (in kN)

The confinement provided by the surrounding elastomeric bearing increases the vertical load carrying capacity of the system.

Two different hysteresis loop patterns compared to Figure 2.3 are also observed in some tests. These hysteresis loops are idealized and presented in Figure 4.4 and Figure 4.5.

Lower characteristic strength in initial one-fourth of the first cycle (see Figures 4.4 and 4.5) is ignored in calculations.

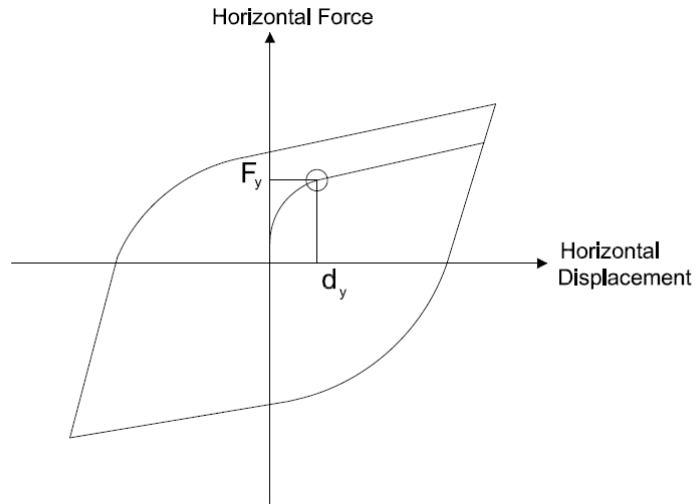


Figure 4.4. Hysteresis Loops Observed in Tests-1st Case

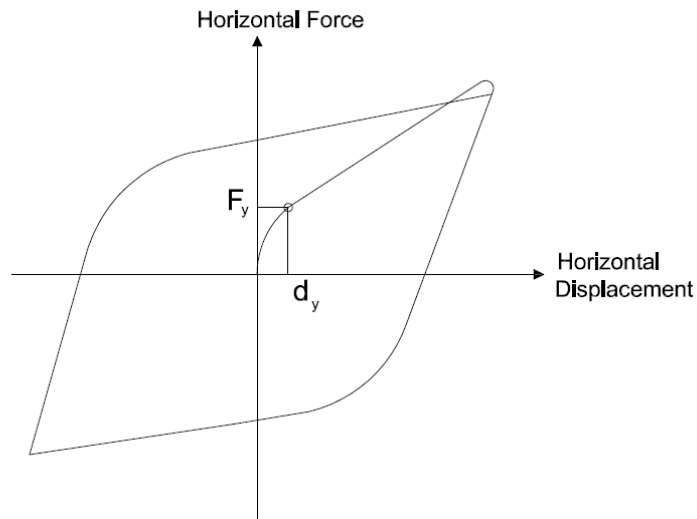


Figure 4.5. Hysteresis Loops Observed in Tests-2nd Case

The different hysteresis loop patterns may have resulted from initially un-uniform pore spaces between steel balls. Wroth [71] performed simple shear tests on steel balls, initially

packed at different densities. The rate of dilation is higher for denser samples. Test results have revealed that the samples dilate until they reach the same critical void ratio, irrespective of their initial density, at which they can continue to shear with no further changes in density. Test results of simple shear tests are presented in Figure 4.6. The tests performed by Wroth [71] indicate that initially un-uniform pore spaces between steel balls may affect the horizontal behavior of BRBs at the initial quarter of the first cycle.

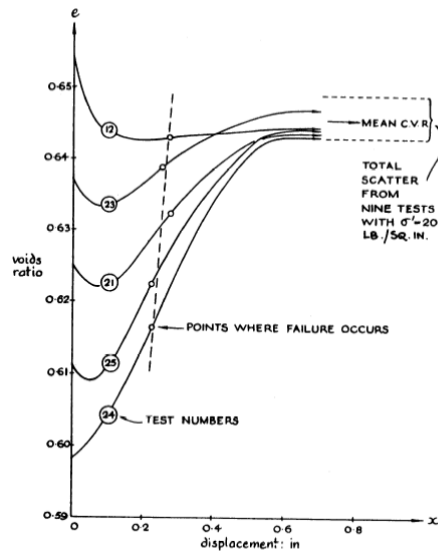


Figure 4.6 Critical Void Ratio (CVR) for Steel Balls [71]

Void ratio can be defined as [72]:

$$e = \frac{V_v}{V_s} \quad (4.2)$$

where

- e : void ratio
- V_s : volume of solids
- V_v : volume of voids

4.3. Ball Rubber Bearing (BRB) Tests and Results

In this section, the BRB test results are presented. The BRB tests are conducted to investigate the effect of various parameters on the performance of the bearing. These parameters are; (i) the presence of steel balls, (ii) steel ball diameter, (iii) diameter of central hole in the bearing, (iv) magnitude of horizontal displacement and (v) level of vertical compression force. The effect of each parameter on the performance of the bearing is presented in the following subsections. In addition, details of non-linear finite element model that is used to verify test results are presented. Behavioral aspects of BRBs are presented with reference to the test results.

4.3.1. Effect of the Presence of Steel Balls

Initial tests are performed in order to observe the performance of the steel balls as an energy dissipating core. Figure 4.7 and Table 4.1 illustrate the effect of the steel balls placed in the central hole of a typical test bearing with $D/d=3.0$ and $P_{ver}=120$ kN ($\sigma_{avg}=1.7$ MPa).

Energy dissipation capacities for each cycle in Table 4.1 are calculated by using reference maximum horizontal displacement ($d_{max, ref}$). Reference maximum horizontal displacement can be defined as the lowest maximum horizontal displacement of related tests in the group.

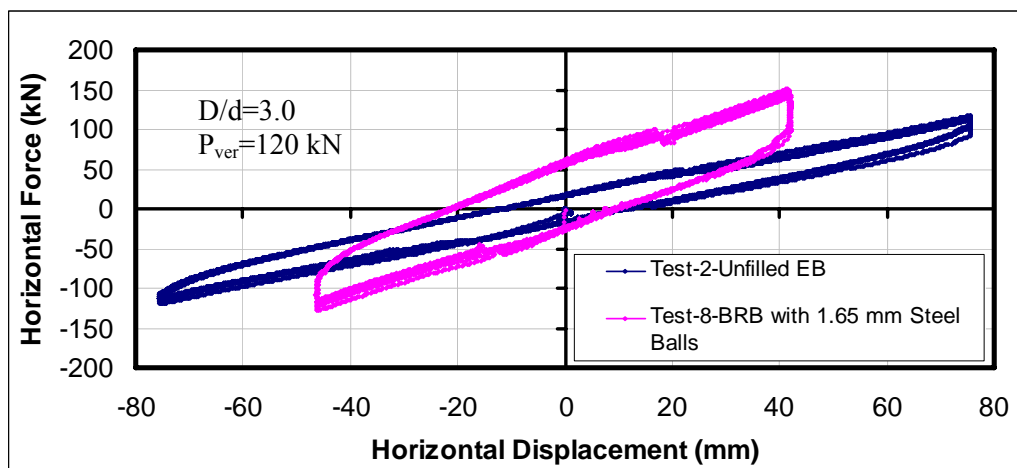


Figure 4.7. Hysteresis Loops of Bearings with and without Fill Material

Table 4.1. Effect of Presence of Steel Balls ($D/d=3.0$, $P_{ver}=120$ kN- $\sigma_{avg}=1.7$ MPa)

Test No:	D/d	Q_d (kN)	d_{max} (mm)	$d_{max, ref}$ (mm)	d_y (mm)	F_{max} (kN)	K_2 (kN/mm)	EDC_{ref} (kN.mm)	Chng in EDC_{ref}
2	3.0	17	75	44	4.70	111	1.25	2672	1.00
8	3.0	40	44	44	1.0	125	1.93	6880	2.57

Comparison of the hysteresis loops of EBs and BRBs filled with steel balls of diameter $d_{sb}=1.65$ mm and the results presented in Table 4.1 clearly show the increase in energy dissipation capacity of the annular bearing due to the presence of the fill material. Indeed, with the use of the steel balls as energy dissipation elements via friction, the equivalent viscous damping ratio increased from 9.69% to 19.91%. No degradation is observed in the horizontal load carrying capacity of the BRB during the eight fully reversed load cycles under the specified vertical load. The hysteresis loop of the BRB justifies the presence of a friction-based energy dissipation mechanism under even a low level of compression. It is also observed that secondary stiffness of the BRB is now 54% higher than the horizontal stiffness of the annular EB.

Tests of BRBs under constant or incremental amplitude cyclic loads yield similar responses to each other as shown in Figure 4.8. The incremental amplitude cyclic load tests are performed via a manual control. In incremental amplitude cyclic load tests, steel balls used in previous tests are re-placed. Almost overlapping hysteresis loops indicate that a core consisting of steel balls with small diameters forms a reliable energy dissipating mechanism. Moreover, steel balls remain undamaged after several tests. Although partial disintegration of the rubber cover is observed in the vicinity of the central core, this local damage does not have any effect on the performance of the bearing.

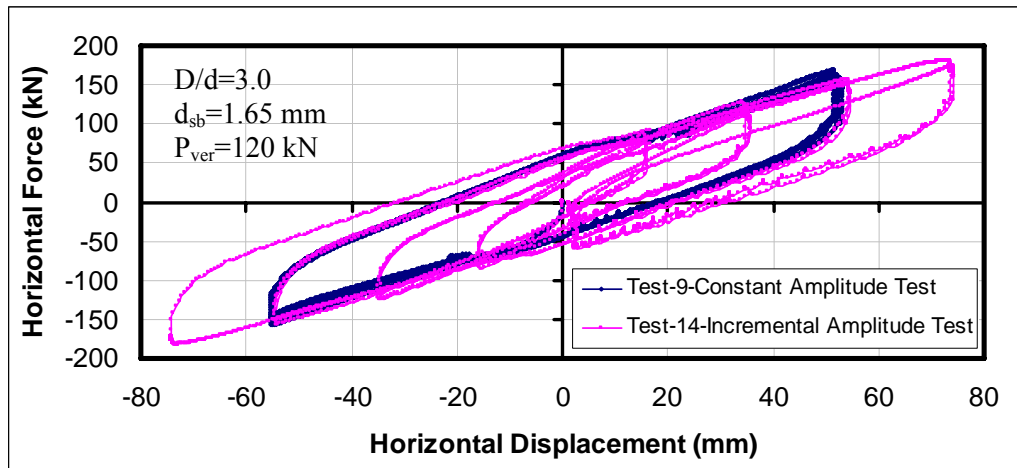


Figure 4.8. Hysteresis Loops of Constant and Incremental Amplitude Tests

It is to be noted that the caps of the bearings are opened immediately after some of the tests to measure the temperature of the granular material. After the tests, the central core had a temperature reading around 45-50 °C (i.e. a temperature rise of 25-30 °C). The increase in the temperature results from energy dissipation through granular friction. It is observed that around these temperature ranges, the performance and integrity of the steel balls are not affected by temperature. Moderate temperature rises in the central core as a result of reversed cyclic loads can be due to the insulation provided by the air pockets present among the steel balls. On the other hand, as intensity of seismic input gets higher, the effect of heat generation on performance of BRB may become more significant. Void ratio measurements conducted via water tests reveal that approximately 30% of the central core volume is filled by air pockets when steel balls with a diameter of $d_{sb}=1.65$ mm are placed in the core. The mild temperature rise does not melt the rubber core surface, either.

The mechanical behavior of granular materials is highly dependent on the arrangement of particles, particle groups and associated pore spaces [69].

It is observed that vertical load level varies during the tests due to rotation and horizontal displacement of test bearings. Variation of vertical load during a test (Test-105) that is presented in Figure 4.9 may result in unsymmetrical hysteresis loops since friction dominates the movement of steel balls.

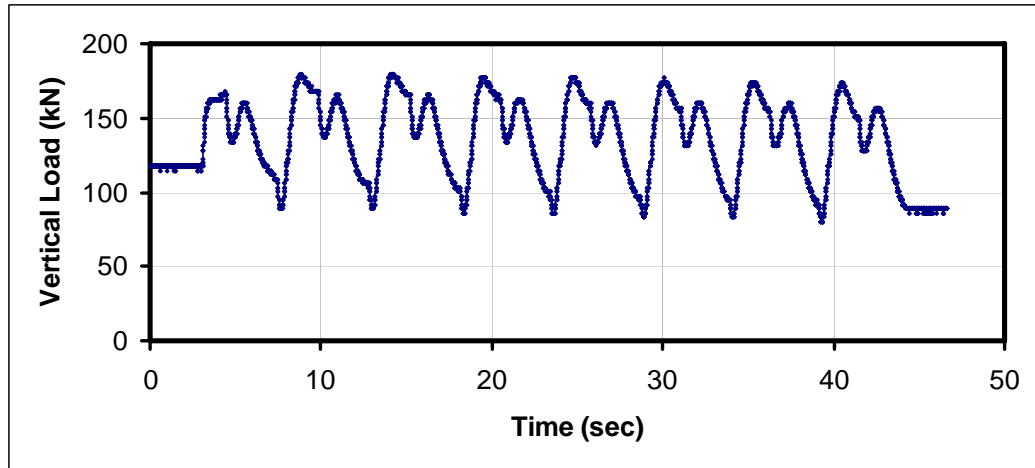


Figure 4.9. Variation of Vertical Load During Test-105.

After initial tests, an extensive testing program is commenced in order to fully understand the performance of BRBs in ultimate and service state conditions.

4.3.2. Effect of Steel Ball Diameter

In Figure 4.10 and Figure 4.11, steel ball diameter (d_s) is the only variable. In Figure 4.10, central hole diameter of the test bearings is 100 mm ($D/d=3.0$), whereas in Figure 4.11 hole diameter is 150 mm ($D/d=2.0$). Bearings are tested under 120 kN ($\sigma_{avg}= 1.7$ MPa) vertical compressive load. Main response parameters are also presented in Table 4.2 and Table 4.3.

Since yield displacement for Test-53 can not be observed from the test data, it is ignored.

Test results reveal that the steel balls with 1.65 mm and 3 mm diameters are efficient to be used in BRBs in terms of energy dissipation compared to steel balls with 5 mm diameter.

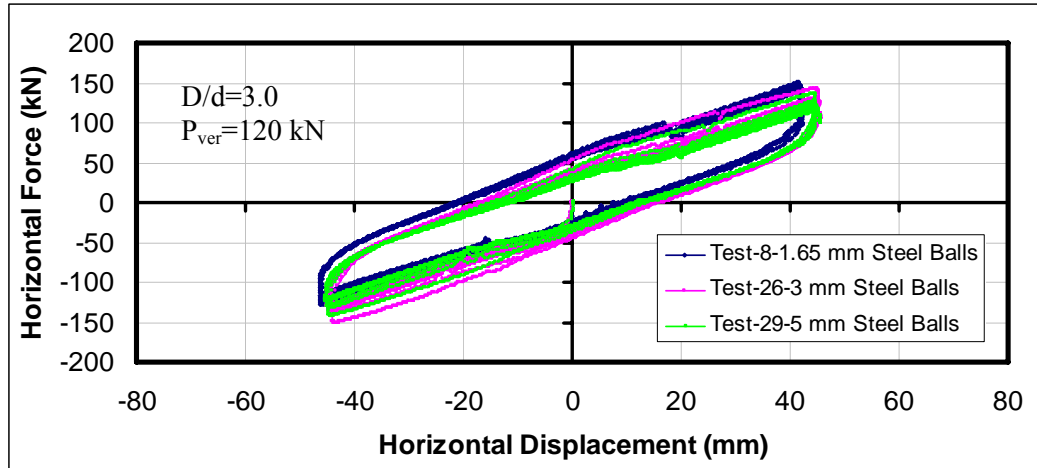


Figure 4.10. Effect of Steel Ball Diameter ($D/d=3.0$ and $P_{ver}=120$ kN- $\sigma_{avg}=1.7$ MPa)

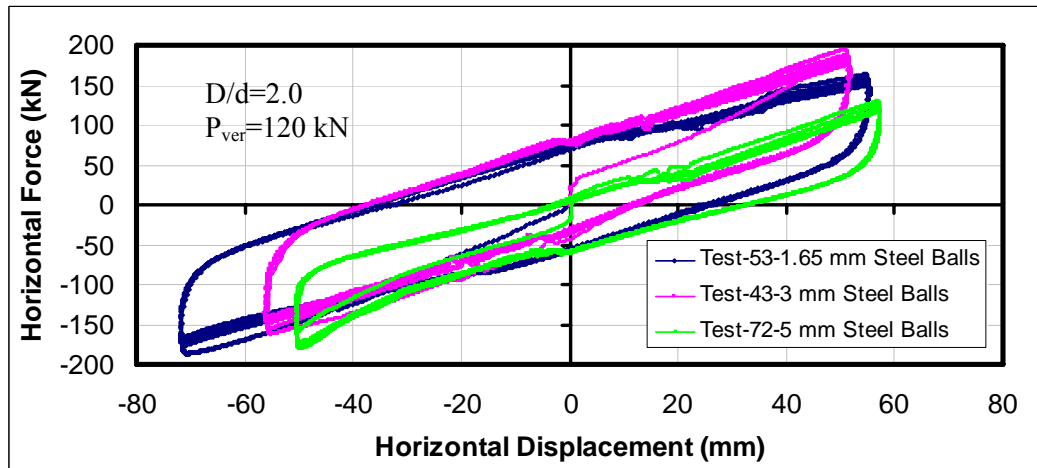


Figure 4.11. Effect of Steel Ball Diameter ($D/d=2.0$ and $P_{ver}=120$ kN- $\sigma_{avg}=1.7$ MPa)

Table 4.2 Effect of Steel Ball Diameter on Main Response Parameters of BRBs ($D/d=3.0$ and $P_{ver}=120$ kN- $\sigma_{avg}=1.7$ MPa)

Test No:	d_{sb} (mm)	Q_d (kN)	d_{max} (mm)	$d_{max, ref}$ (mm)	d_y (mm)	EDC_{ref} (kN.mm)	Chng in EDC_{ref}
8	1.65	40	44	44	1.0	6880	1.00
26	3	40	45	44	4.5	6320	0.92
29	5	28	45	44	1.5	4760	0.69

Table 4.3 Effect of Steel Ball Diameter on Main Response Parameters of BRBs ($D/d=2.0$ and $P_{ver}=120$ kN- $\sigma_{avg}=1.7$ MPa)

Test No:	d_{sb} (mm)	Q_d (kN)	d_{max} (mm)	$d_{max, ref}$ (mm)	d_y (mm)	EDC_{ref} (kN.mm)	Chng in EDC_{ref}
53	1.65	64	63.0	53.5	N/A	13696	1.00
43	3	55	53.5	53.5	3.20	11066	0.81
72	5	32	53.5	53.5	1.95	6598	0.48

The contact between two rigid spherical particles is a point. On the other hand, for particles that are not perfectly rigid, there is a contact radius (r_c) between the particles, as presented in Figure 4.12.

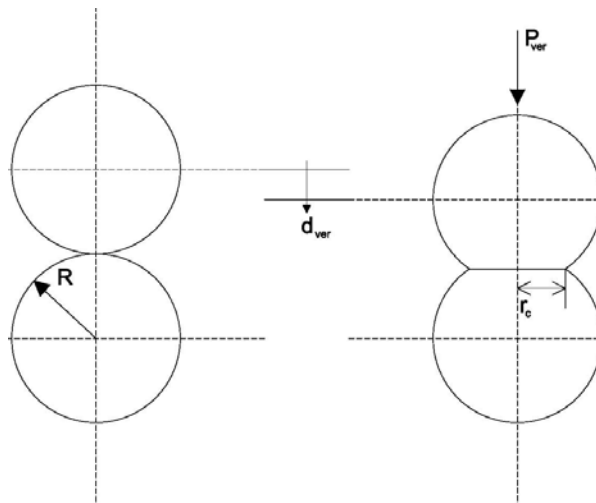


Figure 4.12. Contact Radius of Rigid Spheres [69]

The contact radius increases as the vertical stress and diameter increase [69]. Increase in contact radius with increase in steel ball diameter may alter the performance of BRBs since in practice steel balls may not be infinitely rigid.

The stress-strain behavior of granular materials is dependent on the size, arrangement, density state, shape and surface roughness of particles. These properties typically affect the magnitude of interlocking and sliding resistance between the particles. It is a known fact that for higher interlocking effect, higher friction resistance occurs between the

particles [69]. It is worth mentioning that the steel balls utilized in the tests do not have perfectly smooth surfaces, which results in interlocking between the particles.

Frictional force is directly related to the total contact surface area in a given volume. In a bucket of steel balls, the total contact surface area of the steel balls with smaller diameter is larger than the total contact surface area of steel balls with larger diameter. As expected, lower characteristic strengths are observed for BRBs filled with larger size granular material as in the case of the 5 mm steel balls. Although the tests results for the bearings with 1.65 mm diameter and 3 mm diameter steel balls are comparable, small size steel balls with 1.65 mm diameter are recommended to be used in the BRBs in view of the fact that triaxial tests on glass beads [69] have indicated that peak friction angle decreases as particle diameter increases.

4.3.3. Effect of Diameter of Central Hole in the Bearing

Test results given in Table 4.4 and Figure 4.13 present the effect of central hole diameter on the characteristics and main response parameters of BRBs with $d_{sb}=1.65$ mm under $P_{ver}=200$ kN ($\sigma_{avg}=2.8$ MPa).

Table 4.4. Effect of Hole Diameter on Main Response Parameters of BRBs ($d_{sb}=1.65$ mm, $P_{ver}=200$ kN- $\sigma_{avg}=2.8$ MPa)

Test No:	d (mm)	D/d	Q_d (kN)	d_{max} (mm)	$d_{max, ref}$ (mm)	d_y (mm)	F_{max} (kN)	K_2 (kN/mm)	EDC_{ref} (kN.mm)
62	60	5	26.00	84.0	53.5	2.90	130	1.24	5262
107	80	3.75	52.50	54.0	53.5	2.05	143	1.68	10804
57	100	3.0	43.00	54.0	53.5	3.20	142	1.83	8652
100	120	2.5	57.25	54.0	53.5	2.30	168	2.05	11725
55	150	2.0	64.00	53.5	53.5	N/A	150	1.61	13696

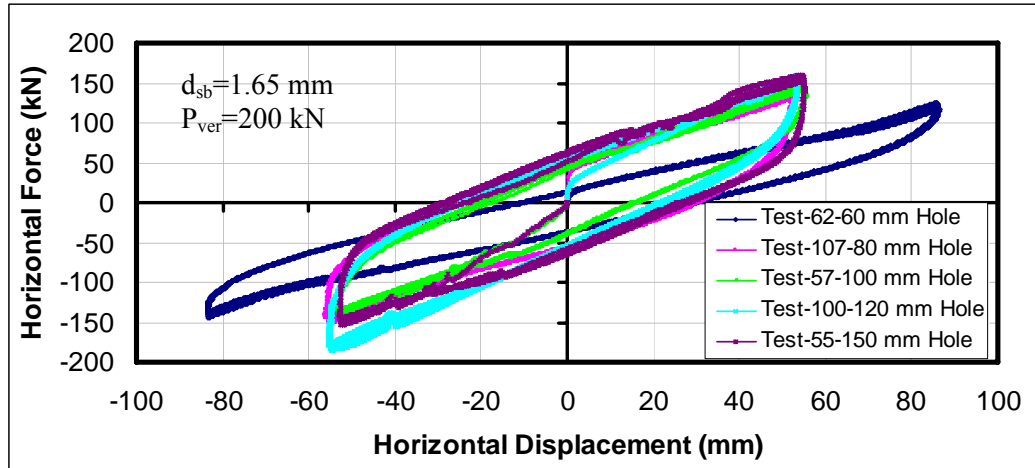


Figure 4.13. Effect of Hole Diameter ($d_{sb}=1.65$ mm, $P_{ver}=200$ kN- $\sigma_{avg}=2.8$ MPa)

Since yield displacement for Test-55 can not be observed from the test data, it is ignored.

The bearings with 60 mm central hole ($D/d=5.0$) have the lowest energy dissipation capacity within the bearings tested in this group. Secondary stiffness of these bearings is also observed to be low when compared to bearings having lower D/d ratios.

BRBs with 80 mm, 100 mm, 120 mm and 150 mm central holes resulted in comparable energy dissipation capacities. Thus, in the design of BRBs, the diameter ratio (D/d) can be set in between 2.0 to 3.75. Designing a bearing with $D/d=3.0$ or $D/d=3.75$ provides a high energy dissipation capacity while limiting the maximum horizontal force. Nevertheless, BRBs having lower D/d ratios may be utilized in special applications such as structures that are located in vicinity of a major fault [7].

4.3.4. Effect of Magnitude of Horizontal Displacement

Magnitude of horizontal displacement can significantly affect the energy dissipating mechanism of a BRB. In three successive tests of the same bearing type with two different maximum horizontal displacements, drastic change is observed in the energy dissipation capacities and characteristic strengths, as depicted in Figure 4.14. The figure is plotted for the bearings with $D/d=2.0$, $d_{sb}=1.65$ and $P_{ver}=120$ kN ($\sigma_{avg}= 1.7$ MPa).

A big difference is not observed in successive tests of other set of bearings with a hole size of 80 mm, which is almost half of that in the previous tests, as shown in Figure 4.15.

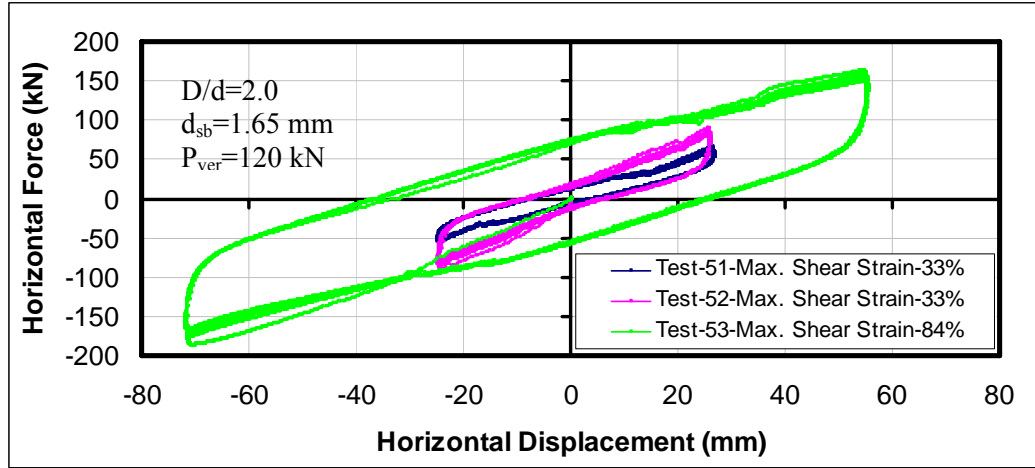


Figure 4.14. Effect of Magnitude of Horizontal Displacement-($D/d=2.0$ and $P_{ver}=120$ kN- $\sigma_{avg}=1.7$ MPa)

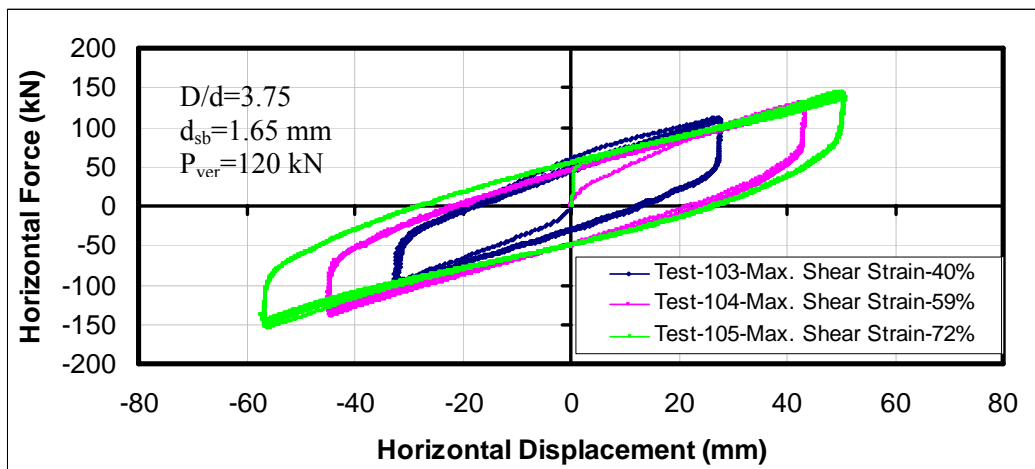


Figure 4.15. Effect of Magnitude of Horizontal Displacement-($D/d=3.75$ and $P_{ver}=120$ kN- $\sigma_{avg}=1.7$ MPa)

The mode of motion may result in such a difference since Marraquin et al. [73] pointed out that steel balls rolling over each other develop less frictional force and hence less energy dissipation capacity (EDC) when compared to the sliding mode of motion. Interlocking

between steel balls at larger shear strains under vertical compressive load may also alter the energy dissipation capacity of BRB. The diameter ratio (D/d) can also influence the energy dissipation mechanism.

BRBs with different central holes are observed to have equivalent viscous damping ratios around 20% as shown in Figure 4.16. As explained earlier, the energy dissipation characteristics of the bearing is directly related to damping and is a complex problem. Steel balls in a small diameter hole may have high contact pressure between each other. Steel balls in a larger hole are likely to have less contact pressure at the same vertical compressive load but have more contact area than the ones in a small hole. Therefore the damping characteristics of steel balls in a larger hole or smaller hole may be similar.

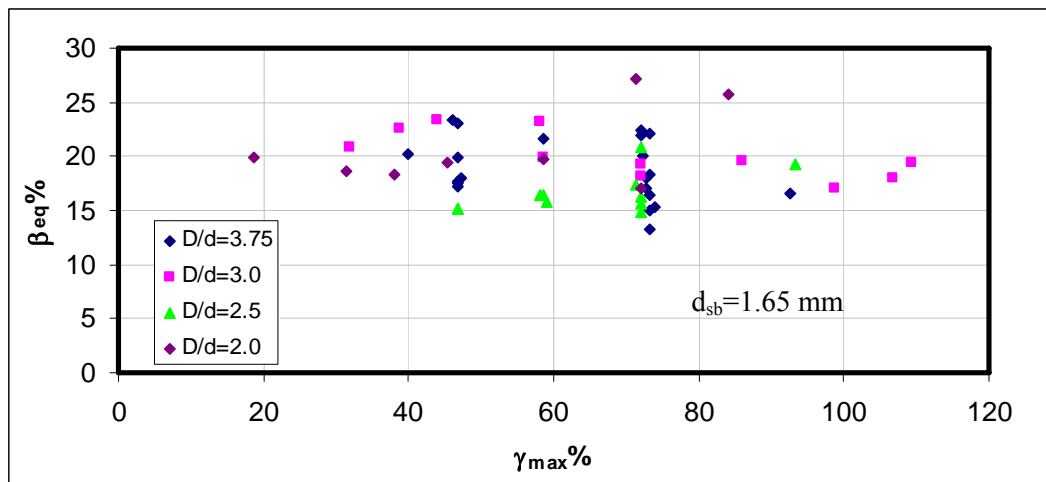


Figure 4.16. β_{eq} vs. γ_{max} of Test Data

4.3.5. Non-Linear Finite Element Analysis- Cyclic Loads

To verify experimental results, finite element model of BRB in Test-8 is studied using ADINA [74] finite element analysis software, as shown in Figure 4.17.

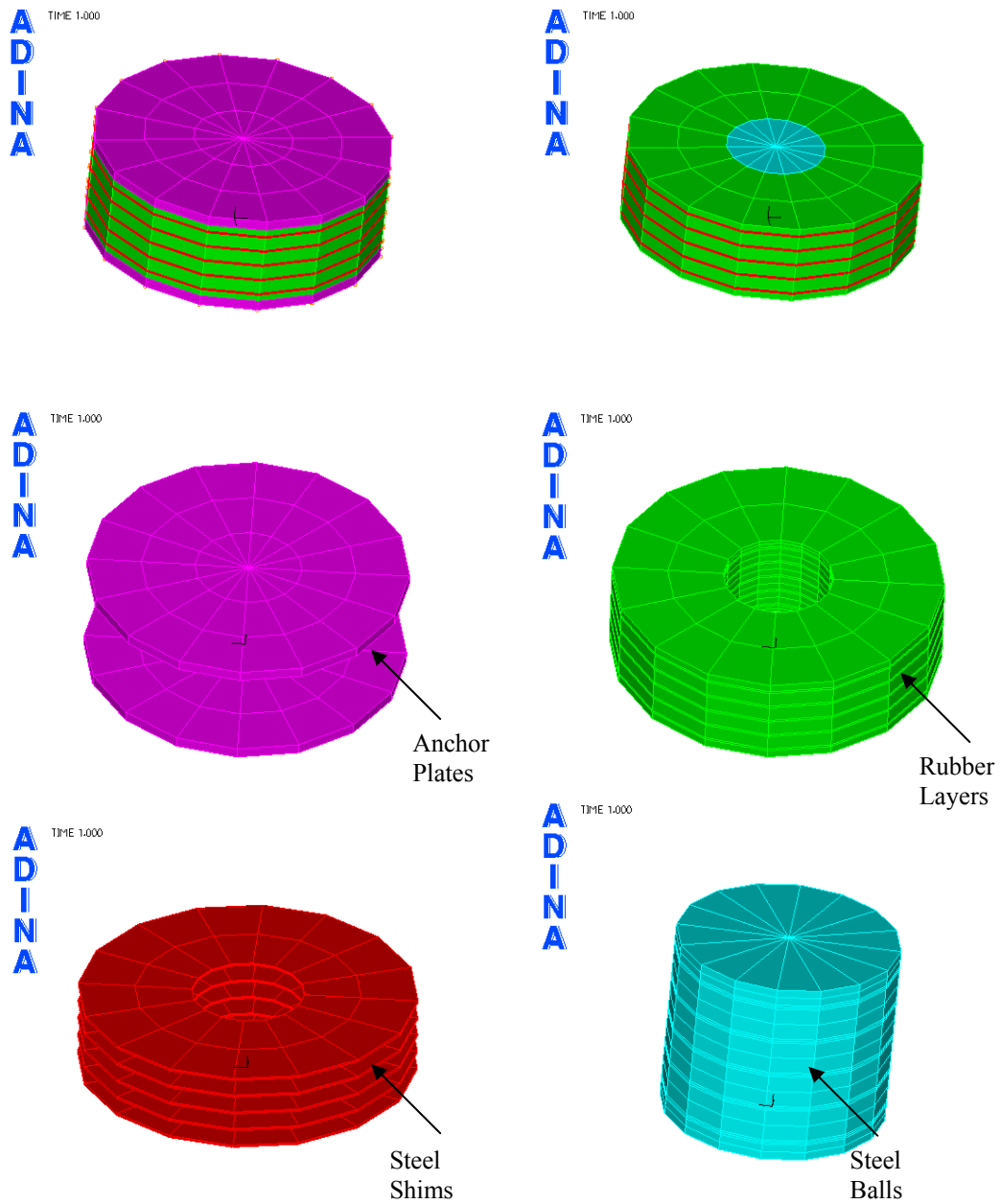


Figure 4.17. General View of the Finite Element Model ($D/d=3.0$)

Steel shims, steel anchors, rubber layers are modelled using 3D solid elements. View of 8 node-3D solid elements is presented in Figure 4.18. Central core is modelled using 6 node-3D solid elements. Mixed interpolation is selected in the analyses. In ADINA, special mixed interpolated elements are available, in which the displacements and pressures are interpolated [74]. These elements are effective and should be preferred in the analysis of

incompressible media and inelastic elements. The use of the 8 node element or 27 node element is recommended in this case [74]. The 27 node element is not selected due to long processing time of the computer. Full Newton-Raphson method is utilized as the iteration method. Small strain-small displacement formulation is used in the analyses, which corresponds to only materially non-linear formulation.

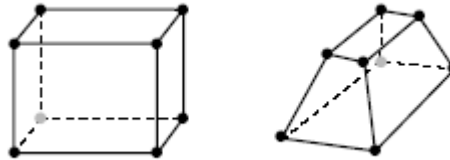


Figure 4.18. View of 8-node Solid Elements

Elastic material properties ($E=200\text{GPa}$, $\nu=0.3$) are selected for steel shims and steel anchors, where E is the elastic modulus and ν is the Poisson's ratio. Rubber is defined using nonlinear material properties that are calculated from Test-2. Bi-linear material definition is utilized for steel balls using the data of Test-8. Equivalent elastic modulus of steel balls ($E_{\text{eq, sb}}=956249\text{ kPa}$) is obtained from vertical compression tests, which will be discussed in Section 4.4. In ADINA, the elasto-plastic stress-strain relation is based on the classical flow theory with the Von-Mises yield criterion [74]. Material models selected in the analyses are summarized in Table 4.5. Bi-linear material definition for steel balls is presented in Figure 4.19. Yield strength of the material in the analysis software is selected appropriately in order to match the experimental characteristic strength.

Table 4.5. Material Properties Used in the F.E. Analyses

Layer	Material	M. Model	E (MPa)	ν	Q_d (kN)
Anchor-Plates	Steel	Elastic	200000	0.300	N/A
Shims	Steel	Elastic	200000	0.300	N/A
Rubber	Rubber	Plastic Bi-linear	2.25	0.495	8.5
Steel Balls	N/A	Plastic- Bi-linear	956.25	0.300	11.5

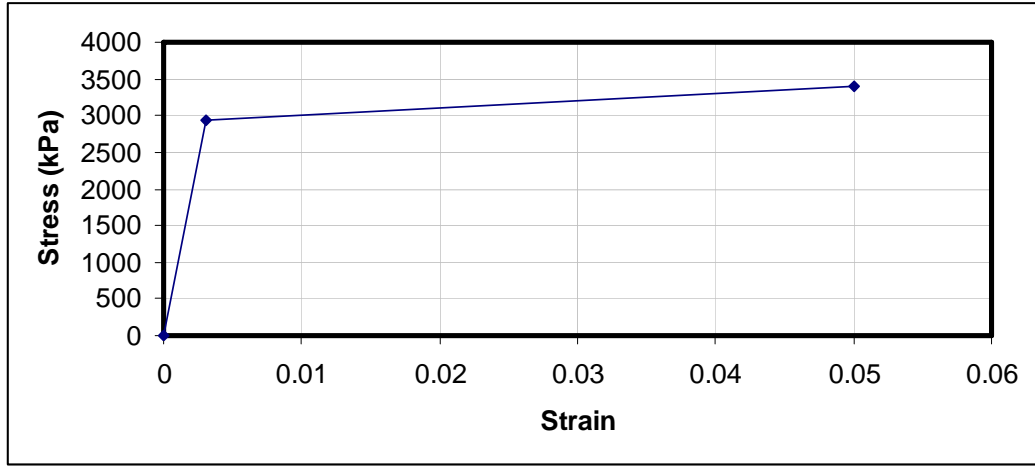


Figure 4.19. Bi-linear Material Definition for Steel Balls

In the analysis software, for the calculation of element matrices, Gauss numerical integration is used. The Gauss integration orders are $2 \times 2 \times 2$ for the 8-node (cube-prism) element and $3 \times 3 \times 3$ otherwise [74].

The stiffness matrix (K_{st}) of an element assemblage can be expressed as:

$$K_{st} = \sum_i \int_{V^i} B_s^{(i)T} C^{(i)} B_s^{(i)} dV^{(i)} = K_{st}^i \quad (4.3)$$

where

B_s : strain-displacement matrix

C : elasticity matrix

K_{st} : stiffness matrix of the element assemblage

Non-linear analysis procedure is adopted with 100 solution steps. The load is set as input to control the displacement. View of horizontally deformed BRB in F.E. (finite element) analysis is presented in Figure 4.20. Comparison of test results (1/2 scaled to obtain hysteresis loop of one single bearing) and F.E. analysis presented in Figure 4.21 indicates close match between the two.

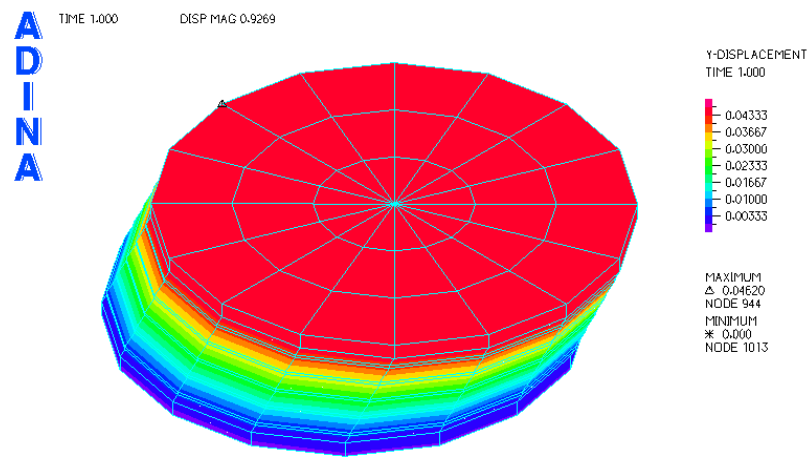


Figure 4.20. Horizontally Deformed BRB in F.E. Analysis

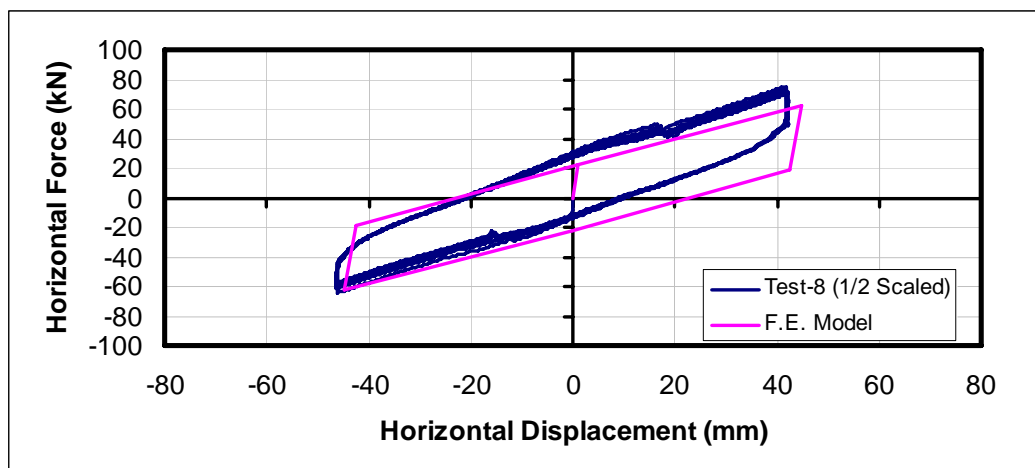


Figure 4.21. Comparison between Test and F.E. Analysis Results

4.3.6. Effect of Level of Vertical Compression Force

Horizontal performance of friction based systems depends highly on the level of vertical load since frictional resistance is equal to friction coefficient (μ) multiplied with vertical compressive load (P_{ver}). The effect of vertical compression on horizontal cyclic behavior of BRBs is investigated by changing the pressure over the test bearings with a fixed D/d ratio and d_{sb} value. Test results are presented in Figure 4.22 for BRBs with $D/d=2.5$ and

$d_{sb}=1.65$ mm. In Table 4.6, main response parameters in these tests are presented together with that of EBs.

EDCs of BRBs are comparable to EDCs of EBs under no vertical load. BRBs subjected to vertical load levels between 120 kN and 500 kN (i.e. vertical pressures between 1.7 MPa and 7.1 MPa), in combination with cyclic horizontal loads have similar equivalent viscous damping ratios, as presented in Figure 4.23.

Variation of Q_d/P_{ver} vs. β_{eq} of test bearings presented in Figure 4.24 indicates that BRBs are efficient for Q_d/P_{ver} ratios from 0.04 up to 0.15 or more in terms of damping.

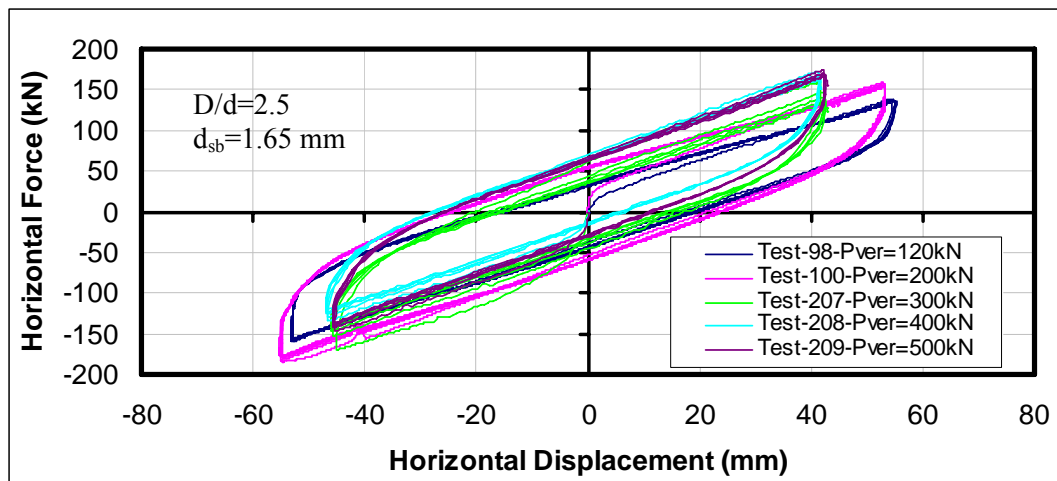


Figure 4.22. Effect of Vertical Compression Level ($D/d=2.5$)

Table 4.6. Effect of Vertical Compression Level on Main Response Parameters of BRBs ($D/d=2.5$, $d_{sb}=1.65$ mm)

Test No:	d_{sb} (mm)	P_{ver} (kN)	σ_{avg} (MPa)	Q_d (kN)	d_{max} (mm)	$d_{max, ref}$ (mm)	d_y (mm)	EDC_{ref} (kN.mm)	Chng in EDC_{ref}
87	-	0	0	11.50	54.5	43.5	2.95	1865	1.00
93	1.65	0	0	11.30	45.0	43.5	4.00	1785	0.96
98	1.65	120	1.7	39.00	54.0	43.5	2.85	6341	3.40
100	1.65	200	2.8	57.25	54.0	43.5	2.30	9435	5.06
207	1.65	300	4.2	41.00	44.3	43.5	4.22	6442	3.45
208	1.65	400	5.6	41.50	44.0	43.5	2.94	6733	3.61
209	1.65	500	7.1	45.00	43.5	43.5	3.99	7112	3.81

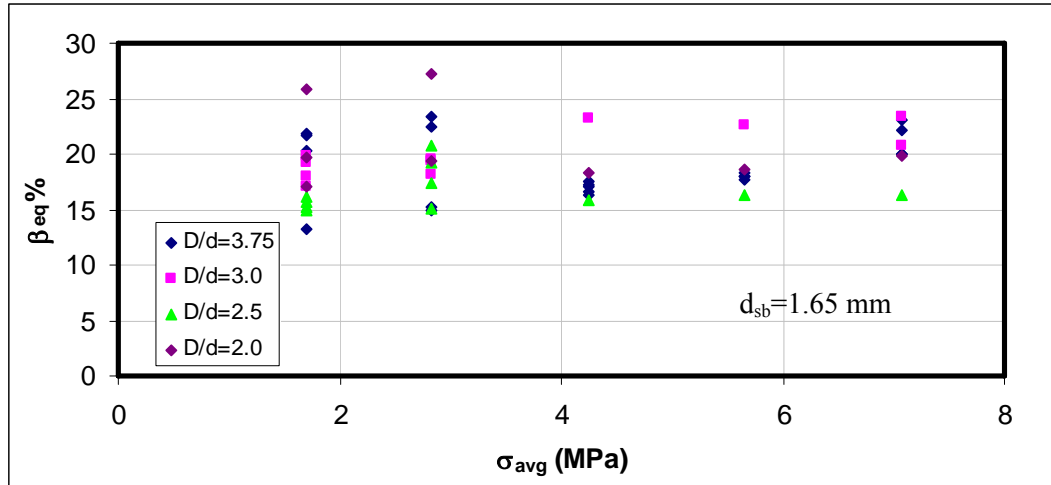


Figure 4.23. β_{eq} vs. σ_{avg} of Test Data

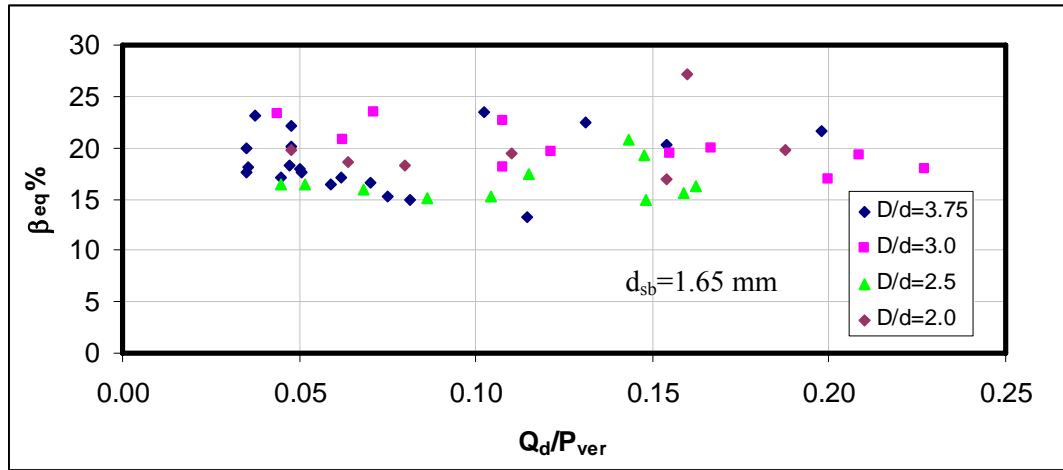


Figure 4.24. β_{eq} vs. Q_d/P_{ver} of Test Data

Characteristic strength of a BRB ($Q_{d,BRB}$) may be computed from the following expression:

$$Q_{d,BRB} = \psi \times P_{ver} \times \mu + Q_{d,EB} \quad (4.4)$$

where

$Q_{d,BRB}$: characteristic strength of ball rubber bearing

$Q_{d,EB}$: characteristic strength of elastomeric part

ψ : a factor that is used to account for the ratio of vertical compressive load resisted by steel balls (See Section 4.4)

μ : coefficient of friction

Generally, elastomeric part of BRB contributes to approximately 20%-40% of the total characteristic strength, as presented in Figure 4.25.

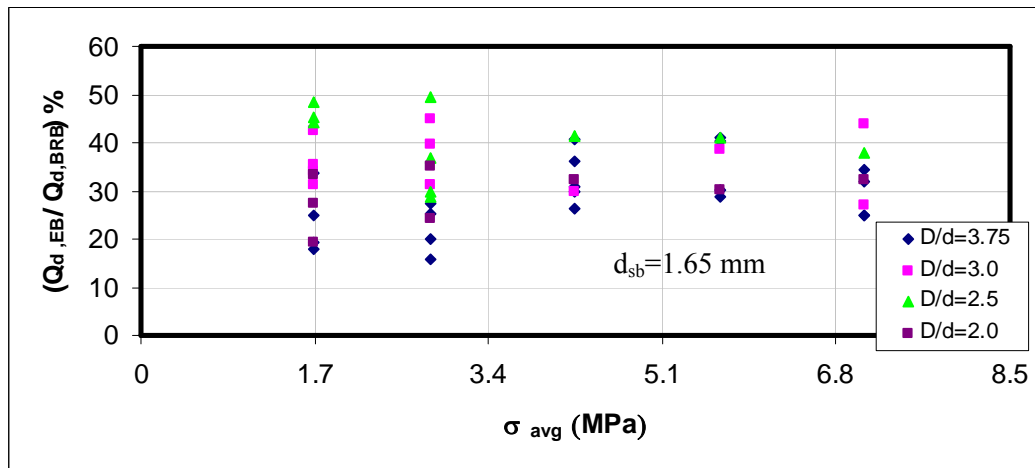


Figure 4.25. ($Q_{d,EB}/Q_{d,BRB}$) of Test Data

Coefficient of friction between steel balls is determined through investigation of BRB tests as follows:

$$\mu = \frac{(Q_{d,BRB} - Q_{d,EB})}{0.5 \times P_{ver}} \quad (4.5)$$

Factor 0.5 in the denominator accounts for ratio of the vertical compressive load resisted by central core, as will be discussed in Section 4.4. Variation of characteristic strength of EBs is based on tests under 200 kN vertical load since tests with higher vertical loads are limited. Test results of EBs having $D/d=3.75$ are observed to have little variation of characteristic strength with vertical load, as presented in Table 4.7. Calculated friction coefficients are presented in Figure 4.26 with respect to vertical stress in the central core. Vertical stress in the central core (σ_{core}) can be calculated by using following equation:

$$\sigma_{core} = \frac{0.5 \times P_{ver}}{0.25 \times \pi \times d^2} \quad (4.6)$$

Table 4.7. Characteristic Strength vs. Vertical Load for EBs with D/d=3.75

Test No:	P _{ver} (kN)	Q _d (kN)
110	120	9.25
111	200	8.25
136	300	11.00
137	400	11.50
138	500	12.00

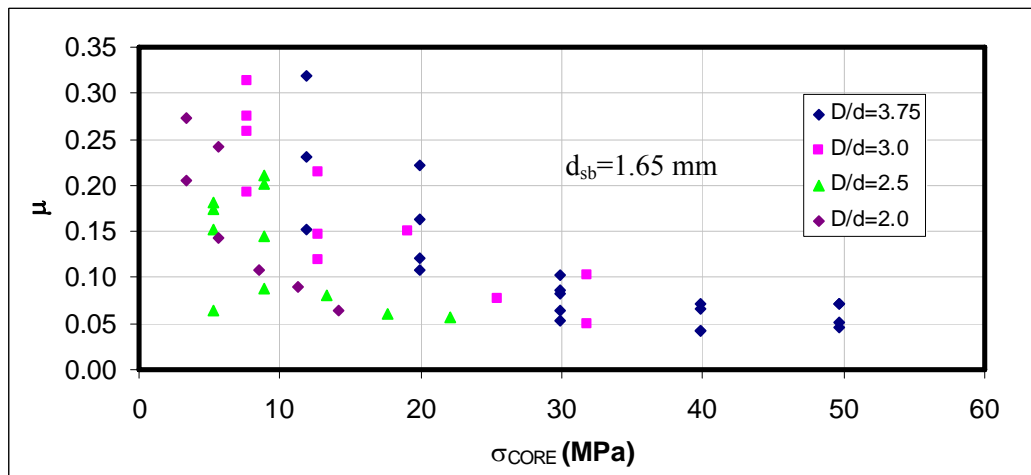


Figure 4.26. Friction Coefficients for Steel Balls with $d_{sb}=1.65$ mm (For One Bearing)

If the variation of characteristic strength with vertical load is neglected for the elastomeric part, then it can be concluded that the characteristic strength of a BRB is almost insensitive to increase in vertical compression since friction coefficient (μ) decreases with increasing vertical compression, as depicted in Figure 4.26. Roussel [69] reported similar results for granular materials. In soil mechanics literature, it is well known that peak friction angle decreases as the confining pressure increases [69].

Relation between coefficient of friction and peak friction angle can be expressed by [72]:

$$\mu = \tan(\phi_p) \quad (4.7)$$

where

ϕ_p : peak friction angle

Horizontal dilation of the steel balls due to Poisson's effect under increasing vertical pressures result in limited characteristic strength. Rubber cannot restrain horizontal dilation of steel balls. Horizontal dilation results in higher void ratios hence lower friction coefficients. Roussel [69] carried out computed tomography analyses on glass beads during triaxial tests. Test results indicated variable local void ratio along cross-section and height of the specimen, as presented in Figure 4.27 for well graded glass beads.

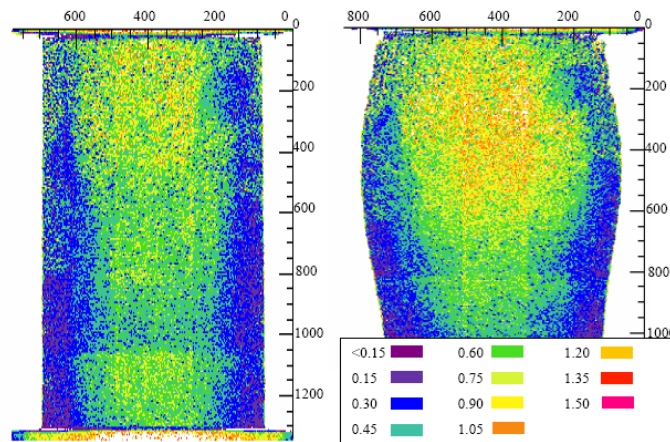


Figure 4.27. Void Ratio at Zero Vertical Strain and at 20% Vertical Strain [69]

To verify horizontal dilation of steel balls in the presence of vertical compression, a finite element model of a BRB is studied using ADINA [74] finite element analysis software. In the finite element model, central hole diameter of the bearing is selected as 100 mm and vertical compressive load on the bearing is set as 300 kN. Elastic modulus of the steel balls

is back calculated from vertical compression tests by using Equation 4.8. In Figure 4.28, horizontal strain distribution in the bearing is presented.

$$E_{eq, sb} = \frac{(K_{eff, ver, BRB, A8} - K_{eff, ver, EB, A7}) \times h}{A_{core}} \quad (4.8)$$

where

- A_{core} : area of the central core
- $E_{eq, sb}$: equivalent elastic modulus of steel balls
- h : height of the bearing excluding external steel anchors
- $K_{eff, ver, BRB, A8}$: Effective vertical stiffness of BRB in Test-A8 (See Section 4.4)
- $K_{eff, ver, EB, A7}$: Effective vertical stiffness of EB in Test-A7 (See Section 4.4)

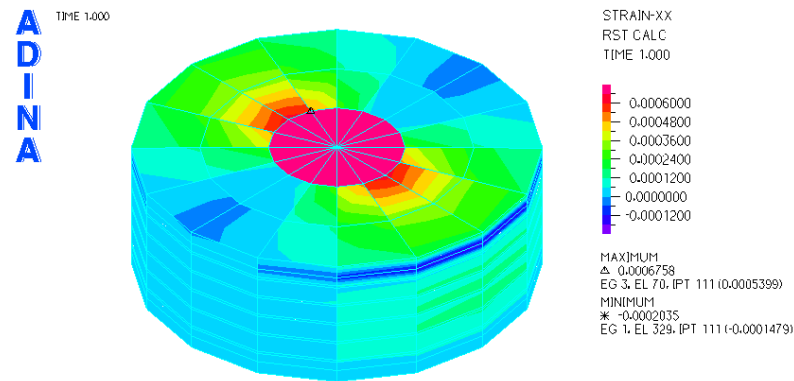


Figure 4.28. Horizontal Strain Distribution in BRB under Vertical Compression ($D/d=3.0$, $P_{ver}=300$ kN- $\sigma_{avg}=4.2$ MPa)

In Figure 4.28, higher horizontal strain in the central core results in horizontal dilation of steel balls. Significantly high vertical compressive stress resisted by the central core results in such dilation.

For problems in rock mechanics where discontinuity between separate particles exists, a numerical technique called discrete element modelling is developed [76]. By using DEM,

granular materials which can freely make and break contacts with their neighbours can be modelled. DEM is capable of analysing interacting deformable bodies undergoing large absolute or relative motions.

One of the important elements of the DEM model is the explicit incorporation of Coulomb's frictional behavior at contacts between elements, as depicted in Figure 4.29.

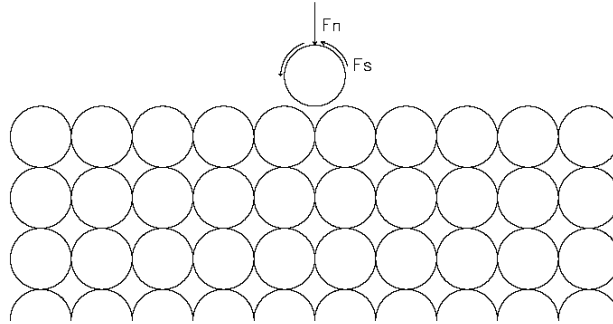


Figure 4.29. Free Body Diagram of Interacting Steel Balls

When the tangential or shear force at a contact exceeds a critical value, F_s^{\max} , slippage between elements is permitted. F_s^{\max} can be defined as [76]:

$$F_s^{\max} = c + F_n \times \tan(\phi) \quad (4.9)$$

where

- c : cohesion
- F_n : normal force at the contact
- ϕ : friction angle

A simple interaction law at the contact of the two interacting bodies can be written as [76]:

$$(F_n)_{new} = (F_n)_{old} + \Delta F_n \quad (4.10)$$

$$(F_s)_{new} = (F_s)_{old} + \Delta F_s \quad (4.11)$$

$$\Delta F_n = K_n \Delta n \quad (4.12)$$

$$\Delta F_s = K_s \Delta s \quad (4.13)$$

where

- K_n : element stiffness in normal direction
- K_s : element stiffness in shear direction
- Δn : relative displacement in the normal direction at a contact
- Δs : relative displacement in the shear direction at a contact
- ΔF_n : incremental normal force
- ΔF_s : incremental shear force

Although it is theoretically possible, discrete element modelling of BRBs under horizontal loads is very impractical due to complexity of the analysis procedure resulting from large number of steel balls and very large shear strains experienced by seismic isolation systems.

4.4. Vertical Compression Tests

Vertical compression tests are performed to determine the contribution of steel balls to the vertical stiffness of the bearings. Test results for various BRBs with 1.65 mm steel balls and EBs with no fill are presented in Table 4.8. In the table, $P_{ver,max}$ and $d_{ver,max}$ correspond, respectively, to the maximum vertical load applied to the bearings and the related maximum vertical displacement, and $K_{eff,ver}$ denotes the effective vertical stiffness of the bearings.

Effective vertical stiffness may be computed from the following expression:

$$K_{eff,ver} = \frac{P_{ver,max}}{d_{ver,max}} \quad (4.14)$$

Table 4.8. Vertical Compression Tests and Test Results (For One Bearing)

Test No:	Hole Diameter-Material.	$P_{ver,max}$ (kN)	$d_{ver,max}$ (mm)	$K_{eff,ver}$ (kN/mm)
A1	120 mm-1.65 mm	169.45	1.095	154.75
A2	120 mm-Empty	166.53	1.464	113.75
A3	80 mm-Empty	164.98	1.397	118.10
A4	80 mm-1.65 mm	167.43	1.455	115.07
A5	150 mm-Empty	161.40	4.062	39.73
A6	150 mm-1.65 mm	183.65	1.607	114.28
A7	100 mm-Empty	168.68	2.649	63.68
A8	100 mm-1.65 mm	165.58	1.089	152.04
A9	80 mm-Empty	166.95	2.919	57.19
A10	120 mm-Empty	166.98	2.564	65.12
A11	120 mm-Empty	172.52	2.565	67.26
A12	100 mm-1.65 mm	176.35	1.287	137.02

It is apparent from Table 4.8 that the effective vertical stiffness of a BRB is substantially higher than that of an EB. This can also be seen from Figure 4.30 which is plotted for an EB with $D/d=3.0$ and for a BRB with the same diameter ratio and $d_{sb}=1.65$ mm: the effective vertical stiffness of a BRB can be 250 % larger than that of an EB. Similar effective vertical stiffnesses of BRBs with different D/d ratios can be explained by relatively low vertical compressive stresses in the central core compared to yield strength of steel balls ($\sigma_{core} \leq 0.2F_{y, St37}$).

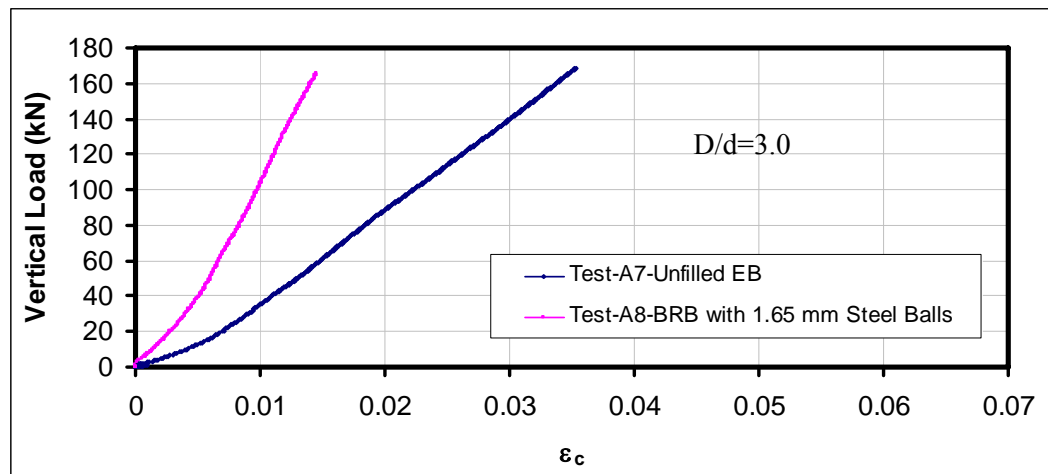


Figure 4.30. Vertical Load-Strain Graphs of Test-A7 & Test-A8

Vertical strain can be defined as:

$$\varepsilon_c = \frac{d_{ver}}{t_r} \quad (4.15)$$

The ratio of vertical load resisted by steel balls to total vertical load carrying capacity of the bearings (ψ) can be computed from vertical test results as follows:

$$\psi = \frac{(P_{ver,BRB} - P_{ver,EB})}{P_{ver,BRB}} \quad (4.16)$$

where $P_{ver,BRB}$ and $P_{ver,EB}$ are the vertical load values measured at a specified vertical displacement, respectively, in a BRB and in an unfilled EB with the same D/d ratio. Table 4.9 presents such calculations for the test bearings defined in Table 4.8.

Table 4.9. Calculation of Vertical Load Resisted by Steel Balls

Test No:	A7 EB	A8 BRB	A2 EB	A1 BRB	A5 EB	A6 BRB
	D/d=3.0		D/d=2.5		D/d=2.0	
P_{ver} (kN)	18.60	58.48	16.82	35.08	8.08	14.53
$\frac{P_{ver,BRB} - P_{ver,EB}}{P_{ver,BRB}}$	39.88		18.26		6.45	
d_{ver} (mm)	0.50	0.50	0.50	0.50	0.50	0.50
ψ	0.68		0.53		0.44	
P_{ver} (kN)	35.18	102.93	40.47	73.28	14.68	27.70
$\frac{P_{ver,BRB} - P_{ver,EB}}{P_{ver,BRB}}$	74.05		32.81		13.02	
d_{ver} (mm)	0.75	0.75	0.75	0.75	0.75	0.75
ψ	0.66		0.45		0.47	
P_{ver} (kN)	51.95	150.43	75.55	134.40	23.45	58.70
$\frac{P_{ver,BRB} - P_{ver,EB}}{P_{ver,BRB}}$	98.48		58.85		35.25	
d_{ver} (mm)	1.00	1.00	1.00	1.00	1.00	1.00
ψ	0.66		0.44		0.60	

As it can be inferred from Table 4.9, approximately 50% of the vertical compressive load applied to a BRB is resisted by its central core if it is filled with 1.65 mm diameter steel

balls. Thus, $\psi=0.5$ can be used in Equation 4.4 when $d_{sb}=1.65$ mm. The role of central core in resisting vertical compression is also verified by comparing F.E. analysis of a BRB and an annular EB with $D/d=3.0$, under $P_{ver}=300$ kN. The vertical stresses at both cases are presented in Figure 4.31.

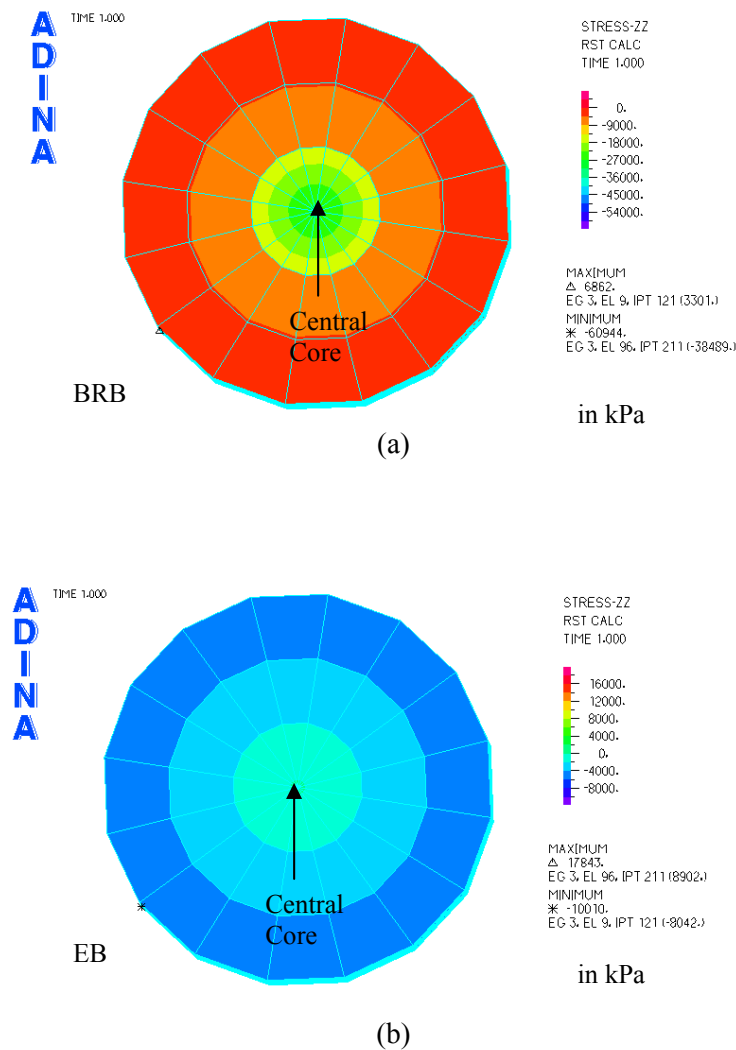


Figure 4.31. Contribution of Central Core to Vertical Load Resistance ($D/d=3.0$, $P_{ver}=300$ kN) (a) BRB (b) annular EB

A schematic view of a horizontally deformed BRB is presented in Figure 4.32. It is to be noted that the horizontal displacement pattern of the bearing inside the hole is in fact very complex due to the fact that at this boundary face two different materials try to move in

different direction: rubber layers restrained by the internal steel plates try to bulge out through the inside of the hole; on the other hand, compressed steel balls due to the applied vertical load try to move just in the opposite direction due to Poisson's effect.

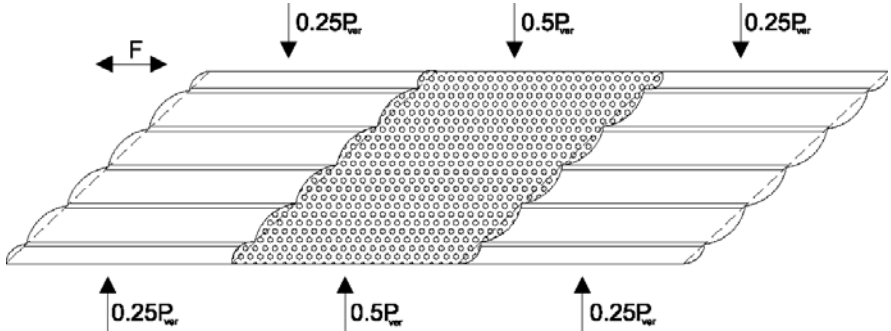


Figure 4.32. Schematic View of a Horizontally Deformed BRB

Test bearings have very low shape factors and still there was no noticeable damage on the bearings due to high compressive applied loads except some permanent traces at rubber-steel shim interfaces. A view of bulged bearings under 500 kN vertical compressive load is presented in Figure 4.33.



Figure 4.33. Bulged Bearings under $P_{ver}=500$ kN

Some BRBs and unfilled EBs are tested under 2500 kN vertical compressive load. This vertical load level is about 10 times the upper limit of AASHTO requirements [6, 27] for test EBs. Significant bulging is observed in the tests. Compressive strains are in excess of 0.1. No permanent damage is observed in tested bearings at unloaded stage.

As one alternative, shape factors of BRBs can be calculated by not taking into account the restraining effect of the steel balls. AASHTO [6, 27] checks required for EBs are believed to be used also for BRBs provided that 50% of the total vertical compressive load is used in the computations since approximately 50% of the total vertical compressive load is resisted by steel balls, provided that the diameter ratio (D/d) is kept in between 2.0-3.75.

As a verification, finite element models of a BRB and an annular EB are studied using ADINA [74] finite element analysis software. In the finite element model, central hole diameter of the bearing is selected as 100 mm and the vertical compressive load on the bearing is set as 300 kN. Maximum compressive strain is 0.03664 in BRB compared to 0.07973 in annular EB, as presented in Figure 4.34. The compressive strains obtained from F.E. analyses are within 10% of those obtained from code [27] equations.

Checks presented in Table 3.1, Figures 3.13 and 3.14 can be repeated for BRBs. Checks are presented in Table 4.10, Figures 4.35 and 4.36 by using 50% of the total vertical compressive load.

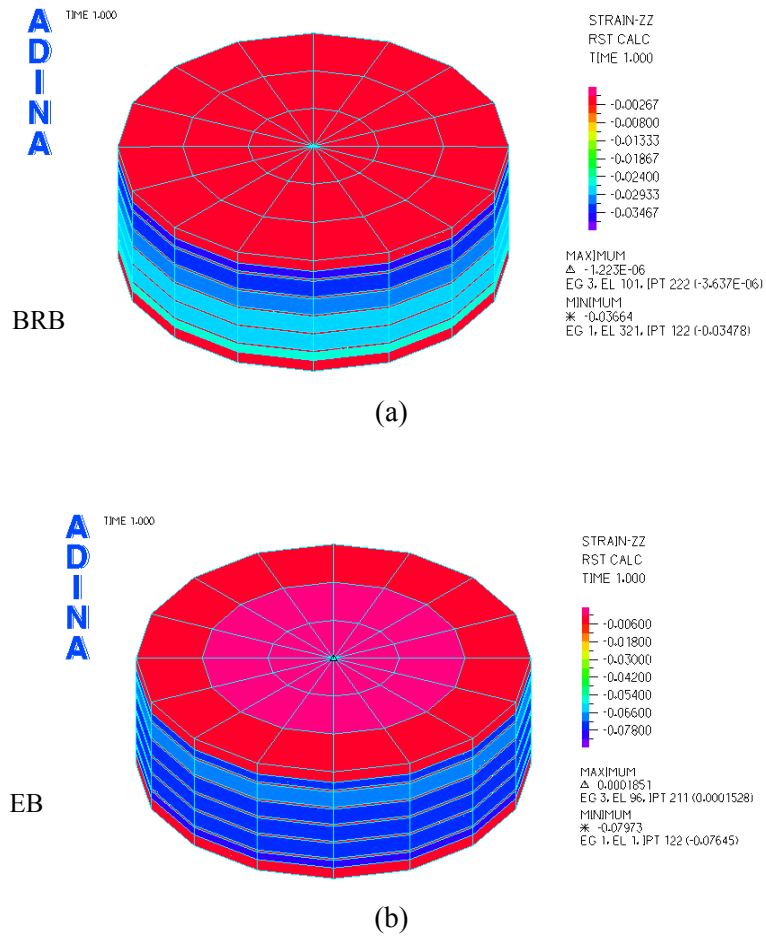


Figure 4.34. Compressive Strains in (a) BRB (b) annular EB with $D/d=3.0$ under $P_{ver}=300$ kN

Table 4.10. Conformance of Test BRBs to AASHTO Requirements

D/d	S	ψP_{ver}	ϵ_c (Eqn. 3.5)	σ_s (comp) (Eqn. 3.4)	σ_s (comp+rot) (Eqn. 3.6)	γ_c (Eqn. 3.14)
3.75	3.67	60 kN	0.012<0.07 OK	0.91<5.78 OK	0.91<1.96 NOT OK	0.48<2.5 OK
3.75	3.67	100 kN	0.02<0.07 OK	1.52<5.78 OK	1.52<1.96 NOT OK	0.81<2.5 OK
3.75	3.67	150 kN	0.03<0.07 OK	2.28<5.78 OK	2.28>1.96 OK	1.21<2.5 OK
3.75	3.67	200 kN	0.04<0.07 OK	3.05<5.78 OK	3.05>1.96 OK	1.61<2.5 OK

Table 4.10 (Continued)

D/d	S	ψP_{ver}	ϵ_c (Eqn. 3.5)	σ_s (comp) (Eqn. 3.4)	σ_s (comp+rot) (Eqn. 3.6)	γ_c (Eqn. 3.14)
3.75	3.67	250 kN	0.05<0.07 OK	3.81<5.78 OK	3.81>1.96 OK	2.01<2.5 OK
3.0	3.33	60 kN	0.015<0.07 OK	0.95<5.26 OK	0.95<1.78 NOT OK	0.53<2.5 OK
3.0	3.33	100 kN	0.025<0.07 OK	1.59<5.26 OK	1.59<1.78 NOT OK	0.89<2.5 OK
3.0	3.33	150 kN	0.038<0.07 OK	2.39<5.26 OK	2.39>1.78 OK	1.33<2.5 OK
3.0	3.33	200 kN	0.05<0.07 OK	3.18<5.26 OK	3.18>1.78 OK	1.77<2.5 OK
3.0	3.33	250 kN	0.063<0.07 OK	3.98<5.26 OK	3.98>1.78 OK	2.21<2.5 OK
2.5	3.00	60 kN	0.02<0.07 OK	1.01<4.73 OK	1.01<1.60 NOT OK	0.59<2.5 OK
2.5	3.00	100 kN	0.033<0.07 OK	1.68<4.73 OK	1.68>1.60 OK	0.98<2.5 OK
2.5	3.00	150 kN	0.049<0.07 OK	2.53<4.73 OK	2.53>1.60 OK	1.48<2.5 OK
2.5	3.00	200 kN	0.066<0.07 OK	3.37<4.73 OK	3.37>1.60 OK	1.97<2.5 OK
2.5	3.00	250 kN	0.082>0.07 NOT OK	4.21<4.73 OK	4.21>1.60 OK	2.46<2.5 OK
2.0	2.50	60 kN	0.032<0.07 OK	1.13<3.94 OK	1.13<1.34 NOT OK	0.71<2.5 OK
2.0	2.50	100 kN	0.053<0.07 OK	1.89<3.94 OK	1.89>1.34 OK	1.18<2.5 OK
2.0	2.50	150 kN	0.079>0.07 NOT OK	2.83<3.94 OK	2.83>1.34 OK	1.77<2.5 OK
2.0	2.50	200 kN	0.106>0.07 NOT OK	3.77<3.94 OK	3.77>1.34 OK	2.36<2.5 OK
2.0	2.50	250 kN	0.132>0.07 NOT OK	4.72>3.94 NOT OK	4.72>1.34 OK	2.95>2.5 NOT OK

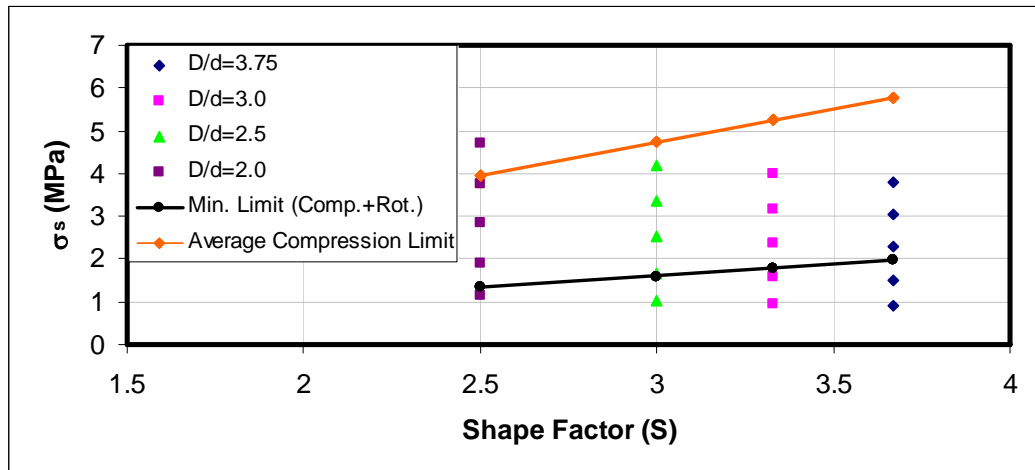


Figure 4.35. Compressive Stress Check for Test BRBs

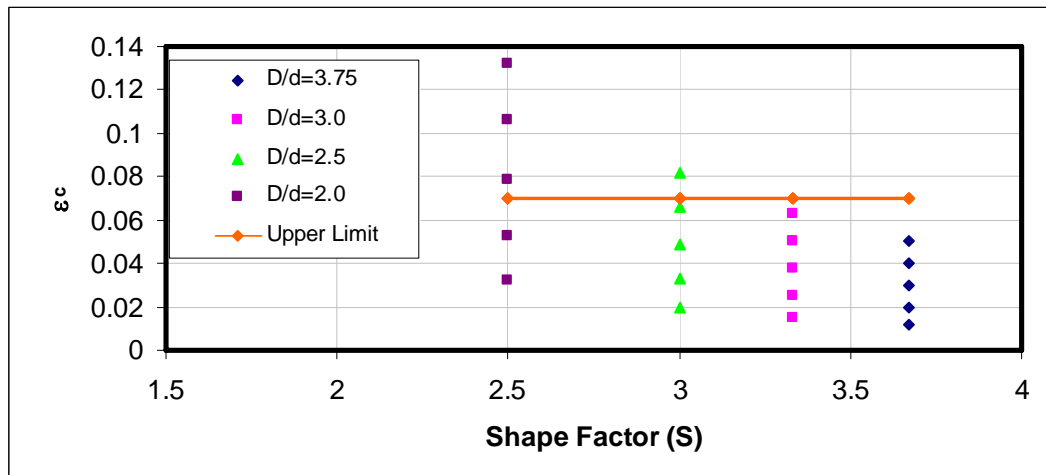


Figure 4.36. Compressive Strain Check for Test BRBs

It is observed from Table 4.10, Figures 4.35 and 4.36 that compressive strain, compressive stress and shear strain due to compressive stress is less critical in the case of a BRB when compared to an EB with the same dimensions. On the other hand, lower vertical compressive stresses in the elastomeric portion may result in tensile stresses and uplift at the corners of the bearing, which reduces fatigue life of the bearing [27].

4.5. Variation of Energy Dissipation Capacities (EDC) of Ball Rubber Bearings with Number of Cycles

In Figure 4.37 to Figure 4.39, variation of EDC with number of cycles is presented. Reference maximum horizontal displacements are used in calculation of energy dissipation capacities. Calculated EDCs are also presented in Table 4.11. In Table 4.11, $Q_{d,r}^{\text{th}}$ and EDC_r^{th} stands for characteristic strengths and energy dissipation capacities in the r^{th} cycle.

The bearings with $D/d=3.0$ are not included in this section since at most three cycles are applied to the bearings with $D/d=3.0$ and 1.65 mm steel balls under 300 kN, 400 kN and 500 kN vertical compressive loads.

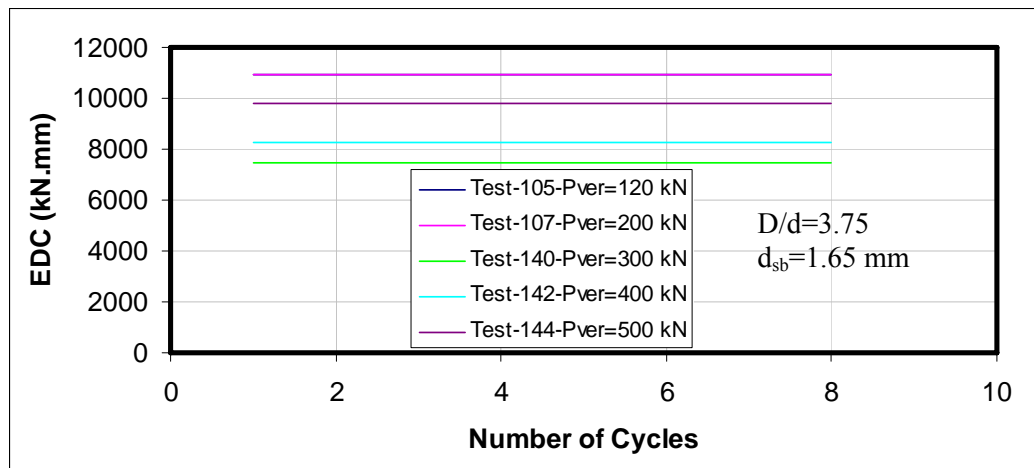


Figure 4.37. Variation of EDC for $D/d=3.75$

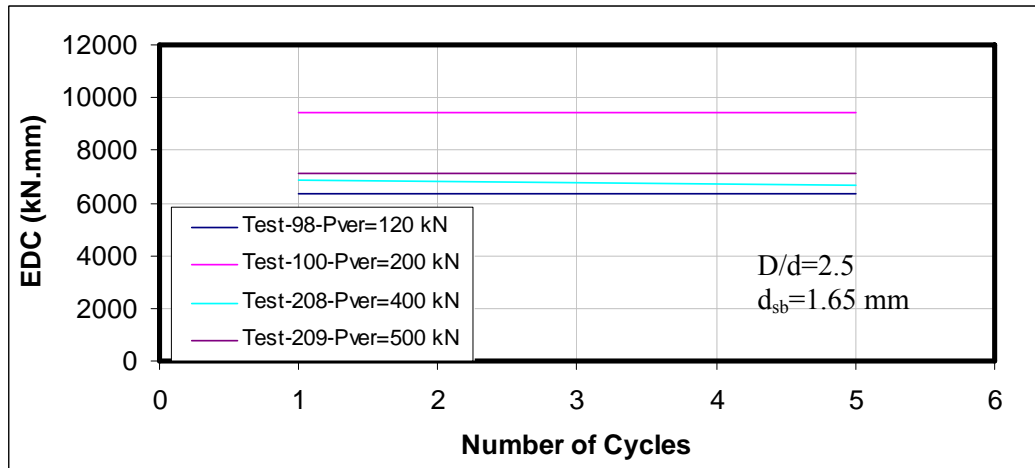


Figure 4.38. Variation of EDC for $D/d=2.5$

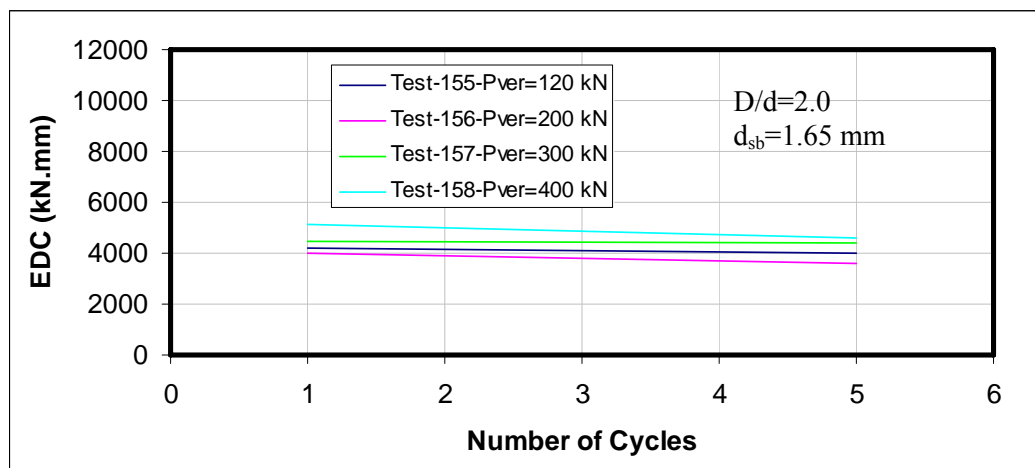


Figure 4.39. Variation of EDC for $D/d=2.0$

Table 4.11. Variation of EDC for Different Diameter Ratios (a) D/d=3.75 (b) D/d=2.5 (c) D/d=2.0

(a)

Test No:	P _{ver} (kN)	d _{max} (mm)	d _{max,ref.} (mm)	d _y (mm)	Q _{d,1} st (kN)	Q _{d,8} th (kN)	EDC ₁ st (kN.mm)	EDC ₈ th (kN.mm)
105	120	54	54	1.50	52	52	10920	10920
107	200	54	54	2.05	52.5	52.5	10910	10910
140	300	55	54	2.44	35.5	35.5	7322	7322
142	400	54.5	54	2.70	40	40	8208	8208
144	500	54.25	54	3.30	48	48	9734	9734

(b)

Test No:	P _{ver} (kN)	d _{max} (mm)	d _{max,ref.} (mm)	d _y (mm)	Q _{d,1} st (kN)	Q _{d,5} th (kN)	EDC ₁ st (kN.mm)	EDC ₅ th (kN.mm)
98	120	54	43.5	2.85	39	39	6341	6341
100	200	54	43.5	2.30	57.25	57.25	9435	9435
208	400	44	43.5	2.94	42.5	41.25	6895	6692
209	500	43.5	43.5	3.99	45	45	7112	7112

(c)

Test No:	P _{ver} (kN)	d _{max} (mm)	d _{max,ref.} (mm)	d _y (mm)	Q _{d,1} st (kN)	Q _{d,5} th (kN)	EDC ₁ st (kN.mm)	EDC ₅ th (kN.mm)
155	120	44	23.5	1.30	47	44.75	4174	3974
156	200	34	23.5	1.48	45.25	40.5	3986	3567
157	300	28.5	23.5	0.38	48.5	47.5	4485	4393
158	400	23.5	23.5	0.66	56.25	50.7	5139	4632

Test results indicate that energy dissipation capacities of BRBs do not degrade significantly with increasing number of loading cycles since temperature rise due to internal friction does not influence the EDC characteristics of the BRB. Proposed BRB is observed to have remarkably reliable seismic performance.

4.6. Service Load Tests

In seismic tests, a variety of bearings are tested. Only one type of bearing is selected for the service tests. Selection is based on the best seismic performance. The selected bearings have a 100 mm diameter central hole (D/d=3.0) and steel balls with 1.65 mm diameter. Testing velocity is approximately 2 mm/s, being the practical lower limit of the

testing equipment. In service load conditions, small horizontal displacements are expected due to daily temperature changes, wind, braking loads etc. Typical hysteresis loops are presented in Figure 4.40 for various vertical load levels at small shear strain values.

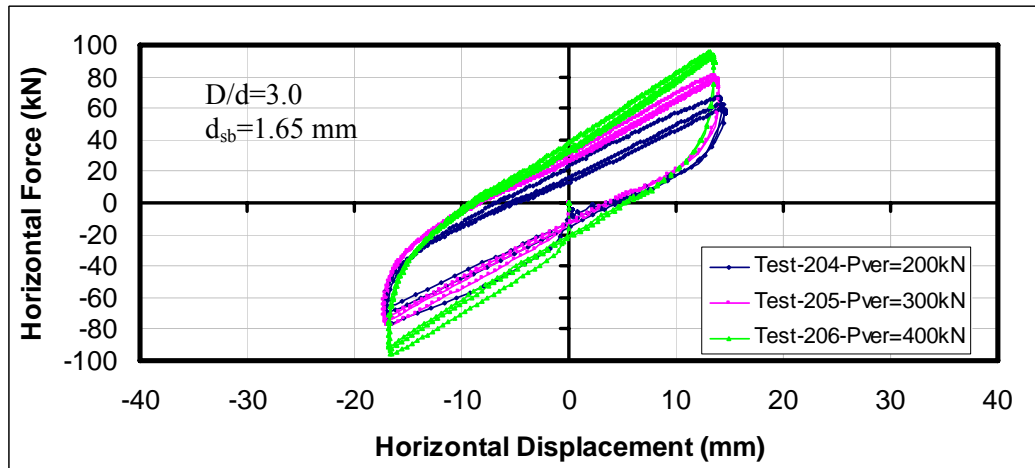


Figure 4.40. Service Load Tests of BRBs ($D/d=3.0$)

The ratio of the characteristic strength of the bearings tested under horizontal loads simulating the service loading conditions, denoted as $Q_{d, serv}$, to that of the bearings tested under horizontal loads simulating seismic load conditions, denoted as Q_d are also computed and listed in Table 4.12.

Table 4.12. Comparison between Characteristic Strengths Observed in Seismic & Service Load Tests

Test No:	P_{ver} (kN)	σ_{avg} (MPa)	γ_{max} %	Q_d (kN)	$\frac{Q_{d, serv}}{Q_d}$	K_2 (kN/m)
204	200	2.8	21	15.50	0.318	3165
122	200	2.8	86	48.60		1487
205	300	4.2	21	19.50	0.302	3774
177	300	4.2	58	64.50		2494
206	400	5.6	20	28.50	0.57	4400
178	400	5.6	39	50.00		2897

Test results presented in Figure 4.40 and Table 4.12 indicate that the characteristic strength of ball rubber bearings (BRBs) can be different at service load conditions and at seismic loading conditions. In literature [77], it is pointed out that response of granular materials is very sensitive to the rate of loading.

On the other hand, horizontal stiffness of a BRB is high at small horizontal displacement demands. Overall stiffness of the bearing system with low characteristic strength can be increased by high secondary stiffness of BRB since at service load conditions isolation system should be horizontally stiff in order to prevent excessive movement [78].

4.7. Effect of Supplementary Confinement

In Section 4.3.6, it is pointed out that the characteristic strength of a BRB does not change noticeably with increasing vertical compression. Energy dissipation capacity (EDC) of a seismic isolation system is related to its characteristic strength. Increased characteristic strengths under high vertical compressive loads may be desirable for some special seismic isolation applications. By utilizing supplementary confinement in the central core, increase in characteristic strength with vertical load is intended. Steel washer plates and FRP wraps are utilized in some tests as confinement.

4.7.1. Tests with Steel Washer Plates

To provide supplementary confinement to steel balls, 5 mm thick steel washer plates are utilized. As shown in Figure 4.41, washer plates have internal holes, which are filled with 1.65 mm diameter steel balls in subsequent tests. Outer diameter of the washer plates is 95 mm and their internal hole diameter is 17.5 mm.

First, the bearings having only these washer plates are tested. In the tested bearings, the diameter ratio (D/d) is 3.0 and the vertical load level is the only variable. Hysteresis loops of the bearings with only washer plates are presented in Figure 4.42.

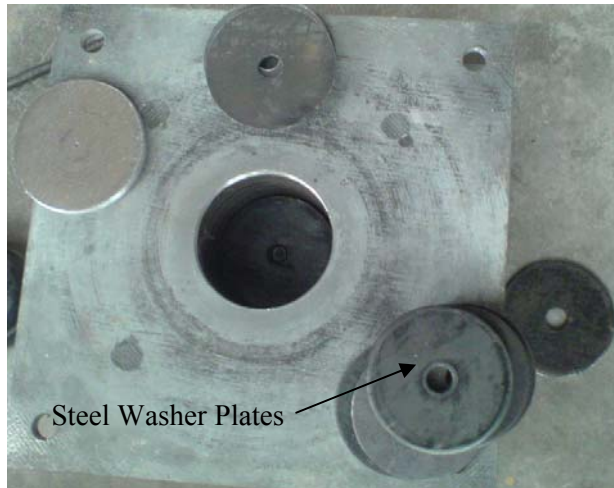


Figure 4.41. Plan View of Steel Washer Plates

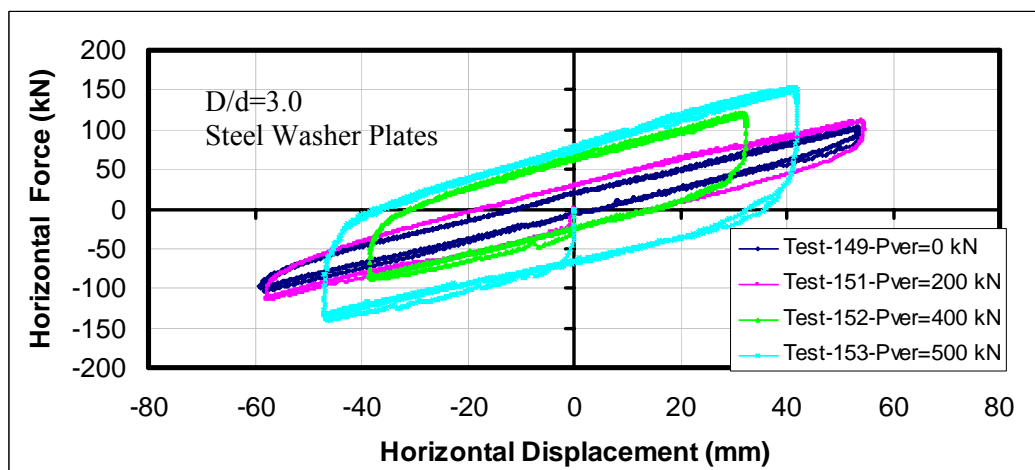


Figure 4.42. Effect of Vertical Load Level on Bearings with Washer Plates ($D/d=3.0$)

Under 400 kN and 500 kN vertical compressive load, the bearings with steel washer plates are observed to have equivalent damping ratios of 27.15% and 29.50%, respectively. Figure 4.40 also indicates that behavior of the central core with 5 mm thick steel washer plates is purely frictional.

Next, steel balls with 1.65 mm diameter are accommodated in the internal holes of the washer plates and tested under different vertical pressures. View of a bearing with both

steel washer plates and steel balls is presented in Figure 4.43. Hysteresis loops of these tests are presented in Figure 4.44 for different vertical load levels.



Figure 4.43. Steel Washer Plates with Steel Balls (Washer Hole Diameter: 17.5 mm)

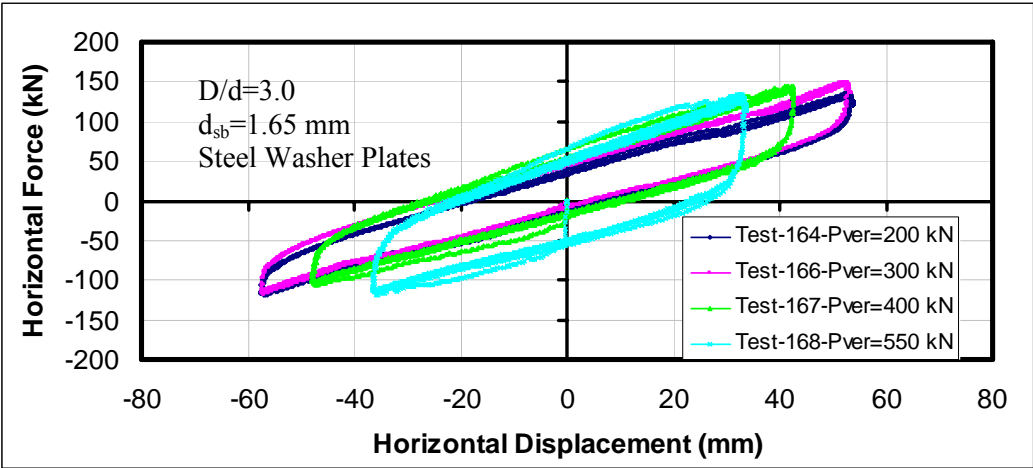


Figure 4.44. Effect of Vertical Load on Steel Washer Plates (Hole Diameter: 17.5 mm) & 1.65 mm Steel Balls

When compared to Figure 4.42, it is easily observed that involvement of steel balls diminished the EDC of the bearings. Bearings in Test-152 ($D/d=3.0$, $P_{ver}=400$ kN, Steel Washer Plates) have approximately 33% higher characteristic strength when compared to bearings in Test-167 ($D/d=3.0$, $P_{ver}=400$ kN, Steel Washer Plates & Steel Balls). Probably, steel balls restrained free sliding of the steel washer plates over each other (17 steel washer

plates). In subsequent tests, internal hole diameters of the washer plates are increased to 80 mm. View of a BRB with steel washer plates having 80 mm central holes and 1.65 mm steel balls is presented in Figure 4.45. Bearings are tested under five different vertical load levels. Hysteresis loops of the tests are presented in Figure 4.46.



Figure 4.45. Steel Washer Plates with Steel Balls (Washer Hole Diameter: 80 mm)

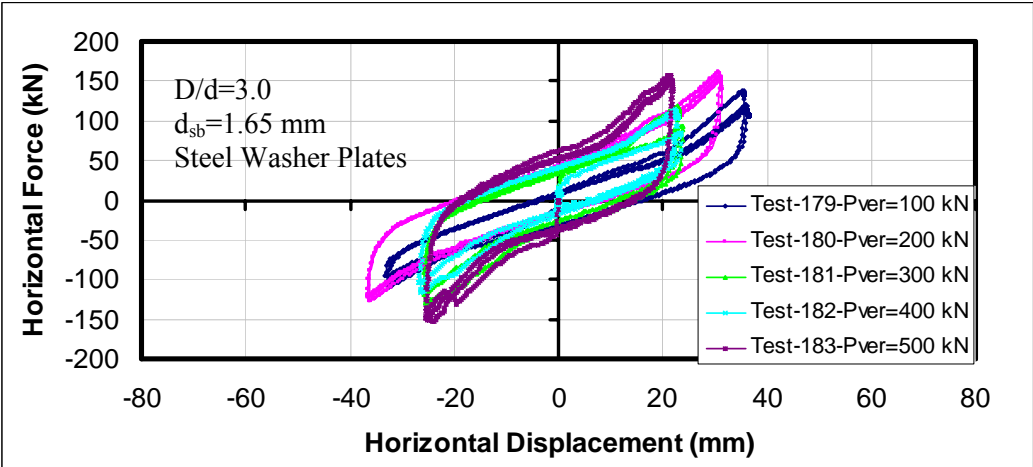


Figure 4.46. Effect of Vertical Load on Steel Washer Plates (Hole Diameter: 80 mm) & 1.65 mm Steel Balls

Figure 4.46 indicates that tested bearings do not have sufficient EDCs and there is significant stiffening at the ends of the hysteresis loops. Washer plates restrained the horizontal motion instead of providing confinement since such stiffening has not been

observed in BRB tests. Test results indicate that steel washer plates having large internal holes may not provide an efficient confinement.

4.7.2. Tests with FRP Wraps

Alternatively, FRP wraps may be used as supplementary confinement for BRBs to decrease the amount of horizontal dilation of steel balls under high vertical compressive loads. Therefore, FRP wraps are accommodated in the peripheries of the central holes of BRBs with $D/d=3.0$. FRP wraps are approximately 20 mm in height and they are overlapped in the circumferential direction to provide full confinement under combined compression and shear loading. In the vertical direction, FRP wraps are not overlapped.

View of a bearing with FRP wraps before testing is presented in Figure 4.47. View of the FRP wraps after testing is presented in Figure 4.48. There is some disintegration of the FRP wraps after about 10 tests. However, it is thought that FRP wraps are still capable of providing confinement. Elastomeric bearings with only FRP wraps are also tested under monotonically increasing vertical compression, up to 2500 kN. At the end of the test, it is observed that FRP wraps are broken into small pieces. However, the maximum vertical compressive load in test is much higher than the upper limit in AASHTO specifications [6, 27].



Figure 4.47. FRP Wraps (Before Testing)



Figure 4.48. FRP Wraps (After Testing)

Bearings with FRP wraps and 1.65 mm steel balls are tested at different vertical load levels to establish efficiency of the FRP wraps, as presented in Figure 4.49.

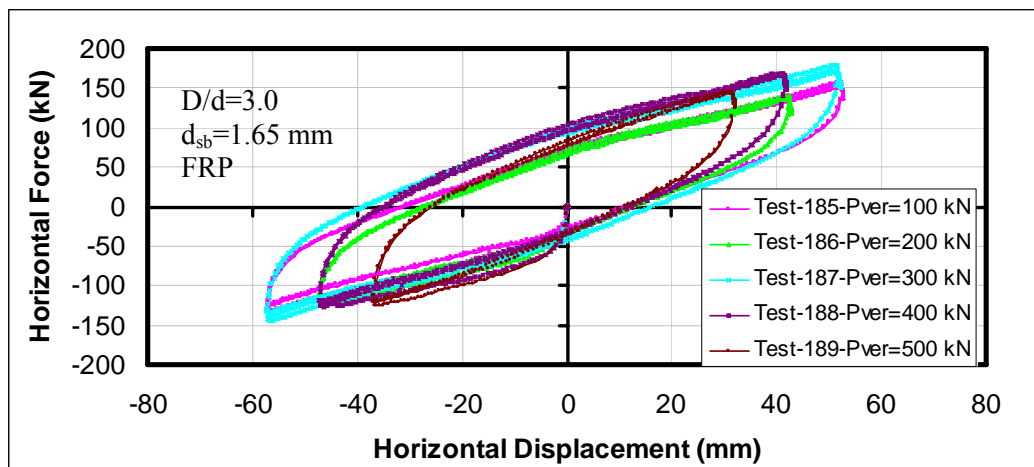


Figure 4.49. Effect of Vertical Load on FRP Confined BRB ($D/d=3.0$)

In Table 4.13, characteristic strengths of FRP confined ball rubber bearings (CBRBs) are compared with those of ball rubber bearings (BRBs).

Table 4.13. Characteristic Strengths of FRP Confined BRBs & BRBs

Test No:	P_{ver}	σ_{avg} (MPa)	d_{max} (mm)	Q_d (kN)	$\frac{Q_{d,CBRB}}{Q_{d,BRB}}$
186 (CBRB)	200 kN	2.8	45.0	50.0	1.16
57 (BRB)	200 kN	2.8	54.0	43.0	
187 (CBRB)	300 kN	4.2	54.5	68.0	1.05
177 (BRB)	300 kN	4.2	43.5	64.5	
188 (CBRB)	400 kN	5.6	44.5	67.0	1.34
178 (BRB)	400 kN	5.6	29.0	50.0	
189 (CBRB)	500 kN	7.1	34.5	59.0	0.83
175 (BRB)	500 kN	7.1	33.0	71.0	

Test results imply a confinement provided by FRP wraps. On the other hand, FRP wraps may not be a fully effective confining mechanism as indicated by comparison of Test-189 (CBRB) and Test-175 (BRB).

CHAPTER 5

DESIGN GUIDELINE

5.1. General

Design of Ball Rubber Bearings (BRBs) involves determination of yield displacement (d_y), characteristic strength (Q_d) and secondary stiffness (K_2).

Design equations for bearings with 1.65 mm diameter granular material are developed through investigation of test data. Equations are written for one single bearing.

5.2. Yield Displacement (d_y)

Mean yield displacement obtained from the log-normal distribution [79] of test data is 2.64 mm with standard deviation equal to 1.58 mm. Log-normal distribution is selected since it may be useful in applications where the values of the variate are known to be strictly positive [79]. Log-normal distribution of the test data is presented in Figure 5.1.

Probability density function for log-normal distribution can be expressed as [79]:

$$f_x(x) = \frac{1}{\zeta x \sqrt{2\pi}} \times \exp \left[-\frac{1}{2} \times \left(\frac{\ln x - \lambda}{\zeta} \right)^2 \right] \quad (5.1)$$

where

$f_x(x)$: probability density function

x : variable

- λ : mean value of $\ln x$
 ζ : standard deviate of $\ln x$

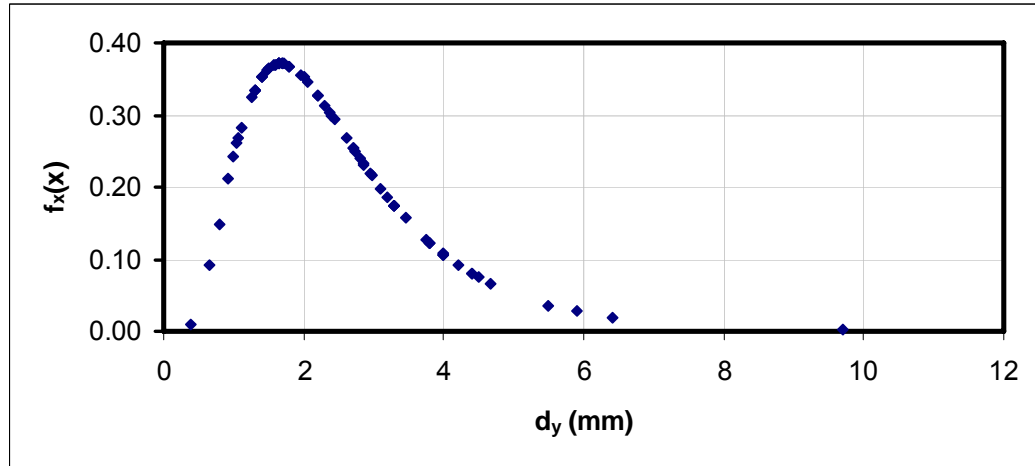


Figure 5.1. Log-Normal Distribution of Test Data for Yield Displacement

Mean value and standard deviate of $\ln x$ can be calculated by using Equation 5.2 and Equation 5.3, respectively.

$$\lambda = \ln \mu_{mean} - \frac{1}{2} \zeta^2 \quad (5.2)$$

$$\zeta = \sqrt{\ln\left(1 + \frac{\sigma_{dev}^2}{\mu_{mean}^2}\right)} \quad (5.3)$$

where

- μ_{mean} : mean value of x
 σ_{dev} : standard deviate of x

Lower and upper limits of $(1-\alpha C)$ confidence interval may be set by using Equation 5.4a and Equation 5.4b:

$$x_{Lower} = e^{\lambda - k_{\alpha/2} \times \zeta} \quad (5.4a)$$

$$x_{Upper} = e^{\lambda + k_{\alpha C/2} \times \zeta} \quad (5.4b)$$

where

$\pm k_{\alpha C/2}$: values of the standard normal variate with cumulative probability levels $\alpha C/2$ and $1 - \alpha C/2$

For 90% confidence interval with $\alpha C = 0.10$:

$$k_{0.05} = 1.65 \text{ [78]}$$

Upper and lower limits for d_y can be calculated as:

$$\zeta = \sqrt{\ln\left(1 + \frac{1.58^2}{2.64^2}\right)} = 0.553$$

$$\lambda = \ln 2.64 - \frac{1}{2} \times 0.553^2 = 0.818$$

$$d_{y,lower} = e^{0.818 - 1.65 \times 0.553} = 0.91 \text{ mm}$$

$$d_{y,upper} = e^{0.818 + 1.65 \times 0.553} = 5.64 \text{ mm}$$

Test data with minimum and maximum 90% confidence lines is presented in Figure 5.2.

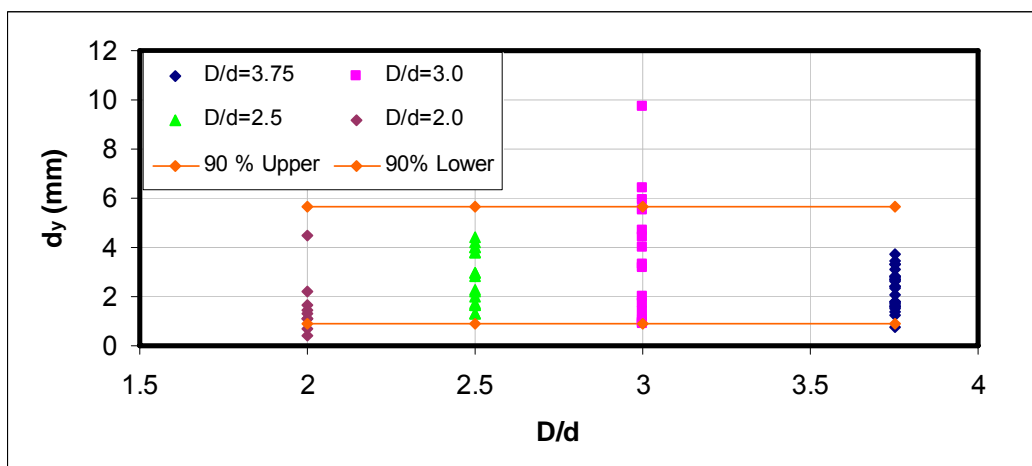


Figure 5.2. Test Data for Yield Displacement with 90% Confidence Interval

Expected yield displacement shall be most likely between upper and lower limits. Dimensional analysis results indicated that response of bilinear systems having large values of ductility, which is the case in seismic isolation systems, is not affected by yield displacement [80]. Therefore, the lower limit may be used in design of building structures since slick-stip type motions may be observed in these structures in presence of sliding frictional isolation systems [59]. The upper limit may be used in design of bridge structures. Alternatively, the designer may select an intermediate value between upper and lower limits.

Mean value of the yield displacement is similar to the ones determined for friction pendulum systems [81]. Yield displacement is generally accepted as 2.54 mm (0.1 inch) in design of friction pendulum systems.

5.3. Characteristic Strength (Q_d)

Log-normal distribution of test results is utilized to determine characteristic strength. Log-normal distribution of the test data is presented in Figure 5.3.

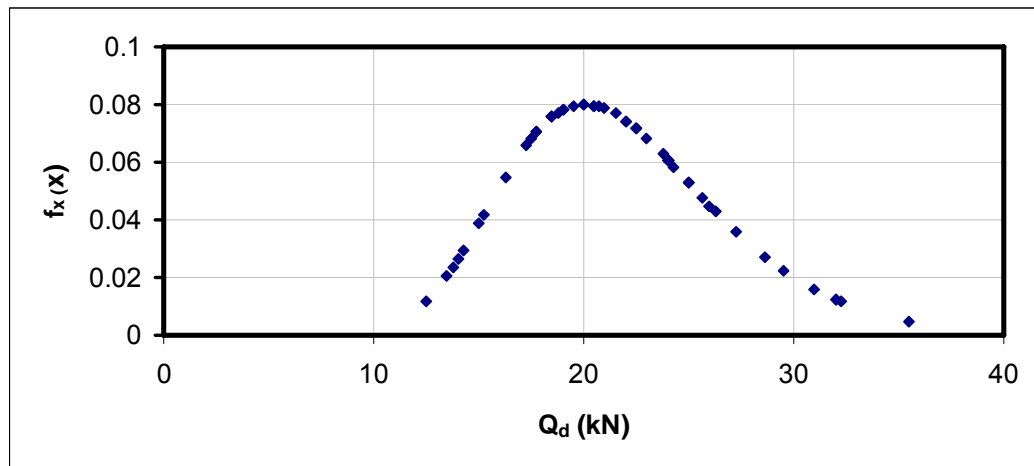


Figure 5.3. Log-Normal Distribution of Test Data for Characteristic Strength

Mean value (μ_{mean}) of the test data is 21.90 kN with a standard deviation (σ_{dev}) of 5.36 kN.

Equation 5.2 through Equation 5.4 can be utilized in calculation of 90% confidence interval for test data. By specifying such an interval, 90% of the time, characteristic strength shall be in between upper and lower limits.

$$\zeta = \sqrt{\ln\left(1 + \frac{5.36^2}{21.90^2}\right)} = 0.241$$

$$\lambda = \ln 21.90 - \frac{1}{2} \times 0.241^2 = 3.057$$

$$Q_{d,lower} = e^{3.057 - 1.65 \times 0.241} = 14.28 \text{ kN}$$

$$Q_{d,upper} = e^{3.057 + 1.65 \times 0.241} = 31.64 \text{ kN}$$

Test data with minimum and maximum 90% confidence lines is presented in Figure 5.4.

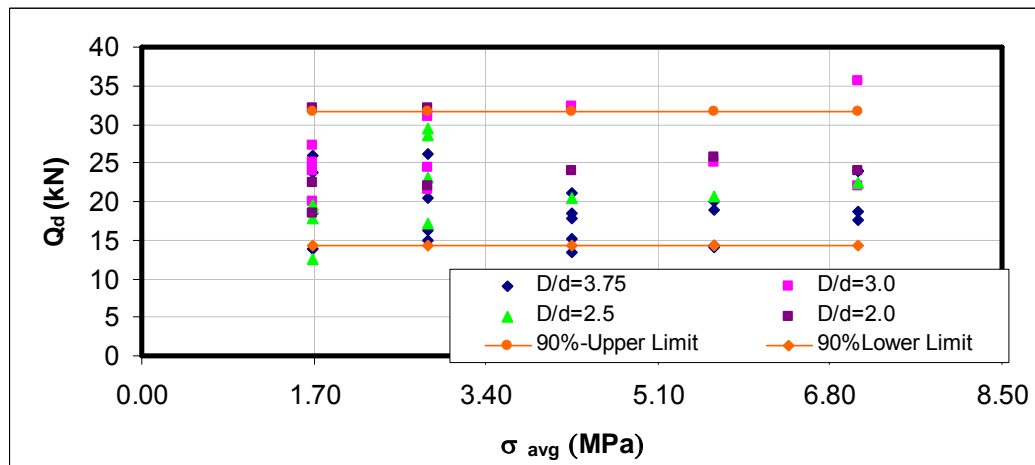


Figure 5.4. Test Data for Characteristic Strength with 90% Confidence Interval (1 Bearing)

Characteristic strengths of BRBs can be expressed simply by using the following equation:

$$Q_d = \alpha_r \times P_{ver, 3.4MPa} \quad (5.5)$$

Equation 5.5 is written using the trend of the test data presented in Figure 5.4. Figure 5.4 indicates that characteristic strength does not change with D/d ratio and vertical compression. By using the test data, upper and lower limits of characteristic strengths for BRBs can be expressed by Equation 5.6 and Equation 5.7;

$$Q_{d,lower} = 0.06 \times P_{ver,3.4MPa} \quad (5.6)$$

$$Q_{d,upper} = 0.13 \times P_{ver,3.4MPa} \quad (5.7)$$

where

$Q_{d,lower}$: lower limit of characteristic strength (in kN)

$Q_{d,upper}$: upper limit of characteristic strength (in kN)

$P_{ver,3.4MPa}$: vertical compressive load corresponding to 3.4 MPa average compressive stress

α_r : an empirical coefficient determined from test data

Plan dimensions of BRBs can be selected to accommodate 3.4 MPa average vertical compressive stress (Eqn. 4.1) induced by an unfactored total load, with $\pm 10\%$ tolerance. Vertical load ($P_{ver,3.4MPa}$) corresponding to 3.4 MPa average vertical stress should be used in computing characteristic strength.

In investigation of experimental results, only tests having maximum shear strains larger than 30% are taken into account except one particular test with $D/d=2.0$, under 500 kN vertical load, as presented in Figure 5.5.

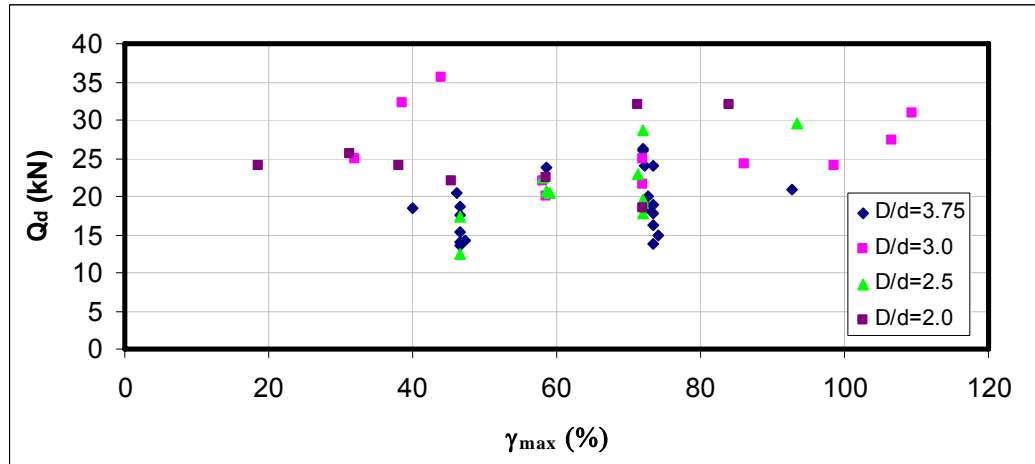


Figure 5.5. Q_d vs. γ_{max} of Test Data

Upper and lower limits specified in Equations 5.6 and 5.7 can be due to production quality of BRBs, mainly due to the filling process of the hole and due to small differences in laboratory temperature between tests. Characteristic strengths and stiffness of most of the isolation systems are affected by temperature, heat generation, aging, scragging, wear, sealing type etc [6].

5.4. Secondary Stiffness (K_2)

Contribution of steel balls to secondary stiffness is expressed as percentage of the horizontal stiffness of the elastomeric part (K_h) of the bearing. Secondary stiffness of ball rubber bearings (BRBs), a function of maximum shear strain, decreases as maximum shear strain increases as depicted in Figure 5.6 for four D/d ratios. Equation 5.8 is utilized in calculating supplementary stiffness provided by steel balls and this equation is based on test results.

$$K_h \% = \frac{(F_{\max} - Q_{d, BRB})}{d_{\max} \times K_h} \times 100 \quad (5.8)$$

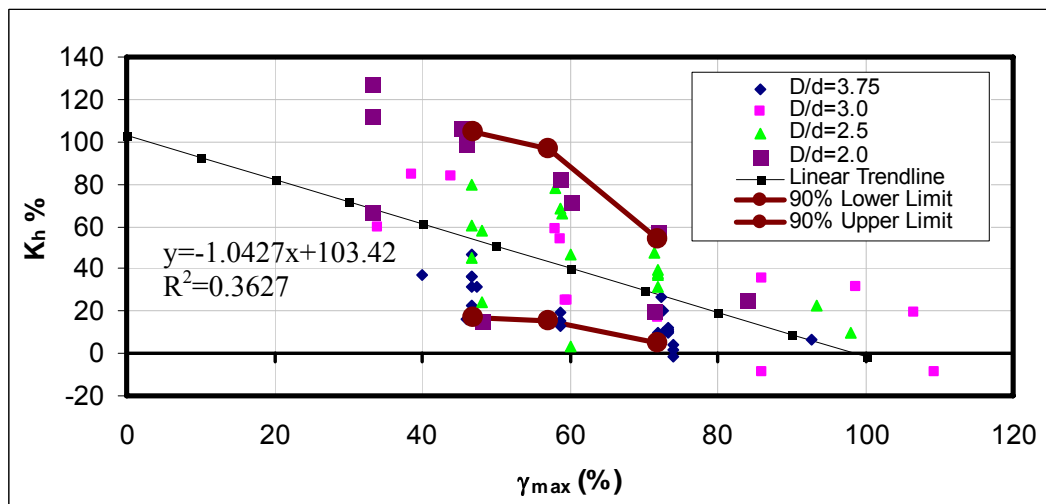


Figure 5.6. Contribution of Steel Balls to K_2

Negative contribution of steel balls to secondary stiffness in some tests may result from small variations in the laboratory temperature between reference EB and BRB tests. Some

tests have been performed at winter time when the heating system of the structural laboratory is under repair.

Secondary stiffness of BRBs varies with diameter (D/d) ratio, as depicted in Figure 5.6. For bearings with D/d=2.0, contribution of steel balls to secondary stiffness is higher when compared to bearings with D/d=2.5, D/d=3.0 and D/d=3.75, due to presence of more steel balls in the central core. Therefore, defining a single equation valid for all D/d ratios is not possible. Defining a confidence interval is not feasible since the upper limit of the confidence interval is very close to secondary stiffness values observed in bearings with D/d=2.0. Similarly, the lower limit is very close to secondary stiffness values observed in bearings with D/d=3.75. The difference between two limits implies a very large interval. Therefore different equations can be utilized for different diameter (D/d) ratios. A designer may select the diameter of the central hole so as to calibrate the secondary stiffness of the bearing.

In literature [82], tests on well-graded and poor-graded granular materials have indicated that angle of friction decreases with increasing shear strain, as presented in Figure 5.7.

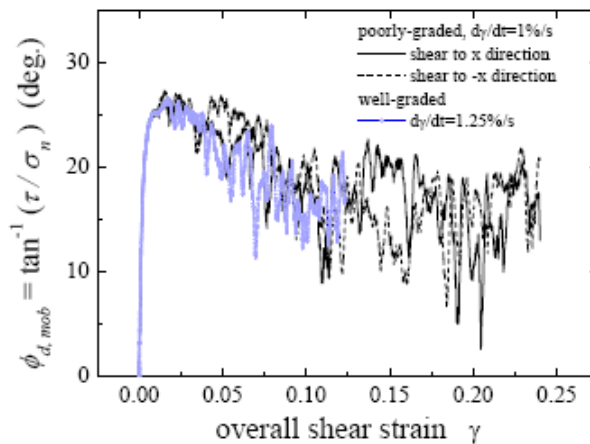


Figure 5.7. Variation of Angle of Friction with Shear Strain for Well-Graded and Poorly-Graded Granular Materials [82]

Lower secondary stiffness at higher shear strains may be attributed to relation between frictional resistance and angle of friction. Moreover, complex mechanisms like rolling,

sliding, interlocking and shear band formation that are involved in movement of steel balls may result in lower secondary stiffness at higher shear strains.

5.4.1. $D/d=3.75$ (80 mm Hole Diameter)

A linear trendline is used to fit the experimental data and fit of the trendline is satisfactory as presented in Figure 5.8. At shear strains larger than 87.7 %, contribution of steel balls to secondary stiffness comes out be less than zero if a linear trendline is used. On the other hand, at larger shear strain levels, there is limited test data. Therefore, a lower limit of 1.10 is set for f_L . The factor f_L is previously defined in Equation 2.8 for LRBs.

By using test results, contribution of steel balls to the secondary stiffness can be expressed as:

$$f_L = 1 + 0.01 \times (-0.7252 \times \gamma_{\max} \% + 63.606) \geq 1.10 \quad (5.9)$$

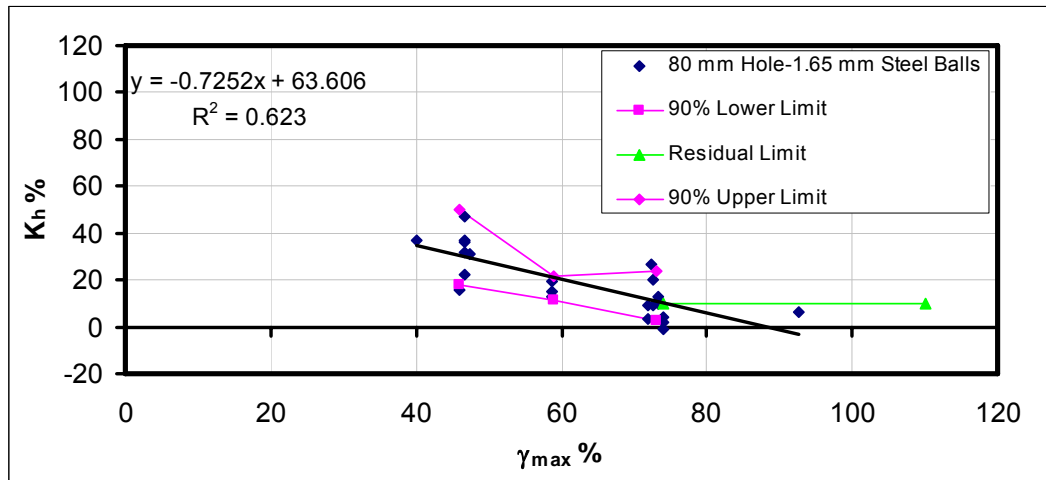


Figure 5.8. Contribution of Steel Balls to K_2 ($D/d=3.75$)

Figure 5.8 reveal that defining upper and lower confidence limits for secondary stiffness may not be feasible since upper limit and lower limit are close to each other.

5.4.2. $D/d=3.0$ (100 mm Hole Diameter)

In Figure 5.9, it is observed that contribution of steel balls to secondary stiffness is higher compared to bearings with 80 mm central holes. Higher stiffness is expected since volume of steel balls is higher in bearings with 100 mm central holes. Therefore, a residual f_L value of 1.20 is set for bearings with $D/d=3.0$ when compared to a lower f_L value of 1.10 for bearings with $D/d=3.75$.

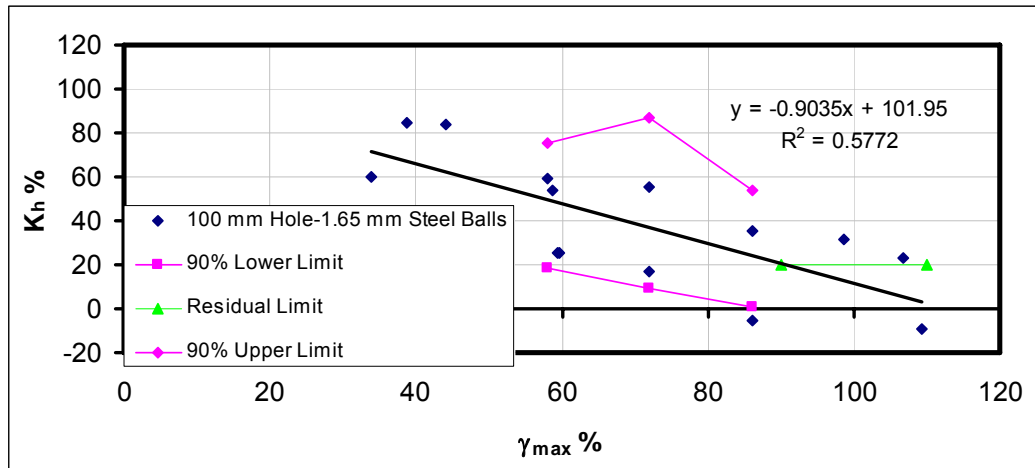


Figure 5.9. Contribution of Steel Balls to K_2 ($D/d=3.0$)

In equation form, contribution of steel balls to the secondary stiffness can be expressed as:

$$f_L = 1 + 0.01 \times (-0.9035 \times \gamma_{max} \% + 101.95) \geq 1.20 \quad (5.10)$$

The difference between upper limit and lower limit observed in Figure 5.9 results from limited number of tests at a pre-determined shear strain level. Setting upper and lower confidence limits by utilizing only two or three test data at a shear strain level using log-normal distribution may result in unjustified limits. For this reason, it is recommended to use Equation 5.10 instead of defining a confidence interval.

5.4.3. $D/d=2.5$ (120 mm Hole Diameter)

A graph representing variation of secondary stiffness with maximum shear strain is presented in Figure 5.10 for BRBs having a diameter ratio (D/d) of 2.5.

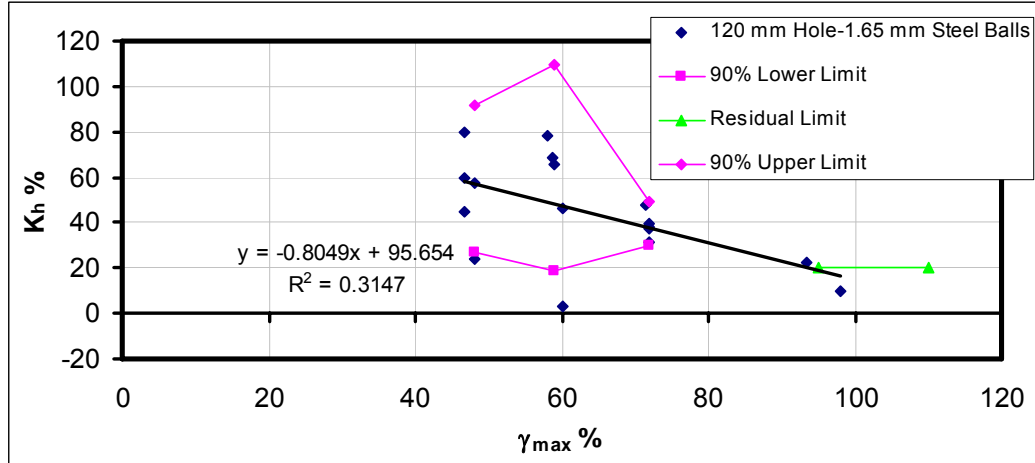


Figure 5.10. Contribution of Steel Balls to K_2 ($D/d=2.5$)

Contribution of steel balls to secondary stiffness is close to each other in BRBs having $D/d=2.5$ and $D/d=3.0$. Therefore, if a designer wants to design a BRB having $D/d=2.5$, he/she is advised to use Equation 5.10.

5.4.4. $D/d=2.0$ (150 mm Hole Diameter)

In bearings with $D/d=2.0$, contribution of steel balls to secondary stiffness is very high. Higher contribution of steel balls to secondary stiffness may result from relatively higher total volume of steel balls. Under 300 kN, 400 kN and 500 kN vertical compression, extremely high secondary stiffness is observed, as presented in Table 5.1.

For BRBs with $D/d=2.0$, contribution of steel balls to K_2 is presented in Figure 5.11. In Figure 5.11, the tests performed under vertical compressive loads higher than 200 kN are excluded.

Table 5.1. Contribution of Steel Balls to Secondary Stiffness under High Vertical Compressive Loads (D/d=2.0)

Test No:	P _{ver} (kN)	γ _{max} %	K ₂ %
157	300	38.0	206.82
158	400	31.3	277.67
159	500	18.7	402.88

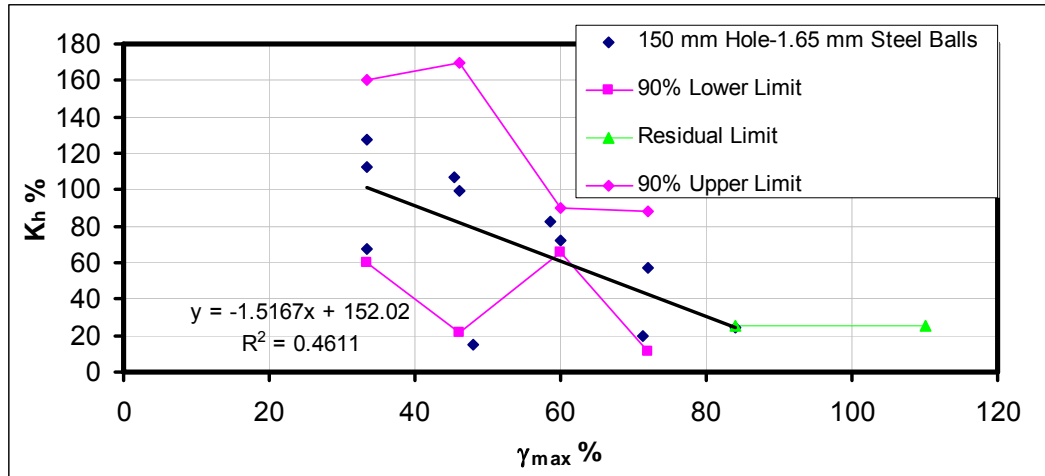


Figure 5.11. Contribution of Steel Balls to K₂ (D/d=2.0)

In equation form, contribution of steel balls to the secondary stiffness can be expressed as:

$$f_L = 1 + 0.01 \times (-1.5167 \times \gamma_{\max} \% + 152.02) \geq 1.25 \quad (5.11)$$

5.5. Conformance of Proposed Design Equations and Test Data

The test data should be in between the lower and upper limits that are defined by the proposed design equations. The conformance of the test data to proposed design equations are checked for five randomly selected tests, as presented in Figure 5.12 through 5.16. The checks are performed for one bearing using the average (1/2 scaled) of the test data.

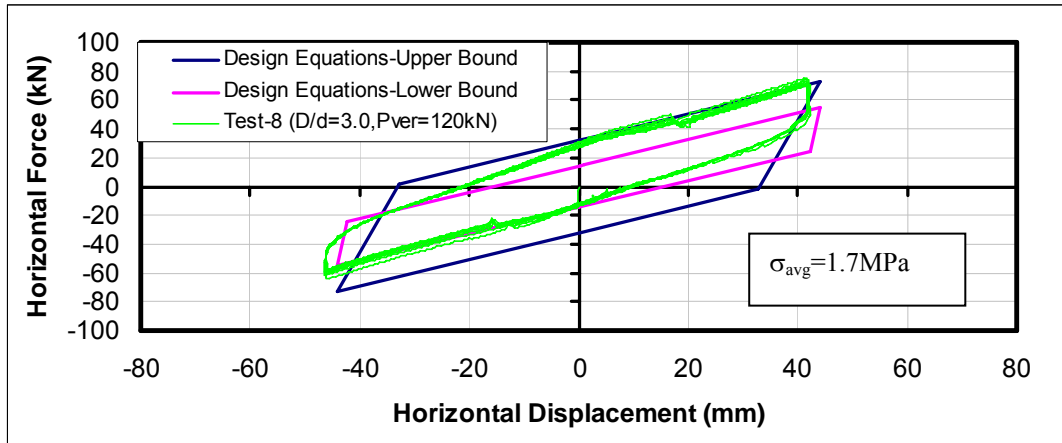


Figure 5.12 Design Equations and Test-8

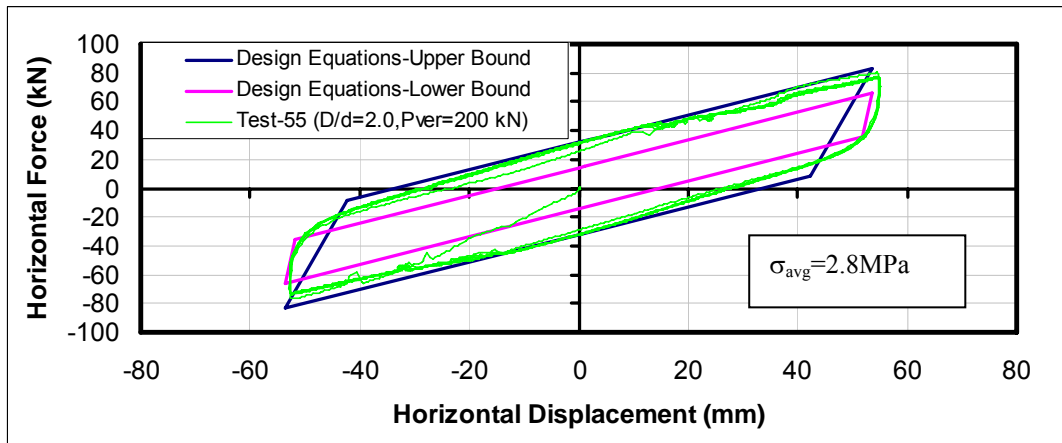


Figure 5.13 Design Equations and Test-55

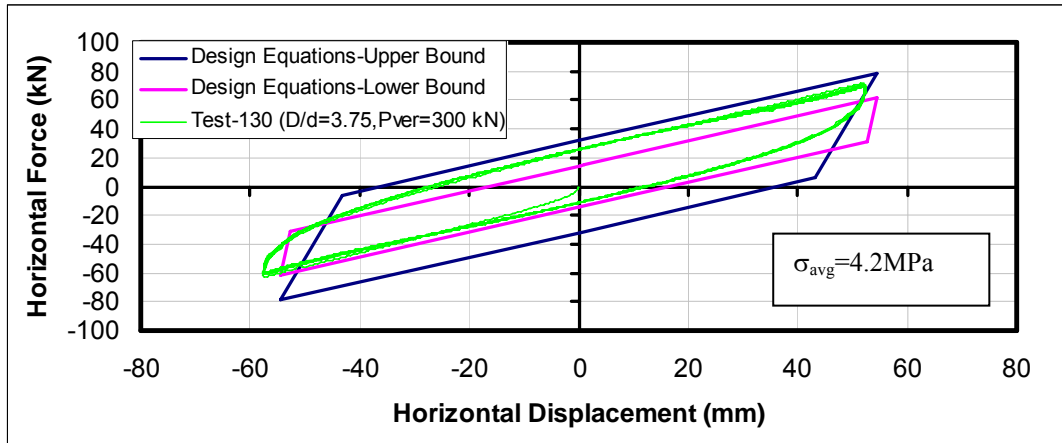


Figure 5.14. Design Equations and Test-130

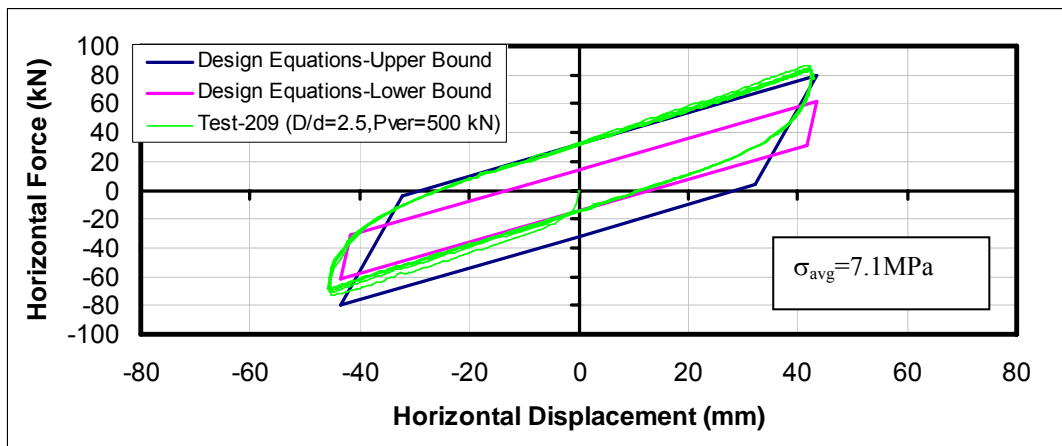


Figure 5.15. Design Equations and Test-209

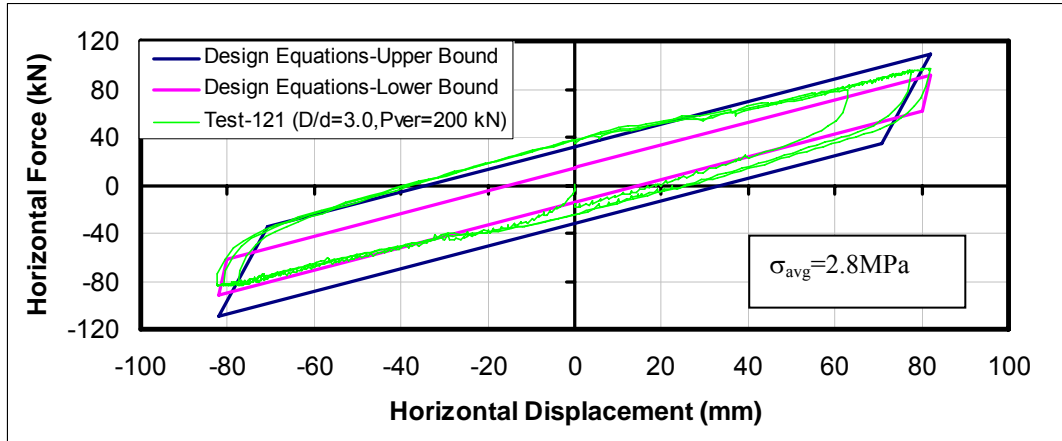


Figure 5.16. Design Equations and Test-121

Figure 5.12 through Figure 5.16 indicate that the design equations are representative of the test data and the design equations can be used in design of BRBs, while both upper bound and lower bound solutions should be checked.

5.6. Design Example

5.6.1. Practical Design Approach

In this section, a design example shall be presented for a BRB with $D/d=3.0$. The design example is presented in order to provide a guideline in design of BRBs. Structural details of bridges, buildings, storage tanks etc. are not included in the design example. A simple flowchart for design of BRBs is presented in Figure 5.17.

Design Example:

In the example, vertical compressive load on the bearing and desired effective isolation period are set as input. It is common to specify isolation period as input in design stage of a seismic isolation system [3]. Design spectrum in AASTO Guide Specification for Seismic Isolation [6] is used with $PGA=0.4g$ and $S_c=1.5$ (Site Coefficient). Spectrum for design basis earthquake is presented in Figure 5.18.

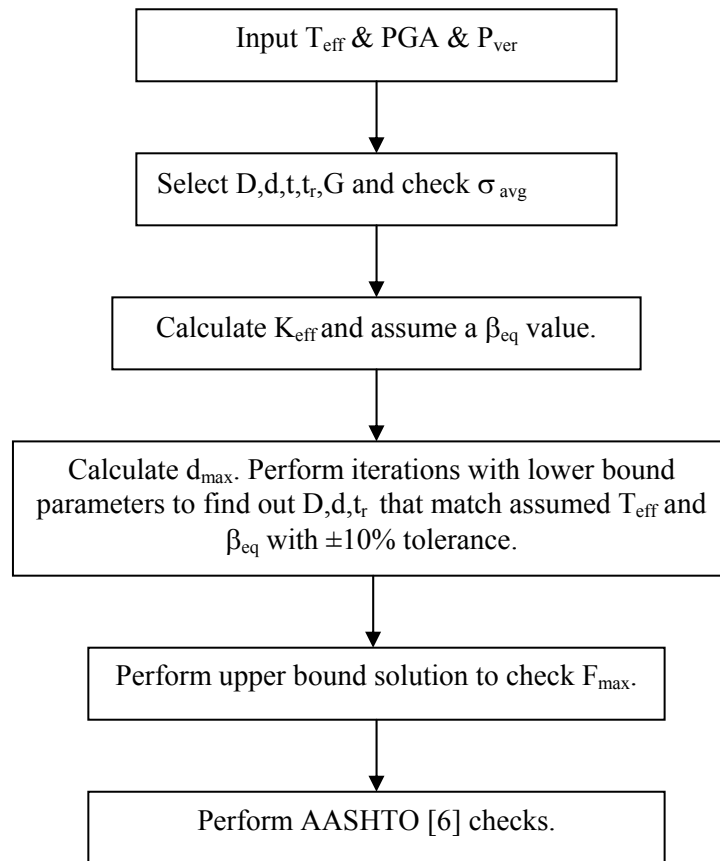


Figure 5.17. Flowchart for Design of BRBs

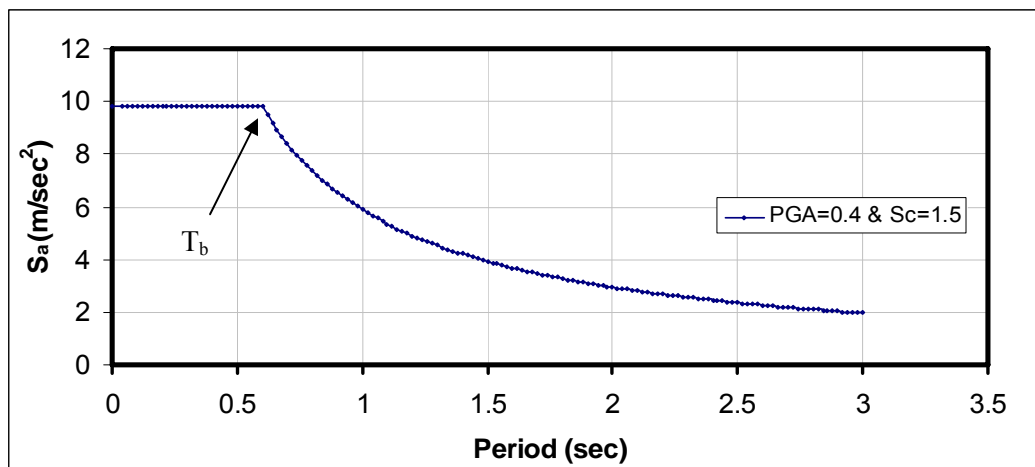


Figure 5.18. Design Spectrum for $PGA=0.4g$ and $Sc=1.5$ [6]

Input Data:

PGA=0.4g

$T_b = 0.6$ sec.

$T_{eff} = 2.5$ sec.

$P_{ver} = 1000$ kN

Effective period can be calculated by ignoring the effect of damping using Equation 5.12:

$$T_{eff} = 2 \times \pi \times \sqrt{\frac{P_{ver}}{g \times K_{eff}}} \quad (5.12)$$

where

g : gravitational acceleration (m/sec²)

PGA : peak ground acceleration

T_b : longer corner period (in sec.)

T_{eff} : effective period (in sec.)

Effective stiffness of the isolation system is calculated as:

$$K_{eff} = \frac{4 \times \pi^2 \times P_{ver}}{g \times T_{eff}^2} = \frac{4 \times \pi^2 \times 1000}{9.81 \times 2.5^2} = 644 \text{ kN / m} \quad (5.13)$$

Spectral acceleration at 2.5 sec. is,

$$S_a = 2.35 \text{ m/sec}^2 = 0.24g$$

Assume an equivalent viscous damping ratio of BRB as 16.5%. Reduction in response due to damping can be expressed by [3]:

$$\frac{1}{B} = 0.25 \times (1 - \ln \beta_{eq}) \quad (5.14)$$

where

B : reduction in response due to energy dissipation

B=1.428 for $\beta_{eq,lower}=0.165$

Horizontal displacement demand of the isolation system is expressed by the expression [9]:

$$d_{max} = \frac{S_a \times g \times T_{eff}^2}{4 \times \pi^2 \times B} \quad (5.15)$$

$d_{max,lower} = 0.261 \text{ m}$

Designer should perform iterations to find out optimum dimensions of the bearing. In this design example, only final solution step is presented.

Assume D=600 mm (0.60 m), d=200 mm (0.2 m), $t_r=245 \text{ mm}$ (0.245 m), $t=25 \text{ mm}$ (0.025 m) and G=0.45 MPa (450 kPa);

Check average vertical compressive stress:

$$\sigma_{avg} = \frac{P_{ver}}{A} = \frac{1000kN}{\pi \times 0.3m^2} = 3536kPa = 3.536MPa$$

Average compressive stress is within $\pm 10\%$ of 3.4 MPa. Therefore, diameter of the bearing is satisfactory. Compute vertical load corresponding to 3.4 MPa average compressive stress.

$$P_{ver,3.4MPa} = \pi \times 0.3m^2 \times 3400kPa = 961kN$$

$$A_{rubber} = \pi \times (0.30^2 - 0.10^2) = 0.2513m^2$$

$$K_h = \frac{G \times A_{rubber}}{t_r} = \frac{0.45 \times 1000 \times 0.2513}{0.245} = 462kN / m$$

Since shear strain is larger than 100%, use $f_L=1.20$ (Equation 5.10).

$$K_2 = f_L \times K_h = 1.20 \times 462 = 554kN / m$$

In order to check maximum horizontal displacement of the isolation system, lower bound solution should be performed [6]. Therefore, Equation 5.6 shall be utilized for characteristic strength.

$$Q_{d,lower} = 0.06 \times P_{ver,3.4MPa} = 57.66kN$$

Horizontal Force at 0.261 m horizontal displacement:

$$F_{max} = Q_d + K_2 \times d_{max}$$

$$F_{max,lower} = 57.66kN + 554kN / m \times 0.261m = 202kN$$

Effective stiffness of the isolation system is calculated as:

$$K_{eff,lower} = \frac{F_{max}}{d_{max}} = 774kN / m$$

If the structure is a bridge structure with $d_y=5.64$ mm, then effective damping ratio is calculated by using Equation 3.1:

$$\beta_{eq,lower} = \frac{4 \times 57.66 \times (0.261 - 0.00564)}{2 \times \pi \times 774 \times 0.261^2} = 0.178$$

$$T_{eff,lower} = 2 \times \pi \times \sqrt{\frac{1000}{9.81 \times 774}} = 2.28 \text{ sec}$$

Solution has converged. Calculated β_{eq} and T_{eff} are within 10% of the assumed values. Dimensions of the bearing are set. Now, upper bound solution should be performed in order to check F_{max} .

$$Q_{d,upper} = 0.13 \times P_{ver,3.4MPa} = 124.93kN$$

Iterations are required to find d_{max} for upper bound solution. However, in this example, only the final step is presented.

Assume $d_{max,upper}=170$ mm:

$$F_{max,upper} = 124.93kN + 554kN / m \times 0.17m = 219kN$$

$$K_{eff,upper} = \frac{F_{max}}{d_{max}} = 1288kN / m$$

$$T_{eff,upper} = 2 \times \pi \times \sqrt{\frac{1000}{9.81 \times 1288}} = 1.77 \text{ sec.}$$

For $T_{eff,upper}=1.77$ sec, $S_a=3.32m/sec^2$

$$\beta_{eq,upper} = \frac{4 \times 124.93 \times (0.17 - 0.00564)}{2 \times \pi \times 1288 \times 0.17^2} = 0.351$$

Since a time history analysis is not performed and equivalent damping exceeds 0.30, the upper limit for B is 1.70 per AASHTO [6].

$$d_{max,upper} = \frac{S_a \times g \times T_{eff}^2}{4 \times \pi^2 \times B} = \frac{3.32 \times 1.77^2}{4 \times \pi^2 \times 1.70} = 0.155m$$

The solution has converged.

Now, checks using AASHTO Guide Spec. for Seismic Isolation [6] shall be made.

Shape factor of the designed bearing is:

$$S = \frac{D^2 - d^2}{4t \times (D + d)} = \frac{0.60^2 - 0.20^2}{4 \times 0.025 \times (0.60 + 0.20)} = 4.00$$

At 261 mm horizontal displacement ($D_b=0.59m$):

$$\chi = \sqrt{D_b^2 - d_{max}^2} = 0.529m$$

$$A_r = 0.5 \left(D^2 \sin^{-1} \left(\frac{\chi}{D_b} \right) - d_{max} \times \chi \right) = 0.131m^2$$

$$\gamma_c = \frac{0.5 \times P_{ver}}{A_r \times GS} = \frac{0.5 \times 1000kN}{0.131 \times 450 \times 4.0} = 2.12$$

$$\gamma_{s,eq} = \frac{0.261m}{0.245m} = 1.065$$

Assume $\theta=0.01$ radians rotation:

$$\gamma_r = \frac{(D^2 \theta)}{(2t r)} = \frac{0.6^2 \times 0.01}{2 \times 0.025 \times 0.245} = 0.294$$

Assume a service load displacement of $d_s = \pm 50$ mm:

$$\gamma_{s,s} = \frac{0.05m}{0.245m} = 0.204$$

$$\gamma_c = 2.12 \leq 2.5 \quad \text{OK}$$

$$\gamma_c + \gamma_{s,s} + \gamma_r = 2.62 \leq 5.0 \text{ OK}$$

$$\gamma_c + \gamma_{s,eq} + 0.5\gamma_r = 3.33 \leq 5.5 \text{ OK}$$

Similar checks are also available at other codes [27, 49, 50].

5.6.2. Design Evaluation with Non-linear Time History Analysis

As a supplementary check of the design example, non-linear time history analyses (NLTH) are performed on a single degree of freedom system (SDOF). The governing equation of motion for an inelastic SDOF system can be expressed as [83]:

$$m\ddot{d}_b(t) + c_b\dot{d}_b(t) + f_s(d_b, \dot{d}_b) = -m\ddot{d}_g(t) \quad (5.16)$$

where

- c_b : viscous damping coefficient of the bearing
- d_b : bearing displacement
- d_g : ground displacement
- f_s : resisting force for the inelastic system
- m : mass supported by the bearing

In an inelastic system, the input seismic energy is dissipated by both viscous damping and yielding. The various energy terms can be defined by integrating the equation of motion of an inelastic system [83]:

$$\int_0^{d_b} m\ddot{d}_b(t) dd_b + \int_0^{d_b} c_b\dot{d}_b(t) dd_b + \int_0^{d_b} f_s(d_b, \dot{d}_b) dd_b = - \int_0^{d_b} m\ddot{d}_g(t) dd_b \quad (5.17)$$

The right side of the equation is the energy input (E_I) into the structure since the earthquake began:

$$E_I(t) = - \int_0^{d_b} m\ddot{d}_g(t) dd_b \quad (5.18)$$

The first term on the left side of Equation 5.17 is the kinetic energy (E_K) of the mass associated with its motion relative to the ground:

$$E_K(t) = \int_0^{d_b} m \ddot{d}_b(t) dd_b = \frac{m \dot{d}_b^2}{2} \quad (5.19)$$

The second term on the left side of Equation 5.17 is the energy dissipated by viscous damping (E_D):

$$E_D(t) = \int_0^{d_b} c_b \dot{d}_b(t) dd_b \quad (5.20)$$

The third term on the left side of Equation 5.17 is the sum of the energy dissipated by yielding and the recoverable strain energy of the system (E_S):

$$E_S(t) = \frac{[f_s(t)]^2}{2K_1} \quad (5.21)$$

where K_1 is the primary stiffness of the inelastic system.

Energy dissipated by yielding (E_Y) is:

$$E_Y(t) = \int_0^{d_b} f_s(d_b, \dot{d}_b) dd_b - E_S(t) \quad (5.22)$$

Based on the Equations through 5.16 to 5.22, statement of the energy balance for the system can be expressed as:

$$E_I(t) = E_K(t) + E_D(t) + E_S(t) + E_Y(t) \quad (5.23)$$

In NLTH analyses, Newmark's direct integration solution with full Newton-Raphson iteration method is selected. Basic procedure of Newmark's method consists of two following time-stepping equations [83]:

$$\dot{d}_{b,i+1} = \dot{d}_{b,i} + [(1 - \kappa)\Delta t] \ddot{d}_{b,i} + (\kappa\Delta t) \ddot{d}_{b,i+1} \quad (5.24)$$

$$d_{b,i+1} = d_{b,i} + (\Delta t) \dot{d}_{b,i} + [(0.5 - \beta)(\Delta t)^2] \ddot{d}_{b,i} + [\beta(\Delta t)^2] \ddot{d}_{b,i+1} \quad (5.25)$$

where the parameters β and κ define the variation of acceleration over a time step and determine the stability and accuracy characteristics of the method. The procedure for non-linear systems is extension of the procedure for linear systems [83].

The ground motions that are utilized in NLTH analyses should be representative of site condition and expected earthquake properties [84], as presented in Table 5.2. Since seven earthquake records are utilized, the average response of the parameter of interest shall be used in design [6].

Table 5.2. Basic Features of Ground Motions Utilized In NLTH Analyses [85, 86]

Name	Earthquake	Mw	Distance to Fault (km)	Soil Condition	PGA _L (m/s ²)	PGA _T (m/s ²)
Kagel Canyon	1994-Northridge	6.7	10.6	Rock	4.24	2.95
Castaic	1994-Northridge	6.7	24.1	Rock	5.04	5.57
Los Angeles City Terrace	1994-Northridge	6.7	35.8	Rock	3.10	2.58
Santa Cruz	1989-Loma Prieta	7.0	18.8	Rock	4.01	4.33
Izmit	1999-Izmit	7.4	4.26	Rock	1.64	2.23
Gebze	1999-Izmit	7.4	7.74	Rock	2.64	1.40
Cape Mendocino	1991-Petrolia	6.0 (M _L)	15.4	Rock	2.55	1.29

The selected earthquakes are amplitude scaled so that average of the SRSS (Square root of sum of squares) spectra of the selected records does not fall below 1.3 times the design basis spectrum in the range of $0.5T_{eff}$ and $1.5T_{eff}$ [6], as presented in 5.19. The un-scaled SRSS spectra of selected earthquake records are presented in Figure 5.20 and scaled spectra are presented in Figure 5.21.

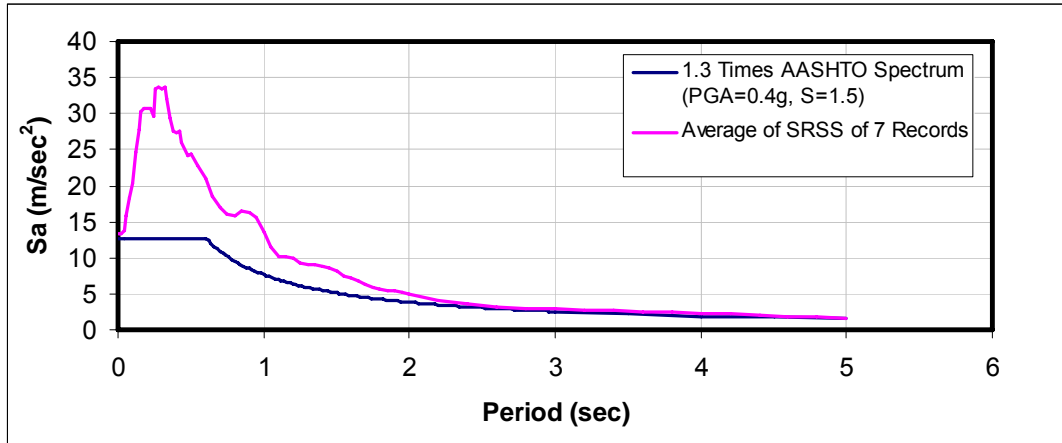


Figure 5.19. Average Spectrum of Design Spectrum Compatible Ground Motions

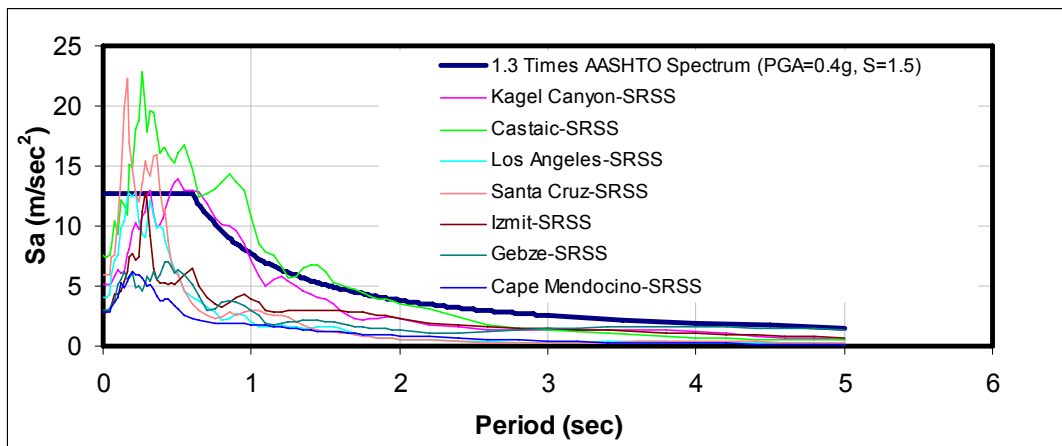


Figure 5.20. SRSS Spectra of Selected Earthquake Records-Un-scaled

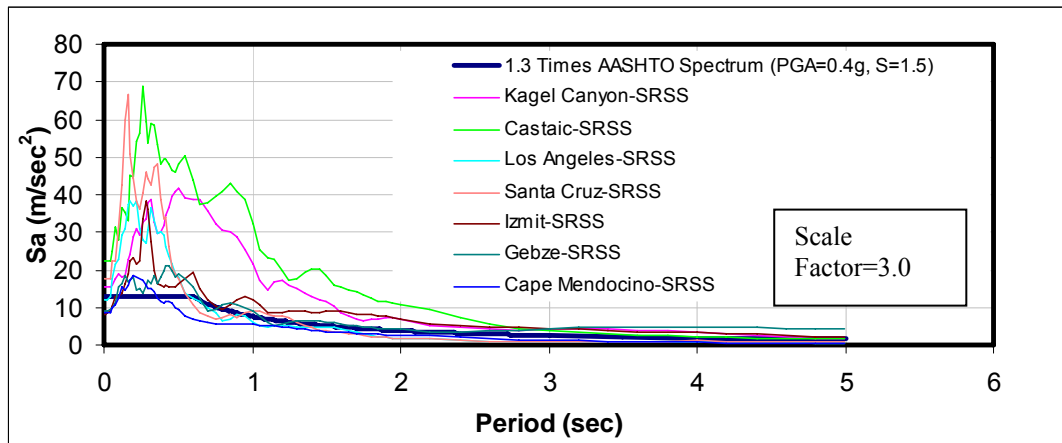


Figure 5.21. SRSS Spectra of Selected Earthquake Records-Scaled

The nonlinear time history analyses are performed uni-directionally for both lower bound and upper bound BRB properties ($Q_{d,lower}=57.93$ kN, $Q_{d,upper}=124.93$ kN, $K_2=554$ kN/m, $d_y=5.64$ mm) using Larsa 4D software [87]. In the analysis software, non-degrading bi-linear hysteretic translational spring element [88] is utilized for isolator definition. A view of the SDOF model is presented in Figure 5.22. The isolator displacements and forces are summarized in Table 5.3 and hysteresis loops observed during NLTH analyses using Izmit-Transverse record are presented in Figure 5.23.

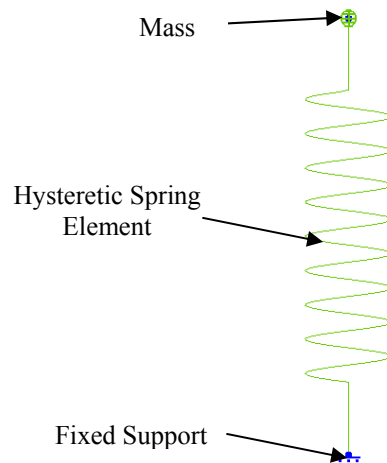


Figure 5.22. View of the SDOF Model [87]

Table 5.3. NLTH Analyses Results

Name	Lower Bound		Upper Bound	
	d_{\max} (mm)	F_{\max} (kN)	d_{\max} (mm)	F_{\max} (kN)
Kagel Canyon,L	471	318	339	312
Kagel Canyon,T	394	276	359	324
Castaic,L	553	364	485	393
Castaic,T	620	401	493	398
Los Angeles City Terrace,L	80	102	66	161
Los Angeles City Terrace,T	91	108	73	165
Santa Cruz,L	80	102	45	150
Santa Cruz,T	101	113	114	188
Izmit,L	335	243	145	205
Izmit,T	543	358	320	302
Gebze,L	488	328	350	319
Gebze,T	193	164	84	171
Cape Mendocino,L	59	91	41	148
Cape Mendocino,T	144	137	126	194
Average:	297	222	217	245
Diff. in d_{\max}	80			
Diff. in F_{\max}	23			

The analysis results indicate that structural response is not very much affected by the scatter in the test data in terms of base shear forces. On the other hand, the difference in the isolator displacements reveals that upper bound and lower bound solutions should always be checked. The effect of scatter in the test data can be compensated by non-degrading EDC characteristic of BRB, as the number of loading cycles increases.

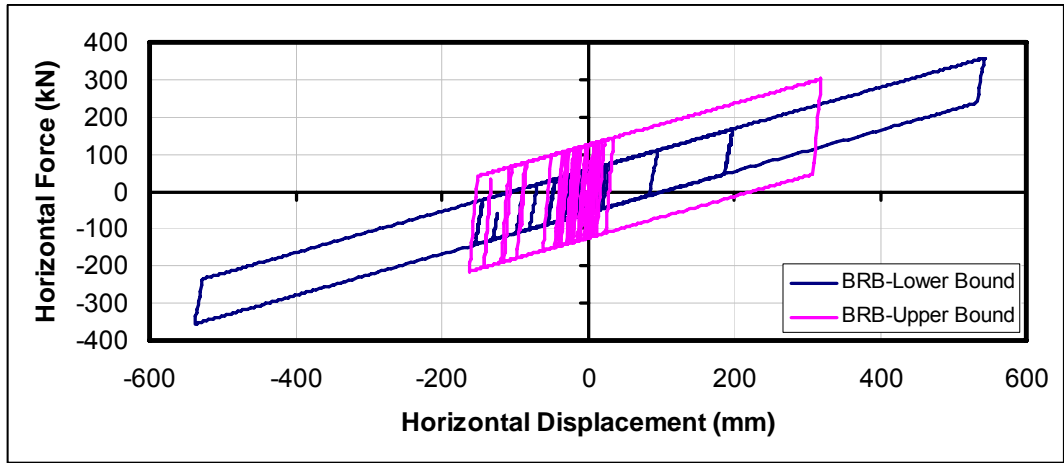


Figure 5.23. Hysteresis Loops Observed in NLTH Analyses Using Izmit-Transverse Record

CHAPTER 6

SUMMARY AND CONCLUSION

6.1. Summary

The experimental research presented in this dissertation aims to develop a new rubber-based seismic isolator type on the basis of the idea that the damping of a conventional annular elastomeric bearing (EB) can be increased by filling its central core with small diameter steel balls, which dissipate energy via friction inside the confined hole of the bearing during their movements under horizontal loads. The proposed bearing type is called “Ball Rubber Bearing (BRB)”. More than 200 tests were conducted to determine the cyclic horizontal load-deformation characteristics of the test bearings with different geometric and material properties. Effects of steel ball diameter, central hole diameter (D/d ratio), magnitude of horizontal displacement, vertical compression force level and supplementary confinement in the central core are studied in detail. Vertical loading tests are also performed to determine the change in vertical stiffness of the bearings due to the addition of the fill material. In addition to these “seismic” tests, BRBs are also investigated under service load conditions. A detailed non-linear finite element model is developed to verify the test results. The proposed analytical model is determined to simulate the structural hysteretic behaviour of the bearings. In design of BRBs, the proposed design guideline can be used in conjunction with the proposed non-linear finite element analysis to verify the structural response prior to testing of the bearings.

The steel balls provide high energy dissipation capacity (EDC), horizontal restoring force and large vertical stiffness, which are the three basic requirements of a seismic isolation system [6].

Using the extensive test results, design equations of BRBs are developed by taking into account the scatter in the test data. A design example is also presented in the dissertation in order to provide a guideline in the design of BRBs. The non-linear time history analysis results indicate that structural response is not very much affected by the scatter in the test data in terms of base shear forces, whereas the difference in the isolator displacements reveals that upper bound and lower bound solutions should always be checked. The effect of scatter in the test data can be compensated by non-degrading EDC characteristic of BRB.

The scatter in test results may have resulted from production quality of BRBs, mainly due to the filling process of the hole, complex mechanical behavior of granular materials and small variations in laboratory temperature. Moreover, re-using steel balls in many tests may have resulted in such a scatter since it is expected that surface roughness of steel balls abrades after few tests.

6.2. Conclusion

The following conclusions are drawn based on the studies presented in this dissertation;

1. BRBs generally provide equivalent viscous damping ratios around 20%. Energy is dissipated in the central core of the bearing by friction developed between pressurized steel balls, when the bearing is subjected to horizontal loads.
2. Test results indicate that ideal steel ball diameter to be used in the central core of a BRB is 1.65 mm. Steel balls with an average diameter of 3 mm may also be used. However, steel balls having larger diameters should be avoided. The bearings with 5 mm steel balls have lower EDCs when compared to the bearings with 1.65 mm and 3 mm steel balls.
3. There is almost no degradation in EDC of BRB, as the number of loading cycles increases. Heat generated in the central core due to friction has no pronounced effect on performance of BRB since measured temperature is no more than 45-50 °C (i.e. temperature rise is about 25-30 °C). On the other hand, as intensity

of seismic input gets higher, the effect of heat generation on performance of BRB may become more significant.

4. Approximately 50% of the vertical compressive load on the bearing is resisted by the steel balls placed in the central hole of the bearing. Because of this speciality, BRBs may have lower shape factors than EBs. In designing a BRB, the shape factor of the elastomeric part may be selected to be lower than 5.0, by ignoring the presence of steel balls.
5. Characteristic strength of a BRB does not increase noticeably at uniform vertical compressive stress higher than 1.70 MPa due to horizontal dilation of steel balls, which results in lower friction coefficients.
6. AASHTO [6, 27] service & seismic design equations are typically satisfied between a minimum compressive stress of 1.78 MPa and a maximum compressive stress of 5.26 MPa for tested BRBs with $D/d=3.0$. Plan dimensions of BRBs can be selected to provide 3.4 MPa average vertical stress with $\pm 10\%$ tolerance under unfactored total load.
7. Contribution of steel balls to secondary stiffness of a BRB decreases with increasing horizontal displacement demands. Secondary stiffness of BRB increases with decreasing D/d . Contribution of steel balls to secondary stiffness is approximately 2.5 times for BRBs with $D/d=2.0$ compared to BRBs with $D/d=3.75$, if a linear trendline is used to fit the test data.
8. BRBs are efficient for Q_d/P_{ver} ratios from 0.04 up to 0.15 or more in terms of energy dissipation as indicated by friction coefficients between steel balls.
9. Designing BRBs with $D/d=3.0$ or $D/d=3.75$ provides a high EDC while limiting the maximum horizontal force. Nevertheless, BRBs having lower D/d ratios may be utilized in special applications.

10. Higher horizontal stiffness of BRBs at smaller horizontal displacement demands provide service load rigidity while lower horizontal stiffness at larger horizontal displacement demands provide flexibility without using any supplementary device.

6.3. Recommendations for Future Researches

Following recommendations are made for future researches and researchers:

1. BRBs having different shape factors may be tested.
2. BRBs having different shapes such as square & rectangle may be tested.
3. BRBs having rubber with low shear modulus may be tested.
4. BRBs may be tested at low temperatures in order to obtain property modification factor [6].
5. BRBs with steel balls in mixed size may be tested.
6. BRBs with glued steel balls may be tested.
7. BRBs with smaller diameter steel balls may be tested.
8. Discrete element model of a BRB may be investigated.

REFERENCES

- [1] Christopoulos, C., Filiatrault, A., “Principles of Passive Supplemental Damping and Seismic Isolation,” IUSS Press, Pavia, Italy, 2006.
- [2] Buckle, I.G., Mayes, R.L., “Seismic Isolation: History, Application and Performance-A World View,” *Earthquake Spectra*, Vol.6, No.2, 1990, pp. 161-201.
- [3] Naeim, F., Kelly, J.M., “Design of Seismic Isolated Structures: From Theory to Practice,” John Wiley&Sons, 1999.
- [4] Nakashima, M., Pan, P., Zamfirescu, D., Weitzmann, R., “Post-Kobe Approach for Design and Construction of Base-Isolated Buildings,” *Journal of Japan Association for Earthquake Engineering*, Vol. 4, No. 3 (Special Issue), 2004, pp. 259-264.
- [5] Buckle, I., Constantinou, M.C., Dicleli, M., Ghasemi, H., “Seismic Isolation of Highway Bridges,” Special Report MCEER-06-SP07, 21 August 2006.
- [6] American Association of State Highway and Transportation Officials (AASHTO), “Guide Specifications for Seismic Isolation Design,” 1999.
- [7] Dicleli, M., “Supplemental Elastic Stiffness to Reduce Isolator Displacements for Seismic Isolated Bridges in Near-Fault Zones,” *Engineering Structures*, 29, 2007, pp. 763-775.
- [8] Panza, G.F., Cioflan, C., “Vrancea Earthquakes: A Special Challenge for Seismic Isolation In Bucharest,” *Proceedings of the International Symposium on Modern Systems for Mitigation of Seismic Action*, Bucharest, Romania, 31 October-1 November 2008, pp. 339-355.
- [9] Kelly, T.E., “Base Isolation of Structures,” Holmes Consulting Group Ltd., Revision 0, June 2001, New Zealand.

- [10] Marioni, A., "The Use of High Damping Rubber Bearings for the Protection of the Structures from the Seismic Risk," Jornadas Portuguesas de Engenharia de Estruturas, Lisbon, 25-28 November 1998.
- [11] Chihiro, H., Tetsuo, O., Kunitomo, N., Yoshio, O., "Seismic Isolation Effects of Laminated Rubber Bearing Paced with Granular Material," Bulletin of Aichi Institute of Technology, Part B, Volume 35, 2000, pp. 135-142. [In Japanese]
- [12] Hayashi, S., Watanabe, H., Nakamura, Y., Yoshizawa, T., Nakamura, T., "Response Characteristics of Base-Isolated Structure With Silicone Rubber Bearings," Smirt-12, K24/3, Elsevier Science Publishers B.V., 1993, pp. 339-344.
- [13] Dolce, M., Cardone, D., Marnetto, R., Nigro, D., Palermo, G., "A New Added Damping Rubber Isolator (ADRI): Experimental Tests and Numerical Simulations," 8th World Seminar on Seismic Isolation, Energy Dissipation and Active Vibration Control of Structures, Yerevan, Armenia, 6-10 October 2003.
- [14] Matsushita, H., Fujisawa, K., Sasaki, T., "Development of Peripherally Restraining Type Seismic Isolator," Smirt-12, K25/4, Elsevier Science Publishers B.V., 1993, pp. 375-380.
- [15] Tanaka, K., Hirasawa, M., Ishiguro, Y., and Ohyama, H., Nakamura, Y., "Base Isolation System with Hybrid Lead Rubber Bearings," Smirt-12, K25/5, Elsevier Science Publishers B.V., 1993, pp. 381-386.
- [16] Özden, B., Türer, A., "Seismic Isolation with Cheap Scrap Automobile Tires," Workshop on Increase of Seismic Safety of Masonry Structures, Middle East Technical University, Ankara, 17 February 2005. [In Turkish]
- [17] Kelly, J.M., "Analysis of Fiber-Reinforced Elastomeric Isolators," JSEE, Fall 1999, Vol. 2, No.1, pp. 19.34.
- [18] Zhou, F.L., "Seismic Isolation of Civil Buildings in the People's Republic of China," Progress in Structural Engineering and Materials, 2001, 3: 268-276.
- [19] Xiao, H., Butterworth, J.W., Larkin, T., "Low-Technology Techniques for Seismic Isolation," 2004 NZSEE Conference, Paper Number 36.
- [20] Jangid, R.S., Londhe, Y.B., "Effectiveness of Elliptical Rolling Rods for Base Isolation," Journal of Structural Engineering, ASCE, April 1998, pp. 469-472.

- [21] Kunde, M.C., Jangid, R.S, "Seismic Behavior of Isolated Bridges: A-State-of-the-Art-Review," *Electronic Journal of Structural Engineering*, 3-2003, pp. 140-170.
- [22] Roussis, P.C., Constantinou, M.C., "Uplift-Restraining Friction Pendulum Seismic Isolation System," *Earthquake Engineering and Structural Dynamics*, 2006, 35:577-593.
- [23] Fenz, D.M., Constantinou, M.C., "Spherical Sliding Isolation Bearings with Adaptive Behavior: Theory," *Earthquake Engineering and Structural Dynamics*, 2007, DOI: 10.1002/eqe.751.
- [24] Robinson, W.H., Gannon, C.R., Meyer, J., "The RoGlider-A Sliding Bearing with An Elastic Restoring Force," 2006 NZSEE Conference, Paper Number 54.
- [25] Wilde, K., Gardoni, P., Fujino, Y., "Base Isolation System with Shape Memory Alloy Device for Elevated Highway Bridges," *Engineering Structures*, 22-2000, pp. 222-229.
- [26] Ramallo, J.C., Johnson, E.A., Spencer, B.F., "'Smart' Base Isolation Systems," *Journal of Engineering Mechanics*, ASCE, October 2002, pp. 1088-1099.
- [27] American Association of State Highway and Transportation Officials (AASHTO), "LRFD Bridge Design Specification," 4th Edition, 2007.
- [28] Robinson, W.H., "Seismic Isolation of Civil Buildings in New Zealand," *Progress in Structural Engineering and Materials*, 2000, 2: 328-334.
- [29] Adnan, A., Sunaryati, J., "Mechanical Characteristics of Circular Elastomeric Hollow Rubber Bearings," *Proceedings of the 6th Asia-Pacific Structural Engineering and Construction Conference*, Kuala Lumpur, Malaysia, 5-6 September 2006, pp. B18- B24.
- [30] Tajirian, F.F., Kelly, J.M., Aiken, I.D., Veljovich, W., "Elastomeric Bearings for Three Dimensional Seismic Isolation," *Proceedings, 1990 ASME PVP Conference*, ASME PVP 200, Nashville, Tennessee, June 1990.
- [31] Pınarbaşı, S., Akyüz, U., "Seismic Isolation and Elastomeric Bearing Tests," *Technical Journal of Turkish Chamber of Civil Engineers*, Paper 237, 2005, pp. 3581-3598. [In Turkish]

- [32] Yakut, A., Yura, J.A., "Evaluation of Low-Temperature Test Methods for Elastomeric Bridge Bearings," *Journal of Bridge Engineering*, January-February 2002, pp. 50-56.
- [33] Kelly, J.M., "Tension Buckling in Multilayer Elastomeric Bearings," *Journal of Engineering Mechanics*, ASCE, December 2003, pp. 1363-1368.
- [34] Tsai, H.-C., Kelly, J.M., "Buckling Load of Seismic Isolators Affected by Flexibility of Reinforcement," *International Journal of Solids and Structures*, 42-2005, pp. 255-269.
- [35] Warn, G.P., Whittaker, A.S., Constantinou, M.C., "Vertical Stiffness of Elastomeric and Lead-Rubber Seismic Isolation Bearings," *Journal of Structural Engineering*, ASCE, September 2007, pp. 1227-1236.
- [36] Braga, F., Laterza, M., Gigliotti, R., "Seismic Isolation Using Slide and Rubber Bearings: Large Amplitude Free Vibration Tests on "Rapolla Residence Building"," 7th International Seminar on Seismic Isolation, Passive Energy Dissipation and Active Control of Vibrations of Structures, ASSISI, Italy, 2-5 October 2001.
- [37] Yoshida, J., Abe, M., Fujino, Y., "Constitutive Model of High-Damping Rubber Materials," *Journal of Engineering Mechanics*, ASCE, February 2004, pp. 129-141.
- [38] Aiken, I.D., Kelly, J.M., Clark, P.W., Tamura, K., Kikuchi, M., Itoh, T., "Experimental Studies of the Mechanical Characteristics of Three Types of Seismic Isolation Bearings," *Proceedings, 10th World Conference on Earthquake Engineering*, Madrid, Spain, July 1992.
- [39] Kelly, J.M., "Dynamic and Failure Characteristics of Bridgestone Isolation Bearings," EERC Report No: UCB/EERC-91/04, April 1991.
- [40] Lee, J.-H., Yoo, B., Koo, G.-H., "Characteristic Tests of High Damping Rubber Shear Specimens for Seismic Isolators of KALIMER," *Transactions of the 15th International Conference on Structural Mechanics in Reactor Technology (Smirt-15)*, K16/3, Seoul, Korea, 15-20 August 1999, pp. IX-335-IX 341.
- [41] Burtscher, S., Dorfmann, A., Bergmeister, K., "Mechanical Aspects of High Damping Rubber," 2nd International PhD Symposium in Civil Engineering, Budapest, Hungary, 1998.

- [42] Marioni, A., “Innovative Anti-Seismic Devices Developed by Alga,” Proceedings of the International Symposium on Modern Systems for Mitigation of Seismic Action, Bucharest, Romania, 31 October-1 November 2008, pp. 129-151.
- [43] Constantinou, M.C., Whittaker, A.S., Kalpakidis, Y., Fenz, D.M., Warn, G.P., “Performance of Seismic Isolation Hardware under Service and Seismic Loading,” Technical Report MCEER-07-0012, 27 August 2007.
- [44] Matsagar, V.A., Jangid, R.S, “Viscoelastic Damper Connected to Adjacent Structures Involving Seismic Isolation,” Journal of Civil Engineering and Management, 2005, pp. 309-322.
- [45] Doudoumis, I. N., Gravalas, F., Doudoumis, N.I., “Analytical Modeling of Elastomeric Lead-Rubber Bearings with the Use of Finite Element Micromodels,” 5th GRACM International Congress on Computational Mechanics, Limasol, 29 June-1 July 2005.
- [46] Tsai, C.S., “Finite Element Formulations for Friction Pendulum Seismic Isolation Bearings,” International Journal for Numerical Methods in Engineering, Vol. 40, 1997, pp. 29-49.
- [47] Politecnico Di Milano, “Tests on Xslide Special Sliding Material,” Milano, January 2009.
- [48] Constantinou, M.C., Kartoum, A., Reinhorn, A.M., Bradford, P., “Sliding Isolation System for Bridges: Experimental Study,” Earthquake Spectra, Vol.8, No.3, 1992, pp. 321-344.
- [49] Turkish Association for Seismic Isolation, “Seismic Isolation Specification,” Istanbul, May 2008. [In Turkish]
- [50] European Standard, “Anti-Seismic Devices-Final Draft FprEN15129,” European Committee for Standardization, Brussels, June 2009.
- [51] EuCentre (European Center for Training and Research in Earthquake Engineering), “Pre-Characterization and Characterization Tests of LRB Algasism 1100×580,” Pavia, Italy, October 2009.
- [52] Aiken, I.D., “Testing of Seismic Isolators and Dampers-Considerations and Limitations,” Proceedings, Structural Engineering World Congress, San Francisco, California, July 1998.

- [53] Unjoh, S., Ohsumi, M., "Earthquake Response Characteristics of Super-Multi-Span Continuous Menshin (Seismic Isolation) Bridges and the Seismic Design," ISET Journal of Earthquake Technology, Paper No: 377, Vol.35, No.4, December 1998, pp.95-104.
- [54] Tongaokar, N.P., Jangid, R.S., "Seismic Response of Bridges with Sliding Isolation Devices," ISET Journal of Earthquake Technology, Paper No. 373, Vol. 35, No. 1-3, March-September 1998, pp. 9-27.
- [55] Bolt, B.A., "Seismic Input Motions for Nonlinear Structural Analysis," ISET Journal of Earthquake Technology, Paper No: 448, Vol. 41, No. 2-4, June-December 2004, pp. 223-232.
- [56] Kramer, S.L., "Geotechnical Earthquake Engineering," Prentice Hall, 1996.
- [57] Jangid, R.S., Kelly, J.M., "Base Isolation for Near-Fault Motions," Earthquake and Structural Dynamics, 2001, 30:691-707.
- [58] Kelly, J.M., "The Role of Damping in Seismic Isolation," Earthquake Engineering and Structural Dynamics, 1999, 28, pp. 3-20.
- [59] Kelly, J.M., "Earthquake-Resistant Design with Rubber," Springer-Verlag, 1993.
- [60] Sharma, A., Jangid, R.S., "Behaviour of Base-Isolated Structures with High Initial Isolator Stiffness," Proceedings of World Academy of Science, Engineering and Technology, Volume 38, February 2009, ISSN: 2070-3740, pp.186-191.
- [61] Özkaya, C., Çelebi, N., Tulumtaş, F., Dicleli, M., "Hybrid Seismic Isolation Design of Sakarya-II Viaduct in the Proximity of the North Anatolian Fault," IABMAS 2010, Philadelphia, 11-15 July 2010.
- [62] Marioni, A., Özkaya, C., Dicleli, M., Gerçek, M., "Rock Steady: Sakarya Bridge in Turkey," Bridge Design and Engineering, Issue No. 59, 2nd Quarter 2010, pp. 52-53.
- [63] Park, J.-G., Otsuka, H., "Optimal Yield Level of Bilinear Seismic Isolation Devices," Earthquake Engineering and Structural Dynamics, 28, 1999, pp. 941-955.

- [64] Caner, A., Akyuz, U., Pınarbaşı, S., Özkaya, C. “Experimental Development of a Rubber Based Seismic Isolator Capable of High Damping,” TÜBİTAK Report, February 2009. [In Turkish]
- [65] Akyüz, U., Türer, A., Yakut, A., Baskan, İ.C., Pınarbaşı, S., “Development of Passive Control System and Dynamic Isolator, Application on a Small Scale Model and a Bridge,” BAP Report No: 2002-03-03-04, June 2004. [In Turkish]
- [66] Vishay Micro-Measurements, “Instruction Manual for System 6000-Model 6100 Scanner,” May 2003.
- [67] Gent, A.N., “Engineering with Rubber-How to Design Rubber Components,” Hanser Publishers, Munich, 2001.
- [68] American Association of State Highway and Transportation Officials (AASHTO), “AASHTO M 251 Standard Specification for Plain and Laminated Elastomeric Bridge Bearings,” 2006.
- [69] Roussel, L.E., “Experimental Investigation of Stick-Slip Behavior in Granular Materials,” MS Thesis, Louisiana State University, August 2005.
- [70] Toscelik Granule Industry, “Products,” <http://www.toscelikgranul.com.tr>, Last Access Date; 12/10/2009.
- [71] Houlsby, G.T., “How the Dilatancy of Soils Affects Their Behaviour,”10th European Conference on Soil Mechanics and Foundation Engineering, 1991.
- [72] Cernica, J.N., “Geotechnical Engineering: Soil Mechanics,” John Wiley & Sons, 1995.
- [73] Marraquin, F.A., Vardoulakis, I., “Micromechanics of Shear Bands in Granular Media,” www.physics.uq.edu.au/people/fernando/papers/shear-alonso05.pdf, Last Access Date; 25/12/2009.
- [74] ADINA R&D Inc., “ADINA-Automatic Dynamic Incremental Nonlinear Analysis-Version 8.5,” Watertown, Mass., 2008.
- [75] Bathe, K.J., “Finite Element Procedures,” Prentice Hall, 2006.

- [76] Sitharam, T.G., “Numerical Simulation of Particulate Materials Using Discrete Element Modelling,” *Current Science*, Vol.78, No.7, April 2000.
- [77] Sitharam, T.G., “Discrete Element Modelling of Cyclic Behaviour of Granular Materials,” *Geotechnical and Geological Engineering*, Kluwer Academic Publishers, 21:297-329, 2003.
- [78] Castellano, M.G., Infanti, S., Baldo, P., Kaya, M., “Italian Experience in Seismic Isolation of Bridges,” 1st Bridges and Viaducts Conference, Antalya, 29-30 November 2007, pp. 13-23.
- [79] Ang, A.-H.S., Tang, W.H., “Probability Concepts in Engineering Planning and Design: Volume 1-Basic Principles,” John Wiley & Sons, 1975.
- [80] Makris, N., Black, C.J., “Dimensional Analysis of Bilinear Oscillators Under Pulse-Type Excitations,” *ASCE Journal of Engineering Mechanics*, Vol. 130, No.9, September 2004, pp. 1019-1031.
- [81] Earthquake Protection Systems Inc., “Friction Pendulum Seismic Isolation Bearing- Details and Specifications for Bridges,” March-1999.
- [82] Matsushima, T., “On the Shear Behavior of Well-Graded Granular Assembly,” <http://shake.iis.u-tokyo.ac.jp/seismic-fault/workshop/papers-2/Matsushima.pdf>, Last Access Date; 27/12/2009.
- [83] Chopra, A.K., “Dynamics of Structures-Theory and Applications to Earthquake Engineering,” Prentice Hall, 2000.
- [84] American Association of State Highway and Transportation Officials (AASHTO), “AASHTO Guide Specifications for LRFD Seismic Design,” 1st Edition, 2009.
- [85] Cosmos- Consortium of Organizations for Strong Motion Observation Systems, “Virtual Data Centers,” <http://www.cosmos-eq.org>, Last Access Date; 25/07/2010.
- [86] Özkaya, C., Caner, A., “Assessment of Seismic Performance of Seismically Isolated Bridges with Inverted T-Cap Beams,” *Concrete Bridge Conference*, St. Louis, May 2008.

- [87] Larsa Inc., "Larsa 4D-Structural and Earthquake Engineering Integrated Analysis and Design Software," New York, 2010.
- [88] Sivaselvan, M.V., Reinhorn, A.M., "Hysteretic Models for Cyclic Behavior of Deteriorating Inelastic Structures," Technical Report MCEER-99-0018, University at Buffalo, State University of New York, 1999.

APPENDIX A

TEST RESULTS

In Table A.1, Table A.2 and Table A.3, general information about tests and test results are presented. It should be reminded that presented test results are valid for two simultaneously tested bearings. For one bearing, characteristic strength (Q_d), effective stiffness (K_{eff}) and maximum horizontal force values are 50% of the values in Table A.1, Table A.2 and Table A.3, while equivalent damping ratio is unaltered.

Table A.1. Test Results-1

Test No:	d (mm)	Fill Material	P_{ver} (kN)	d_{max} (mm)	F_{max} (kN)	$\beta_{eq}\%$
1	100	Sand (%50)- Gravel(%50)	120	74.4	128.2	12.68
2	100	Empty	120	75	111	9.69
3	100	Sand(%50)- Gravel(%50)	120	75	120	8.73
4	150	Empty	120	75	102	7.63
5	150	Rub. Sheets(%33)- Gravel(%67)	120	75	100	8.68
6	100	Gravel(%67)- Barite (%33)	120	74	145	9.37
7	100	Gravel(%67)- Barite (%33)	120	75	136	9.47
8	100	1.65 mm Steel Balls	120	44	125	19.91
9	100	1.65 mm Steel Balls	120	54	155	19.28
10	100	1.65 mm Steel Balls (85%) - Shredded Rubber (15%)	120	35	80	10.96

Table A.1 (Continued)

Test No:	d (mm)	Fill Material	P _{ver} (kN)	d _{max} (mm)	F _{max} (kN)	β _{eq} %
11	100	1.65 mm Steel Balls (85%) - Shredded Rubber (15%)	120	65	130	8.71
12	100	1.65 mm Steel Balls (95%) - Shredded Rubber (5%)	120	45	100	11.83
13	100	1.65 mm Steel Balls (95%) - Shredded Rubber (5%)	120	65	130	9.90
14	100	1.65 mm Steel Balls	120	74	170	17.01
15	60	Empty	120	76	110	8.39
16	60	1.65 mm Steel Balls	120	45.5	80	15.61
17	60	1.65 mm Steel Balls	120	75	120	13.46
18	60	1.65 mm Steel Balls	120	66	97.5	13.88
19	60	1.65 mm Steel Balls	120	66	100	13.98
20	60	3 mm Steel Balls	120	45	78	12.48
21	60	3 mm Steel Balls	120	76	110	12.27
22	60	3 mm Steel Balls	0	37	52	5.89
23	60	5 mm Steel Balls	120	46	81	12.38
24	60	5 mm Steel Balls	120	75	115	11.88
25	60	5 mm Steel Balls	0	36	52	8.62
26	100	3 mm Steel Balls	120	45	130	17.63
27	100	3 mm Steel Balls	120	75	170	18.43
28	100	3 mm Steel Balls	0	36	78	6.12
29	100	5 mm Steel Balls	120	45	124	13.89
30	100	5 mm Steel Balls	120	64	150	15.90
31	100	5 mm Steel Balls	0	36	77	5.05
32	100	5 mm Steel Balls	200	45	133	17.14
33	100	5 mm Steel Balls	200	55	150	18.81
34	150	1.65 mm Steel Balls	120	-	-	-
35	150	1.65 mm Steel Balls	120	36	110	9.90
36	150	1.65 mm Steel Balls	120	54	138.5	17.01
37	150	1.65 mm Steel Balls	200	34.5	125	14.62
38	150	1.65 mm Steel Balls	0	36	65	4.90
39	150	3 mm Steel Balls	200	33	172	19.32
40	150	3 mm Steel Balls	200	-	-	-
41	150	3 mm Steel Balls	200	34.5	115	10.27
42	150	3 mm Steel Balls	200	-	-	-
43	150	3 mm Steel Balls	120	53.5	168	19.59
44	150	3 mm Steel Balls	0	36	63	5.05
45	150	3 mm Steel Balls	200	22.5	150	17.76
46	150	3 mm Steel Balls	200	22.5	135	15.35
47	150	3 mm Steel Balls	200	23	133	13.08

Table A.1 (Continued)

Test No:	d (mm)	Fill Material	P _{ver} (kN)	d _{max} (mm)	F _{max} (kN)	β _{ref} %
48	150	3 mm Steel Balls	120	23.5	124	12.20
49	100	3 mm Steel Balls	200	25	78	11.36
50	100	3 mm Steel Balls	200	54	145	14.38
51	150	1.65 mm Steel Balls	120	25	60	9.72
52	150	1.65 mm Steel Balls	120	25	82	10.43
53	150	1.65 mm Steel Balls	120	63	158	25.80
54	150	1.65 mm Steel Balls	200	25	87	10.68
55	150	1.65 mm Steel Balls	200	53.5	150	27.17
56	100	1.65 mm Steel Balls	200	25.5	84	12.54
57	100	1.65 mm Steel Balls	200	54	142	18.13
58	60	3 mm Steel Balls	200	55	92	12.57
59	60	3 mm Steel Balls	200	65	104	11.46
60	60	3 mm Steel Balls	200	85	131	10.68
61	60	1.65 mm Steel Balls	200	75	120	11.68
62	60	1.65 mm Steel Balls	200	84	130	12.29
63	60	5 mm Steel Balls	200	75	118	11.34
64	60	5 mm Steel Balls	200	85	125.6	11.13
65	150	Empty	0	36	65	8.68
66	150	Empty	0	65	105	6.39
67	150	Empty	200	36	59	13.67
68	150	Empty	200	65	102.5	9.20
69	150	5 mm Steel Balls	0	25	54	9.54
70	150	5 mm Steel Balls	0	64	134.5	6.14
71	150	5 mm Steel Balls	120	25.5	60	13.14
72	150	5 mm Steel Balls	120	53.5	150	13.09
73	150	5 mm Steel Balls	200	29	94	9.46
74	150	3 mm Steel Balls	200	34	130	11.44
75	150	3 mm Steel Balls	200	48.5	165	18.34
76	60	Empty	0	46	66.3	7.62
77	60	Empty	200	46	68	8.96
78	60	Empty	200	85.5	116	7.77
79	100	Empty	0	45.5	91	7.01
80	100	Empty	200	45.8	92.5	9.87
81	100	Empty	200	75	137	8.36
82	100	1.65 mm Steel Balls	0	44.8	112	7.06
83	100	1.65 mm Steel Balls	0	44.5	109	5.90
84	60	1.65 mm Steel Balls	0	46	72.5	7.40
85	60	1.65 mm Steel Balls	0	45.7	67.5	7.98
86	60	1.65 mm Steel Balls	120	85	128	10.37
87	120	Empty	0	54.5	100	6.92
88	120	Empty	0	74	128	5.60
89	120	Empty	120	54.5	95	9.61

Table A.1 (Continued)

Test No:	d (mm)	Fill Material	P _{ver} (kN)	d _{max} (mm)	F _{max} (kN)	β _{ref} %
90	120	Empty	120	74	128	8.15
91	120	Empty	200	55	93	8.92
92	120	Empty	200	74.5	126.5	8.10
93	120	1.65 mm Steel Balls	0	45	84.4	7.76
94	120	1.65 mm Steel Balls	0	73.5	140.5	5.64
95	120	1.65 mm Steel Balls	120	35	106	12.81
96	120	1.65 mm Steel Balls	120	54	149	15.62
97	120	1.65 mm Steel Balls	120	35	101	15.17
98	120	1.65 mm Steel Balls	120	54	145	16.22
99	120	1.65 mm Steel Balls	200	35	127	15.12
100	120	1.65 mm Steel Balls	200	54	168	20.77
101	80	1.65 mm Steel Balls	0	44	102	9.36
102	80	1.65 mm Steel Balls	0	44	97	9.96
103	80	1.65 mm Steel Balls	120	30	103	20.24
104	80	1.65 mm Steel Balls	120	44	129	21.68
105	80	1.65 mm Steel Balls	120	54	147	21.90
106	80	1.65 mm Steel Balls	200	34.5	106	23.41
107	80	1.65 mm Steel Balls	200	54	143	22.49
108	80	Empty	0	46	84	6.95
109	80	Empty	0	37	68.5	5.47
110	80	Empty	120	44	80	7.02
111	80	Empty	200	36.5	67.5	7.17
112	120	1.65 mm Steel Balls	0	36	80	7.12
113	120	1.65 mm Steel Balls	120	36	102.5	10.37
114	120	1.65 mm Steel Balls	200	35.5	119.5	11.73
115	80	Lead Core	200	39	171.5	10.17
116	80	Lead Core	120	39	157	8.93
117	80	Lead Core	200	35	146	12.95
118	80	Lead Core	200	35	141.5	10.39
119	80	Lead Core	0	35	107.8	5.95
120	100	1.65 mm Steel Balls	120	80	177.5	17.98
121	100	1.65 mm Steel Balls	200	82	179	19.44
122	100	1.65 mm Steel Balls	200	64.5	144.5	19.59
123	100	1.65 mm Steel Balls	120	64.5	143.5	13.70
124	120	1.65 mm Steel Balls	120	54	147	14.91
125	120	1.65 mm Steel Balls	200	53.5	162	17.41
126	120	1.65 mm Steel Balls	200	70	185	19.20
127	80	1.65 mm Steel Balls	120	55	125	13.29
128	80	1.65 mm Steel Balls	200	55	132	14.99
129	80	1.65 mm Steel Balls	300	35	96.5	17.18
130	80	1.65 mm Steel Balls	300	54.5	130	17.09
131	80	1.65 mm Steel Balls	300	69.5	157	16.64

Table A.1 (Continued)

Test No:	d (mm)	Fill Material	P _{ver} (kN)	d _{max} (mm)	F _{max} (kN)	β _{eq} %
132	80	1.65 mm Steel Balls	400	35.5	96	18.02
133	80	1.65 mm Steel Balls	400	55	125.5	18.33
134	80	1.65 mm Steel Balls	500	35	101	23.10
135	80	1.65 mm Steel Balls	500	55	132	22.15
136	80	Empty	300	55.5	97.5	6.48
137	80	Empty	400	56	92.7	7.19
138	80	Empty	500	56.2	89.5	7.93
139	80	1.65 mm Steel Balls	300	35	105	17.54
140	80	1.65 mm Steel Balls	300	55	132	16.36
141	80	1.65 mm Steel Balls	400	35	97	17.64
142	80	1.65 mm Steel Balls	400	54.5	135	17.93
143	80	1.65 mm Steel Balls	500	35	106	19.94
144	80	1.65 mm Steel Balls	500	54.3	143	20.07
145	80	1.65 mm Steel Balls	60	55.5	113	10.69
146	80	1.65 mm Steel Balls	120	55.5	116	13.05
147	80	1.65 mm Steel Balls	200	55.5	119	15.30
148	100	Steel Washer Plates- 5 mm	0	26.6	57.7	12.77
149	100	Steel Washer Plates- 5 mm	0	56.3	101.5	7.44
150	100	Steel Washer Plates- 5 mm	200	36	84.5	16.95
151	100	Steel Washer Plates- 5 mm	200	56.1	111	15.20
152	100	Steel Washer Plates- 5 mm	400	35	102.5	27.15
153	100	Steel Washer Plates- 5 mm	500	44.5	146	29.50
154	150	1.65 mm Steel Balls	60	45	112.5	10.90
155	150	1.65 mm Steel Balls	120	44	141	19.72
156	150	1.65 mm Steel Balls	200	34	138	19.42
157	150	1.65 mm Steel Balls	300	28.5	165	18.27
158	150	1.65 mm Steel Balls	400	23.5	170	18.65
159	150	1.65 mm Steel Balls	500	14	142.2	19.85
160	150	1.65 mm Steel Balls	90	34	139.5	12.51
161	150	1.65 mm Steel Balls	150	33.8	157	17.26
162	100	1.65 mm Steel Balls- FRP	55	16	57	11.72
163	100	17.5 mm Steel Washer Plates- 1.65 mm Steel Balls	120	55.5	120	10.09

Table A.1 (Continued)

Test No:	d (mm)	Fill Material	P_{ver} (kN)	d_{max} (mm)	F_{max} (kN)	$\beta_{eq}\%$
164	100	17.5 mm Steel Washer Plates- 1.65 mm Steel Balls	200	55	124	11.40
165	100	17.5 mm Steel Washer Plates - 1.65 mm Steel Balls	300	45.5	110	14.25
166	100	17.5 mm Steel Washer Plates -1.65 mm Steel Balls	300	55.2	132	11.66
167	100	17.5 mm Steel Washer Plates - 1.65 mm Steel Balls	400	45	121	17.09
168	100	17.5 mm Steel Washer Plates – 1.65 mm Steel Balls	550	35	122	25.29
169	100	17.5 mm Steel Washer Plates – 1.65 mm Steel Balls	150	55.6	112.5	9.55
170	100	1.65 mm Steel Balls-FRP	120	21	71	14.43
171	100	1.65 mm Steel Balls-FRP	200	17	70	15.65
172	100	1.65 mm Steel Balls-FRP	300	13.5	71	20.85
173	100	1.65 mm Steel Balls-FRP	400	10.3	70	25.01
174	100	1.65 mm Steel Balls-FRP	500	7.5	70	28.56
175	100	1.65 mm Steel Balls	500	33	166	23.39
176	100	1.65 mm Steel Balls	500	24	129	20.76
177	100	1.65 mm Steel Balls	300	43.5	173	23.23
178	100	1.65 mm Steel Balls	400	29	134	22.61
179	100	80 mm Steel Washer Plates – 1.65 mm Steel Balls	100	34	114	10.90
180	100	80 mm Steel Washer Plates – 1.65 mm Steel Balls	200	33.5	143	11.91
181	100	80 mm Steel Washer Plates – 1.65 mm Steel Balls	300	24	120	15.80

Table A.1 (Continued)

Test No:	d (mm)	Fill Material	P_{ver} (kN)	d_{max} (mm)	F_{max} (kN)	$\beta_{eq}\%$
182	100	80 mm Steel Washer Plates – 1.65 mm Steel Balls	400	25	104	15.52
183	100	80 mm Steel Washer Plates - 1.65 mm Steel Balls	500	23.5	149	20.91
184	100	1.65 mm Steel Balls-FRP	0	55	135	12.78
185	100	1.65 mm Steel Balls-FRP	100	55	142	19.39
186	100	1.65 mm Steel Balls-FRP	200	45	132	22.12
187	100	1.65 mm Steel Balls-FRP	300	54.5	159	24.91
188	100	1.65 mm Steel Balls-FRP	400	44.5	146	26.46
189	100	1.65 mm Steel Balls-FRP	500	34.5	136	24.82
190	100	4 Steel Washer Plates-1.65 mm Steel Balls	0	55	118	6.42
191	100	4 Steel Washer Plates-1.65 mm Steels Balls	100	64.5	150	14.06
192	100	4 Steel Washer Plates-1.65 mm Steel Balls	200	64.5	146	13.84
193	100	4 Steel Washer Plates-1.65 mm Steel Balls	300	55	134	19.89
194	100	4 Steel Washer Plates-1.65 mm Steel Balls	400	54.5	138	22.41
195	100	4 Steel Washer Plates-1.65 mm Steel Balls	500	54	150	23.82
196	100	4 Steel Washer Plates-3 mm Steel Balls	0	55	120.5	6.34
197	100	4 Steel Washer Plates-3 mm Steel Balls	100	69	168	13.75

Table A.1 (Continued)

Test No:	d (mm)	Fill Material	P _{ver} (kN)	d _{max} (mm)	F _{max} (kN)	β _{eq} %
198	100	4 Steel Washer Plates-3 mm Steel Balls	200	54.5	135	17.15
199	100	4 Steel Washer Plates-3 mm Steel Balls	300	54.5	141	18.51
200	100	4 Steel Washer Plates-3 mm Steel Balls	400	44.5	128	21.76
201	100	4 Steel Washer Plates-3 mm Steel Balls	500	44.5	140	25.74
202	100	4 Steel Washer Plates-3 mm Steel Balls	200	16	52.5	10.95
203	100	4 Steel Washer Plates-3 mm Steel Balls	400	16	89	15.77
204	100	1.65 mm Steel Balls	200	15.8	65.5	12.21
205	100	1.65 mm Steel Balls	300	15.5	78	14.16
206	100	1.65 mm Steel Balls	400	15	94.5	17.31
207	120	1.65 mm Steel Balls	300	44.3	149	15.85
208	120	1.65 mm Steel Balls	400	44	150.5	16.38
209	120	1.65 mm Steel Balls	500	43.5	159	16.37
210	120	1.65 mm Steel Balls	200	45	123	12.94

Table A.2. Test Results-2

Test No:	d (mm)	Fill Material	K_{eff} (kN/m)	Q_d (kN)	d_y (mm)	Actual Test Velocity (mm/s)
1	100	Sand (%50)- Gravel(%50)	1724	27.25	4.70	16
2	100	Empty	1480	17	0.50	16
3	100	Sand(%50)- Gravel(%50)	1600	17.50	4.50	21
4	150	Empty	1360	12.30	0.50	21
5	150	Rub. Sheets(%33)- Gravel(%67)	1333	14	2.00	-
6	100	Gravel(%67)- Barite (%33)	1959	22	2.20	19
7	100	Gravel(%67)- Barite (%33)	1838	20.66	1.50	-
8	100	1.65 mm Steel Balls	2841	40	1.00	18
9	100	1.65 mm Steel Balls	2870	50	3.30	17
10	100	1.65 mm Steel Balls (85%) - Shredded Rubber (15%)	2286	15	2.85	16
11	100	1.65 mm Steel Balls (85%) - Shredded Rubber (15%)	2000	18	0.80	18
12	100	1.65 mm Steel Balls (95%) - Shredded Rubber (5%)	2222	19	1.00	18
13	100	1.65 mm Steel Balls (95%) - Shredded Rubber (5%)	2000	21	2.40	20
14	100	1.65 mm Steel Balls	2297	48	4.00	MP
15	60	Empty	1447	14.50	N/A	21
16	60	1.65 mm Steel Balls	1758	21	3.00	17
17	60	1.65 mm Steel Balls	1600	27	4.50	46
18	60	1.65 mm Steel Balls	1477	23	5.00	23
19	60	1.65 mm Steel Balls	1515	23	3.00	41
20	60	3 mm Steel Balls	1733	16	2.00	48
21	60	3 mm Steel Balls	1447	22	2.80	49
22	60	3 mm Steel Balls	1405	5.0	1.40	52
23	60	5 mm Steel Balls	1761	16.50	2.10	49
24	60	5 mm Steel Balls	1533	22.50	3.50	49
25	60	5 mm Steel Balls	1444	7.5	2.20	50
26	100	3 mm Steel Balls	2889	40	4.50	42
27	100	3 mm Steel Balls	2267	52	4.00	37
28	100	3 mm Steel Balls	2167	7.50	N/A	48
29	100	5 mm Steel Balls	2756	28	1.50	44
30	100	5 mm Steel Balls	2344	39	2.50	42

Table A.2 (Continued)

Test No:	d (mm)	Fill Material	K_{eff} (kN/m)	Q_d (kN)	d_y (mm)	Actual Test Velocity (mm/s)
31	100	5 mm Steel Balls	2139	6.50	2.20	49
32	100	5 mm Steel Balls	2956	38	2.60	43
33	100	5 mm Steel Balls	2727	46	2.00	42
34	150	1.65 mm Steel Balls	-	-	0.70	-
35	150	1.65 mm Steel Balls	3055	18	1.80	47
36	150	1.65 mm Steel Balls	2565	37	N/A	43
37	150	1.65 mm Steel Balls	3623	33	4.50	42
38	150	1.65 mm Steel Balls	1806	5.0	N/A	51
39	150	3 mm Steel Balls	5212	59	3.80	6
40	150	3 mm Steel Balls	-	-	1.70	-
41	150	3 mm Steel Balls	3333	20	2.50	43
42	150	3 mm Steel Balls	-	-	3.00	-
43	150	3 mm Steel Balls	3141	55	3.20	40
44	150	3 mm Steel Balls	1750	5.0	N/A	50
45	150	3 mm Steel Balls	6667	43	0.60	34
46	150	3 mm Steel Balls	6000	33	0.30	15
47	150	3 mm Steel Balls	5783	27.50	0.15	37
48	150	3 mm Steel Balls	5277	25.50	1.60	41
49	100	3 mm Steel Balls	3120	15	1.80	44
50	100	3 mm Steel Balls	2685	34	2.00	43
51	150	1.65 mm Steel Balls	2400	10	2.10	20
52	150	1.65 mm Steel Balls	3280	14	1.00	45
53	150	1.65 mm Steel Balls	2507	64	N/A	36
54	150	1.65 mm Steel Balls	3480	16	2.20	45
55	150	1.65 mm Steel Balls	2803	64	N/A	40
56	100	1.65 mm Steel Balls	3294	20	4.40	45
57	100	1.65 mm Steel Balls	2630	43	3.20	43
58	60	3 mm Steel Balls	1672	19.50	3.80	48
59	60	3 mm Steel Balls	1600	19.50	2.60	48
60	60	3 mm Steel Balls	1541	23	3.80	48
61	60	1.65 mm Steel Balls	1600	23	3.20	48
62	60	1.65 mm Steel Balls	1548	26	2.90	47
63	60	5 mm Steel Balls	1573	23	6.50	48
64	60	5 mm Steel Balls	1478	22.80	3.10	48
65	150	Empty	1806	10	4.10	47
66	150	Empty	1615	11	2.70	48
67	150	Empty	1639	15	5.60	48
68	150	Empty	1577	15.50	2.90	48
69	150	5 mm Steel Balls	2160	8.50	1.20	20
70	150	5 mm Steel Balls	2102	13.50	2.50	19
71	150	5 mm Steel Balls	2353	13.50	2.10	20
72	150	5 mm Steel Balls	2803	32	1.95	19

Table A.2 (Continued)

Test No:	d (mm)	Fill Material	K_{eff} (kN/m)	Q_d (kN)	d_y (mm)	Actual Test Velocity (mm/s)
73	150	5 mm Steel Balls	3241	15	2.00	19
74	150	3 mm Steel Balls	3823	24	0.90	41
75	150	3 mm Steel Balls	3402	50	2.40	27
76	60	Empty	1441	8.90	5.00	50
77	60	Empty	1478	10.84	5.40	50
78	60	Empty	1357	15	4.80	50
79	100	Empty	2000	10.62	2.60	49
80	100	Empty	2019	17.50	8.28	49
81	100	Empty	1827	19.30	5.10	47
82	100	1.65 mm Steel Balls	2500	13	2.00	45
83	100	1.65 mm Steel Balls	2449	10.50	1.70	50
84	60	1.65 mm Steel Balls	1576	9.50	5.20	53
85	60	1.65 mm Steel Balls	1477	8.85	2.00	22
86	60	1.65 mm Steel Balls	1506	22.50	6.25	48
87	120	Empty	1835	11.50	2.95	47
88	120	Empty	1730	11.50	1.50	47
89	120	Empty	1743	15	2.40	48
90	120	Empty	1730	17.25	3.70	47
91	120	Empty	1691	13.63	2.40	49
92	120	Empty	1698	17.01	4.00	41
93	120	1.65 mm Steel Balls	1876	11.30	4.00	49
94	120	1.65 mm Steel Balls	1912	13.12	3.80	43
95	120	1.65 mm Steel Balls	3029	22.15	1.30	44
96	120	1.65 mm Steel Balls	2759	38.10	2.20	18
97	120	1.65 mm Steel Balls	2886	25.00	1.30	44
98	120	1.65 mm Steel Balls	2685	39.00	2.85	42
99	120	1.65 mm Steel Balls	3629	34.50	4.40	18
100	120	1.65 mm Steel Balls	3111	57.25	2.30	14
101	80	1.65 mm Steel Balls	2318	16.40	3.75	18
102	80	1.65 mm Steel Balls	2205	15.75	1.60	46
103	80	1.65 mm Steel Balls	3433	37.00	3.45	45
104	80	1.65 mm Steel Balls	2932	47.50	3.30	42
105	80	1.65 mm Steel Balls	2722	52.00	1.50	42
106	80	1.65 mm Steel Balls	3072	41.00	1.70	36
107	80	1.65 mm Steel Balls	2648	52.50	2.05	42
108	80	Empty	1826	9.61	2.10	31
109	80	Empty	1851	8.10	10.10	49
110	80	Empty	1818	9.25	2.07	30
111	80	Empty	1849	8.25	2.85	53
112	120	1.65 mm Steel Balls	2222	9.75	2.97	48
113	120	1.65 mm Steel Balls	2847	17.50	1.65	46
114	120	1.65 mm Steel Balls	3366	23.00	1.52	44

Table A.2 (Continued)

Test No:	d (mm)	Fill Material	K_{eff} (kN/m)	Q_d (kN)	d_y (mm)	Actual Test Velocity (mm/s)
115	80	Lead Core	4397	28.50	1.50	21
116	80	Lead Core	4026	24.50	3.95	39
117	80	Lead Core	4171	31	1.47	43
118	80	Lead Core	4042	25	2.67	40
119	80	Lead Core	3079	10.50	1.40	45
120	100	1.65 mm Steel Balls	2219	54.5	6.40	MP
121	100	1.65 mm Steel Balls	2183	62	9.70	MP
122	100	1.65 mm Steel Balls	2240	48.60	5.50	42
123	100	1.65 mm Steel Balls	2225	34.00	5.90	44
124	120	1.65 mm Steel Balls	2722	35.5	1.65	42
125	120	1.65 mm Steel Balls	3028	46	1.97	39
126	120	1.65 mm Steel Balls	2643	59	3.80	MP
127	80	1.65 mm Steel Balls	2273	27.50	2.80	44
128	80	1.65 mm Steel Balls	2400	32.50	2.40	44
129	80	1.65 mm Steel Balls	2757	27	1.25	45
130	80	1.65 mm Steel Balls	2385	37	3.10	44
131	80	1.65 mm Steel Balls	2259	42	1.58	42
132	80	1.65 mm Steel Balls	2704	28.50	1.65	46
133	80	1.65 mm Steel Balls	2282	38	2.70	45
134	80	1.65 mm Steel Balls	2886	37.5	0.79	45
135	80	1.65 mm Steel Balls	2400	48	2.37	44
136	80	Empty	1757	11	5.44	50
137	80	Empty	1655	11.50	5.00	51
138	80	Empty	1593	12	4.00	51
139	80	1.65 mm Steel Balls	3000	30.50	1.80	44
140	80	1.65 mm Steel Balls	2400	35.50	2.44	44
141	80	1.65 mm Steel Balls	2771	28	1.40	45
142	80	1.65 mm Steel Balls	2477	40	2.70	71
143	80	1.65 mm Steel Balls	3028	35	1.80	71
144	80	1.65 mm Steel Balls	2636	48	3.30	68
145	80	1.65 mm Steel Balls	2036	20	2.86	75
146	80	1.65 mm Steel Balls	2090	25	2.73	74
147	80	1.65 mm Steel Balls	2144	30	2.61	74
148	100	Steel Washer Plate- 5 mm Thick	2169	12.50	1.98	49
149	100	Steel Washer Plate- 5 mm Thick	1804	12.50	2.87	50
150	100	Steel Washer Plate- 5 mm Thick	2347	23.5	1.54	48
151	100	Steel Washer Plate- 5 mm Thick	1979	27.15	1.32	49

Table A.2 (Continued)

Test No:	d (mm)	Fill Material	K_{eff} (kN/m)	Q_d (kN)	d_y (mm)	Actual Test Velocity (mm/s)
152	100	Steel Washer Plate-5 mm Thick	2929	44.50	0.62	44
153	100	Steel Washer Plate-5 mm Thick	3280	72	2.70	39
154	150	1.65 mm Steel Balls	2500	20	1.65	46
155	150	1.65 mm Steel Balls	3204	45	1.30	41
156	150	1.65 mm Steel Balls	4058	44	1.48	45
157	150	1.65 mm Steel Balls	5789	48	0.38	38
158	150	1.65 mm Steel Balls	7234	51.25	0.66	28
159	150	1.65 mm Steel Balls	10157	48	1.07	25
160	150	1.65 mm Steel Balls	4103	28	0.70	47
161	150	1.65 mm Steel Balls	4645	44	1.11	36
162	100	1.65 mm Steel Balls -FRP	3563	11	0.73	13
163	100	17.5 mm Steel Washer Plate - 1.65 mm Steel Balls	2162	20	2.71	47
164	100	17.5 mm Steel Washer Plate - 1.65 mm Steel Balls	2254	23	1.91	46
165	100	17.5 mm Steel Washer Plate - 1.65 mm Steel Balls	2417	26	2.42	46
166	100	17.5 mm Steel Washer Plate - 1.65 mm Steel Balls	2391	26	3.90	46
167	100	17.5 mm Steel Washer Plate - 1.65 mm Steel Balls	2688	33.50	1.37	45
168	100	17.5 mm Steel Washer Plate - 1.65 mm Steel Balls	3486	52.50	2.69	42
169	100	17.5 mm Steel Washer Plate - 1.65 mm Steel Balls	2023	18	3.47	49
170	100	1.65 mm Steel Balls -FRP	3381	16.50	0.52	MP
171	100	1.65 mm Steel Balls -FRP	4118	18	0.75	MP
172	100	1.65 mm Steel Balls -FRP	5259	24	0.42	MP
173	100	1.65 mm Steel Balls-FRP	6796	27.50	N/A	MP

Table A.2 (Continued)

Test No:	d (mm)	Fill Material	K_{eff} (kN/m)	Q_d (kN)	d_y (mm)	Actual Test Velocity (mm/s)
174	100	1.65 mm Steel Balls-FRP	9333	35	0.77	MP
175	100	1.65 mm Steel Balls	5030	71	4.66	MP
176	100	1.65 mm Steel Balls	5375	44	1.05	46
177	100	1.65 mm Steel Balls	3977	64.50	0.93	MP
178	100	1.65 mm Steel Balls	4621	50	1.40	47
179	100	80 mm Steel Washer Plate – 1.65 mm Steel Balls	3353	21	2.40	43
180	100	80 mm Steel Washer Plate – 1.65 mm Steel Balls	4269	28	1.48	39
181	100	80 mm Steel Washer Plate – 1.65 mm Steel Balls	5000	30.50	0.56	49
182	100	80 mm Steel Washer Plate – 1.65 mm Steel Balls	4160	27	1.52	52
183	100	80 mm Steel Washer Plate – 1.65 mm Steel Balls	6340	50	0.50	35
184	100	1.65 mm Steel Balls -FRP	2454	27.50	0.79	45
185	100	1.65 mm Steel Balls -FRP	2582	48	5.45	43
186	100	1.65 mm Steel Balls -FRP	2933	50	3.73	45
187	100	1.65 mm Steel Balls -FRP	2917	68	4.65	40
188	100	1.65 mm Steel Balls -FRP	3281	67	4.20	41
189	100	1.65 mm Steel Balls -FRP	3942	59	3.50	41
190	100	4 Steel Washer Plates-1.65 mm Steel Balls	2145	12.50	2.64	49
191	100	4 Steel Washer Plates-1.65 mm Steel Balls	2326	34	1.63	46
192	100	4 Steel Washer Plates-1.65 mm Steel Balls	2263	34	4.32	47

Table A.2 (Continued)

Test No:	d (mm)	Fill Material	K_{eff} (kN/m)	Q_d (kN)	d_y (mm)	Actual Test Velocity (mm/s)
193	100	4 Steel Washer Plates-1.65 mm Steel Balls	2436	43.50	2.08	46
194	100	4 Steel Washer Plates-1.65 mm Steel Balls	2532	52.50	4.08	45
195	100	4 Steel Washer Plates-1.65 mm Steel Balls	2778	60	3.49	42
196	100	4 Steel Washer Plates-3 mm Steel Balls	2191	12	N/A	49
197	100	4 Steel Washer Plates-3 mm Steel Balls	2435	37.50	2.21	43
198	100	4 Steel Washer Plates-3 mm Steel Balls	2477	38	2.33	46
199	100	4 Steel Washer Plates-3 mm Steel Balls	2587	43	2.53	45
200	100	4 Steel Washer Plates-3 mm Steel Balls	2876	45	1.25	45
201	100	4 Steel Washer Plates-3 mm Steel Balls	3146	58	1.07	43
202	100	4 Steel Washer Plates-3 mm Steel Balls	3281	11	2.87	2
203	100	4 Steel Washer Plates-3 mm Steel Balls	5563	25	1.89	7
204	100	1.65 mm Steel Balls	4146	15.50	2.99	2
205	100	1.65 mm Steel Balls	5032	19.50	1.71	2
206	100	1.65 mm Steel Balls	6300	28.50	1.48	2
207	120	1.65 mm Steel Balls	3363	41	4.22	42
208	120	1.65 mm Steel Balls	3420	41.50	2.94	41
209	120	1.65 mm Steel Balls	3655	45	3.99	40
210	120	1.65 mm Steel Balls	2733	26	1.72	46

*MP: Manuel Push

The values indicated by (+) and (-) signs in Table A.3 are the values at the positive and negative sides of the hysteresis loops. In Table A3, only tests with 1.65 mm steel balls are presented. Averages of these values are utilized in calculations.

Table A.3. Test Results-3

Test No:	Q_d^+ (kN)	Q_d^- (kN)	d_{max}^+ (mm)	d_{max}^- (mm)	F_{max}^+ (kN)	F_{max}^- (kN)
8	55	25	42	46	140	110
9	58	42	55.5	52.5	163	147
14	N/A	N/A	N/A	N/A	N/A	N/A
16	22	20	44	47	80	80
17	40	14	73	77	131	109
18	41	5	63.5	68.5	113	82
19	38	8	64.5	67.5	112	88
34	N/A	N/A	N/A	N/A	N/A	N/A
35	26	10	34	38	120	100
36	48	26	52	56	152	125
37	55	11	33	36	142	108
38	7.5	2.5	35	37	68	62
51	12	8	26	24	66	54
52	14	14	25	25	82	82
53	71	57	55	71	152	164
54	27	5	23	27	89.5	84.5
55	64	64	55	52	154	146
56	22	18	26.5	24.5	87	81
57	45	41	55	53	146.5	136.5
61	13	33	76	74	114	126
62	14	38	85	83	120	140
82	6	20	47	42.6	106	118
83	4	17	46	43	106	112
84	8	11	46	46	71	74
85	4.2	13.5	47.2	44.2	66.5	68.5
86	18	27	86	84	126	130
93	10.6	12	45	45	83	85.8
94	8.22	18.02	76	71	137	144
95	18.9	25.4	35	35	101	111
96	34.2	42	54.5	53.5	140	158
97	-4	54	38	32	77	125
98	33	45	55	53	136	154
99	27.5	41.5	37	33	121	133
100	56	58.5	53	55	156	180
101	17.8	15	44	44	103	101

Table A.3 (Continued)

Test No:	Q_d^+ (kN)	Q_d^- (kN)	d_{\max}^+ (mm)	d_{\max}^- (mm)	F_{\max}^+ (kN)	F_{\max}^- (kN)
102	12	19.5	44	44	94	100
103	45	29	28	32	109	97
104	45	50	43	45	127	131
105	54	50	51	57	143	151
106	33	49	35	34	104	108
107	50	55	52	56	136	150
112	4.4	15.1	36	36	80	80
113	12.5	22.5	36	36	105	100
114	12	34	37	34	119	120
120	58	51	79.5	80.5	180	175
121	74	50	82	82	193	165
122	88	9.2	61	68	179	110
123	26	42	65	64	142	145
124	9	62	57	51	134	160
125	18	74	56	51	145	179
126	30	88	70	70	160	210
127	33	22	53	57	125	125
128	41	24	53	57	137	127
129	49	5	32.5	37.5	112	81
130	51	23	52	57	140	120
131	51	33	67	72	164	150
132	45	12	33	38	106.5	85.5
133	55	21	52	58	140	111
134	63	12	33	37	120	82
135	65	31	52.5	57.5	145	119
139	35.5	25.5	34	36	109	101
140	54.5	16.5	52	58	146	118
141	46	10	32.5	37.5	111	83
142	57	23	52	57	150	120
143	56	14	32.5	37.5	119	93
144	71	25	51.5	57	165	121
145	21	19	54	57	114	112
146	38	12	53	58	126	106
147	52	8	52.5	58.5	136	102
154	40	0	42	48	132	93
155	60	30	43	47	152	130
156	96	-8	30	38	179	97
157	78	18	25.5	31.5	183	147
158	100	2.5	20	27	202	138
159	42	54	14	14	137.2	147.2
160	36	20	32	36	141	138
161	61	27	31.3	36.3	173	141

Table A.3. (Continued)

Test No:	Q_d^+ (kN)	Q_d^- (kN)	d_{\max}^+ (mm)	d_{\max}^- (mm)	F_{\max}^+ (kN)	F_{\max}^- (kN)
175	90	52	33	33	170	162.5
176	69	19	22	26	146	112
177	77	52	43	44	176	176
178	88	4	26	32	165	96
204	16	15	14.6	17	69	62
205	27.5	11.5	14	17	80	76
206	36	21	13.5	16.5	95	94
207	45	37	42.6	46	146	152
208	66.5	16.5	41	47	171	130
209	62	28	42	45	174	174
210	28	24	44	46	124	122

APPENDIX B

EXPERIMENTAL HYSTERESIS LOOPS

In Appendix B, experimental hysteresis loops are presented for BRBs with 1.65 mm steel balls. Details about tests and test parameters are presented in Appendix A. The hysteresis loops of all 210 reversed cyclic tests are provided in the CD that is attached to the back cover of this thesis. It should be reminded that presented hysteresis loops are that of two simultaneously tested bearings.

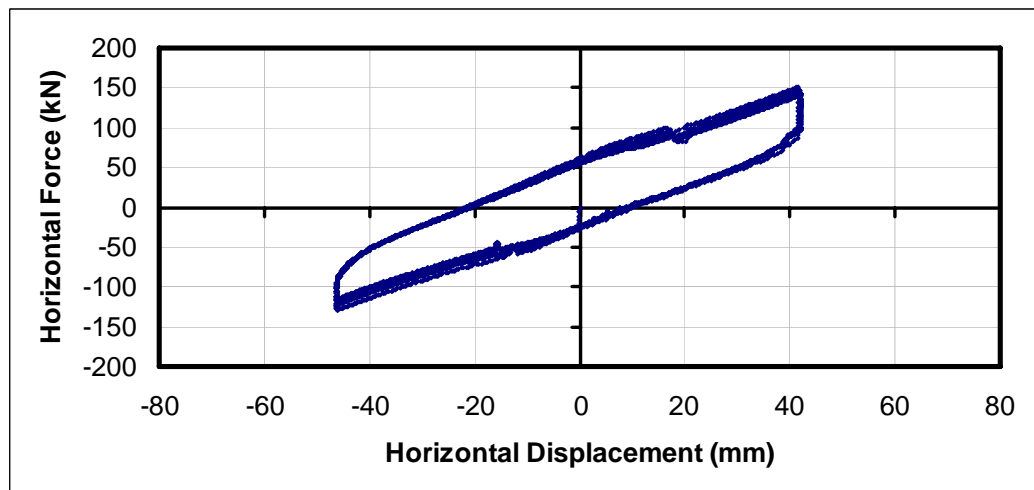


Figure B.1. Hysteresis Loop of Test-8

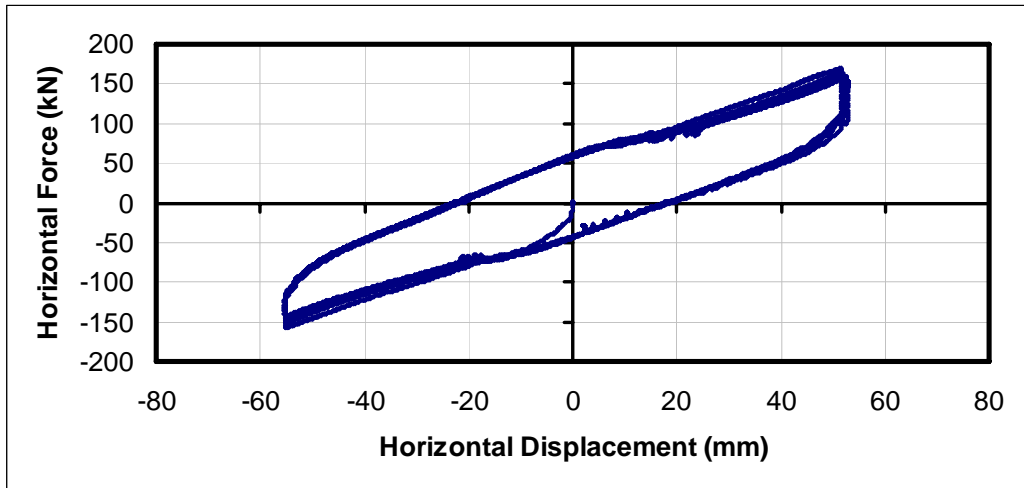


Figure B.2. Hysteresis Loop of Test-9

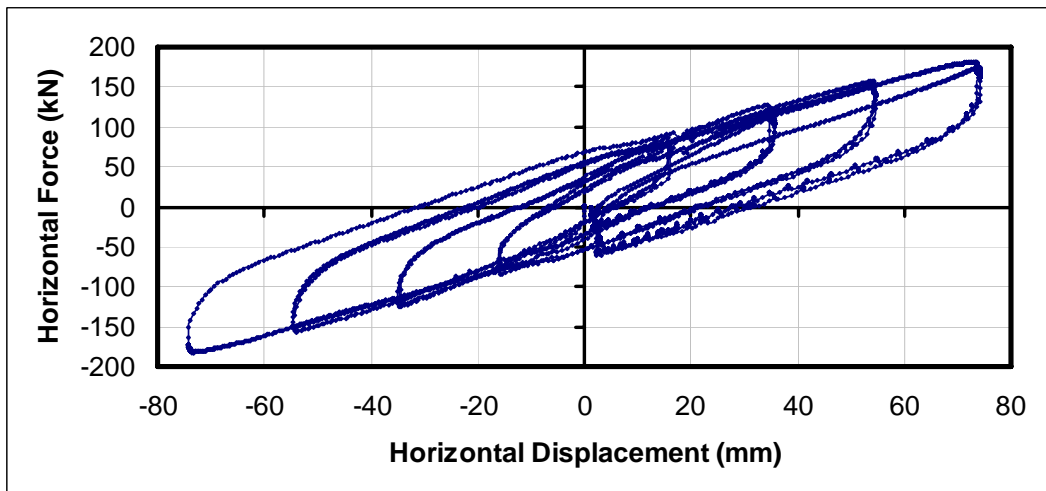


Figure B.3. Hysteresis Loop of Test-14

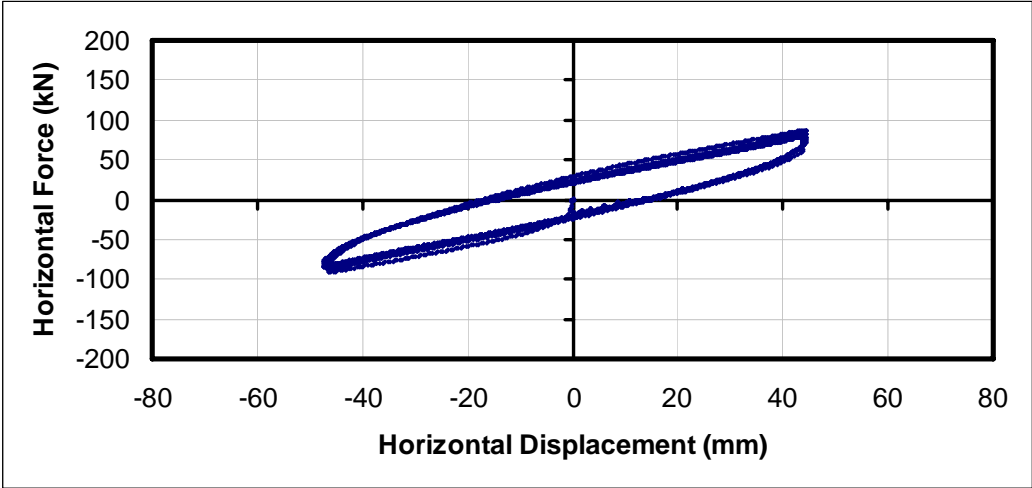


Figure B.4. Hysteresis Loop of Test-16

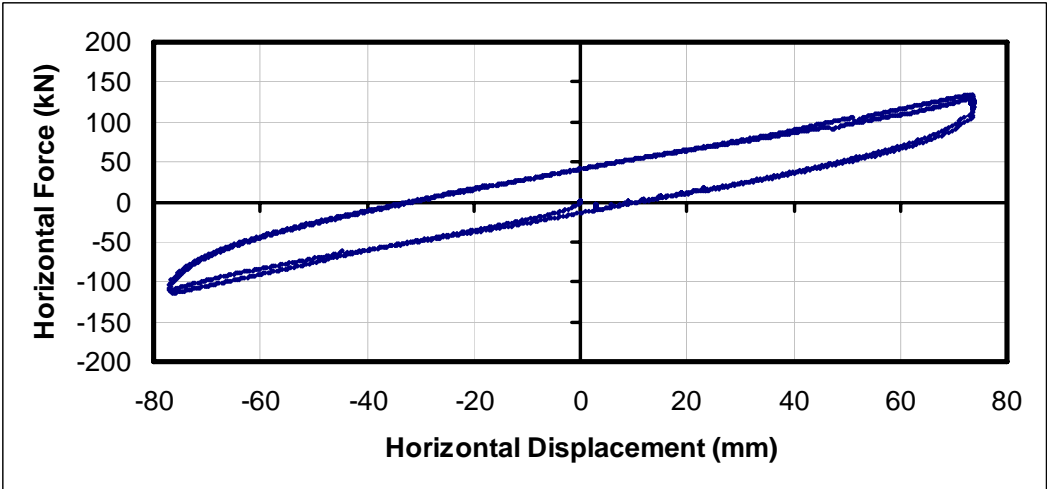


Figure B.5. Hysteresis Loop of Test-17

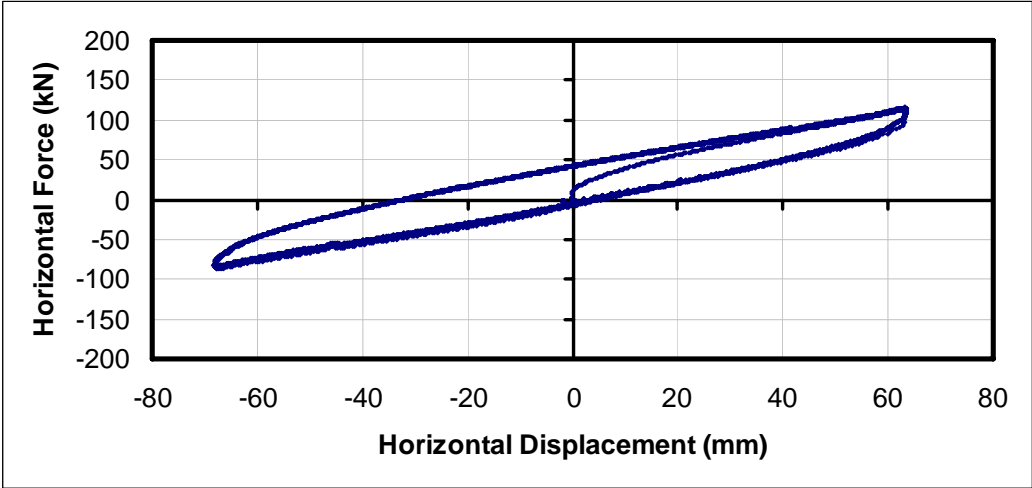


Figure B.6. Hysteresis Loop of Test-18

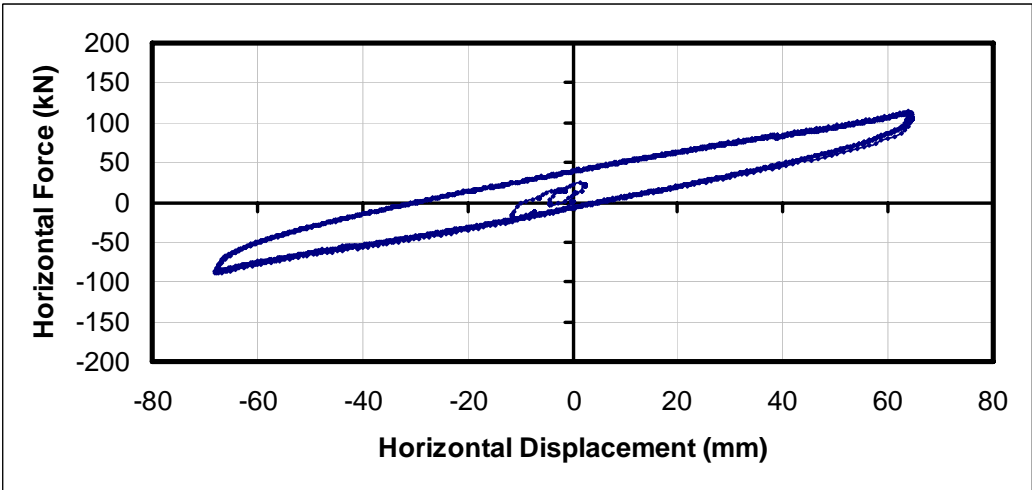


Figure B.7. Hysteresis Loop of Test-19

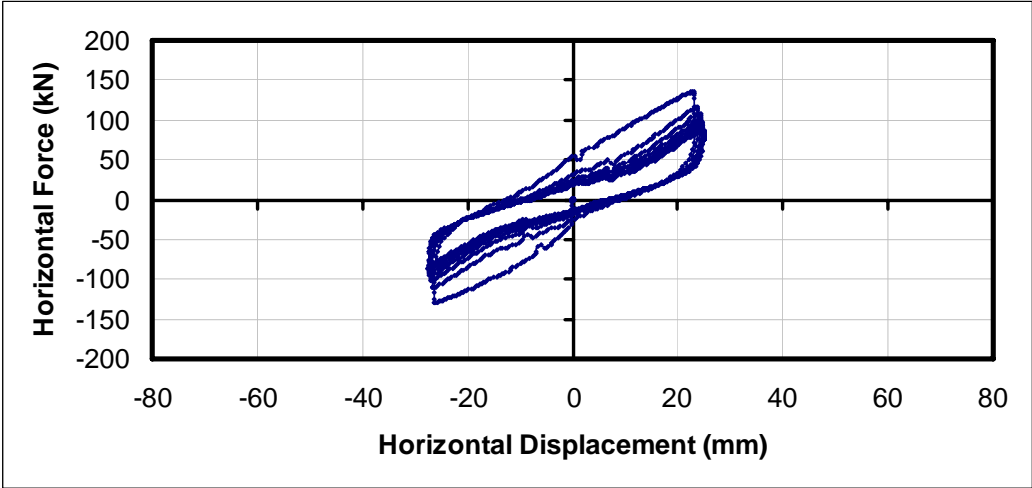


Figure B.8. Hysteresis Loop of Test-34

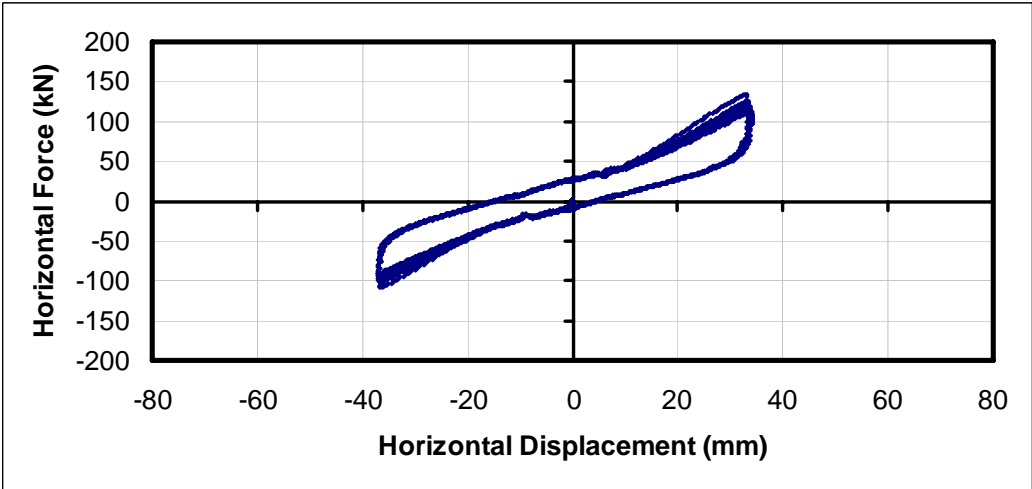


Figure B.9. Hysteresis Loop of Test-35

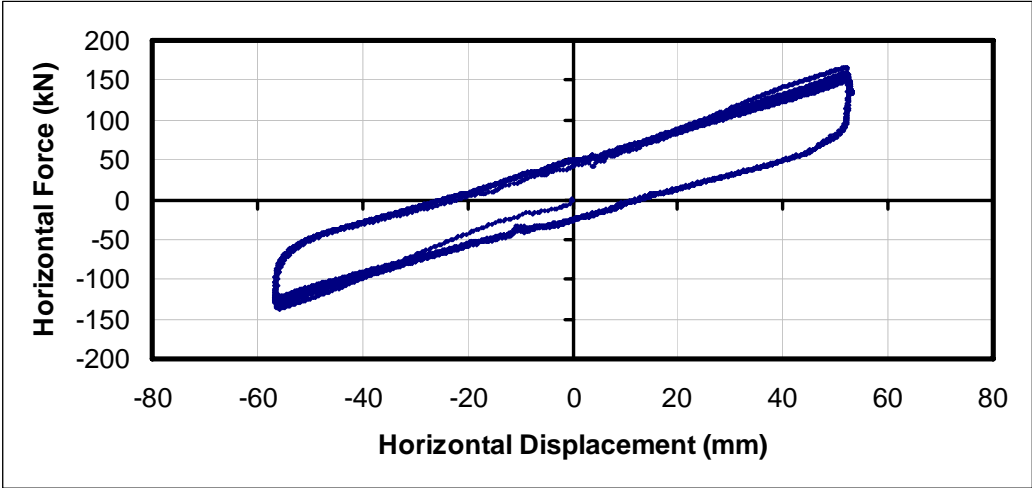


Figure B.10. Hysteresis Loop of Test-36

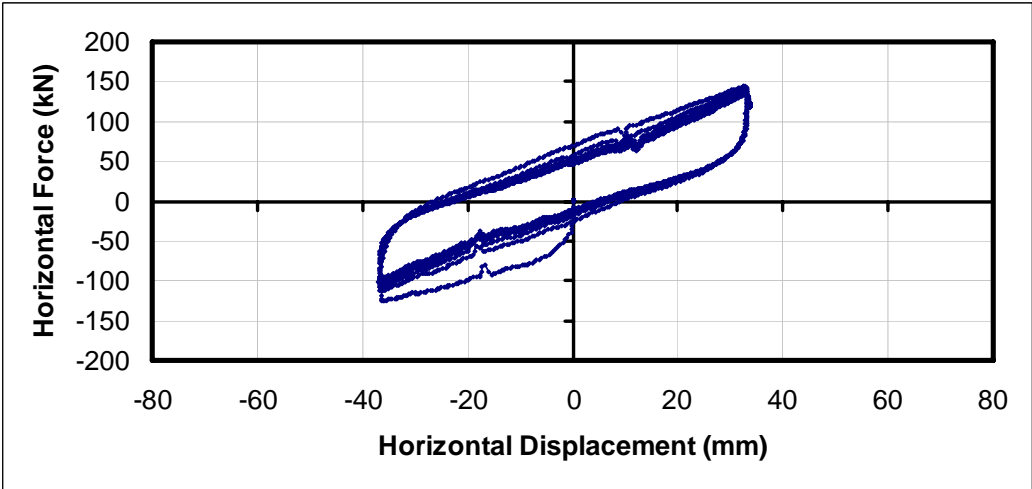


Figure B.11. Hysteresis Loop of Test-37

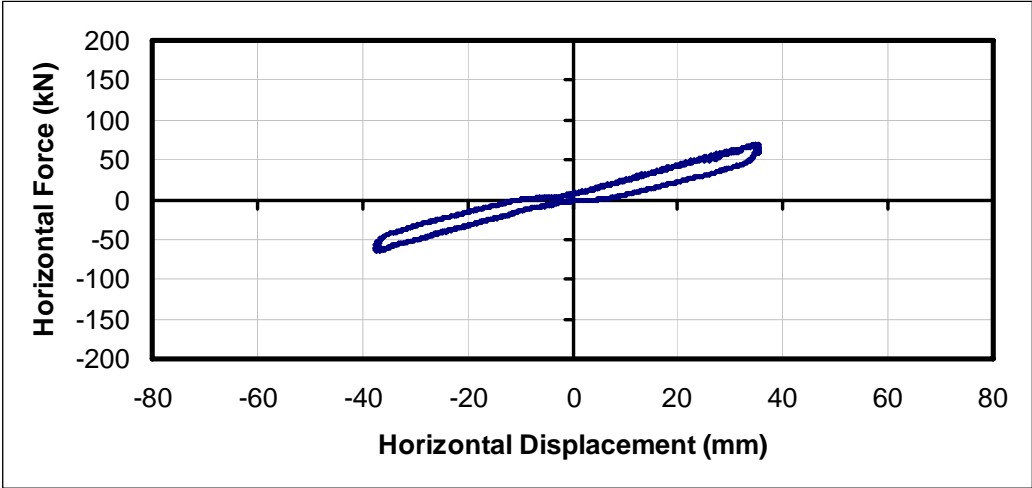


Figure B.12. Hysteresis Loop of Test-38

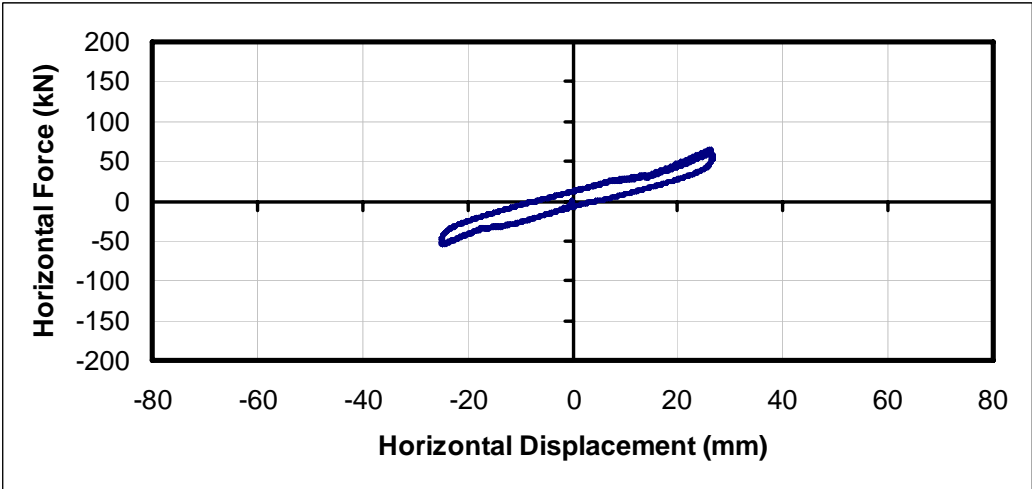


Figure B.13. Hysteresis Loop of Test-51

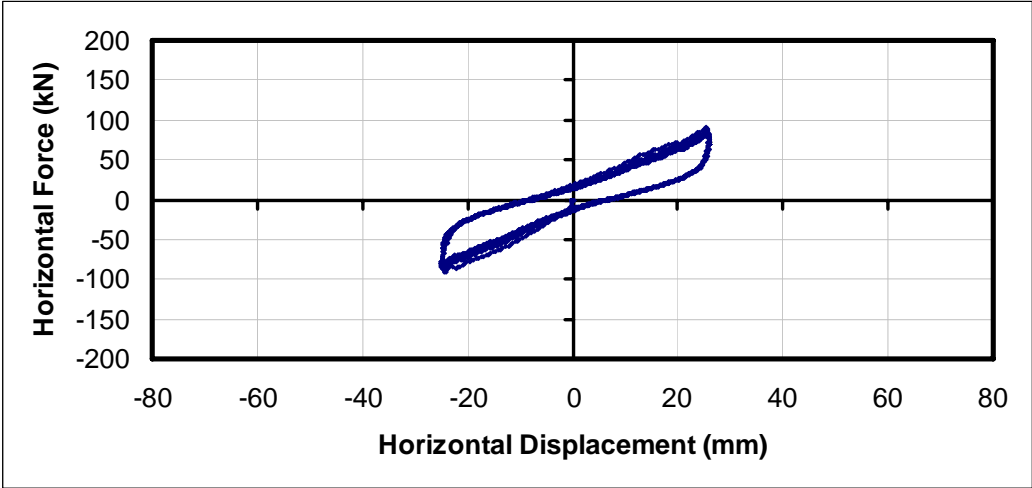


Figure B.14. Hysteresis Loop of Test-52

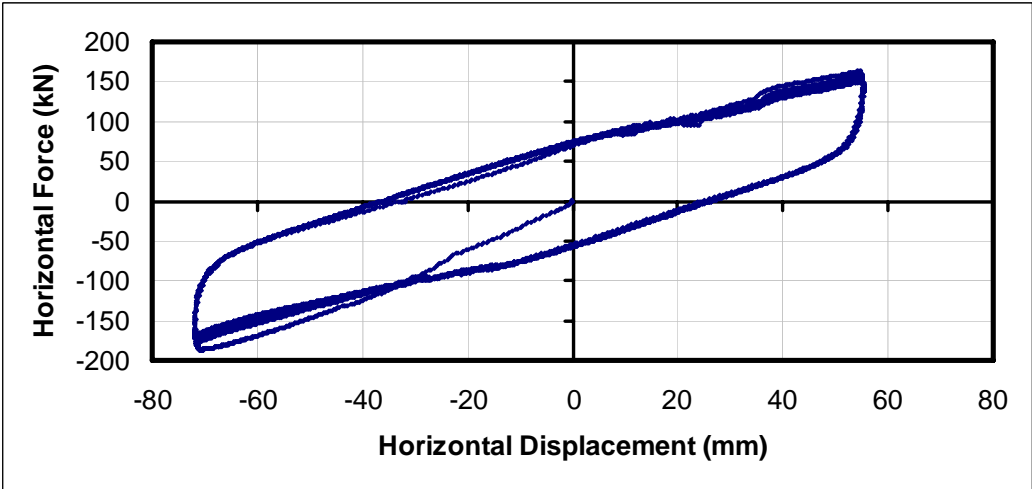


Figure B.15. Hysteresis Loop of Test-53

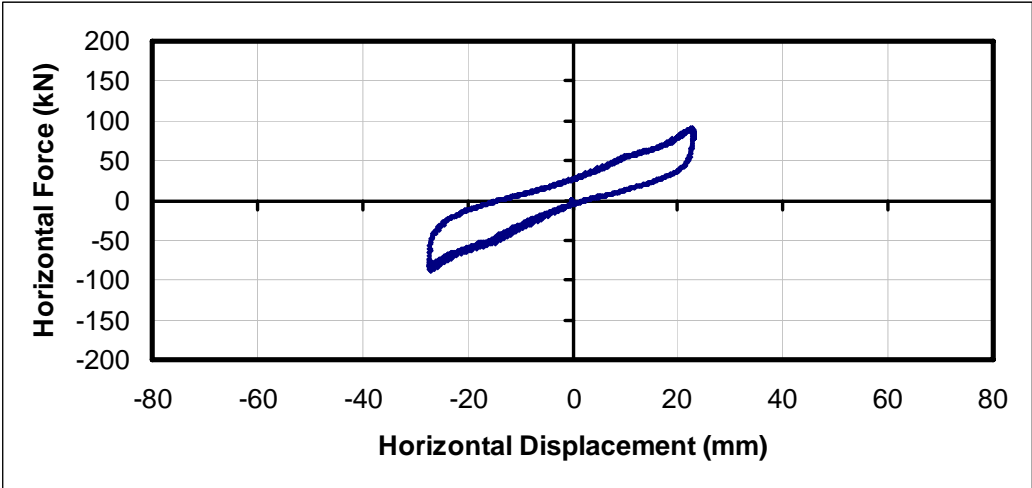


Figure B.16. Hysteresis Loop of Test-54

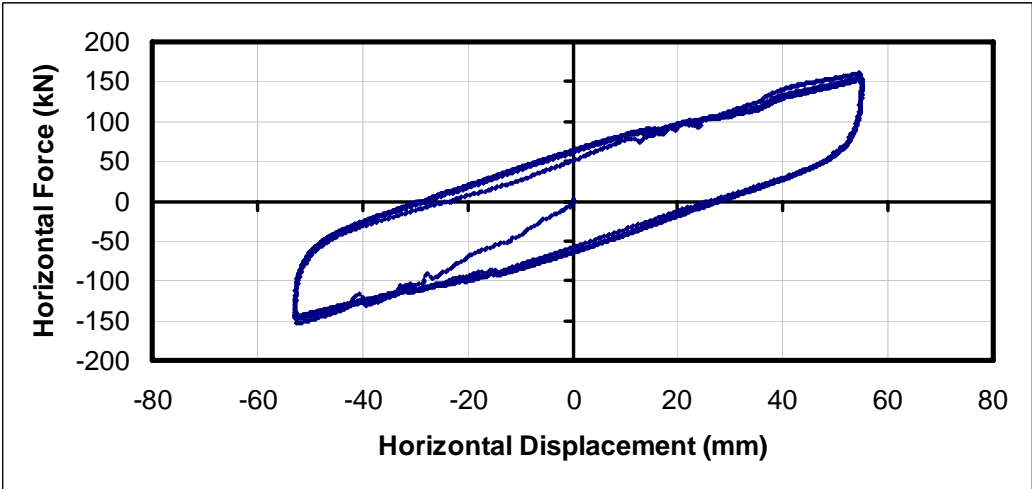


Figure B.17. Hysteresis Loop of Test-55

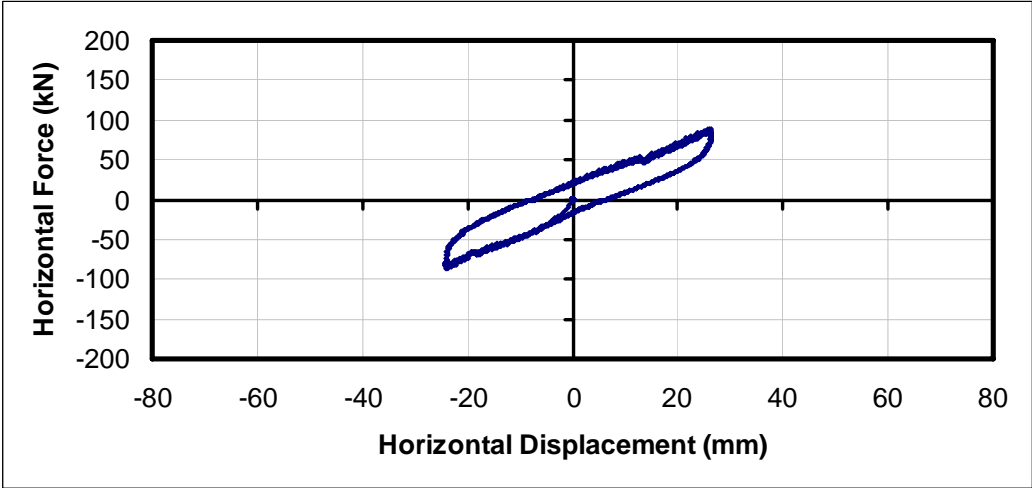


Figure B.18. Hysteresis Loop of Test-56

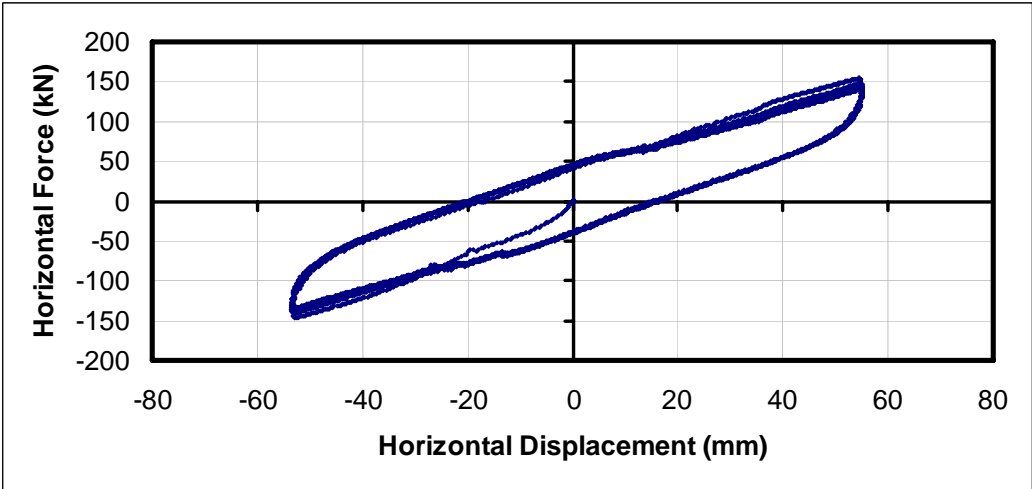


Figure B.19. Hysteresis Loop of Test-57

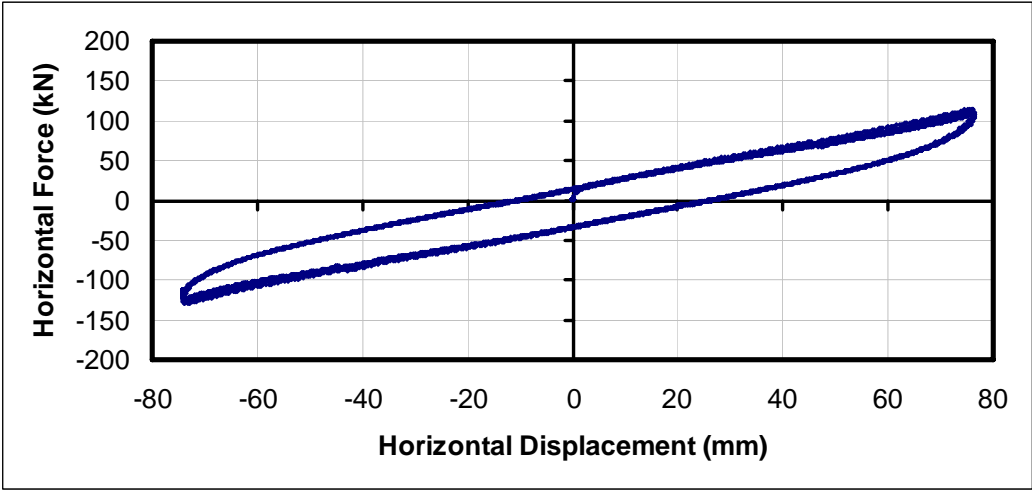


Figure B.20. Hysteresis Loop of Test-61

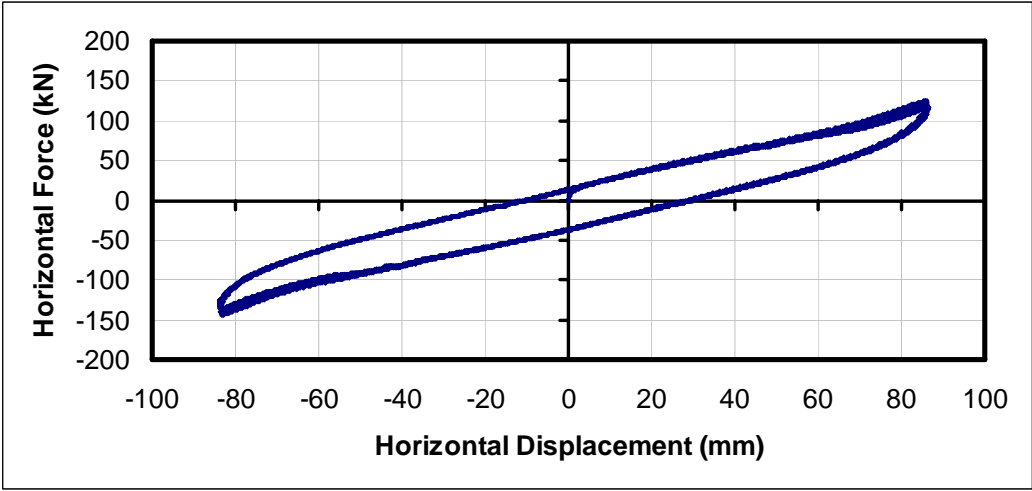


Figure B.21. Hysteresis Loop of Test-62

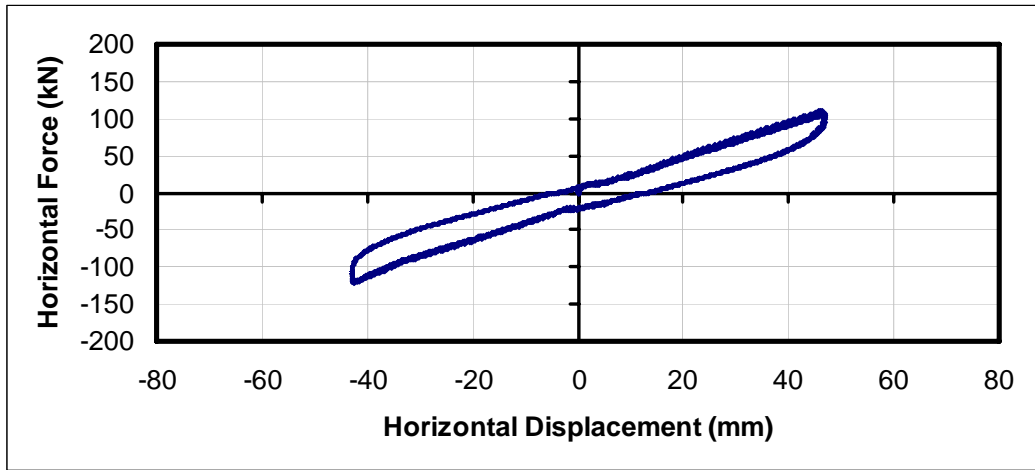


Figure B.22. Hysteresis Loop of Test-82

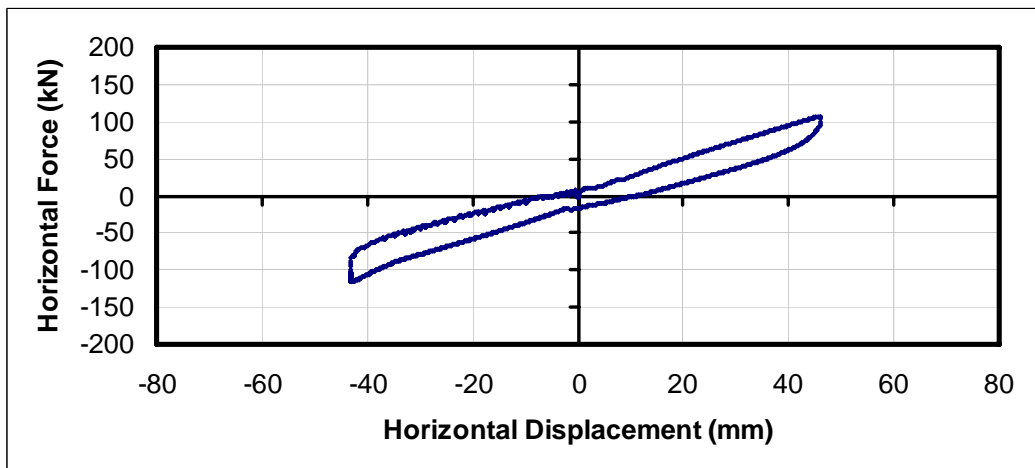


Figure B.23. Hysteresis Loop of Test-83

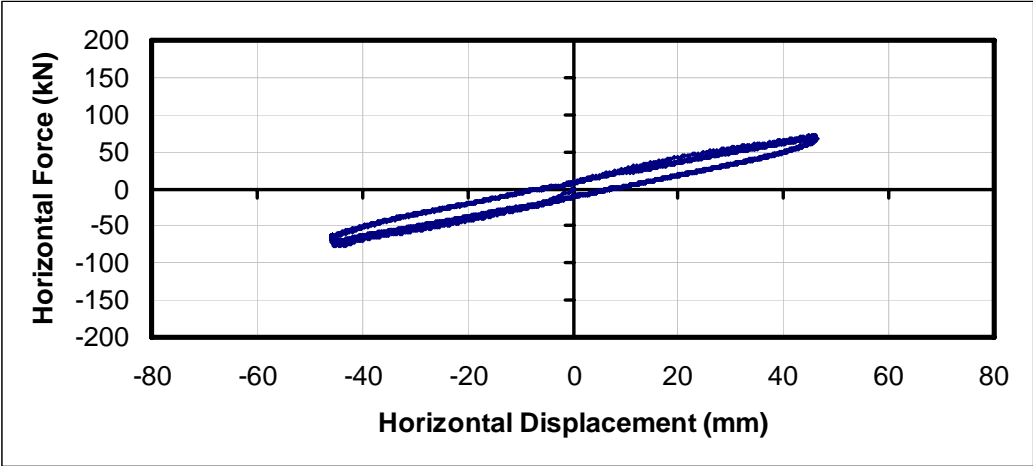


Figure B.24. Hysteresis Loop of Test-84

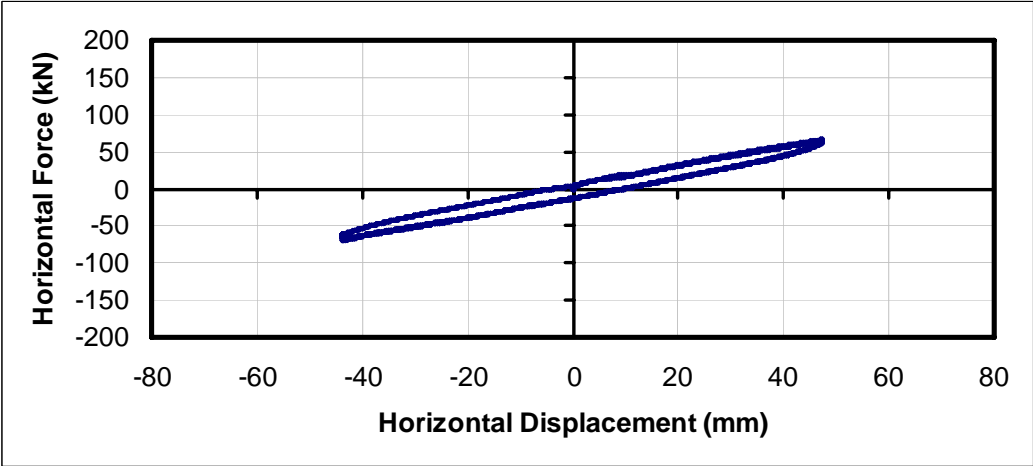


Figure B.25. Hysteresis Loop of Test-85

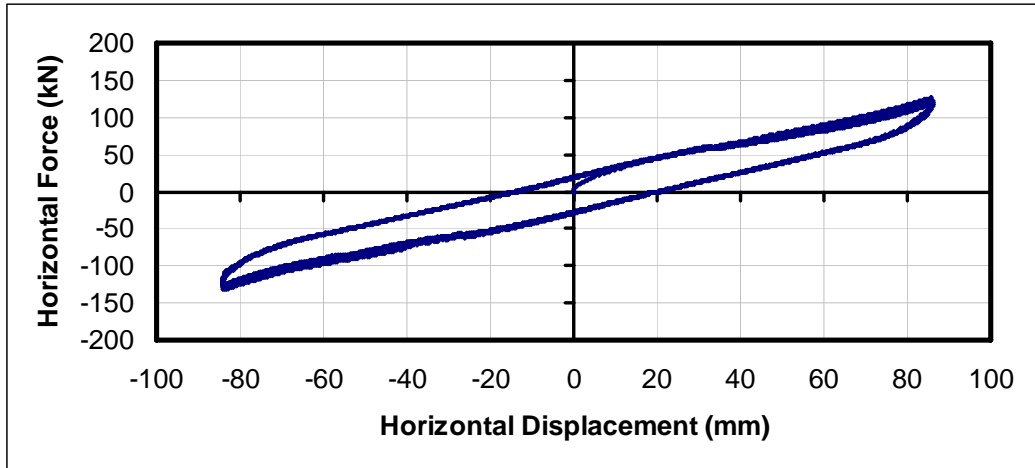


Figure B.26. Hysteresis Loop of Test-86

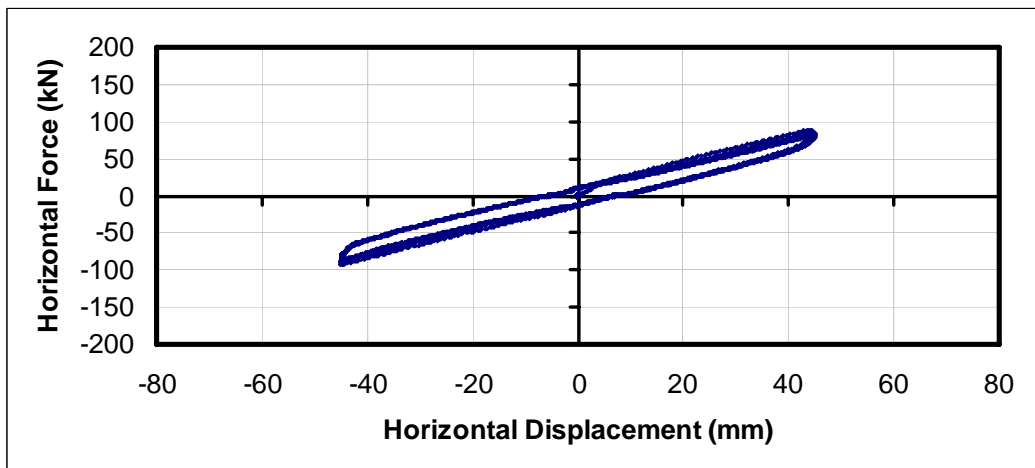


Figure B.27. Hysteresis Loop of Test-93

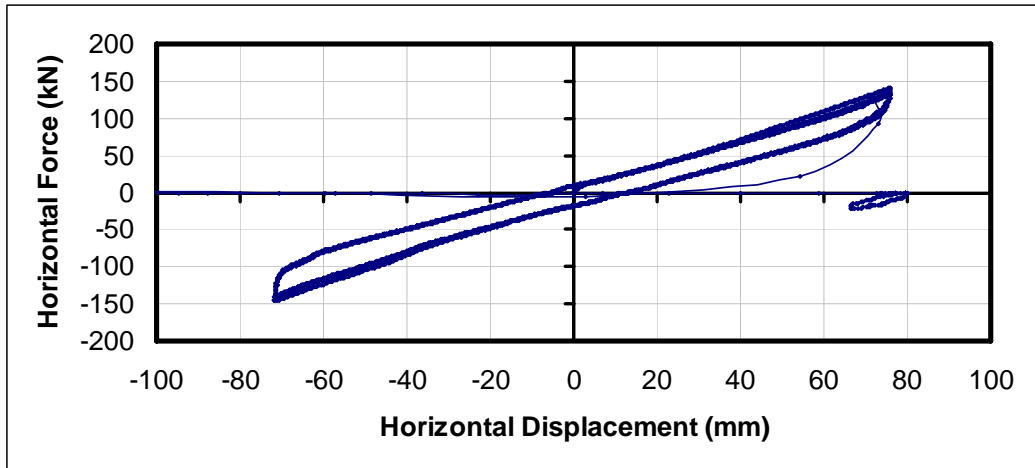


Figure B.28. Hysteresis Loop of Test-94

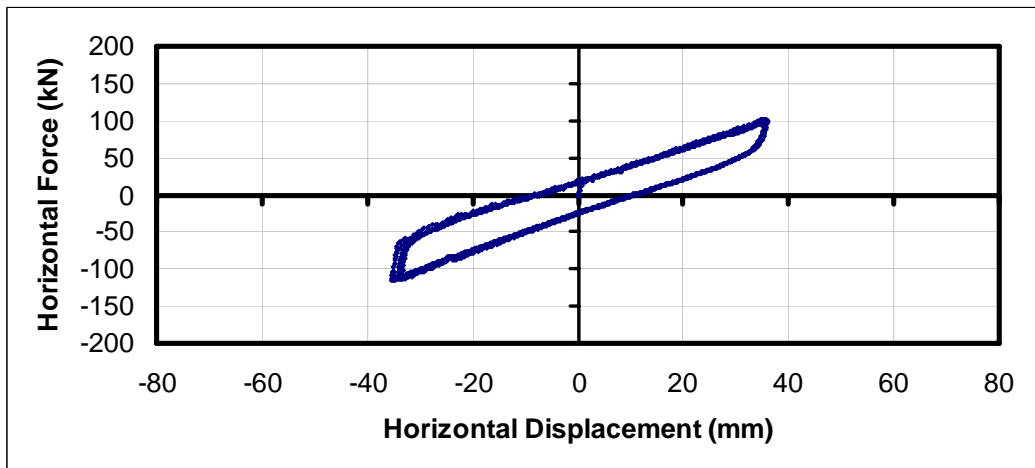


Figure B.29. Hysteresis Loop of Test-95

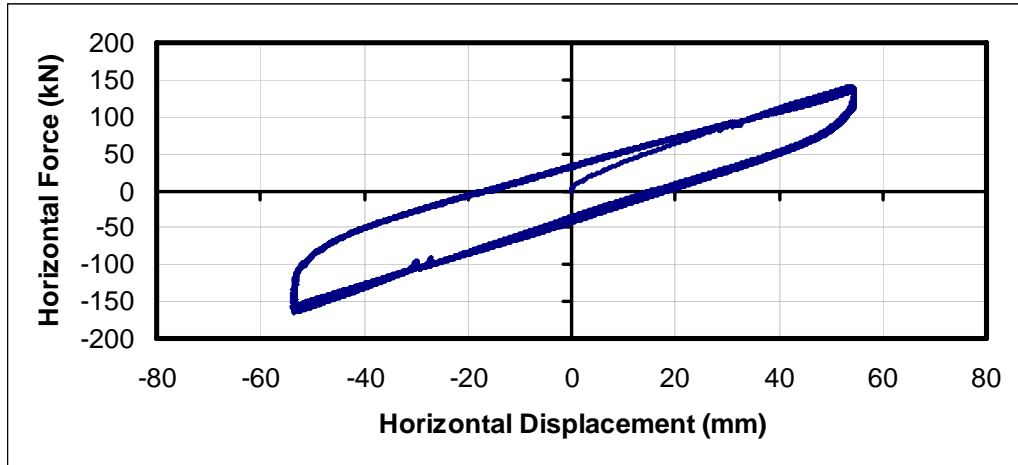


Figure B.30. Hysteresis Loop of Test-96

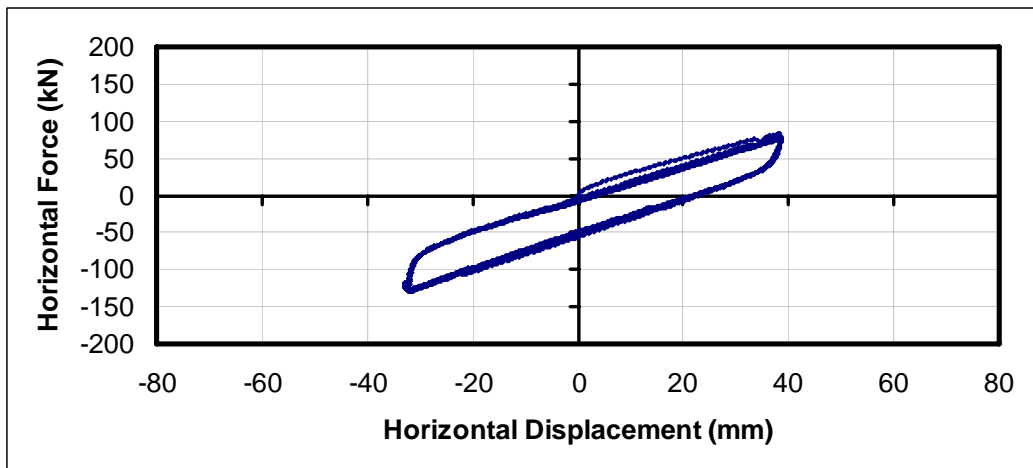


Figure B.31. Hysteresis Loop of Test-97

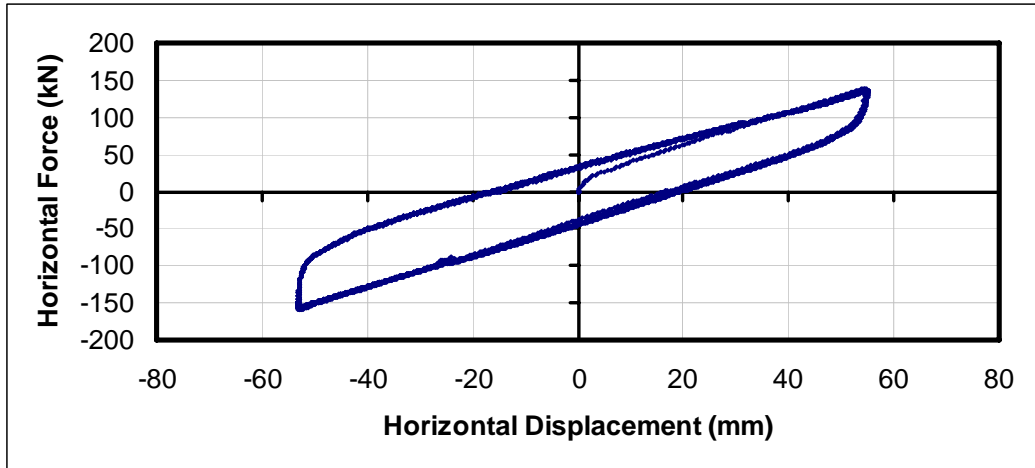


Figure B.32. Hysteresis Loop of Test-98

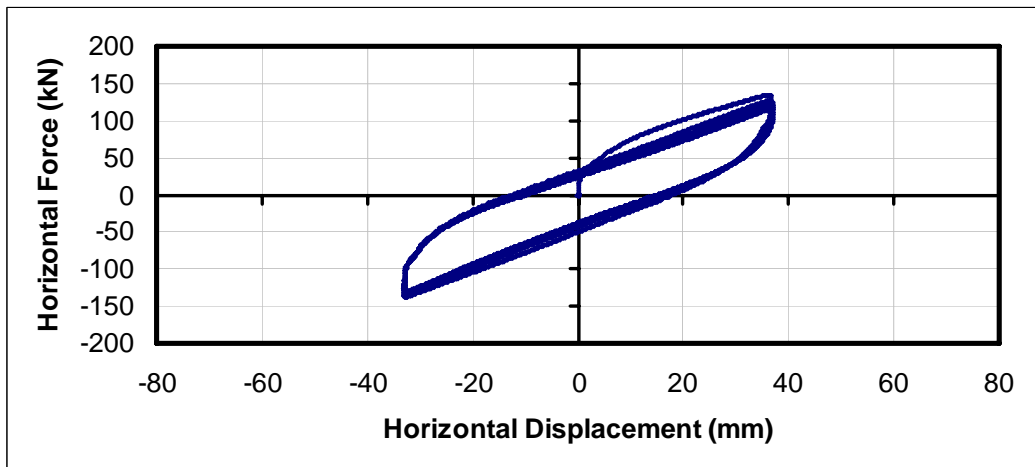


Figure B.33. Hysteresis Loop of Test-99

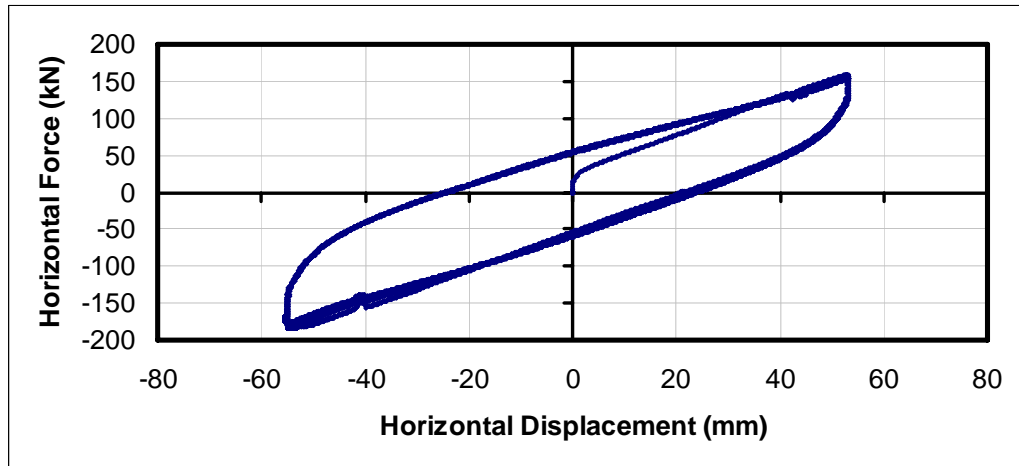


Figure B.34. Hysteresis Loop of Test-100

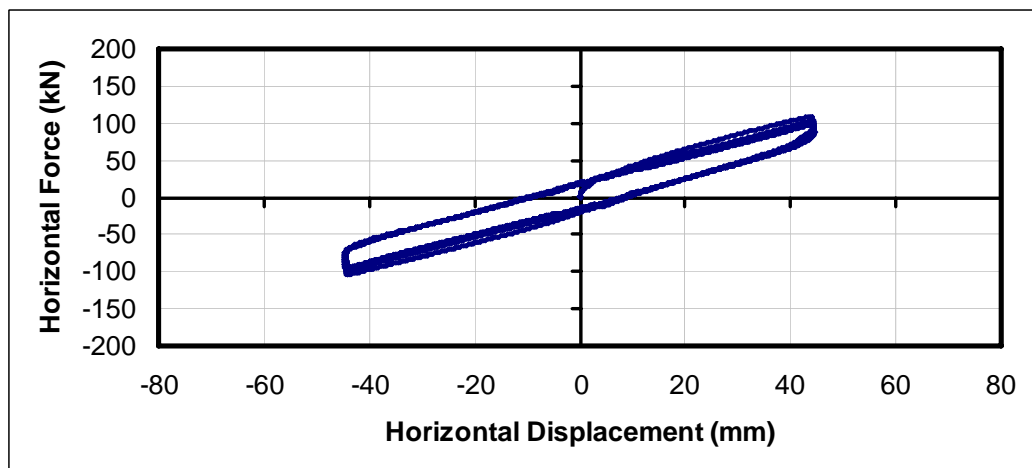


Figure B.35. Hysteresis Loop of Test-101

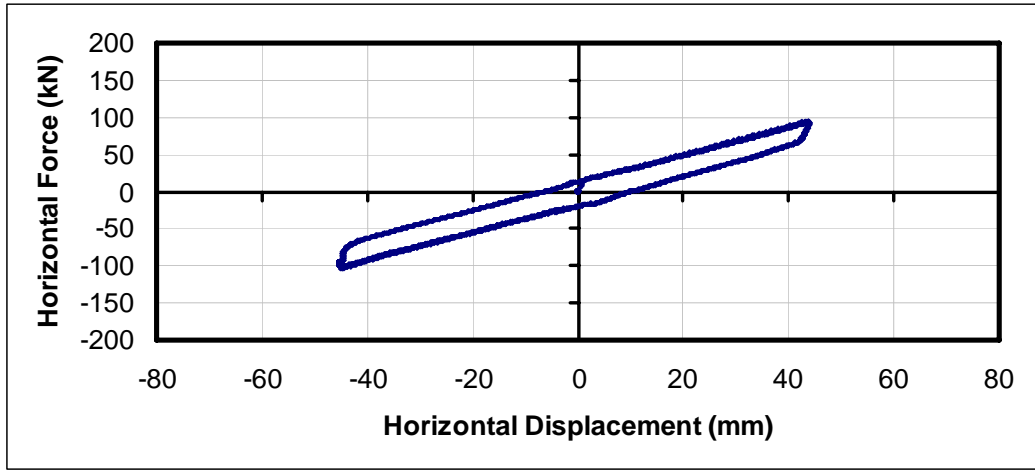


Figure B.36. Hysteresis Loop of Test-102

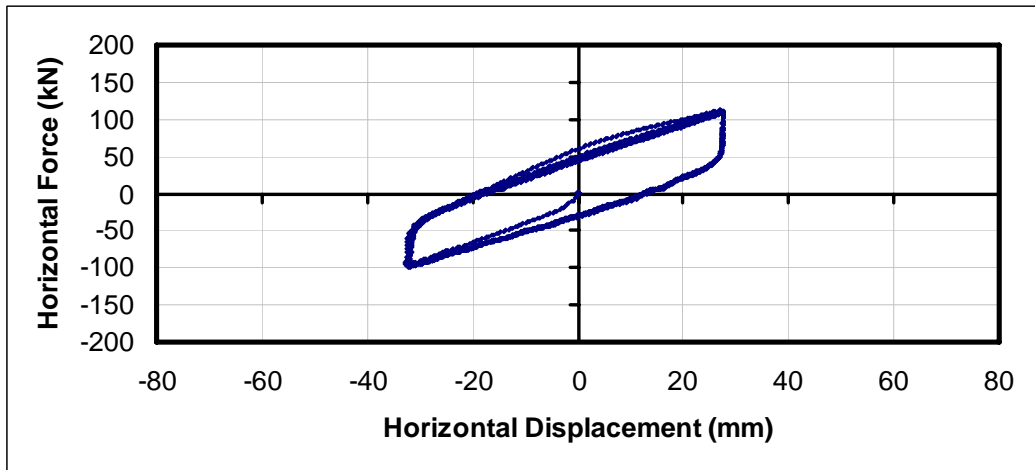


Figure B.37. Hysteresis Loop of Test-103

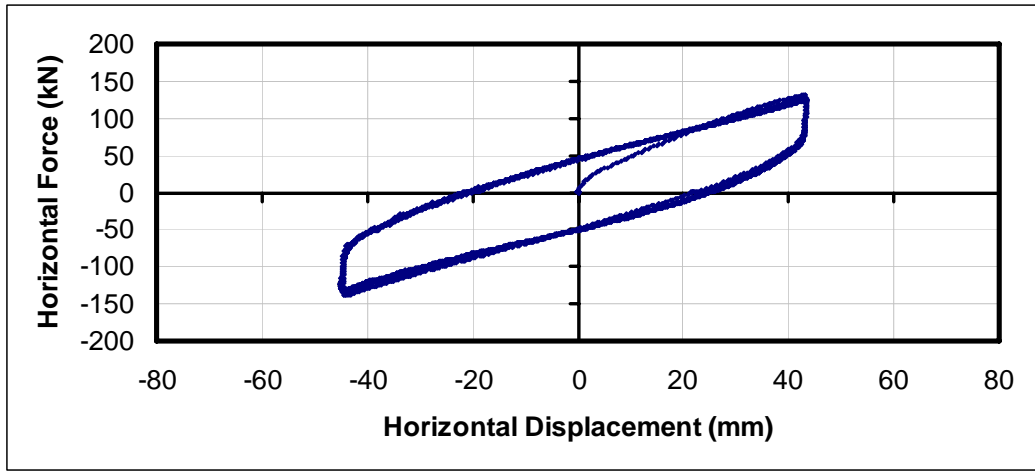


Figure B.38. Hysteresis Loop of Test-104

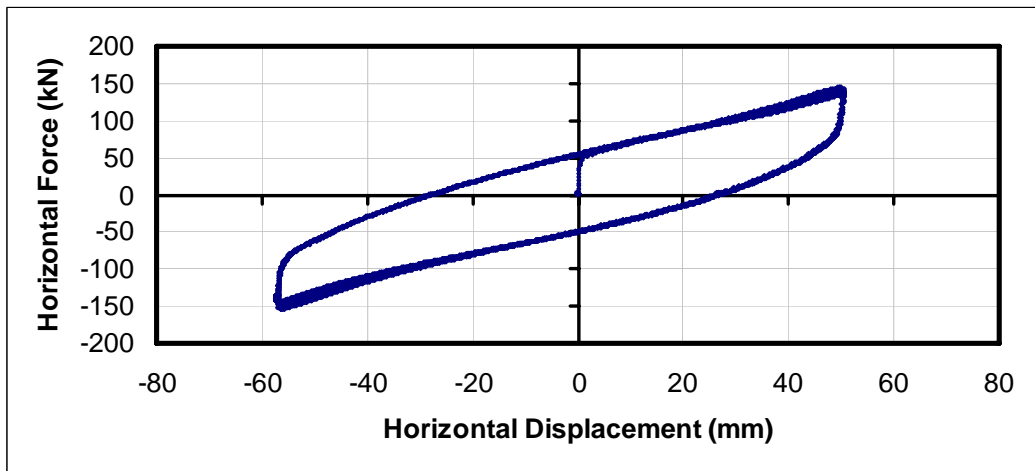


Figure B.39. Hysteresis Loop of Test-105

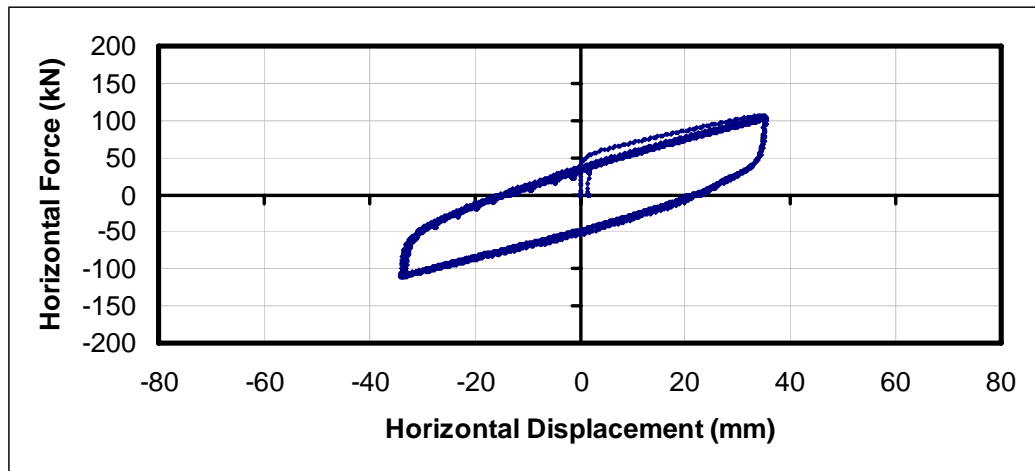


Figure B.40. Hysteresis Loop of Test-106

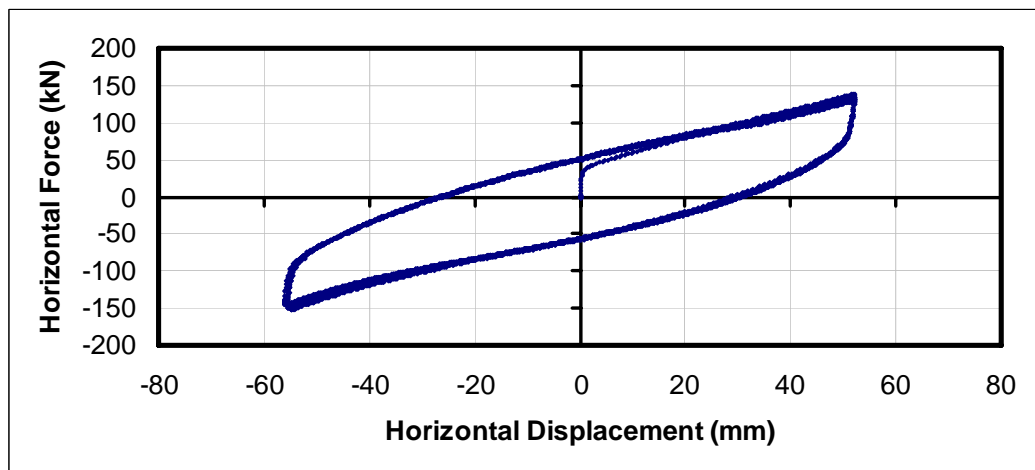


Figure B.41. Hysteresis Loop of Test-107

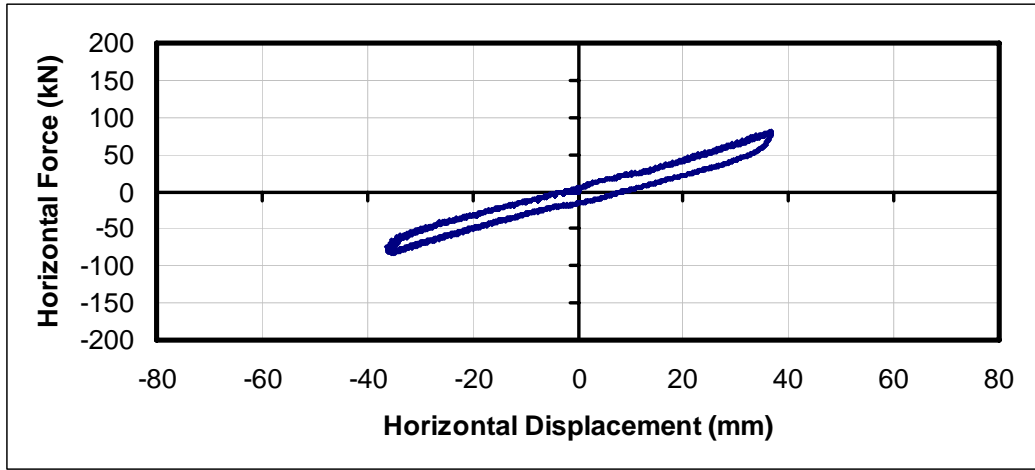


Figure B.42. Hysteresis Loop of Test-112

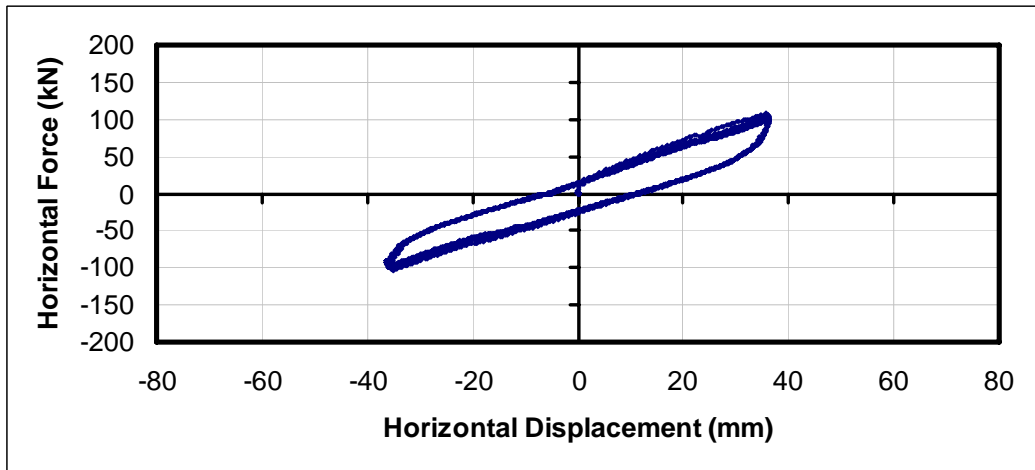


Figure B.43. Hysteresis Loop of Test-113

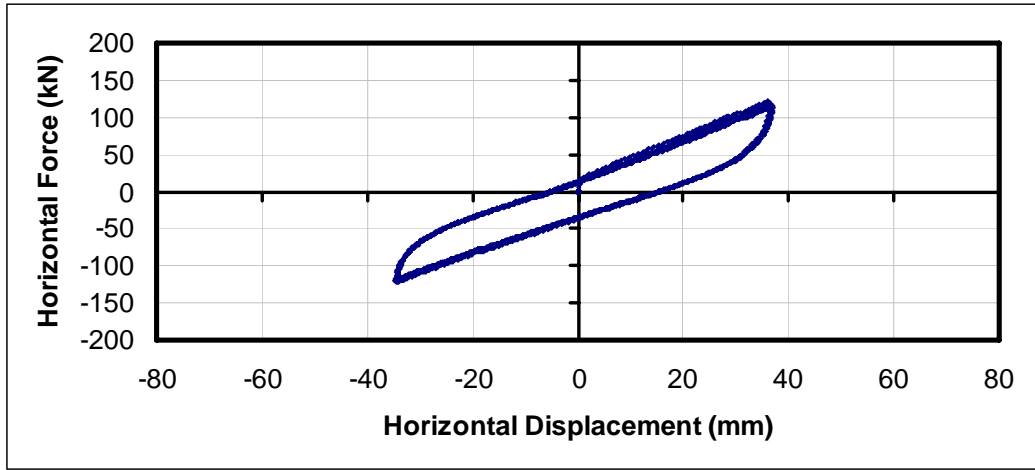


Figure B.44. Hysteresis Loop of Test-114

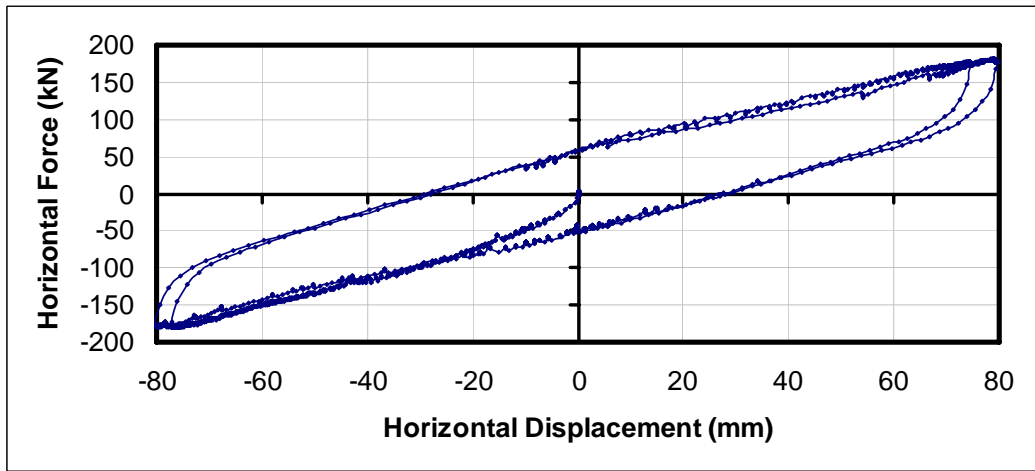


Figure B.45. Hysteresis Loop of Test-120

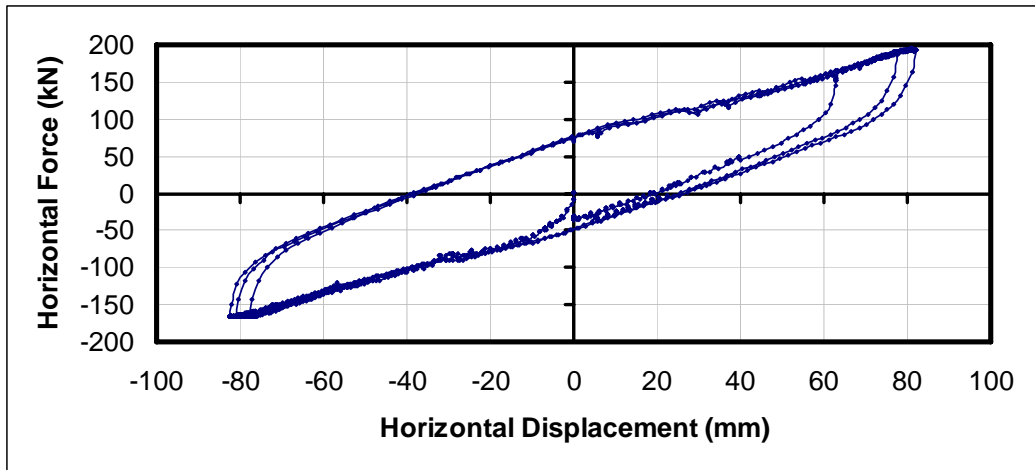


Figure B.46. Hysteresis Loop of Test-121

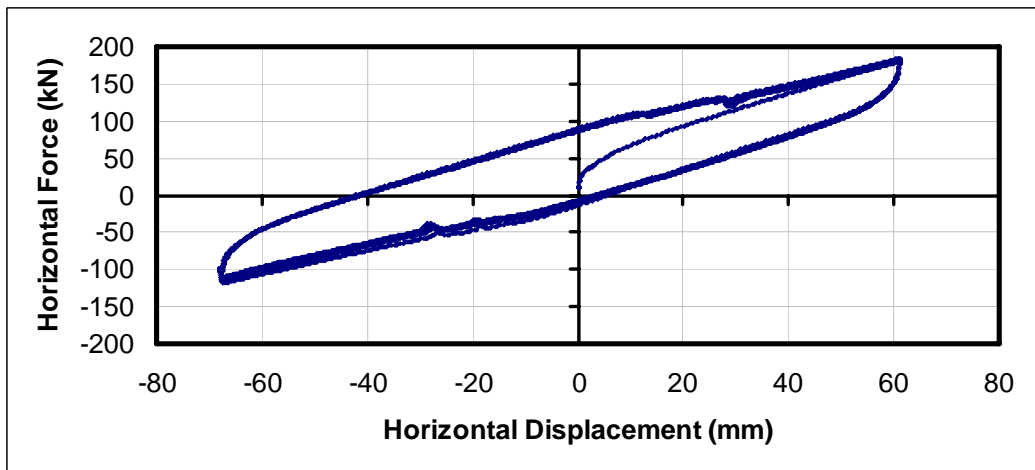


Figure B.47. Hysteresis Loop of Test-122

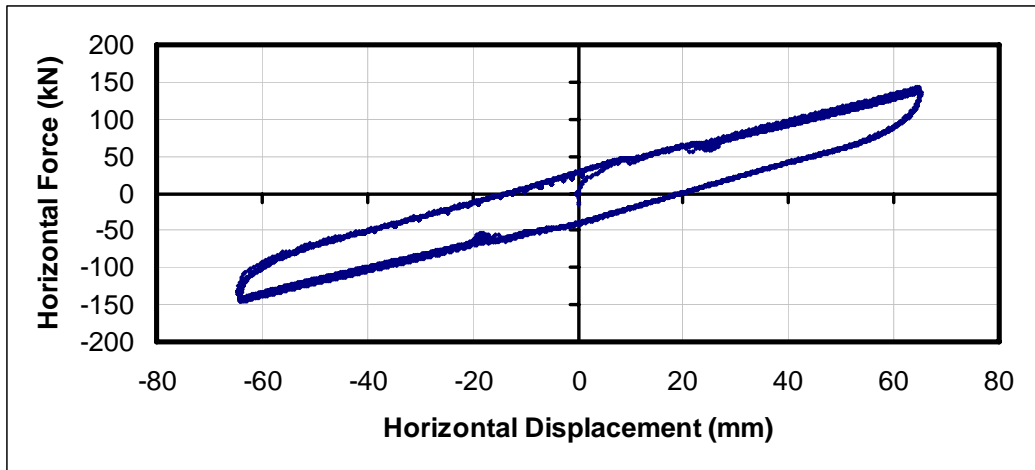


Figure B.48. Hysteresis Loop of Test-123

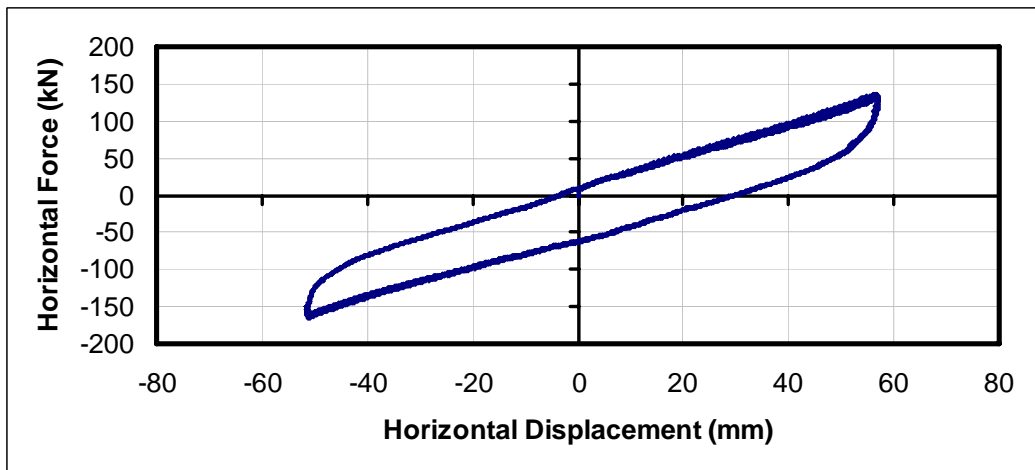


Figure B.49. Hysteresis Loop of Test-124

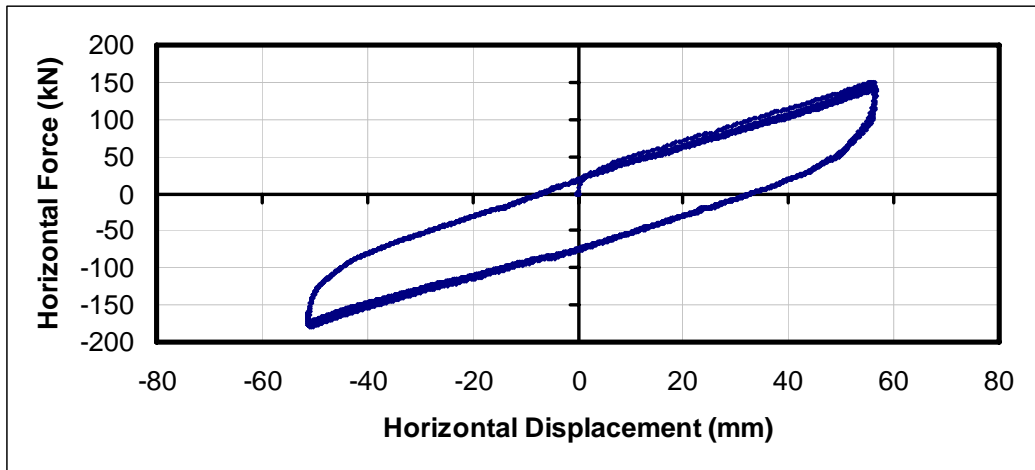


Figure B.50. Hysteresis Loop of Test-125

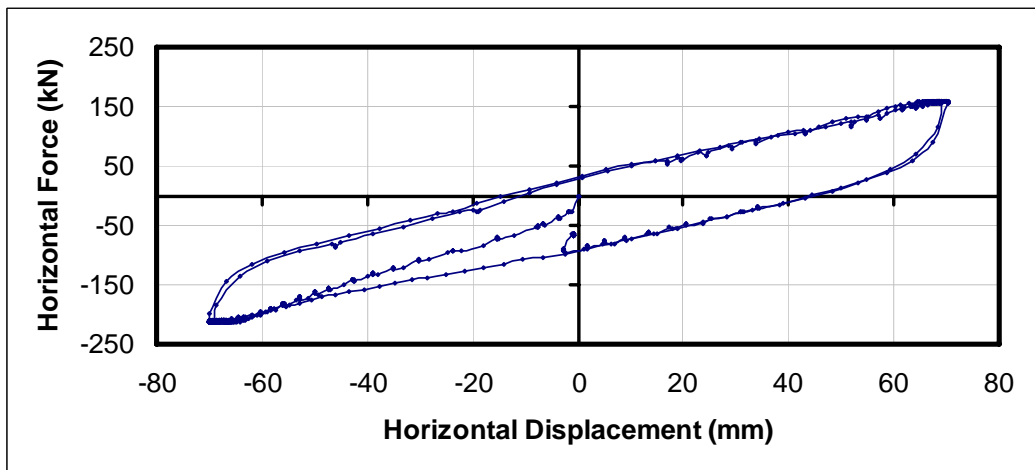


Figure B.51. Hysteresis Loop of Test-126

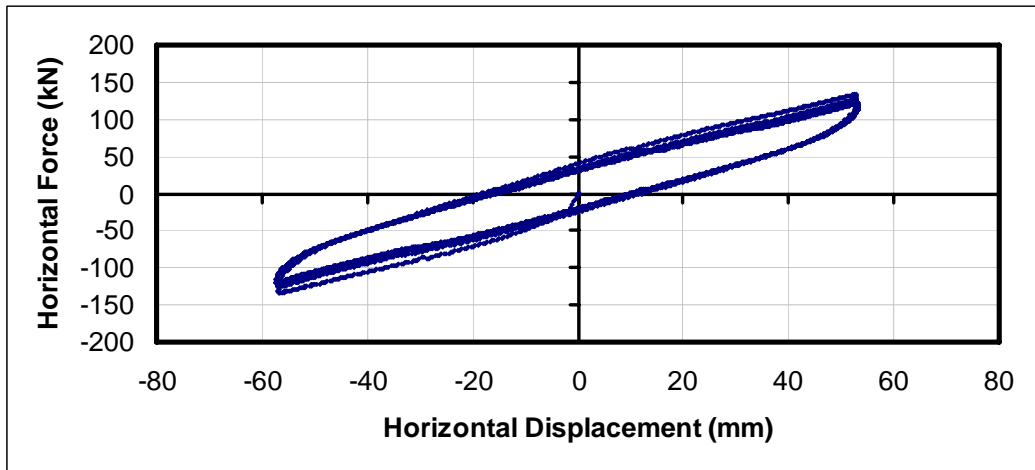


Figure B.52. Hysteresis Loop of Test-127

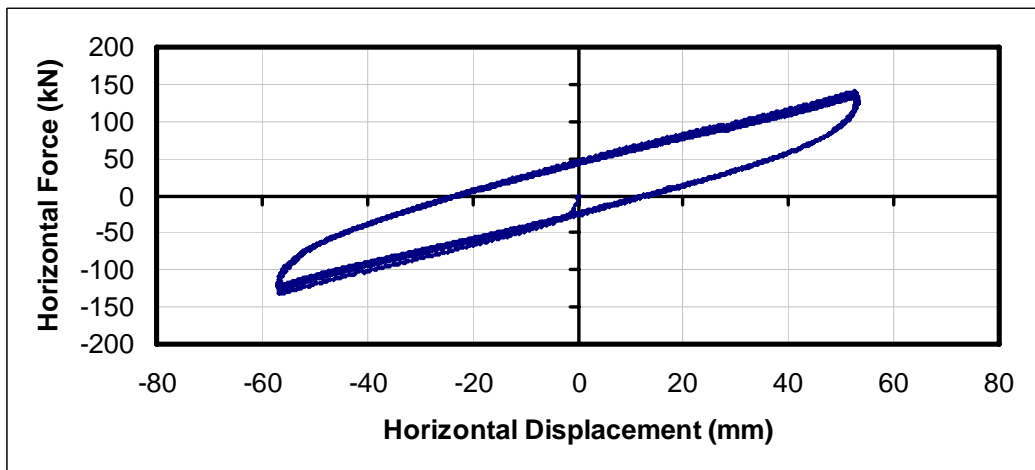


Figure B.53. Hysteresis Loop of Test-128

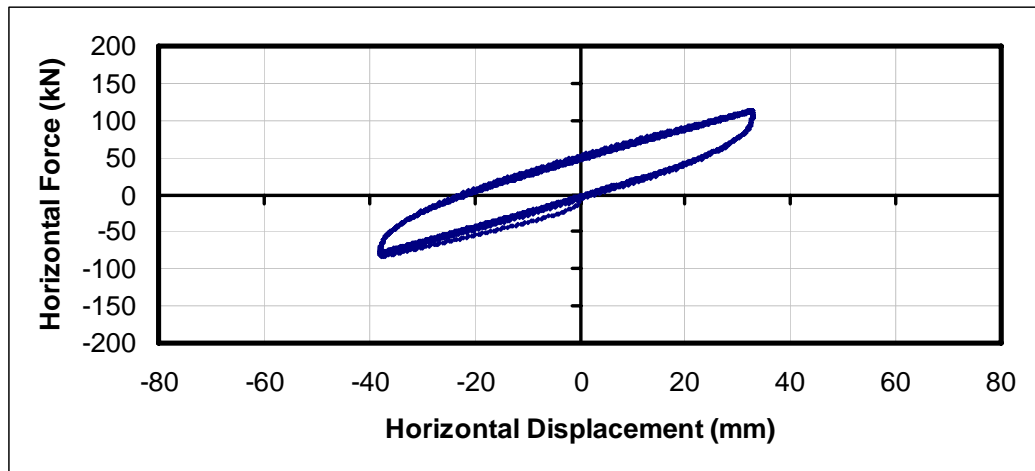


Figure B.54. Hysteresis Loop of Test-129

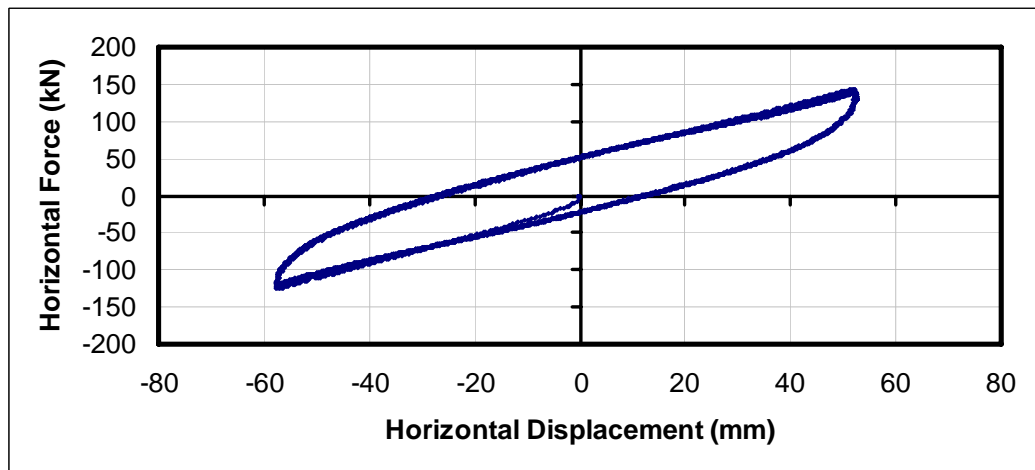


Figure B.55. Hysteresis Loop of Test-130

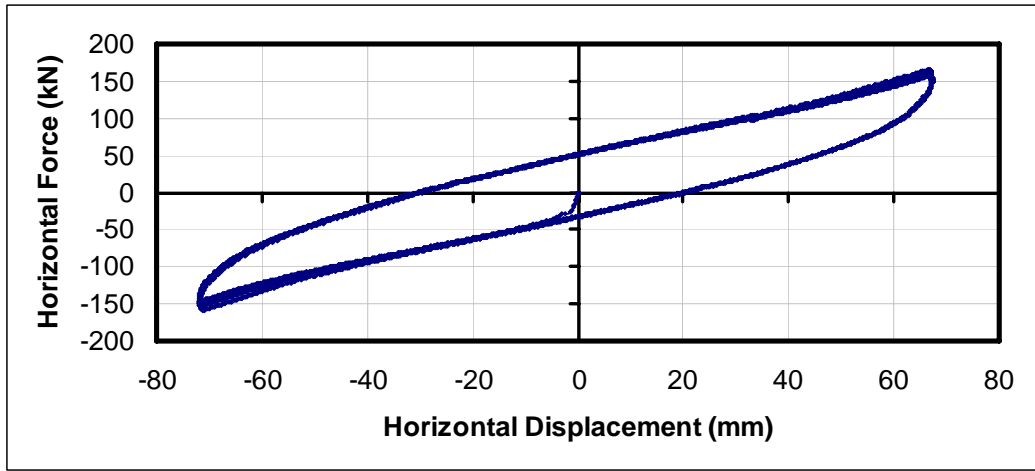


Figure B.56. Hysteresis Loop of Test-131

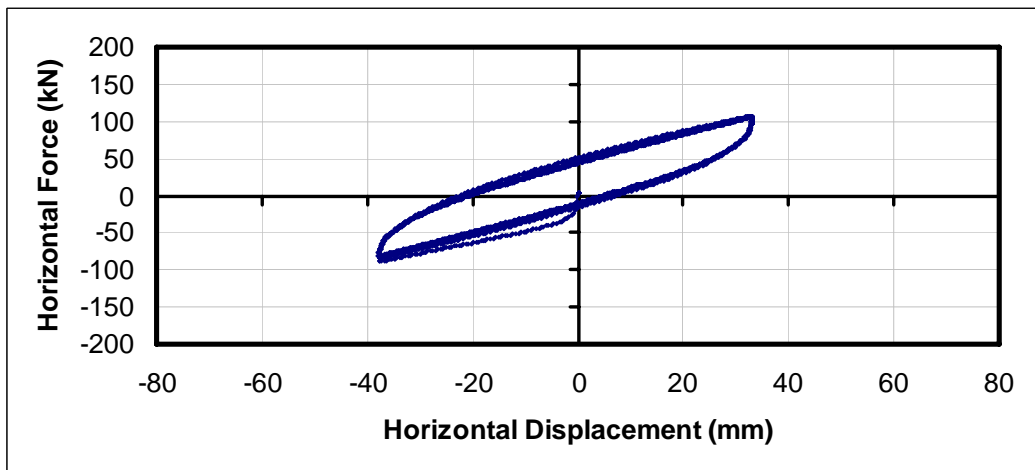


Figure B.57. Hysteresis Loop of Test-132

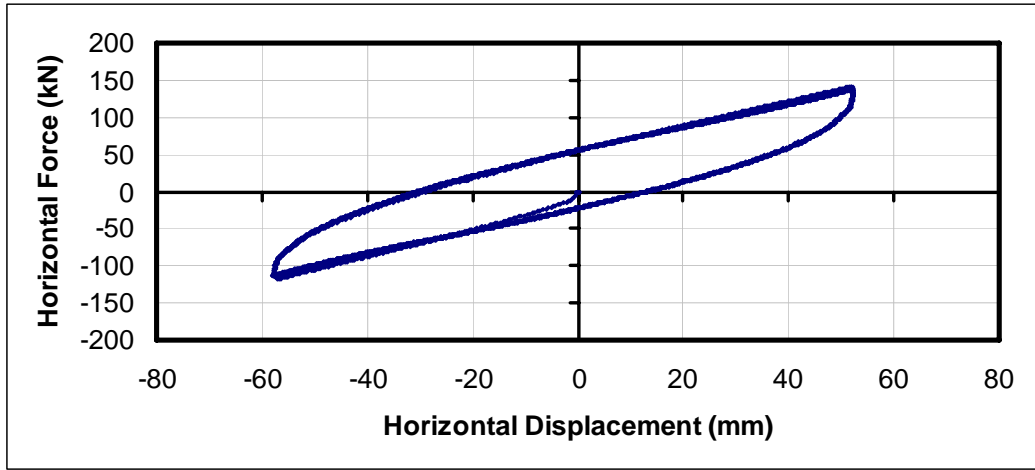


Figure B.58. Hysteresis Loop of Test-133

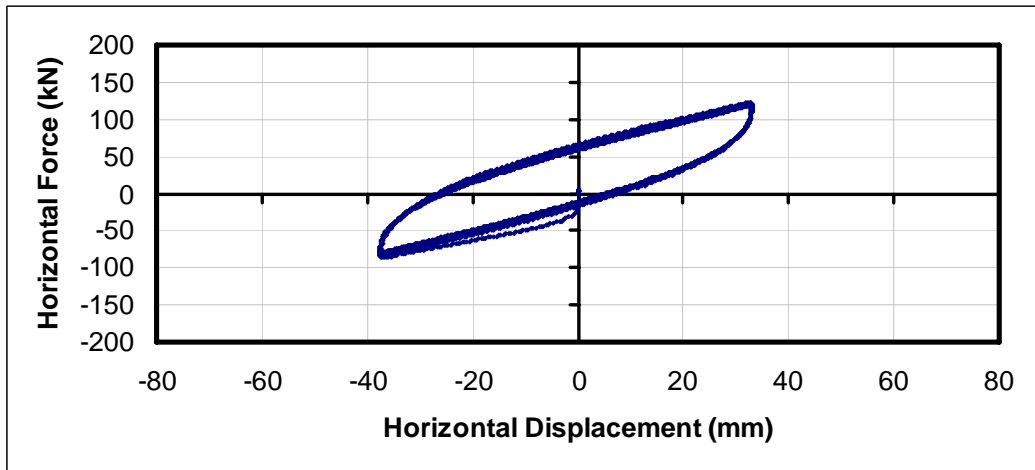


Figure B.59. Hysteresis Loop of Test-134

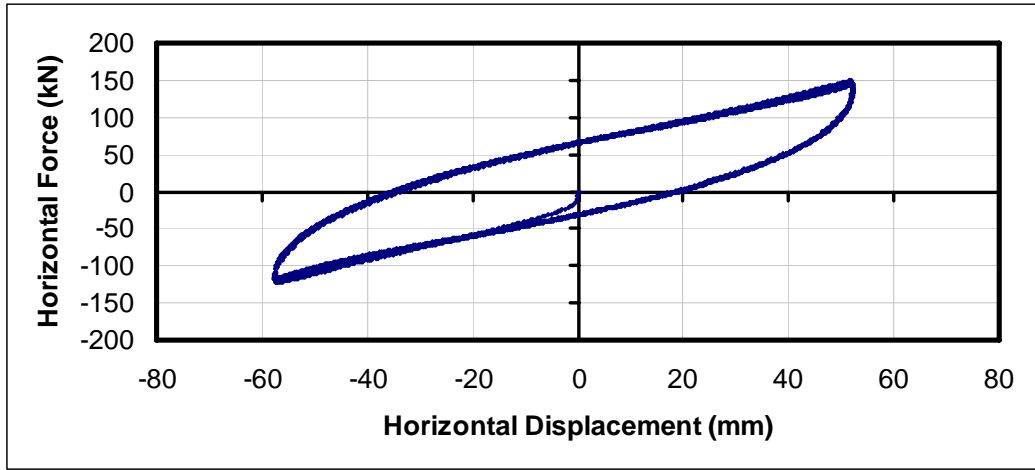


Figure B.60. Hysteresis Loop of Test-135

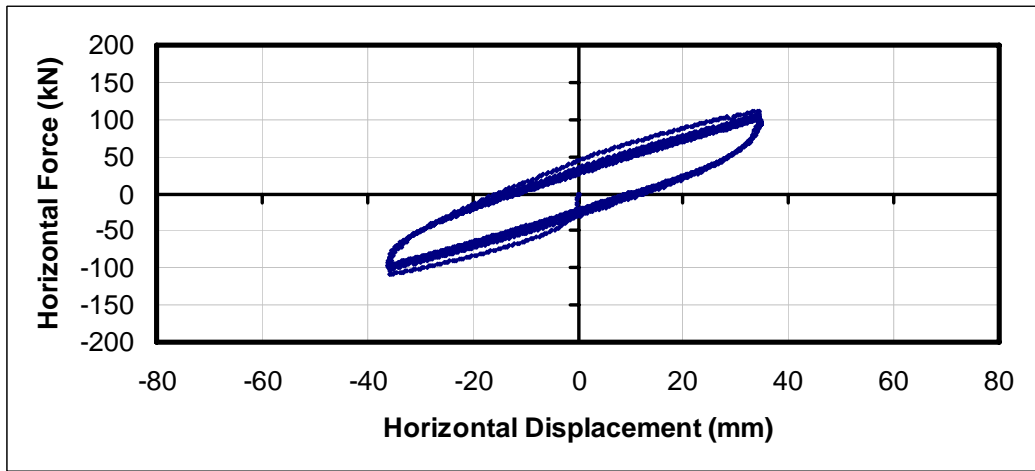


Figure B.61. Hysteresis Loop of Test-139

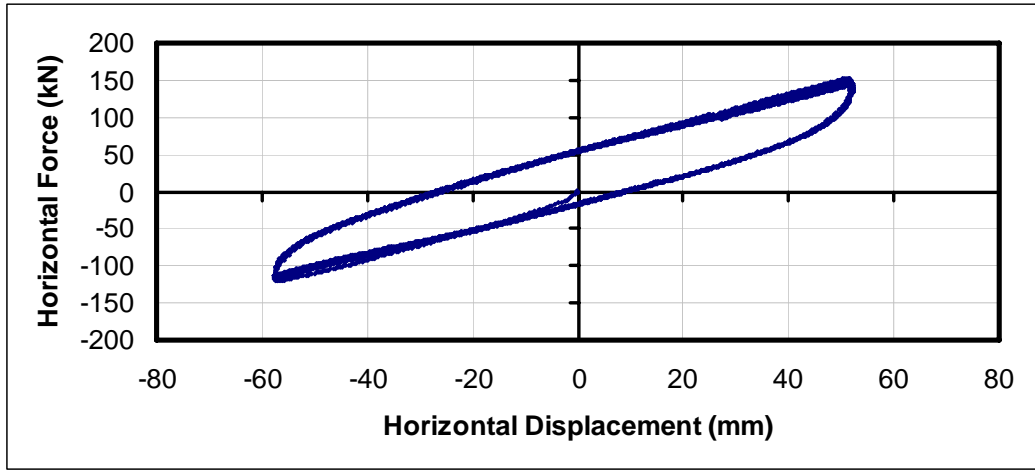


Figure B.62. Hysteresis Loop of Test-140

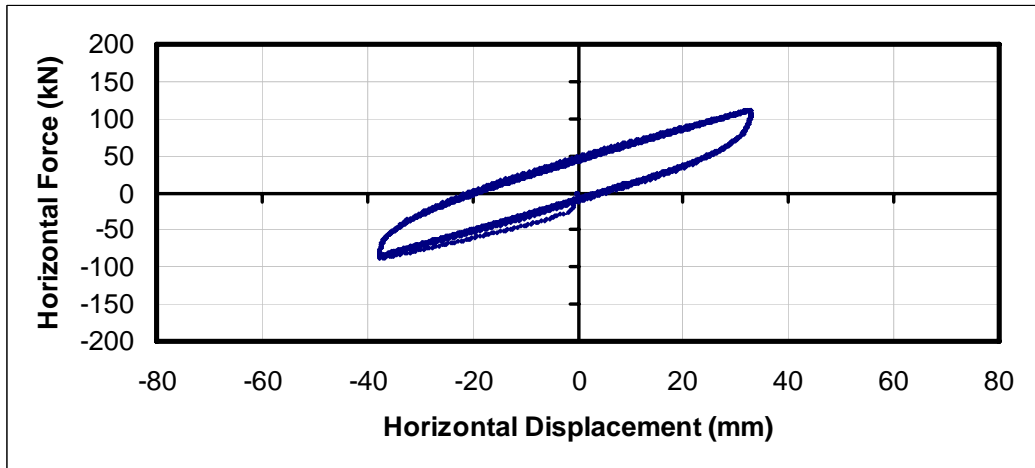


Figure B.63. Hysteresis Loop of Test-141

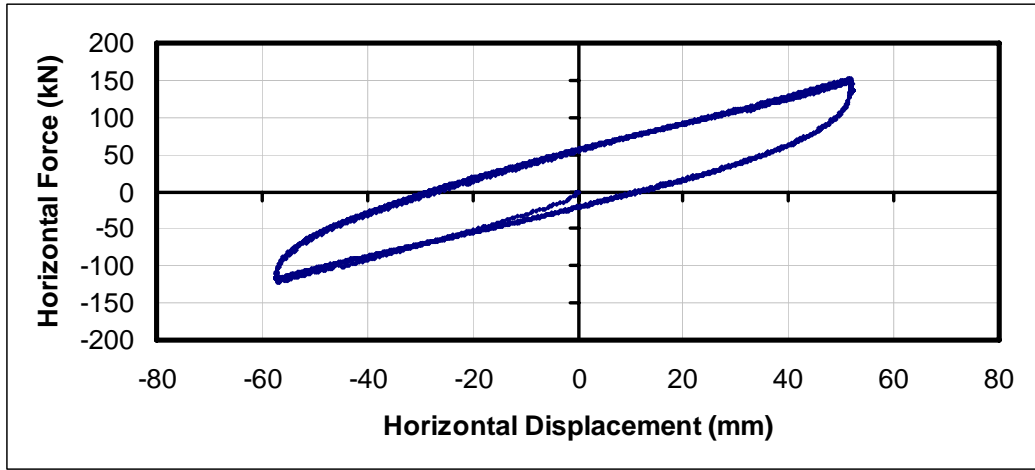


Figure B.64. Hysteresis Loop of Test-142

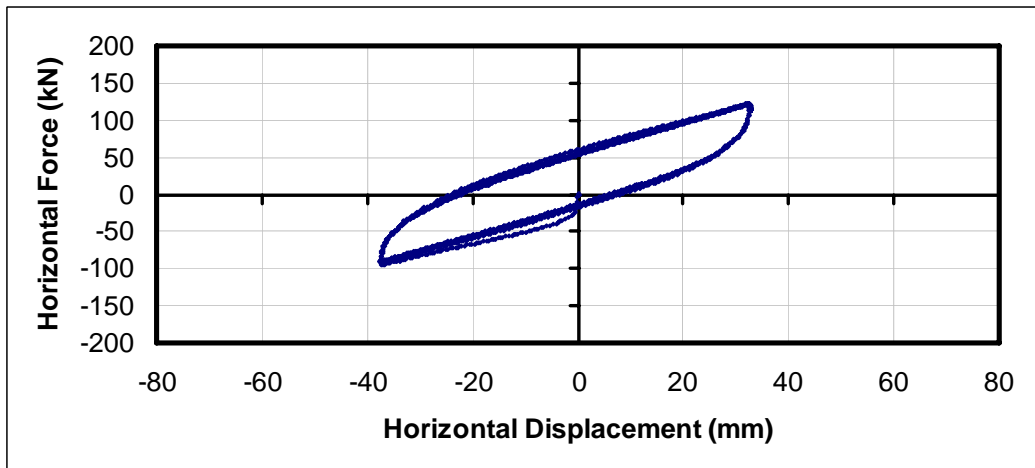


Figure B.65. Hysteresis Loop of Test-143

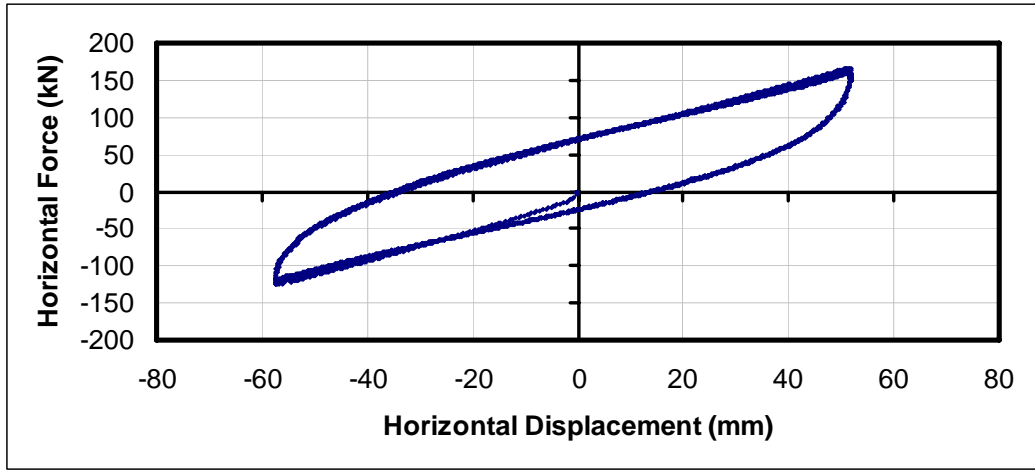


Figure B.66. Hysteresis Loop of Test-144

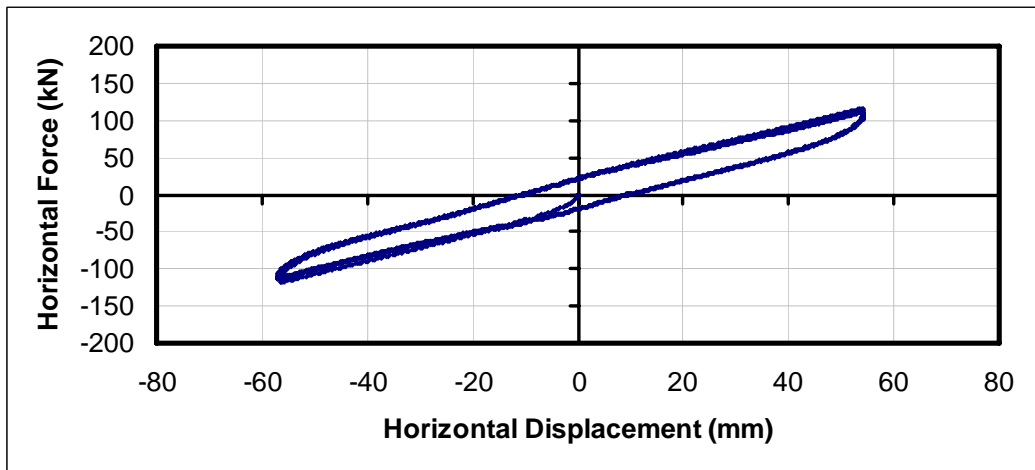


Figure B.67. Hysteresis Loop of Test-145

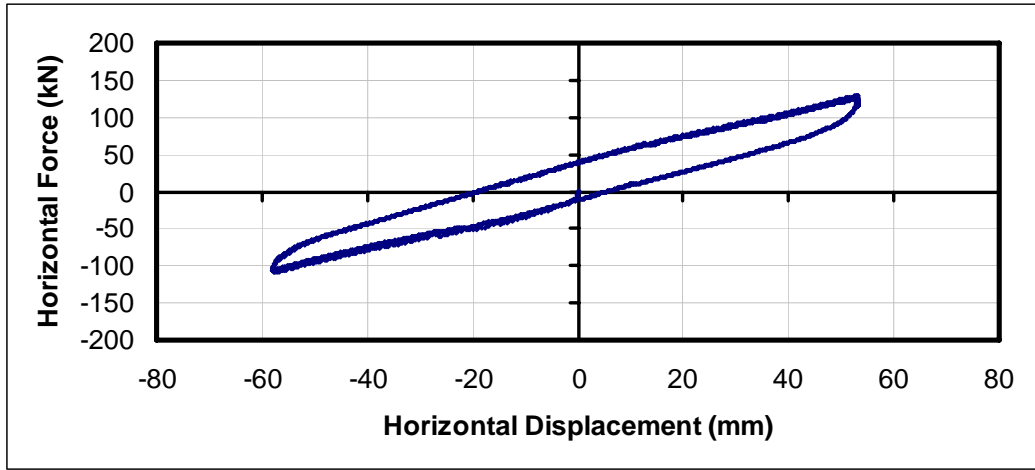


Figure B.68. Hysteresis Loop of Test-146

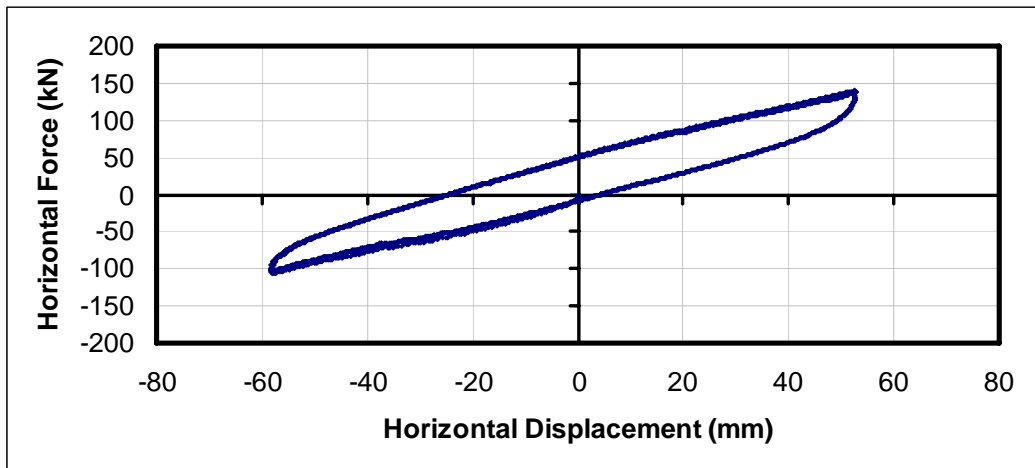


Figure B.69. Hysteresis Loop of Test-147

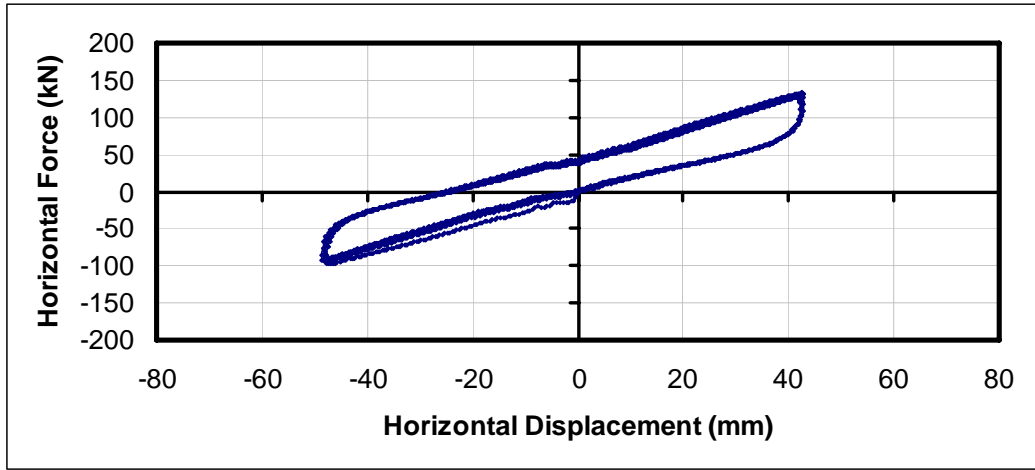


Figure B.70. Hysteresis Loop of Test-154

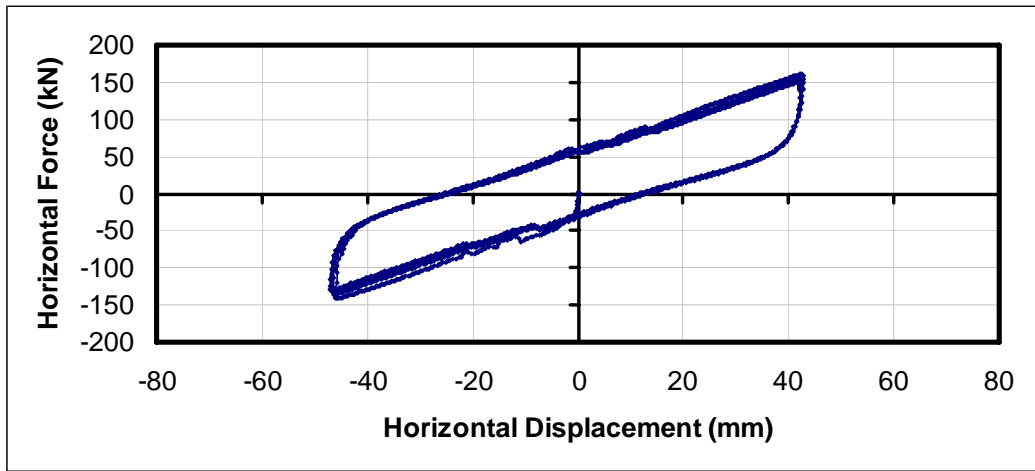


Figure B.71. Hysteresis Loop of Test-155

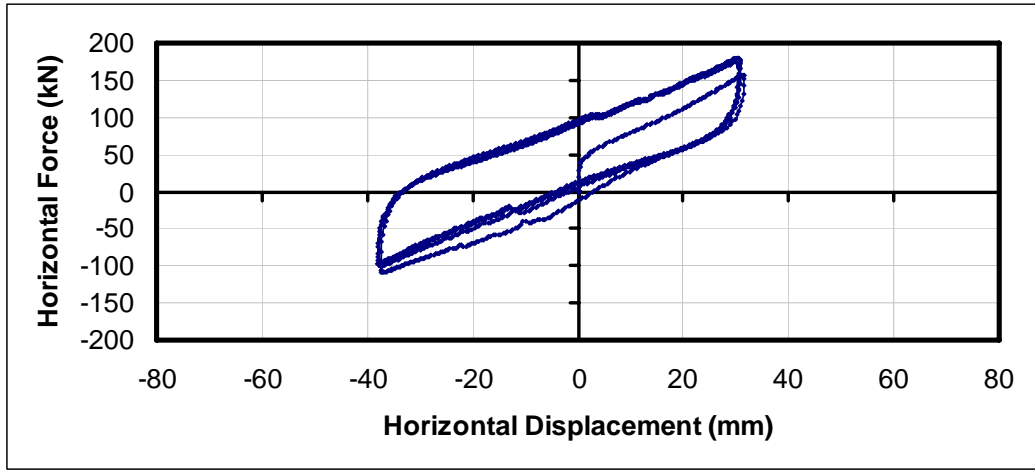


Figure B.72. Hysteresis Loop of Test-156

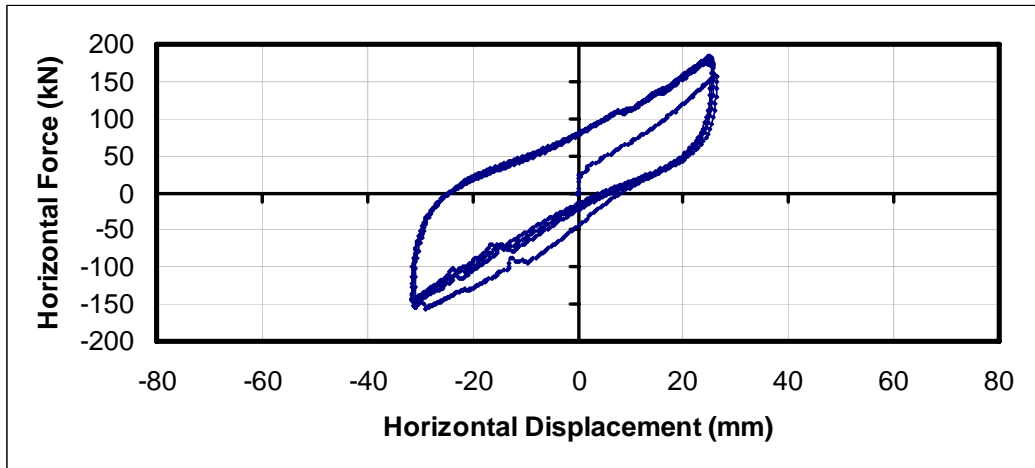


Figure B.73. Hysteresis Loop of Test-157

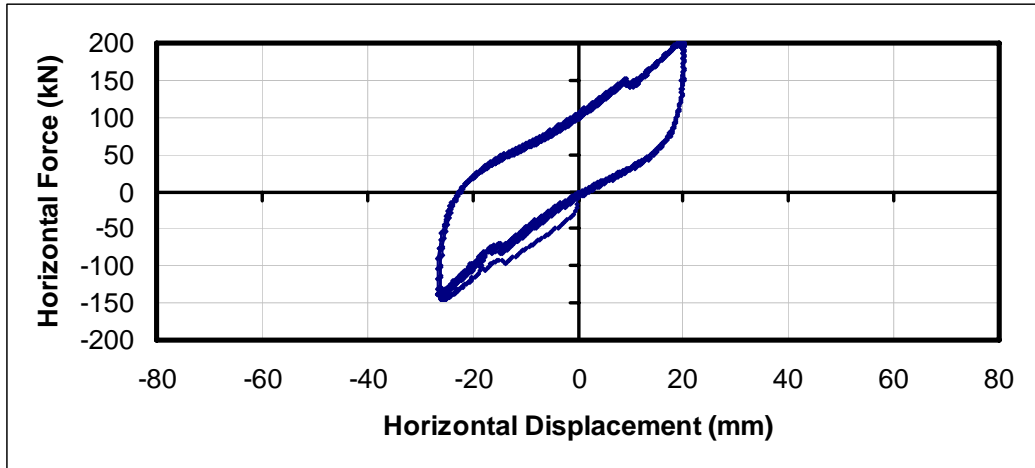


Figure B.74. Hysteresis Loop of Test-158

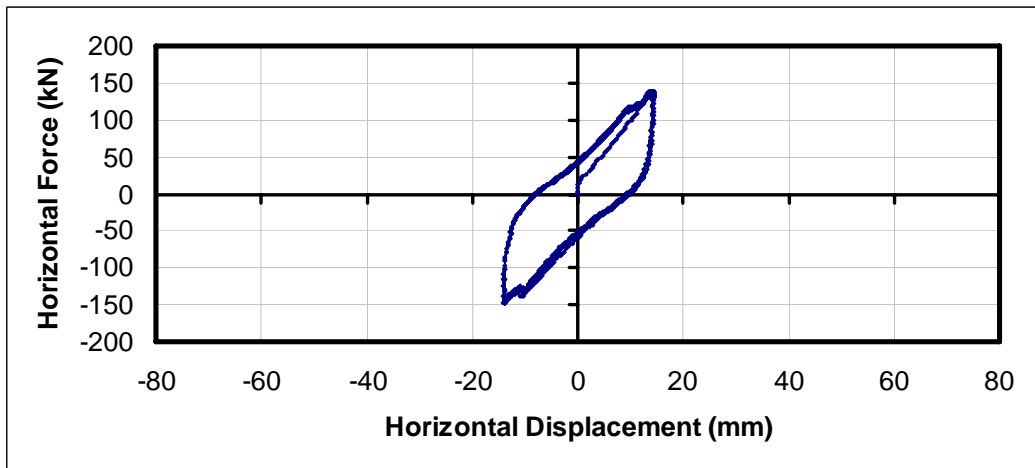


Figure B.75. Hysteresis Loop of Test-159

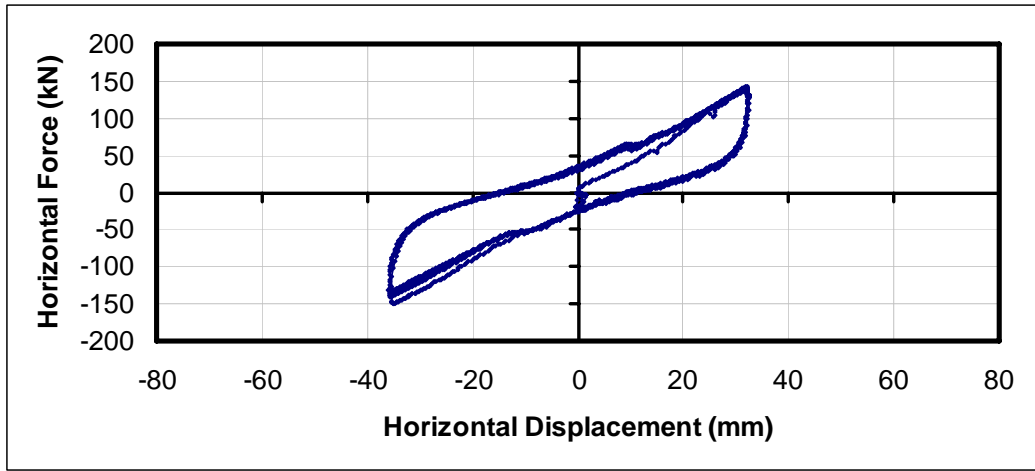


Figure B.76. Hysteresis Loop of Test-160

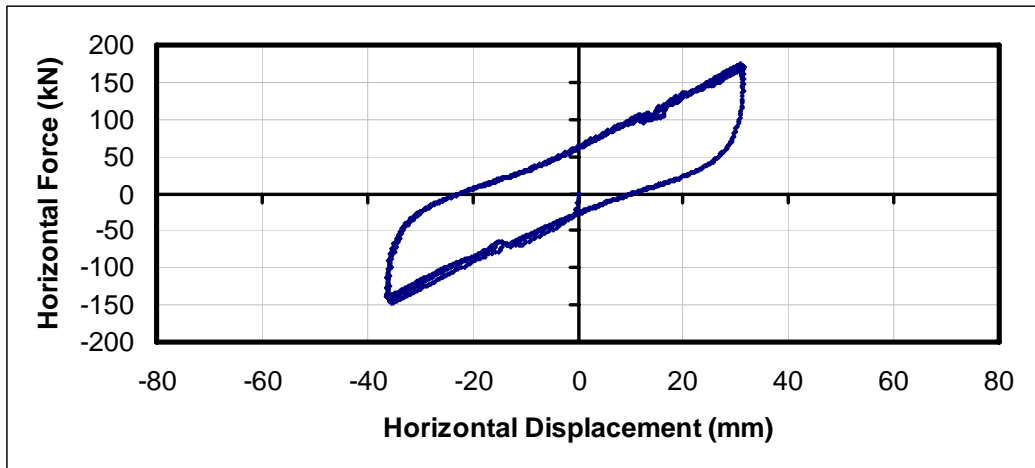


Figure B.77. Hysteresis Loop of Test-161

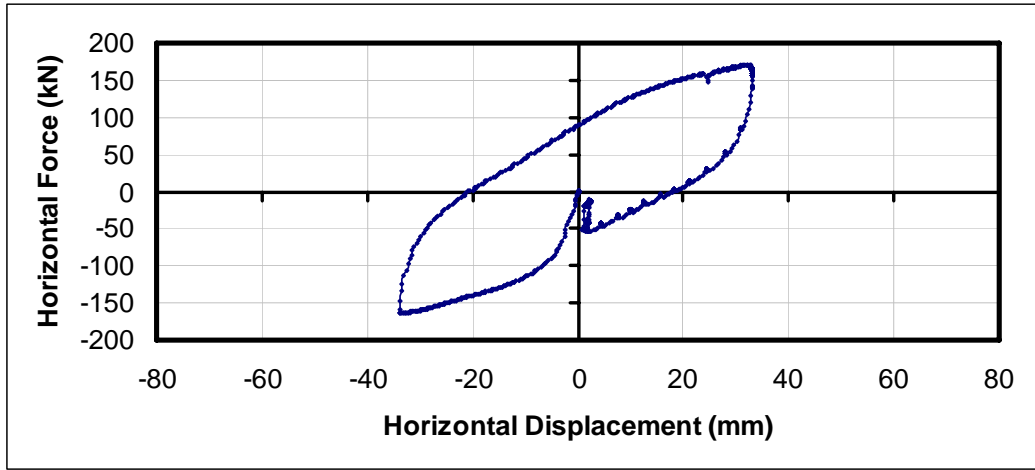


Figure B.78. Hysteresis Loop of Test-175

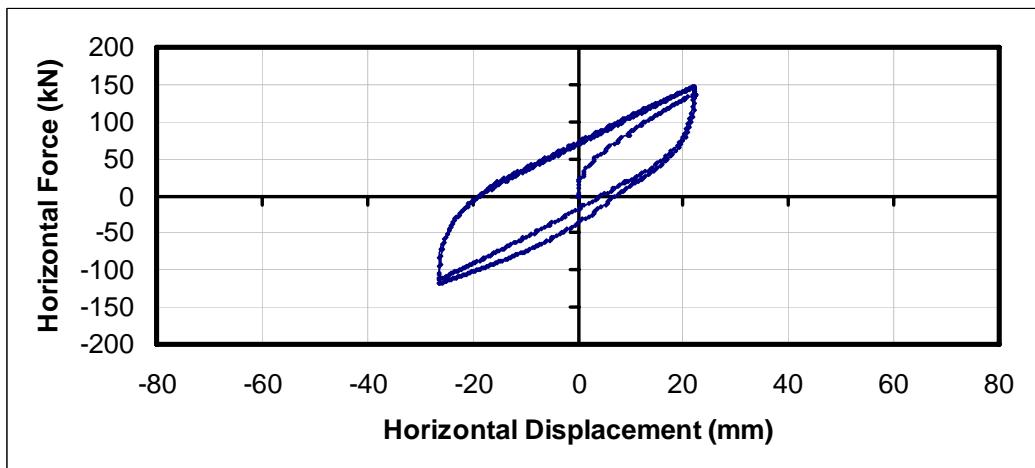


Figure B.79. Hysteresis Loop of Test-176

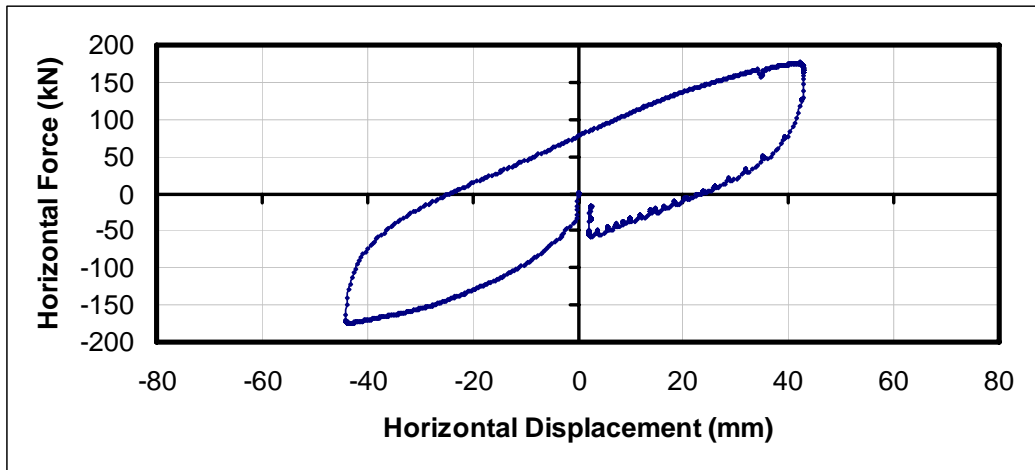


Figure B.80. Hysteresis Loop of Test-177

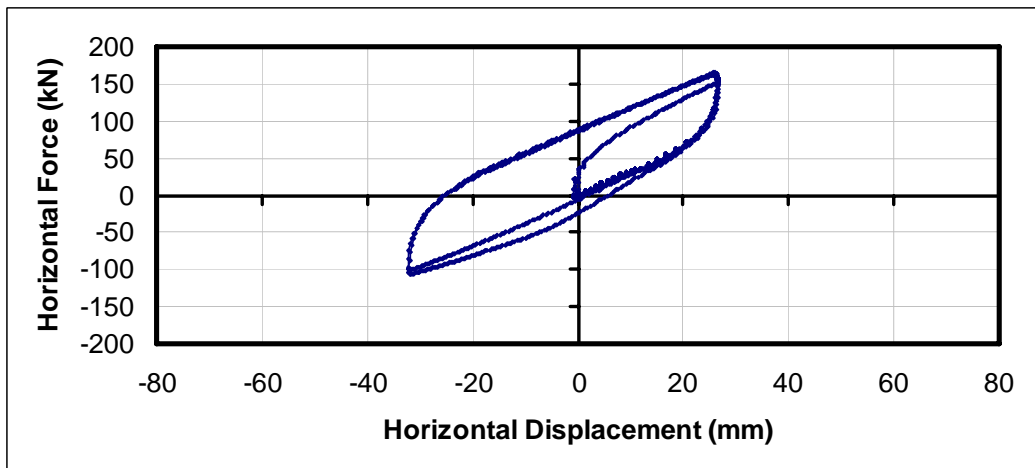


Figure B.81. Hysteresis Loop of Test-178

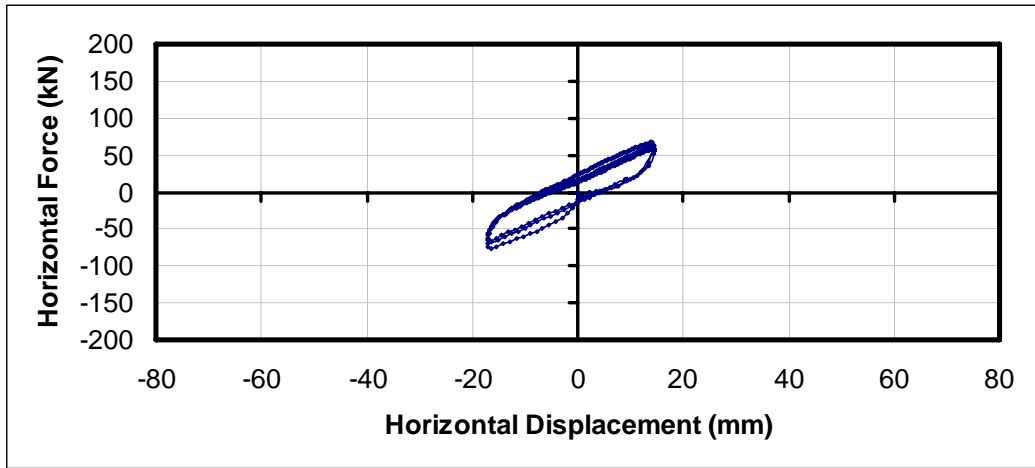


Figure B.82. Hysteresis Loop of Test-204

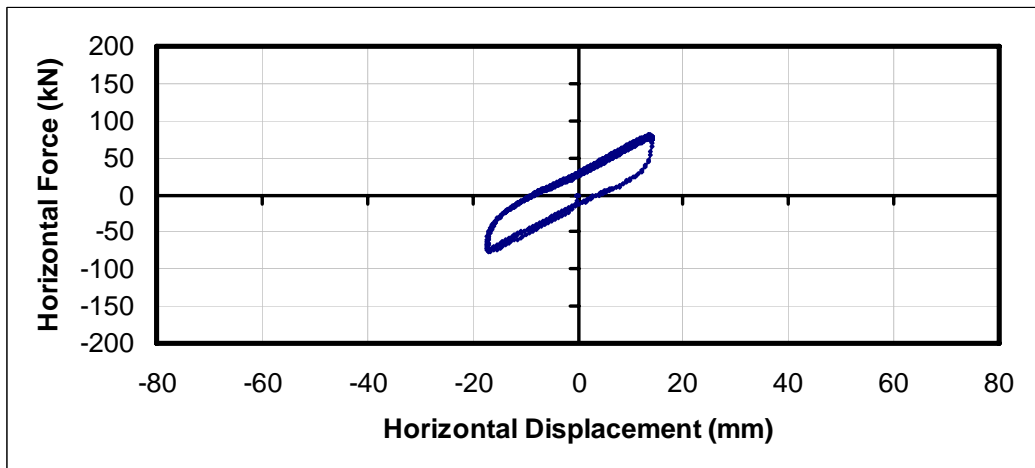


Figure B.83. Hysteresis Loop of Test-205

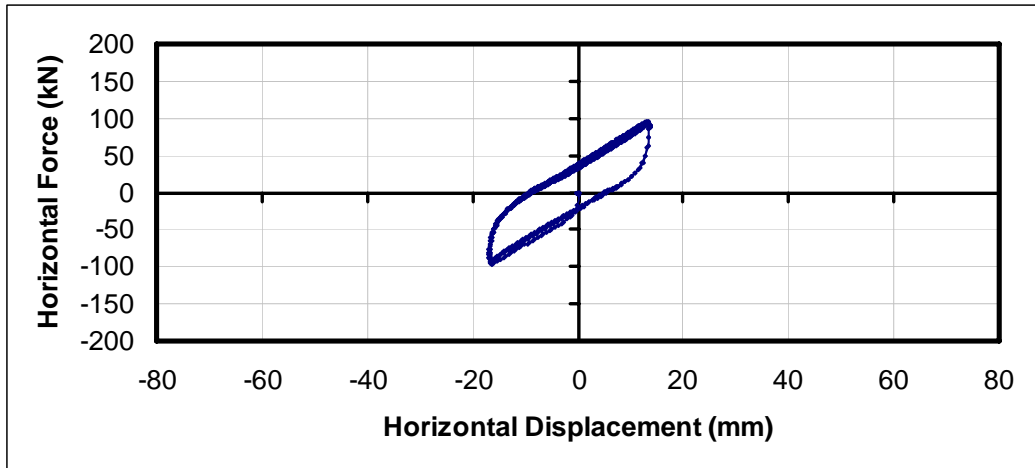


Figure B.84. Hysteresis Loop of Test-206

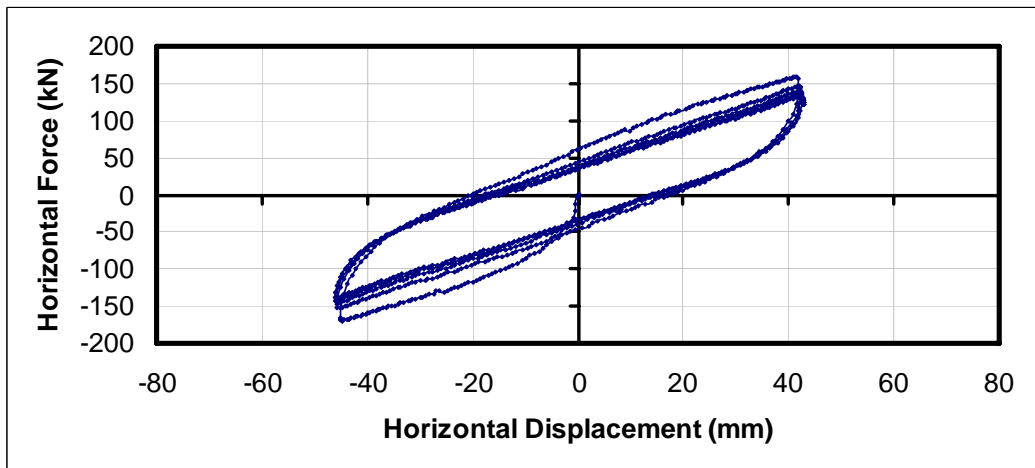


Figure B.85. Hysteresis Loop of Test-207

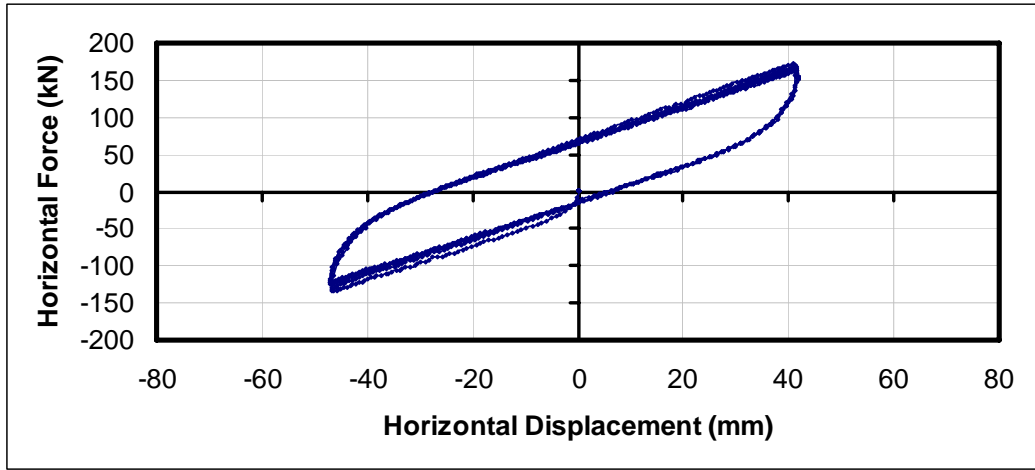


Figure B.86. Hysteresis Loop of Test-208

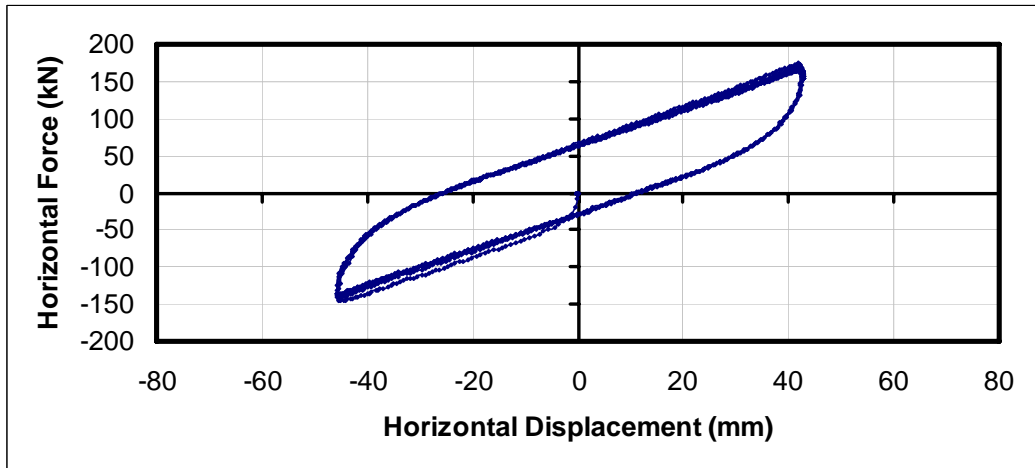


Figure B.87. Hysteresis Loop of Test-209

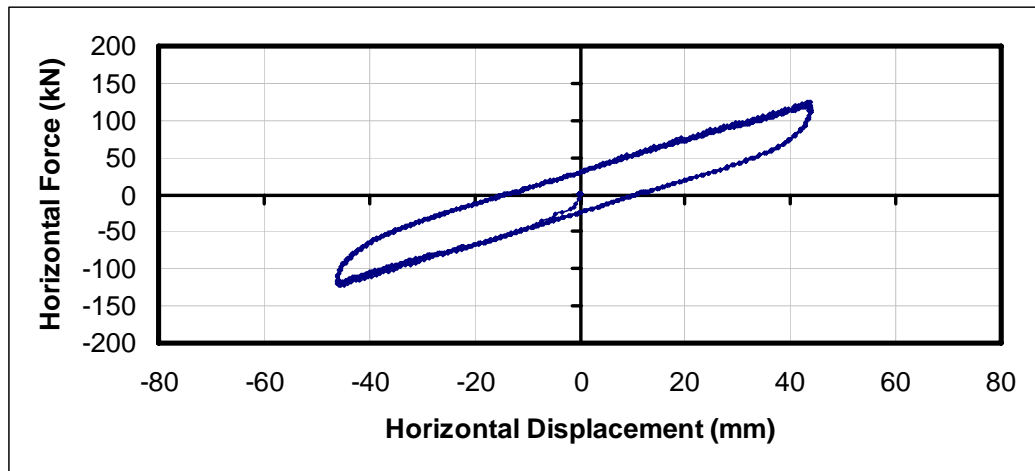


Figure B.88. Hysteresis Loop of Test-210

APPENDIX C

LOAD-DISPLACEMENT GRAPHS OF VERTICAL COMPRESSION TESTS

In Appendix C, load-displacement graphs of 12 vertical compression tests are presented. Detailed information about tests is presented in Table 4.8.

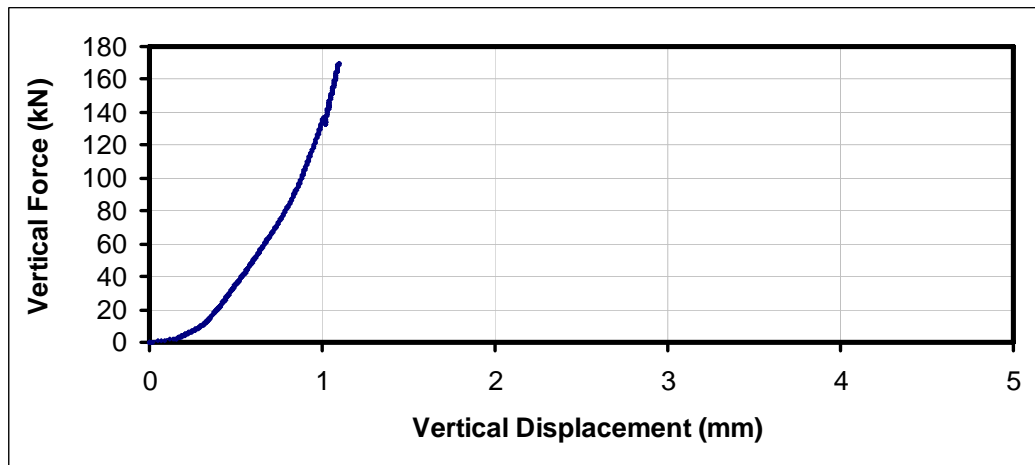


Figure C.1. Vertical Load-Displacement Graph of Test-A1

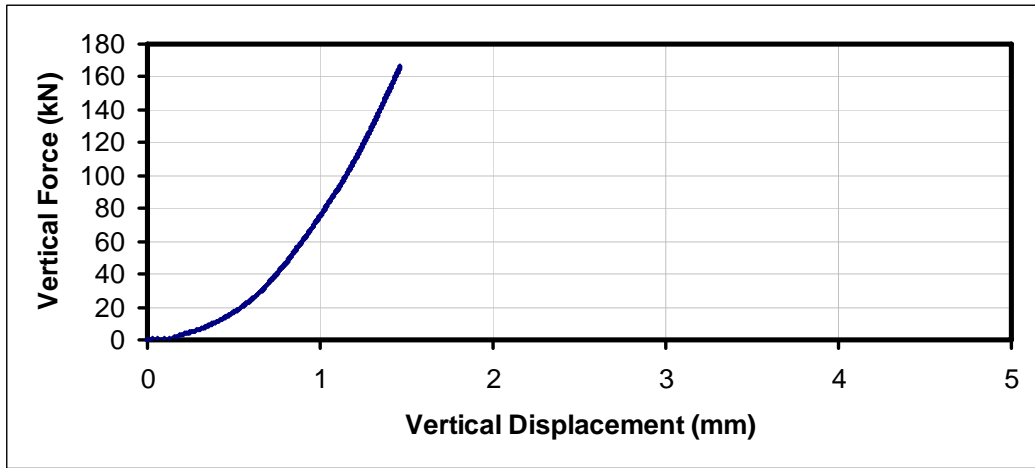


Figure C.2. Vertical Load-Displacement Graph of Test-A2

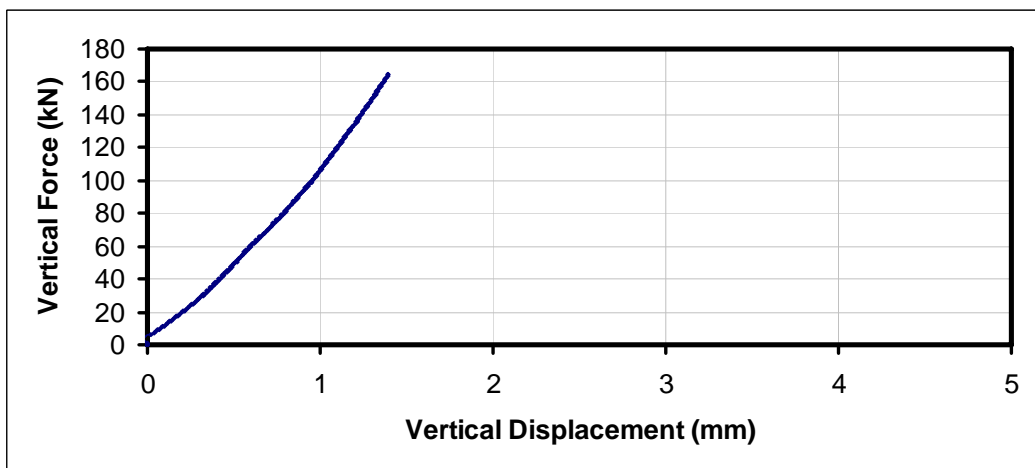


Figure C.3. Vertical Load-Displacement Graph of Test-A3

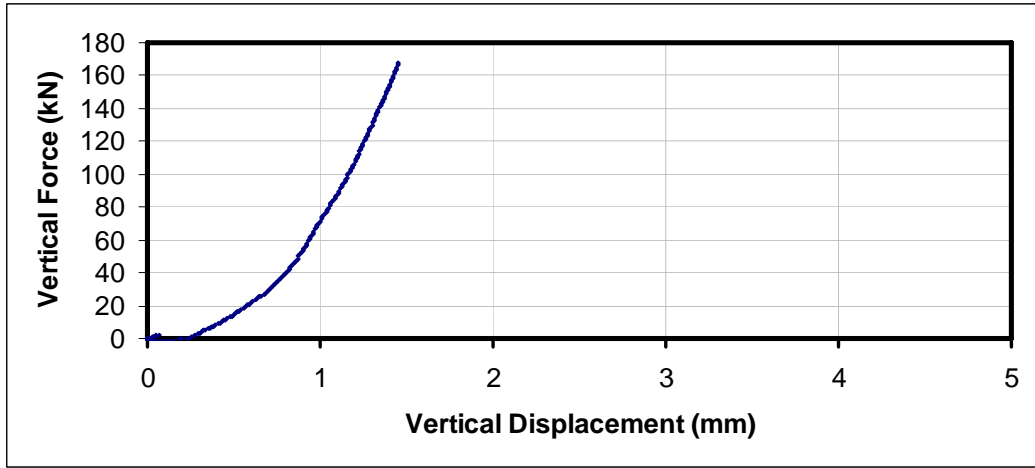


Figure C.4. Vertical Load-Displacement Graph of Test-A4

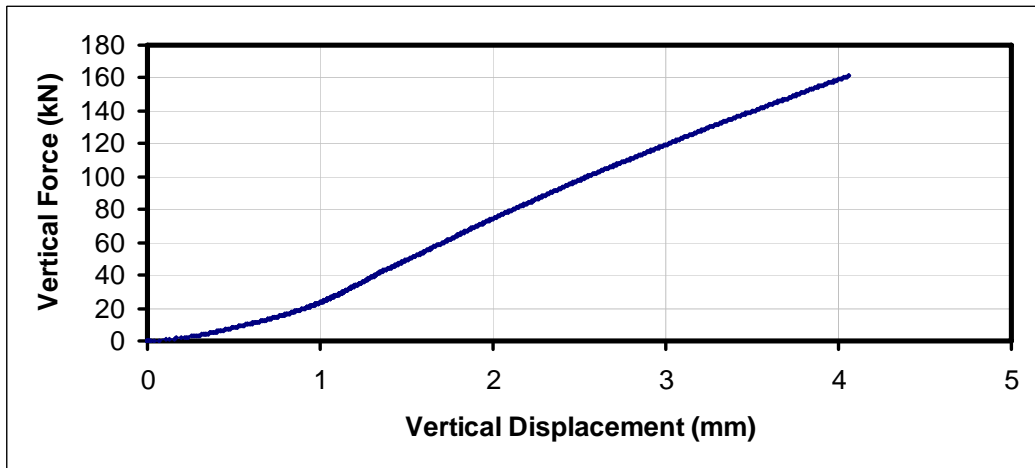


Figure C.5. Vertical Load-Displacement Graph of Test-A5

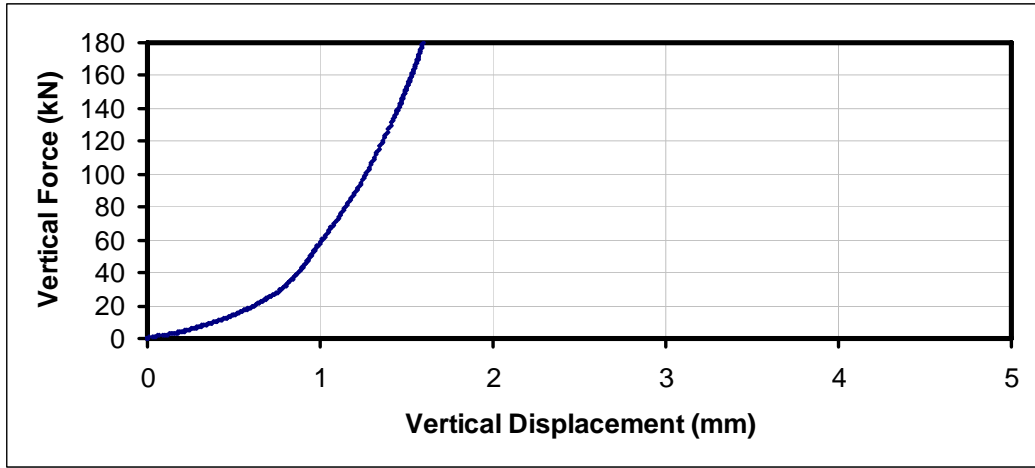


Figure C.6. Vertical Load-Displacement Graph of Test-A6

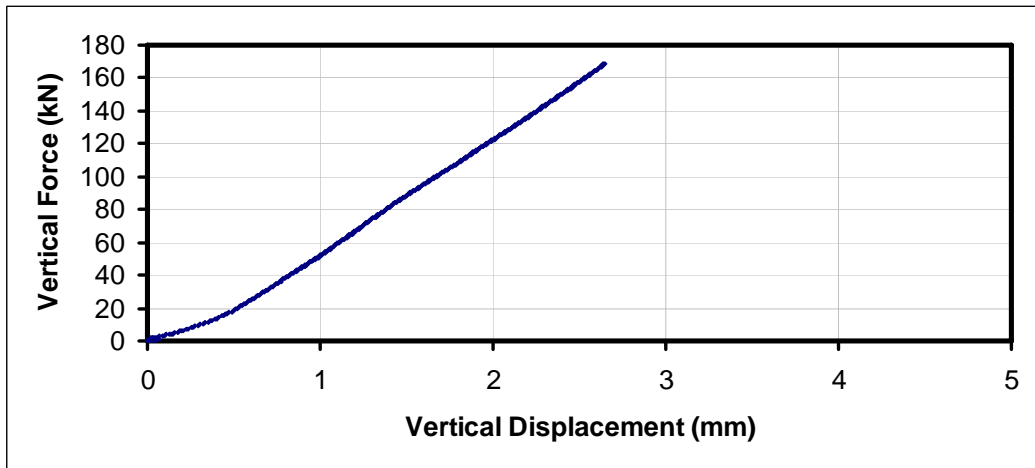


Figure C.7. Vertical Load-Displacement Graph of Test-A7

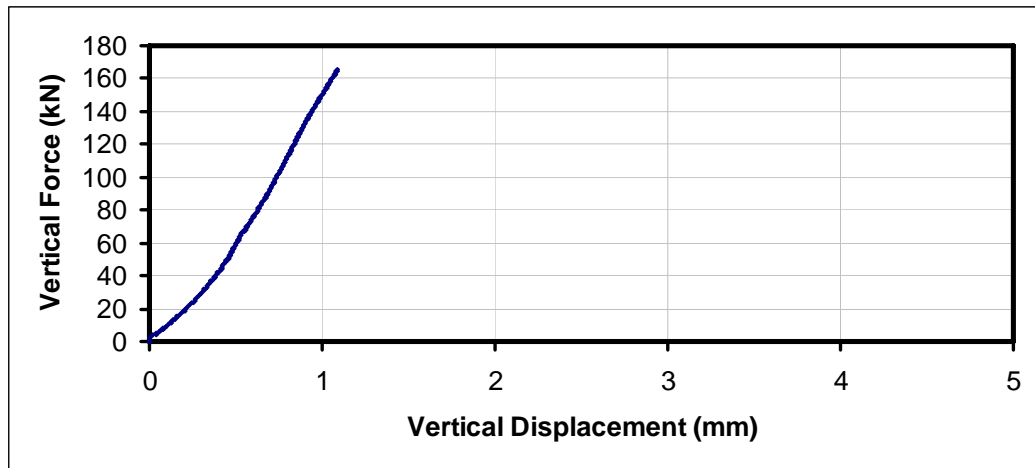


Figure C.8. Vertical Load-Displacement Graph of Test-A8

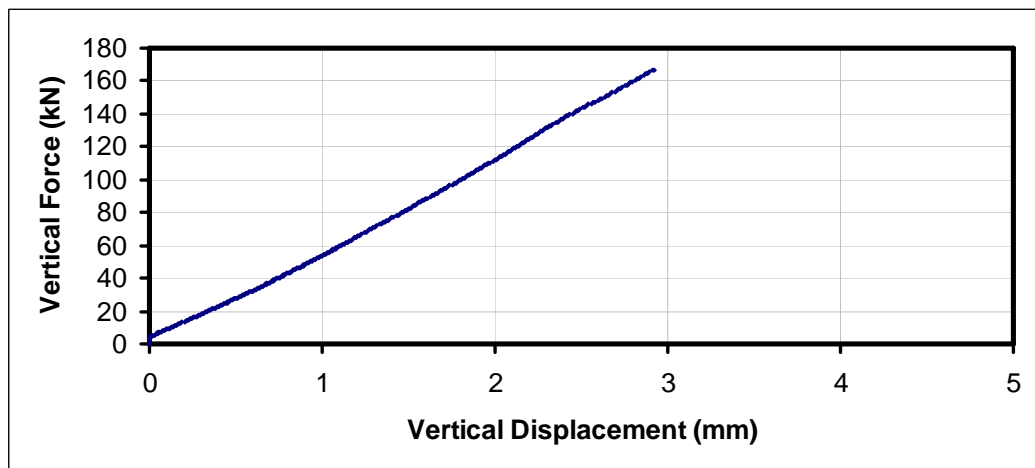


Figure C.9. Vertical Load-Displacement Graph of Test-A9

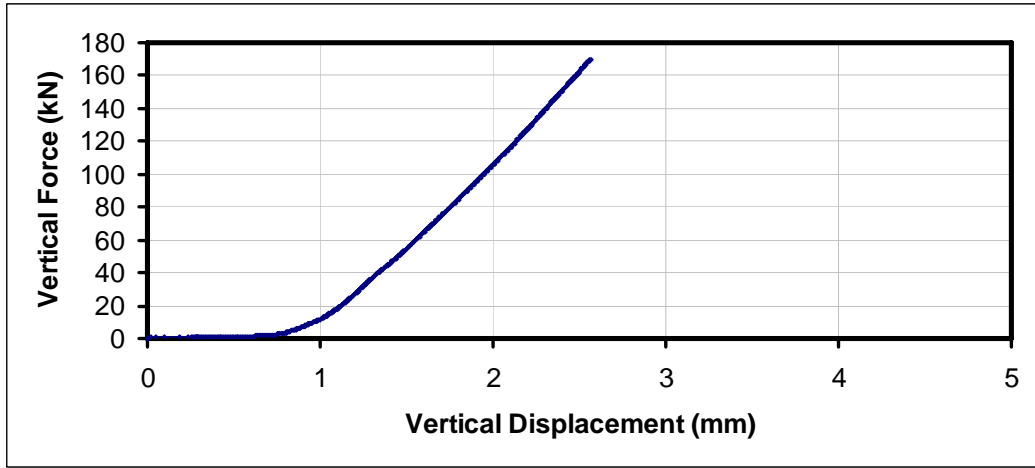


Figure C.10. Vertical Load-Displacement Graph of Test-A10

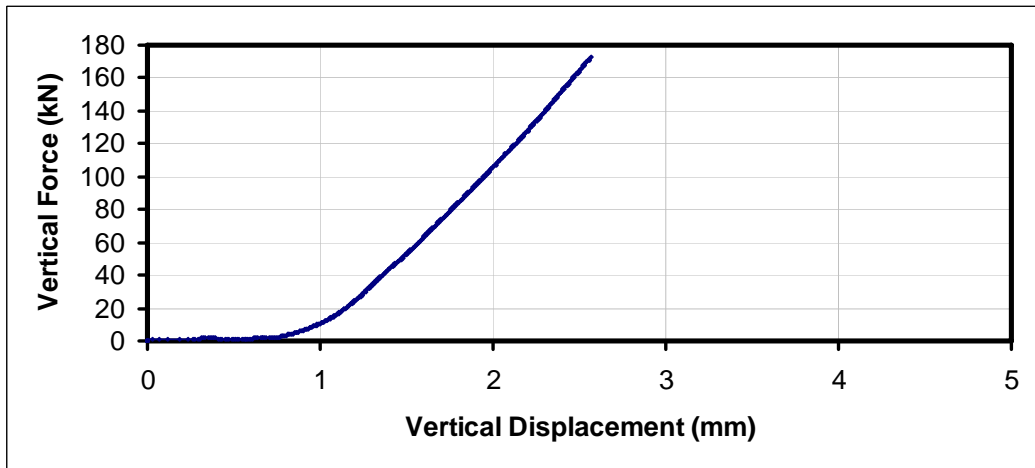


Figure C.11. Vertical Load-Displacement Graph of Test-A11

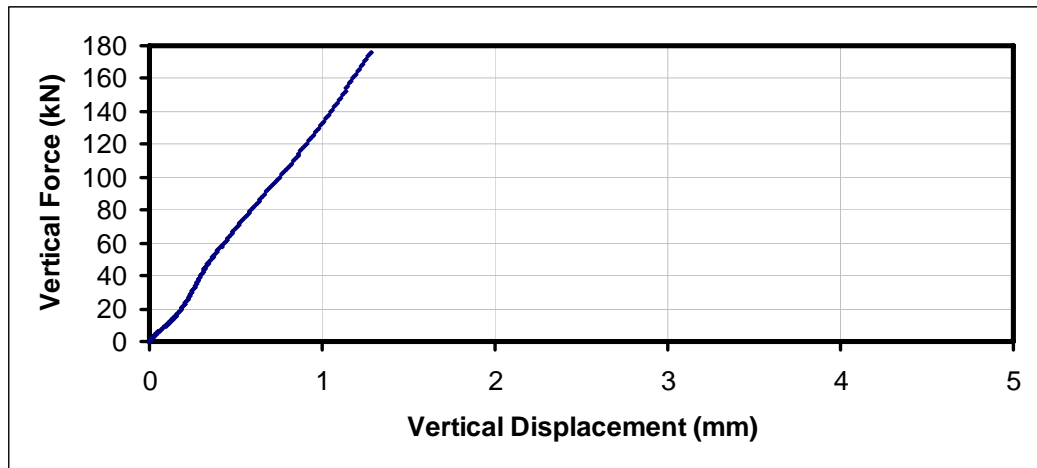


Figure C.12. Vertical Load-Displacement Graph of Test-A12

VITA

PERSONAL INFORMATION

Surname, Name: Özkaya, Cenan

Nationality: Turkish (TC)

Date and Place of Birth: 6 April 1980, Bursa

Marital Status: Single

Phone: +90 312 495 70 00/180

email: kucukdahi@hotmail.com

EDUCATION

Degree	Institution	Year of Graduation
MS	METU Civil Engineering	2005
BS	METU Civil Engineering	2003
High School	Ulubatlı Hasan Anadolu High School, Bursa	1998

WORK EXPERIENCE

Year	Place	Enrollment
2004-Present	Yuksel Proje	Project Engineer

FOREIGN LANGUAGES

Advanced English, Elementary Italian

PUBLICATIONS

1. Caner, A., Özkaya, C., “Performance Based Design of Long-Span Cable Stayed Bridge Towers,” International Bridge Conference, IBC 09-33, Pittsburgh, USA, June-2009.
2. Özkaya C., Caner, A., “Assessment of Seismic Performance of Seismically Isolated Bridges with Inverted T-Cap Beams,” Concrete Bridge Conference, St. Louis, May 2008.
3. Özkaya, C., Caner, A., “Establishing Seismic Performance of Seismically Isolated Standard Highway Bridges with Inverted T-Cap Beams,” 1st Bridges and Viaducts Conference, Antalya, November-2007. [In Turkish]
4. Özkaya, C., Çelebi, N., Tulumtaş, F., Dicleli, M., “Hybrid Seismic Isolation Design of Sakarya-II Viaduct in the Proximity of the North Anatolian Fault,” IABMAS 2010, Philadelphia, 11-15 July 2010.
5. Marioni, A., Özkaya, C., Dicleli, M., Gerçek, M., “Rock Steady: Sakarya Bridge in Turkey,” Bridge Design and Engineering, Issue No. 59, 2nd Quarter 2010, pp. 52-53.

HOBBIES

Reading, Books, Turkish Movies, Travelling,